AGH UNIVERSITY OF SCIENCE AND TECHNOLOGY

FIELD OF SCIENCE: Natural Sciences

SCIENTIFIC DISCIPLINE: Physical Sciences

DOCTORAL THESIS

Thermal fluctuations in high-temperature superconductors

Fluktuacje termiczne w nadprzewodnikach wysokotemperaturowych

Author: Marek Łukasz Giebułtowski

Supervisor: Dr hab. inż. Wojciech Tabiś
Assisting supervisor: Dr Ryszard Zalecki

Completed at the AGH University of Science and Technology,
Faculty of Physics and Applied Computer Science,
Department of Solid State Physics

Krakow, 2023

Oświadczenie autora rozprawy:

Oświadczam, świadomy odpowiedzialności karnej za poświadczenie nieprawdy, że niniejszą pracę doktorską wykonałem osobiście i samodzielnie i nie korzystałem ze źródeł innych niż wymienione w pracy.

data, podpis autora

Oświadczenie promotora rozprawy:

Niniejsza rozprawa jest gotowa do oceny przez recenzentów.

data, podpis promotora rozprawy

Abstract

This PhD thesis focuses on the synthesis and characterization of thallium cuprates, $Tl_2Ba_2Ca_2Cu_3O_x$ (Tl-2223), also doped with ferromagnetic elements (Co, Ni, Gd). The main objectives were to optimize the synthesis process and investigate the superconducting properties of the materials. The optimization process included the determination of the optimal conditions for the precursors preparation, synthesis conditions as well as the post-synthesis treatment. This was achieved by the systematic characterization of the precursors and the samples at each step of the synthesis. This involved structural characterization using XRD and SEM but also employing various techniques such as AC susceptibility, resistivity, magnetization, magnetoresistance, and in some cases specific heat measurements to determine the critical temperature (T_c) and critical current density (j_c). Furthermore, critical exponents and system dimensionality were calculated, providing insights into the behaviour of the samples close to and away from T_c. The analysis reveals that bulk Tl-2223 exhibit three-dimensional (3D) behaviour close to T_c, both below and above it. However, further from T_c, the system transitions to a two-dimensional (2D) behaviour. The thesis also explored the effects of doping with Co, Ni, and Gd on the superconducting properties of Tl-2223. The investigation of doped samples revealed the suppression of superconductivity with increasing Ni concentration, while Co doping initially increased j_c but decreased it beyond a certain Co content. The calculated critical exponents for the doped samples indicate that the dimension of the order parameter is 3D close to T_c, however, becomes hard to determine away from T_c. The general conclusion of the thesis is that superconductivity in the cuprates may be a 3D phenomenon, despite the clearly 2D crystallographic structure of these compounds. It is expected that the results of this thesis will stimulate further theoretical work in the attempt to formulate the comprehensive theory of unconventional superconductivity.

Streszczenie

Niniejsza rozprawa doktorska dotyczy syntezy oraz charakterystyki nadprzewodników miedziowo-tlenowych na bazie talu, $Tl_2Ba_2Ca_2Cu_3O_x$ (Tl-2223), także domieszkowanych elementami ferromagnetycznymi (Co, Ni, Gd). Głównym celem prowadzonych badań była optymalizacja procesu syntezy oraz badanie właściwości nadprzewodzących tych materiałów. Proces optymalizacji obejmował określenie optymalnych warunków przygotowania prekursorów, warunków syntezy próbek oraz wygrzewania otrzymanych materiałów. Cel ten osiągnięto poprzez systematyczną charakterystykę prekursorów i próbek na każdym etapie procesu wytwarzania. Włączano w to charakterystykę strukturalną przy użyciu rentgenografii (XRD) i skaningowej mikroskopii elektronowej (SEM), a także zastosowano różne techniki, takie jak zmiennoprądowa podatność magnetyczna, opór, magnetyzacja, magnetoopór oraz w niektórych przypadkach pomiar ciepła właściwego w celu określenia temperatury krytycznej (T_c) oraz gęstość prądu krytycznego (j_c). Ponadto, obliczono wykładniki krytyczne i wymiarowość systemu, co dostarczyło informacji na temat zachowania próbek w pobliżu i poza T_c. Analiza wykazała, że próbki Tl-2223 w postaci polikrystalicznych pastylek wykazują trójwymiarowe (3D) zachowanie w pobliżu T_c, zarówno poniżej, jak i powyżej tej temperatury. Jednak dla temperatur obiegających znacząco od T_c system wykazuje dwuwymiarowe (2D) zachowanie. W ramach pracy zbadano również efekty domieszkowania Co, Ni i Gd na właściwości nadprzewodzące Tl-2223. Badania domieszkowanych próbek wykazały tłumienie nadprzewodnictwa wraz ze wzrostem stężenia Ni, podczas gdy domieszkowanie Co początkowo zwiększało j_c, jednak po przekroczeniu pewnej zawartości Co spowodowało jego zmniejszenie. Obliczone wykładniki krytyczne dla próbek z domieszkami wskazują, że wymiar parametru porządku wynosi 3D w pobliżu T_c, ale staje się trudny do określenia poza T_c. Ogólny wniosek z pracy doktorskiej jest taki, że nadprzewodnictwo w nadprzewodnikach miedziowo-tlenowych może być zjawiskiem 3D, pomimo wyraźnie dwuwymiarowej struktury krystalicznej tych związków. Oczekuje się, że wyniki tej pracy będą stymulować dalsze prace teoretyczne w celu sformułowania kompleksowej teorii niekonwencjonalnego nadprzewodnictwa.

Contents

1. Introduction

Some substances display unique properties such as zero electrical resistance and the ability to expel magnetic fields from their interior, a phenomenon known as superconductivity. These remarkable characteristics are observed below a specific temperature known as the critical temperature, T_c. The discovery of superconductivity was a consequence of extensive efforts to achieve extremely low temperatures. This milestone was made possible through the successive liquefaction of various gases, marking significant advancements in cryogenic technology.

In 1799, M. van Maruma achieved the condensation of ammonia at a temperature of 239.8 K [1]. Later, in 1823, M. Faraday successfully condensed chlorine at 239.1 K [2] and performed the sublimation of carbon dioxide at 194.7 K [3]. The first condensation of oxygen was accomplished by L. Cailletet in 1877 using the adiabatic expansion method, while almost simultaneously, R.-P. Pictet liquefied oxygen through the cascade method at 90.2 K [2]. K. Olszewski and Z. Wróblewski were able to liquify air, stabilize oxygen, and condense carbon monoxide at a temperature of 81.7 K [1], as well as nitrogen at 77.4 K [2]. In 1898, J. Dewar achieved the condensation of hydrogen at a temperature of 20.3 K [2].

Another key factor contributing to the discovery of superconductivity was the in-depth investigation of electrical resistance. In 1900, P. Drude [4] developed a theory of conductivity that treated conductors as a network of ions and a gas of free electrons, which served as carriers of electric current. According to this theory, resistance was attributed to collisions between the carriers and vibrating ions. As the temperature increased, the vibrations became more pronounced, resulting in an increase in resistance. At absolute zero temperature, it was predicted that conductors would still possess some residual resistivity due to imperfections in the ionic network. These predictions sparked extensive research focused on achieving the lowest possible temperatures to explore the behaviour of materials in these extreme conditions.

In 1908, H. Kamerlingh-Onnes achieved a major breakthrough in low-temperature research by successfully condensing helium [5], setting a new record for the lowest temperatures at 4.2 K [2]. In his laboratory, Kamerlingh-Onnes utilized a liquefying apparatus designed by G. Flim, which consisted of chambers for cooling liquids such as alcohol, air, hydrogen, and helium. The apparatus also included various types of thermometers, including those made of silver, gold, and gas. In 1911, Kamerlingh-Onnes conducted resistance measurements on mercury in the expectation of

observing the residual resistance predicted by Drude's theory. Surprisingly, below 4.18 K, the mercury sample exhibited no measurable resistance[1] [6]. Intrigued by this discovery, Kamerlingh-Onnes conducted a series of experiments to verify the absence of resistance in mercury and lead at low temperatures. One notable experiment involved inducing an electric current within a superconducting ring, which maintained a constant current density for an extended period, demonstrating the unmeasurably low resistivity of the material. This groundbreaking experiment provided the first conclusive evidence of the phenomenon of superconductivity, unveiling it to the scientific community and the world.

The experimental research on superconductivity revealed that this phenomenon is relatively common among elements and alloys at sufficiently low temperatures. Interestingly, metals that exhibit weak conductivity at room temperature often transform into strong superconductors when cooled below their respective critical temperatures, T_c. On the other hand, metals with high conductivity at room temperature, such as copper, do not display any superconducting behaviour. This observed pattern provided an initial clue that eventually contributed to the development of the theory of superconductivity.

In addition to the absence of electrical resistance, another remarkable characteristic of superconductivity, known as ideal diamagnetism, was discovered more than two decades later. In 1933, W. Meissner and R. Ochsenfeld observed that below the critical temperature, T_c, a superconducting tin or lead sample exhibited virtually no magnetic induction within its interior in the presence of an external magnetic field [7]. This phenomenon, known as the Meissner-Ochsenfeld effect, demonstrated that superconductors possess a much stronger diamagnetic response compared to ordinary materials like bismuth or copper at room temperature. This discovery further emphasized the unique and extraordinary nature of the superconducting state.

Subsequently, additional distinctive properties of the superconducting state were discovered. One notable characteristic is the presence of a specific heat jump at the transition temperature, indicating a change in the thermodynamic behaviour of the material. Additionally, upon cooling below the transition temperature, superconductors exhibit an energy gap in the electron states, leading to unique electronic properties. Another significant finding is the observation of the isotope effect, where the transition temperature is influenced by the atomic mass of the elements present in the sample being measured [8]. This phenomenon further deepens our understanding of the

[1] Probably Kamerlingh-Onnes achieved 2.17 K because in his notes it was mentioned that the liquid suddenly stopped to boil, representing the transition to superfluid phase.

underlying mechanisms of superconductivity. Lastly, an intriguing feature is the quantization of magnetic flux through a superconducting ring, which occurs in discrete units of $h/2e$ (where h is Planck's constant and e is the elementary charge).

Superconductivity is susceptible to suppression under certain conditions. The primary factor that disrupts superconductivity is temperature. As the temperature rises above the critical temperature (T_c), the material transitions from the superconducting state to a normal conducting state. Additionally, exceeding a critical current density (j_c) can also cause the loss of superconducting properties. When the current density flowing through a superconductor surpasses this critical value, the material reverts to a resistive state. Similarly, subjecting a superconductor to an excessively high external magnetic field can also have a destructive effect on its superconducting phase. The magnetic field can penetrate the material and disturb the superconducting state, leading to the emergence of resistance. These factors highlight the delicate nature of superconductivity and the conditions that must be carefully controlled to maintain its unique properties.

The discovery of superconductivity sparked the interest of theorists who sought to explain this remarkable phenomenon [9]. However, the early attempts at theoretical explanations were unsuccessful, primarily because only one key feature of superconductivity, namely zero resistivity, was initially known. Another contributing factor to the initial lack of a proper theoretical description was the realization that superconductivity is a macroscopic manifestation of quantum mechanics. As a result, a microscopic understanding of superconductivity could only be constructed once the framework of quantum mechanics had been established, which occurred through the works of Heisenberg [10] and Schrödinger [11]. It was through the lens of quantum mechanics that researchers were able to develop more comprehensive theories to explain the full range of superconducting properties observed in experiments.

The two-fluid model emerged as the first significant theory of superconductivity, drawing inspiration from the analogy with the behaviour of superfluid helium. In the case of helium, the two coexisting fluids—one with viscosity and one without—occupy the same space. Similarly, in a superconducting material, the electron gas can be understood as consisting of carriers that move either with or without resistance. The normal electrons, following Fermi-Dirac statistics, can collide with ions, leading to the manifestation of resistance. On the other hand, the superconducting carriers, following Bose-Einstein statistics, have the ability to undergo a process of condensation. This conceptual framework of the two-fluid model provided a valuable starting point for understanding the behaviour of superconductivity and the coexistence of normal and superconducting carriers within the same material.

Subsequently, in 1935, F. and H. London introduced two phenomenological equations that played a crucial role in understanding superconductivity [12]. The first equation, known as the London equation, describes the behaviour of a material with zero resistance and is analogous to Ohm's law. It provides insight into the flow of electric current in a superconductor. The second equation formulated by the London brothers describes the diamagnetic response of a superconductor, indicating the expulsion of magnetic fields from its interior. When combined with Ampere's law, these equations reveal how magnetic fields penetrate the interior of a superconductor. According to the London model, the magnetic field decays exponentially as it enters the sample, with the decay length (λ_L) determined by the concentration of superconducting carriers. The London equations laid the foundation for further investigations into the electromagnetic properties of superconductors and greatly contributed to our understanding of their behaviour.

In 1951, W. Ginzburg and L. Landau developed a phenomenological theory of superconductivity, known as the Ginzburg-Landau (GL) theory [13]. In their approach, they introduced a complex order parameter that is zero above the superconducting transition temperature and becomes nonzero below it. The GL theory incorporates a free energy functional that is expanded in terms of even powers (2 and 4) of the order parameter and its gradient. This functional includes five terms, including a normal state term and a magnetic field term. The Ginzburg-Landau theory successfully explains the intermediate state, also known as the vortex state, which occurs when some parts of the superconductor remain in the superconducting state while others are in the normal state. This phenomenon arises due to the formation of quantized magnetic flux vortices within the superconductor. The GL theory provides a framework for understanding and describing the behaviour of superconductors in the presence of external magnetic fields and provides valuable insights into the microscopic mechanisms underlying superconductivity.

In 1957, J. Bardeen, L. Cooper, and J. Schrieffer introduced a groundbreaking microscopic theory of superconductivity, known as the BCS theory [14]. This theory not only explains the absence of resistance and diamagnetism in superconductors but also provides insights into other key phenomena. According to the BCS theory, the formation of Cooper pairs of electrons, mediated by electron-phonon interactions, is responsible for superconductivity. These Cooper pairs, consisting of electrons with opposite spins, are able to move through the lattice without scattering off of the ions, resulting in zero resistance. The BCS theory also explains the specific heat jump observed at the superconducting transition temperature. The presence of the energy gap in the electronic states near the Fermi surface leads to a discontinuity in the specific heat. The magnitude

of the energy gap at absolute zero temperature is proportional to the transition temperature, providing a quantitative relationship between these two parameters.

Initially, it was believed that conventional superconductivity, as described by the BCS theory, is limited to relatively low temperatures, typically below 30 K, determined by the energy of phonons. However, recent discoveries have challenged this notion. Experiments under extremely high pressures have demonstrated superconductivity at significantly higher temperatures. For example, hydrogen sulfide (H_2S) exhibits superconductivity just below 200 K at pressures exceeding 96 GPa [15]. Other compounds, such as LaH_3 and LaH_{10}, reach critical temperatures close to 260 K, but at even higher pressures (190 GPa) [16]. Most notably, superconductivity near room temperature (288 K) has been observed in a high-pressure phase of H_2S mixed with CH_4 at 267 GPa [17]. However, this result was challenged and the article was retracted. Nevertheless, the very high values of T_c in these compounds are related to the vibrations of light H atoms, as predicted by Aschroft [18].

For many years after its initial discovery, superconductivity was primarily observed in metals and alloys [19]. However, a major breakthrough occurred in 1986 when J. Bednorz and K. Müller discovered a new class of superconductors [20]. They found that certain ceramic copper oxide materials exhibited superconductivity at relatively high temperatures. These materials, known as cuprates, have a unique structure consisting of CuO_2 planes separated by charge reservoir blocks. The distortion of these reservoir blocks, either through doping or nonstoichiometry, triggers the onset of superconductivity. Subsequent research led to the discovery of cuprate superconductors with even higher transition temperatures, surpassing the boiling point of nitrogen. Currently, the cuprate superconductor based on mercury holds the record for the highest critical temperature under ambient pressure, reaching 134 K [21].

The high critical temperature and unconventional behaviour of cuprate superconductors indicate that the conventional phononic mechanism of electron pairing is not applicable to these materials, as they lack light elements like hydrogen. This poses a significant challenge in understanding the origin and providing a unified description of unconventional superconductivity in cuprates [22]. While the parent compounds of cuprates exhibit strong antiferromagnetic behaviour, suggesting a role for magnetic interactions in electron pairing, a universally accepted theory is still lacking.

Despite these challenges, superconductors in general, and cuprates in particular, have found widespread applications. One of the most notable applications is in the development of zero-resistance cables, which enable efficient electricity transmission and the construction of powerful electromagnets. Superconductivity is also fundamental to the operation of Superconducting

Quantum Interference Devices (SQUIDs), highly sensitive magnetic field detectors. Superconductors are utilized in current limiters to protect electrical networks and in Superconducting Magnetic Energy Storage (SMES) systems. In the medical field, superconductors play a crucial role in Magnetic Resonance Imaging (MRI), where strong magnetic fields are used for diagnostic imaging. Magnetoencephalography (MEG), a technique for measuring brain magnetic fields, relies on the detection of small magnetic fields using SQUIDs. Superconductors are also applied in accelerator technology for particle physics research [23] and in the development of high-speed MAGLEV trains, such as the Shinkansen network [24, 25].

There are several families of cuprate superconductors that are being studied for various applications. These materials are often used as precursors for the preparation of thin films or single crystals. Each family of cuprates may exhibit subtle differences in their superconducting properties, which can also be influenced by the presence of dopants, including magnetic dopants that are sometimes introduced during the fabrication process.

This thesis focuses on the preparation and characterization of thallium cuprates, specifically $Tl_2Ba_2Ca_2Cu_3O_x$ (Tl-2223), also doped with ferromagnetic elements such as cobalt (Co), nickel (Ni), and gadolinium (Gd). Tl-2223 is an ideal material for comparing experimental results with theoretical predictions due to relatively simple structure. Although the synthesis of Tl-2223 is challenging, the material itself is considered "clean" as it is expected to exhibit no ordering other than superconductivity. Additionally, Tl-2223 has a relatively high critical temperature of up to 125 K, making it suitable for research conducted at the lower cost liquid nitrogen temperatures.

The synthesis of bulk Tl-2223 samples involves a multistep process that proved to be quite challenging. The initial goal was to obtain a high-purity material with optimal oxygen stoichiometry and minimal thallium loss. The synthesis method involved the preparation of precursors without thallium, followed by the addition of Tl_2O_3 before the main synthesis step. The complete process included precursor synthesis, final product synthesis, and additional thermal treatment for oxygenation. In the case of the doped samples the introduction of ferromagnetic elements (Co, Ni, and Gd) with varying concentrations in the form of complex oxides was done at the beginning of the synthesis process. Through careful optimization and successful synthesis, the desired Tl-2223 samples doped with ferromagnetic elements were obtained for further characterization and analysis.

Various experimental techniques, including AC susceptibility, resistance measurements, XRD, SEM, VSM, and specific heat measurements, were employed to study the synthesized materials. The obtained results were primarily analysed using the GL approach. While the layered structure

of cuprates imposes some limitations on the direct application of the standard GL theory, phenomenological parameters introduced in the GL theory can still be extracted from experimental data. The order parameters and their fluctuations were among the parameters of interest obtained from the experiments.

The square of the order parameter manifests in the conductance, which is directly proportional to the concentration of superconducting carriers. Additionally, the square of the order parameter can be detected through the magnetic susceptibility, where the diamagnetic portion of the samples provides an estimate of the superconducting carrier concentration.

In cuprates, the superconducting phase transition is characterized as a second-order transition, where thermodynamic functions exhibit continuity without changes in system energy. This type of transition is driven by thermal fluctuations of the order parameter. Notably, the superconducting transition in cuprates is broader compared to conventional superconductors like mercury. The width of the observed fluctuation region is proportional to the fourth power of the transition temperature [26]. As a result, fluctuations are visible in resistance and AC susceptibility measurements within the range accessible by standard experiments. Specific heat measurements are also sensitive to fluctuations, as evidenced by a larger-than-predicted jump in specific heat at the phase transition temperature compared to BCS theory.

The equilibrium state of the order parameter is well determined by the GL theory, providing the most probable configuration. However, in the vicinity of a phase transition, fluctuations introduce small deviations from equilibrium. To describe these fluctuations, a Gaussian correction, represented by the second variational derivative, is added to the GL functional. The Gaussian approximation is valid in a region not too far from the transition but also not too close, as defined by the Ginzburg criterion.

Close to the critical temperature, fluctuations, known as critical fluctuations, become too strong to be accurately described by a Gaussian character. In other words, in the immediate vicinity of T_c, deviations from equilibrium exhibit non-Gaussian behaviour and are influenced by the singularity of the coherence length at the critical point.

By extracting information from experiments, such as order parameter fluctuations and critical exponents, it is possible to determine the effective dimensionality of superconducting systems. These parameters allow for the characterization and understanding of the behaviour of superconductors.

The thesis is structured as follows:

While the current chapter (Chapter 1) serves as the introduction, providing an overview of the research topic, Chapter 2 focuses on the theoretical aspects of superconductivity, with a particular emphasis on the studied materials. Subchapter 2.1 offers a comprehensive review of superconductivity models, including the two-fluid model, London's model, and BCS theory. The phenomenological Ginzburg-Landau theory and its validity conditions, such as second-order phase transitions and equilibrium, are also discussed. The concept of the order parameter, essential in the Ginzburg-Landau theory, as well as the family of mean field theories, are described. This leads to the presentation of the Ginzburg-Landau functional (GLF) and its derivatives with respect to the order parameter or the vector potential. The first differential equation describes the order parameter, while the second describes the diamagnetic response of the superconductor, representing the current density within it. Fluctuations are then treated as an extension of the GL theory, considering their strength and the Gaussian approximation. Critical exponents and scaling laws are introduced, providing a method to determine the effective dimensionality of superconducting systems. The subchapter concludes with experimental examples of fluctuation manifestations in conductivity, susceptibility, and specific heat. In Subchapter 2.2, the cuprate compound class is described, with a particular focus on electronic transport and the relevant properties.

Chapter 3 presents the experimental techniques used in sample preparation and characterization.

The experimental part begins with Chapter 4, which covers sample preparation, including the synthesis and characterization of precursors (4.1), the synthesis and additional thermal treatment of superconducting samples (4.2), the characterization of superconducting samples using XRD and SEM (4.3), and the optimization of synthesis conditions (4.4).

In Chapter 5, the samples are characterized using various techniques, such as AC susceptibility (5.1), four-point resistance (5.2), critical current measurements using contactless or transport methods (5.3), vibrating sample magnetometry (5.4), and specific heat measurements (5.5). Subchapters (5.1), (5.2), and (5.5) provide estimations of critical exponents.

The thesis concludes with a summary and conclusions in Chapter 6.

Additional technical information regarding the experiments and data analysis is provided in the appendices: Appendix A covers furnace calibration, Appendix B discusses the Bean model, Appendix C explores the GL strong coupling limit, Appendix D provides details on sample preparation, and Appendix E contains additional X-ray diffraction data.

Literature:

1. https://www.naukowiec.org/tablice/chemia/wlasciwosci-fizyczne-niektorych-zwiazkow-nieorganicznych_632.html
2. Encyklopedia.pwn.pl
3. https://www.medianauka.pl/suchy-lod
4. P. Drude, Zur Elektronentheorie der Metalle, Lehrbuch der optic, (1900) S. Hirzel.
5. H. Onnes, The condensation of helium, Nature **77**, 559 (1908)
6. H. Onnes, Further experiments with liquid helium. C. On the change of electric resistance of pure metals at very low temperatures etc. IV. The resistance of pure mercury at helium temperatures, KNAW, Proceedings, 13 II, 1910-1911, (1911); H. Onnes, The resistance of pure mercury at helium temperatures. ommun. Phys. Lab. Univ. Leiden (1911); H. Onnes, Leiden Communication, 124c (1911)
7. W. Meissner and R. Ochsenfeld, Ein neuer effekt bei eintritt der supraleitfähigkeit, Naturwissenschaften **21** (44), 787-788 (1933)
8. E. Maxwell, Isotope effect in the superconductivity of mercury, Physical Review 78 (4), 477 (1950) doi: 10.1103/PhysREv.78.477
9. J. Schmalian, Failed theories of superconductivity, Arxiv 1008.0447 (2011); J. Schmalian, Failed theories of superconductivity. Modern Physics Letters B, **24** (27), 2679-2691 (2010) doi: 10.1142/S0217984910025280
10. W. Heisenberg, Quantum-theoretical re-interpretation of kinematic and mechanical relations. Z. Phys, **33**, 879-893 (1925)
11. E. Schrödinger, Quantisierung als Eigenwertproblem, Annalen der Physik **4** (79), 361-376 (1926).
12. F. London and H. London, The electromagnetic equations of the supraconductor, Proc. R. Soc. Lond. A **149** (866), 71-88 (1935) doi: 10.1098/rspa1935.0048
13. V. Ginzburg and L. Landau, The theory of superconductivity, Zurnal Eksp. Teoret. Fiz **12**, 1064-1082 (1950)
14. J. Bardeen, L. Cooper, and J. Schrieffer, Theory of superconductivity, Physical review **108** (5), 1175-1204 (1957) doi: 10.1103/PhysRev.108.1175
15. A. Drozdov *et al*., Conventional superconductivity at 203 K at high pressures, Arxiv 1506.08190 (2015); A. Drozdov *et al.*, Conventional superconductivity at 203 kelvin at high pressures in the sulfur hydride system. Nature **525** (7567), 73-76 (2015) doi: 10.1038/nature14964

16. M. Kostrzewa *et al.,* From LaH_{10} to room-temperature superconductors, Scientific Reports **10**, 1592 (2020) doi: 10.1038/s41598-020-58065-9
17. E. Snider, R. Dias *et al.,* Room temperature superconductivity in a carbonaceous sulfur hydride. Nature **586** (7829), 373-377 (2020) doi: 10.1038/s41586-020-2801-z
18. N. Ashcroft, Metallic hydrogen: A high temperature superconductor? Physical. Review Letters **21** (26), 1748-1749 (1968) doi: 10.1103/PhysRevLett.21.1748
19. J. Hulm and B. Matthias, Overview of superconducting materials development (1981) In: S. Foner, B. Schwartz (eds) Superconductor Materials Science: Metallurgy, Fabrication, and Applications. NATO Advanced Study Institutes Series, **68**, Springer, Boston, MA. doi: 10.1007/978-1-4757-0037-4_1
20. J. Bednorz and K Müller, Possible High T_c superconductivity in the Ba-La-Cu-O system, Z. Phys. B – Condensed Matter **64**, 189-193 (1986) doi: 10.1007/BF01303701
21. Z. Huang *et al.*, Superconductivity, structure and resistivity in $HgBa_2Ca_2Cu_3O_{8+\delta}$, Physica C: Superconductivity **217** (1-2), 1-5 (1993) doi: 10.1016/0921-4534(93)90786-P
22. J. Spałek *et al.*, Superconductivity in high-T_c and related strongly correlated systems from variational perspective: Beyond mean field theory, Physics Reports **959**, 1-117 (2022) doi: 10.1016/j.physrep.2022.02.003
23. I. Georgescu, Superconducting accelerator technologies, Nature Reviews Physics **2** (3), 128 (2020) doi: 10.1038/s42254-020-0155-y
24. Supraconductivite.fr access 1.10.2021
25. K. Sato, Present status and future perspective of high-temperature superconductors, Sei Technical Review – English Edition **66**, 55-67 (2008)
26. A. Varlamov and M. Ausloos, Fluctuation phenomena in superconductors, In: M. Ausloos and A. Varlamov (Eds), Fluctuation Phenomena in High Temperature Superconductors, NATO Advanced Study Institutes Series **32**, 3-41, Springer, Dordrecht (1997) doi: 10.1007/978-94-011-5536-6_1

2. Conventional and unconventional superconductivity

2.1 Models of superconductivity

The importance of investigating matter at low temperatures became apparent soon after the discovery of superconductivity in 1911. In 1986, a significant breakthrough revealed that superconductivity is not solely limited to low temperatures but can also occur at much higher temperatures. There is a hopeful prospect of achieving superconductivity at room temperature in the near future. This chapter focuses on the presentation of three theories that describe the phenomenon of superconductivity. Subsequently, the Ginzburg-Landau formalism is introduced, with a particular emphasis on its application to high-temperature superconductivity.

Experimental results

The discovery of two remarkable phenomena, superconductivity in 1911 [1] and superfluidity in 1927 [2], sparked the need to comprehend these phenomena as well as the behaviour of matter at low temperatures. Both of these transitions to the low-temperature phase exhibit a lambda-type behaviour. Although no discontinuity in entropy is observed, the entropy is affected by these phase transitions. Additionally, in both cases, it is evident that there is some additional ordering compared to the high-temperature phase. However, the analogy between superconductivity and superfluidity runs deeper: in a superfluid, molecules can flow without friction, while in a superconductor, electric carriers can move without resistance. Moreover, both superfluids and superconductors exhibit high conductance, whether it is heat conduction in superfluids or electrical conduction in superconductors.

The first model that attempted to describe both of these extraordinary phenomena was the two-fluid model, introduced by Goertel and Casimir in 1934 [3].

Two fluid model by Goertel and Casimir

The decrease in entropy upon cooling indicated the presence of ordering below the lambda transition temperature for both superconductivity and superfluidity, which disappears above the transition. This ordering enables the frictionless movement of electrons in superconducting materials, leading to perfect conductivity, or the frictionless movement of atoms in the case of superfluids.

Superfluid helium consists of bosons, while the carriers of electricity in superconductors are

fermionic electrons or holes. However, fermions in superconductors exhibit some organization resembling bosonic structures. In the case of superfluidity, the entire sample is either in a superfluid or normal fluid state. In superconductors, only valence electrons, and only a fraction of them at non-zero temperature, contribute to the superconducting fluid. Some normal electrons that scatter due to lattice inhomogeneities do not completely disappear below the transition. Close to the transition temperature, only the normal electronic fluid exists, while near absolute zero, only the superconducting fluid exists. Between these regimes, a certain percentage of electrons are in the normal state, and this percentage changes with temperature. The dependence of thermodynamic functions such as free enthalpy (G) or free energy (F) on this percentage leads to anomalies in thermodynamic properties such as heat capacity. The two-fluid theory, although providing only a qualitative explanation, successfully accounts for the specific heat jump observed in superconductors.

According to the two-fluid model, a superconductor consists of two types of conducting electrons. The first type corresponds to metallic valence electrons, which obey Fermi-Dirac statistics. The second type of electrons is responsible for the superconducting properties of the sample.

It is important to note that the two-fluid model is not a rigorous physical model, particularly as the equations of motion are not well-defined [4]. Furthermore, the existence of two fluids occupying the same space may seem somewhat artificial. However, the model was able to organize the knowledge about superconductors during the 1930s.

London theory

In 1933, another remarkable characteristic of superconductors was discovered: the ability to produce frictionless eddy currents that effectively shield the bulk of the sample from magnetic induction when placed in an external magnetic field [5]. Hence, in addition to perfect conductivity, superconductors exhibit perfect diamagnetism. It became necessary to mathematically describe both infinite conductivity and perfect diamagnetism. The London brothers developed a theory that involved adding two equations to modify the electrodynamics of the system [6].

The first equation describes the electric field intensity inside the superconducting sample. In a normal conductor, electrical resistance counterbalances the accelerating effect of the electric field, resulting in electrons moving uniformly over time. However, in superconductors, electrical resistance is zero, and the presence of an internal electric field would cause an unbounded acceleration of carriers, leading to unphysically high currents. The first London equation is given by:

$$E = \frac{\partial}{\partial t} \Lambda J \,, \qquad (2.1)$$

Where E is an electric field, J is superconducting current density, and Λ a phenomenological constant dependent on the carrier concentration. Experimental results indicate that, for a stable superconducting current density J, the electric field E must be zero. Equation 2.1 ensures this condition.

The parameter Λ can be related to the inverse of the supercurrent electron concentration n_s:

$$\Lambda = \frac{m}{n_s e^2} \,. \qquad (2.2)$$

The supercurrent electron concentration n_s varies from the total valence electron concentration at temperatures close to absolute zero and gradually decreases with increasing temperature, reaching zero at the critical temperature T_c [7], as predicted by the two-fluid model.

The second London equation [8] governs the magnetic properties of the superconducting sample:

$$-\mu_0 h = \nabla \times (\Lambda J_{total}) \qquad (2.3)$$

Here h is a magnetic field strength at a microscopic scale. According to the Ampere's law $J_{total} = \nabla \times h$ or $J_{external} = \nabla \times H$, where H is an averaged macroscopic field. $J_{external}$ represents the nonequilibrium current, excluding currents arising from the equilibrium response of the medium.

When combined with the Ampere's law, Equation 2.3 describes how the magnetic field is expelled from the superconductor:

$$h = \lambda^2 \nabla^2 h. \qquad (2.4)$$

As a result, the magnetic field exponentially diminishes as one moves away from the surface of the sample towards its centre. This property is characterized by the penetration depth parameter λ:

$$\lambda = \sqrt{\frac{m}{\mu_0 n_s e^2}} = \sqrt{\frac{\Lambda}{\mu_0}} \,, \qquad (2.5)$$

where the penetration depth is related to the supercurrent electron concentration n_s. For small penetration depths, the magnetic field is practically expelled from the interior of the superconductor.

In summary, the first of the London equations, Equation 2.1, represents Ohm's law for superconductors, i.e., zero resistance. The flow of current does not require any voltage between different parts of the superconducting specimen. The second equation, Equation 2.3, describes the

diamagnetism resulting from eddy currents. When combined with Ampere's law, it provides an expression for the penetration depth. In essence, the London theory provides a description of the two main characteristics of superconductors: zero resistance and perfect diamagnetism. It also introduces the penetration depth (λ) as a length scale.

Bardeen, Cooper, and Schrieffer (BCS) theory

According to Ampere law, $J_{total} = \nabla \times h$, the current density depends only on the magnetic field in the immediate vicinity of the considered point. However, the response of a superconducting sample to a magnetic field is non-local, meaning that the current depends not only on the magnetic field at a single point but also in a region surrounding that point. Therefore, another length scale, governing the non-local response of the sample, should be introduced [7]. Interestingly, the concept of two length scales also arises in the description of interactions in liquids [9]. In superconductors, the second length scale makes superconductivity insensitive to changes in the magnetic field over short distances, such as at the atomic scale.

The coherence length scale, denoted as ξ_0, was introduced by Pippard in 1953 [10] as an extension of the London theory. He considered tin as a superconductor and treated ξ_0 as a "*vague empirical concept*". Pippard focused on the superconducting transition at zero field, the field variation of the penetration depth, and the interphase surface energy. His conclusion was that there must be something preventing changes in the order parameter over sufficiently short distances

The existence of two length scales naturally emerged from the BCS microscopic theory, which was published by Bardeen, Cooper, and Schrieffer in 1957 [11]. Although applicable to conventional low-temperature superconductors, the BCS theory represented a significant advancement in the understanding and description of superconductivity. Coexistence of two kinds of carriers [3], akin to the two-fluid model, is still present in BCS theory although it came as a consequence, not an assumption. The theory introduced the concept of quasi-bosonic pairing of bonding electrons, with the mechanism of this pairing being phononic in nature. In essence, an electron attracts nearby atoms, causing lattice deformations, and another electron is then attracted to these lattice deformations, resulting in the formation of a bound pair, as schematically depicted in Fig 2.1.

The phonon-mediated pairing mechanism is supported by the observation of the isotope effect in classical superconductors, where the critical temperature is proportional to some power of the isotope mass of the atoms composing the sample [12].

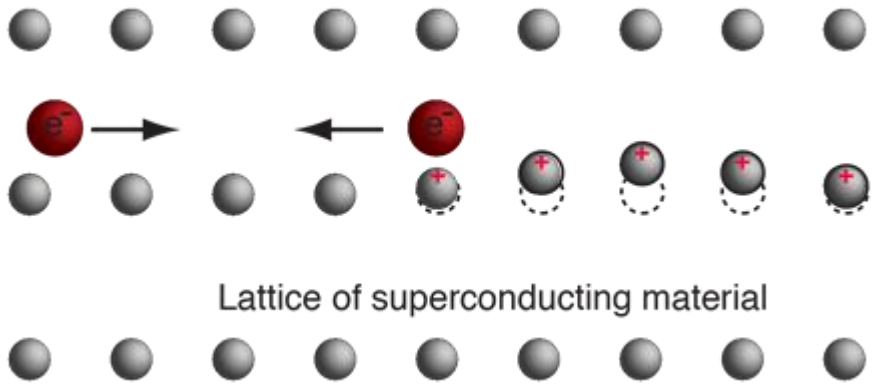

Figure 2.1: Schematic visualization of a single Cooper pair. A passing electron (right) attracts the lattice, causing a slight ripple toward its path. Another electron (left) passing in the opposite direction is attracted to that displacement. [Ref. 13]

In fact, the potential between electrons in a superconductor consists of two terms: the repulsive Coulombic term and a frequency-dependent phonon term. For small phonon frequencies, the phonon potential is also repulsive. However, when the phonon eigenfrequency reaches a certain value, the phonon potential becomes attractive [14], which can exceed the Coulomb repulsion and result in a net attractive interaction

Bardeen, Cooper, and Schrieffer demonstrated that if the phonon-driven potential is attractive, the coupled electrons form a ground state of the system. This bound electronic state can be represented by multiplying two plain waves, corresponding to free electrons, with opposite wave vectors $\boldsymbol{k}$. The wavefunction of the bound state is proportional to $e^{i\boldsymbol{k}\Delta\boldsymbol{r}}$. By symmetrizing the spatial part of the wavefunction, a term proportional to $\cos(\boldsymbol{k}\Delta\boldsymbol{r})$ is obtained. The two-electron Schrödinger equation can then be written as:

$$1/2\Delta_1\Psi + 1/2\Delta_2\Psi + V\Psi = E\Psi. \qquad (2.6)$$

Here, Ψ represents the wavefunction, which can be modelled as a sum of standing (cosine) waves:, $\Psi(r_1\text{-}r_2) = [\Sigma_{k>kF}\, g_k \cos(\boldsymbol{k}(r_1\text{-}r_2))]\cdot$(spin part) [7].

In this equation, g_k represents the probability coefficients of bound electron pairs with a certain wave vector $\boldsymbol{k}$, and V is associated with the interaction between these electrons mediated by the electron-phonon coupling. If the energy difference between the involved electrons is smaller than the energy of phonons, the virtual exchange of phonons results in an attractive interaction, which is responsible for superconductivity.

The potential V can be transformed into momentum space through Fourier transform. In $\boldsymbol{k}$-space, V is non-zero only in the vicinity of the Fermi surface. In the BCS model, it is assumed that V is a constant attractive potential within the region of reciprocal space where it is non-zero [11, 7].

By inserting the bound state wavefunction $\Psi(r_1\text{-}r_2)= [\Sigma_{k>kF}\ g_k \cos(\boldsymbol{k}(r_1\text{-}r_2))]\cdot$(spin part) into the Schrödinger Equation (2.6) a set of equations for the pair energy eigenvalue E can be obtained, where ε_k represents the unperturbed plane wave energies of the electrons:

$$(E - 2\varepsilon_k)g_k = \sum_{k' > k_F} V_{kk'} \cdot g_{k'} \quad (2.7)$$

Here, $V_{kk'}$ are the elements of the potential matrix V, expanded into plane waves. The Equation (2.7) can be divided by (E - $2\varepsilon_k$) and summed over the wave vector k on both sides. It should be noted that $V_{kk'}$ in the vicinity of the Fermi surface is constant and equal to -V, and zero otherwise, as assumed by BCS theory. Additionally, the summation $\Sigma g_k = \Sigma g_{k'}$ holds, allowing both sides of the summed Equation (2.7) to be divided by Σg_k. This simplifies equation (2.7) to (2.8):

$$1/V = \Sigma_{k>kF}(2\varepsilon_k - E)^{-1}. \quad (2.8)$$

The summation in (2.8) can be replaced with integration over the density of states near the Fermi level, denoted as $N(0)$. Assuming that $N(0)V << 1$ (the weak coupling case), integrating from E_F to $E_F+\hbar\omega$, and solving the resulting equation for E, the ground state energy of the interacting system can be obtained:

$$E = 2E_F - 2\hbar\omega e^{-2/[N(0)V]} \quad (2.9)$$

Here $2\hbar\omega e^{-2/[N(0)V]} = 2\Delta$ represents the double energy gap. Therefore, the ground state energy is separated from the excited states by the energy gap (Δ), which is not broader than $\hbar\omega$.

The energy gap is temperature-dependent, with values close to zero near T_c and reaching a maximum value at absolute zero. The maximal value of T_c is proportional to the energy gap at absolute zero. Hence, since the energy gap (Δ) is limited by phonon frequencies in the BCS theory, the maximum T_c is also limited. The estimated T_c limit for phonon-mediated BCS superconductors is around 30 K [11: only formula, 15]. However MgB_2 , with T_c=40 K, is also treated as BCS superconductor [16].

In addition to explaining the behaviour of superconducting current, the existence of the energy gap, and the transition temperature T_c, the BCS theory also provides explanations for many other phenomena related to superconductivity, including the Josephson effect, and its application in SQUID. The Josephson effect occurs in Josephson junctions (JJ), which consist of two superconductors separated by an insulating layer. When a DC voltage is applied to the junction, an AC current flows, and when U_{DC} = 0, a direct current is produced. This behaviour allows the Josephson junction to function as a voltage-to-frequency converter. Moreover, when the Josephson junction is excited by microwaves, a constant DC voltage is generated between its ends. The

SQUID, which consists of two Josephson junctions forming a loop, enables the measurement of very small magnetic fields due to the quantization of magnetic flux through the loop.

In summary, the key feature of the BCS theory is that any attractive potential between carriers leads to the formation of Cooper pairs. According to the BCS theory, the mechanism of pairing is phononic in nature. The ground state of such a coupled fermionic system is separated from the excited states by an energy gap that depends on temperature. The BCS theory provides a microscopic and self-consistent explanation for phenomena such as the Meissner effect, the specific heat jump at the critical temperature, and the isotope effect.

Ginzburg-Landau functional

In all instances of phase transition, a breaking of symmetry occurs: the low temperature phase becomes ordered while the high temperature phase becomes more chaotic. A notable case is the continuous phase transition observed in cuprates, specifically the transition from the normal state to the superconducting state, which is the focus of this thesis. The experimental manifestation of a continuous phase transition is a peak in heat capacity without the presence of latent heat, indicating the continuity of thermodynamic functions at the transition. In the vicinity of the phase transition temperature T_c, when the reduced temperature $\tau = (T - T_c)/T_c$ approaches zero, or at the transition itself under the influence of external factors such as an applied magnetic field, physical quantities like specific heat, susceptibility, and magnetization follow power laws characterized by critical exponents (e.g., α for specific heat and λ for susceptibility). There are six critical exponents that are constrained by four equations, resulting in only two independent critical exponents. These critical exponents exhibit universality within systems of the same dimension. In this thesis, certain experimental results will be used to determine and analyse these critical exponents within the framework of the Ginzburg-Landau approach, which will be presented subsequently.

In order to describe a continuous phase transition, Landau introduced the concept of an order parameter, which assumes a value of zero above the critical temperature T_c and acquires a non-zero value below the transition. The nature of the physical system determines the characteristics of the order parameter, which can be either a scalar quantity or an *n*-component vector. In the case of a superconducting phase transition, the order parameter is a complex number with two dimensions.

When the system is near the critical region (when the reduced temperature τ is close to 0), Landau proposed that all thermodynamic properties can be described using the Landau free energy functional, which takes the form of a power series in terms of the order parameter. By minimizing

this functional with respect to the order parameter, the actual free energy of the system can be obtained.

In its simplest form, the Landau free energy functional is given by:

$$F = F_N + \alpha\tau\Psi^2 + \beta(T)/2\Psi^4 + \mu_0 h^2/2, \qquad (2.10)$$

Here, h represents the strength of the microscopic magnetic field, F_N is the free energy of the non-ordered phase, and α, $\beta(T)$, and μ_0 are coefficients associated with the system's properties.

The coefficient in front of the lowest power of the order parameter should change sign when the system crosses the critical temperature. In particular, we have $\alpha\tau = \alpha(T-T_c)/T_c$ and $\beta(T) = constant$. In equilibrium, the order parameter is such that the free energy F is minimized, which corresponds to the conditions $\partial F/\partial\Psi = 0$ and $\partial^2 F/\partial\Psi^2 > 0$. Therefore, we have $\alpha\tau\Psi + \beta\Psi^3 = 0$, which implies $\Psi = 0$ for $\alpha\tau > 0$, representing the disordered state at $T > T_c$. On the other hand, $\Psi = \mathrm{sqrt}(-\alpha\tau/\beta)$ for the ordered state.

This form of the Landau free energy functional, given by Equation 2.10, is equivalent to the mean field approach. Since the order parameter Ψ is assumed to be uniform in space, it can describe any local object, such as spins or carriers, within an effective potential provided by the crystalline lattice or other species. In this approach, the correlations between objects are not taken into account, and fluctuations are not considered as the potential is effectively averaged. However, this form of the Landau free energy functional is useful for understanding general features of phase diagrams.

In the case of a non-uniform order parameter in space, the Landau functional is extended to include the gradient of the order parameter to ensure that it does not vary rapidly on short length scales ξ. The resulting functional is known as the Ginzburg-Landau functional (GLF) and is given by:

$$F=F_N+\alpha\tau\Psi^2+\beta/2\Psi^4+(\nabla\Psi)^2+\mu_0 h^2/2 \qquad (2.11).$$

This form of the functional was used by Ginzburg and Landau to describe superconductivity. In the case of superconductivity, the order parameter $\Psi(r)$ is complex and can be written as, $\Psi(\boldsymbol{r}) = |\Psi(r)|e^{i\phi(r)}$ resembling the wave function in quantum mechanics (although the GL theory was formulated before the BCS theory). The quantity Ψ represents the condensate of superconducting species, namely Cooper pairs.

Taking these considerations into account, the GL functional is given by:

$$F = F_N + \alpha\tau|\Psi|^2 + \beta/2|\Psi|^4 + (1/2m)|(-i\hbar\boldsymbol{\nabla} - 2e\boldsymbol{A})\Psi|^2 + \mu_0 h^2/2 \qquad (2.12),$$

Here, m is the effective mass of the superconducting carriers with charge e, $\boldsymbol{A}$ is the vector potential, and h is the local magnetic field strength. To ensure the invariance of F, we include the vector potential $\boldsymbol{A}$ multiplied by the Cooper pair charge, $2e$, in Equation 2.11. It is worth noting that the quantum mechanical operator nabla, ∇, is analogous to $(mv+qA)/i\hbar$ [17]. The expression for kinetic energy as a function of momentum is $p^2/2m$, hence the factor $1/(2m)$. Minimizing the GL functional with respect to Ψ leads to the Ginzburg-Landau equation:

$$0 = \alpha\tau\Psi + \beta\Psi^3 + (1/2m)\,(-i\hbar\nabla - 2e\boldsymbol{A}/c)^2\Psi \qquad (2.13),$$

from which Londons' equation, as well as the Meissner effect may be derived.

Minimizing the GL functional provides the equilibrium state of the system, where the system is static but may exhibit some inhomogeneities in the order parameter due to the presence of the gradient term. This description aligns with the concept of ergodicity, which states that after a sufficiently long time, the system will approach its equilibrium state. However, even in equilibrium, there can be deviations from the optimal state due to thermodynamic fluctuations. These fluctuations become stronger as the system approaches the critical point, where the reduced temperature τ approaches zero. Furthermore, if the system is disturbed from its equilibrium state, one can observe its relaxation back to equilibrium, which would not occur in the absence of fluctuations.

As the critical region is approached, the role of fluctuations becomes more prominent. Specific heat is one of the experimental characteristics that defines the critical region. In the Landau approximation (which neglects fluctuations), superconductors exhibit a jump in electronic specific heat, denoted as ΔC, at the critical temperature. However, the presence of fluctuations enhances this jump, resulting in a total jump of δC. When ΔC is much smaller than δC ($\Delta C << \delta C$), the impact of fluctuations is negligible. The critical region can be approximately determined by solving $\Delta C = \delta C$, and the resulting absolute value of the reduced temperature $|\tau|$ is referred to as the Ginzburg parameter, G_i.

In the simplest case, the departure of the system from its equilibrium state can be described by a Gaussian factor. In this scenario, the fluctuations are small and are referred to as Gaussian fluctuations. The GL theory, when supplemented with small fluctuations, remains valid for $G_i << |\tau| << 1$. [9]

The peak in the specific heat, where fluctuations, particularly Gaussian fluctuations, are most pronounced (see e.g. [18, 19]), is associated with the electronic specific heat, which constitutes only a small fraction of the total specific heat of the system. Consequently, observing the specific

heat jump in the regime of Gaussian fluctuations can be challenging, and determining the critical exponent, α, that governs this behaviour is a difficult task. In some cases, the specific heat jump at T_c may not even be visible in bulk thallium cuprates. Specifically, when the fluctuation range is narrow (i.e., small G_i), fluctuations become experimentally inaccessible. The Ginzburg parameter, G_i, is proportional to $(T_c/\varepsilon_F)^4$, and considering T_c/ε_F of the order of 0.001 for conventional superconductors and 0.1 for high-temperature ones, G_i can be on the order of 10^{-8}. This explains why fluctuations are observable primarily in high-temperature superconductors rather than conventional ones. [9]

In the study of superconductors, specific heat or critical current, it is often assumed that the system is in the strong coupling limit of the Ginzburg-Landau theory. In this limit, the kinetic energy of superconducting electrons is smaller than the potential energy that binds these electrons into pairs [see Appendix C]. As the temperature increases, the kinetic energy of the electrons grows proportionally to the macroscopic temperature. When the kinetic energy of the pairs exceeds the bonding energy, superconductivity ceases to exist. By comparing these energies, we can derive the thermal dependence of the critical current in a superconductor.

Not only specific heat, but also other experimentally accessible quantities are affected by fluctuations in the order parameter $|\Psi|^2$. Since $|\Psi|^2$ is proportional to the density of superconducting carriers and the superconducting current affects both conductivity as well as the response to the magnetic field (diamagnetism), fluctuations in $|\Psi|^2$ are certainly visible in conductivity and magnetic characteristics. For example, in cuprates, the subject of this thesis, the normal state linear thermal dependence of resistivity breaks below a certain temperature ($T^*>T_c$):[2] the resistivity lowers faster than linearly. One can subtract the conductivity of normal state (where the resistivity $\rho(T)$ is linear) from the real conductivity achieving the excess conductivity. This excess conductivity, giving some information about carrier type and carrier concentration inside superconducting sample, is often presented on logarithm of excess conductivity σ versus logarithm of reduced temperature τ charts. Since also conductivity close to the critical region exhibits power dependence, such a relation should be linear. The critical parameter λ, which describes the slope of the points in the logarithmic plot, is connected to the dimensionality of the superconducting system and will be determined from experimental data in the subsequent analysis.

[2] Here, T^* is not the pseudogap temperature, defined later in the discussion of the phase diagram of cuprates.

The excess conductivity can be decomposed into three main contributions: the Aslamazov-Larkin (AL), Maki-Thompson (MT), and density-of-states based terms. The AL and MT terms are associated with superconducting carriers, while the density-of-states term is connected to the concentration of normal conduction electrons. As the temperature decreases, the concentration of normal conduction electrons decreases due to the formation of Cooper pairs, while the AL term increases with decreasing temperature. The AL term is a power function of reduced temperature and is related to the critical exponent λ mentioned earlier.

In some cases, the log-log plot of excess conductivity may deviate from a linear dependence [20], where experimental points lie above the straight line. This deviation signifies the presence of the MT term. While the 3D-AL term is proportional to $\tau^{(1/2)}$, the MT term exhibits a more complex relationship and is approximately proportional to $\tau^{(-1)}$.

Resistance experiments on superconductors focus on temperatures above the critical temperature ($T>T_c$) where the resistance is nonzero. However, valuable information about the superconducting state, both above and below T_c, can be obtained through AC susceptibility measurements. The response of the sample to a magnetic field is directly proportional to the concentration (n_s) of Cooper pairs [7], which is equivalent to the square of the absolute value of the order parameter. The susceptibility, like the excess conductivity, follows a power law dependence on reduced temperature (τ) with the critical exponent λ. By studying the susceptibility, it is possible to deduce the dimensionality of the system below T_c, similar to the analysis performed for conductivity, which however is limited to the region above T_c.

It is important to acknowledge that while the GLF can provide valuable insights into any continuous phase transition, each specific case may exhibit unique properties that require a quantum mechanical treatment. However, the general characteristics of continuous phase transitions remain universal within a class of systems sharing the same spatial dimension. Therefore, the GL description must be derived from the microscopic Hamiltonian that describes the particular system under investigation. The GLF can be derived from various models in solid-state physics such as the Ising model or the Heisenberg model.

To begin the derivation, one constructs the partition function from the given Hamiltonian, which typically involves discrete variables. These discrete variables are then transformed into continuous variables using the Hubbard-Stratonovich identity [9]. Subsequently, a physical quantity that can serve as the order parameter is identified. Modes with poor convergence are excluded, and the critical temperature is determined. The classical functional is expanded around the critical point, and finally, an averaging process over microscopic lengths is performed to eliminate “grains” from

the theory and exclude unnecessary modes. During this process, trial parameters are adjusted [9]. It is worth noting that fluctuations of the order parameters can also be derived from the microscopic Hamiltonian.

In this work, fluctuations in selected cuprates will be analysed based on the GL approach. Specifically, conductivity above T_c, susceptibility in the vicinity of the transition temperature, and in one case, specific heat will be studied to investigate these fluctuations.

2.2 Cuprate superconductors

Cuprates, also known as copper-oxide superconductors, have garnered significant attention since their discovery in 1986 due to their potential for high-temperature unconventional superconductivity and their wide range of applications in energy-related fields. However, despite extensive research over the past few decades, the mechanism underlying cuprate superconductivity remains highly debated and controversial. This is primarily due to the complex and unique electronic and magnetic properties exhibited by cuprates, such as the *pseudogap* state, *strange metal* behaviour, and the presence of charge and spin density waves and vortex matter. Additionally, cuprate superconductors are highly sensitive to impurities, defects, and doping, which can strongly influence their properties.

To address the complexity of cuprate superconductivity, numerous theoretical models and proposals have been put forward over the years. These include the *d*-wave pairing theory, resonating valence bond theory, spin-charge separation theory, fluctuation exchange theory, and electronic liquid crystal theory, among others. Each of these theories offers a different perspective on the underlying mechanism, focusing on various aspects of the intricate electronic and magnetic behaviours of cuprates. Some theories highlight the significance of strong electronic correlations and fluctuations, while others emphasize the role of spin and charge interactions or electron-phonon coupling. Despite the diversity of theoretical proposals, a comprehensive understanding of cuprate superconductivity remains elusive, and ongoing research continues to explore new theoretical frameworks and experimental approaches to unravel the complex electronic properties of these materials.

The field of cuprate research is vast, with approximately 3000 research articles published on the topic in 2022 alone. Consequently, providing a comprehensive overview of this broad research field is challenging. In this section, general aspects of cuprate superconductors and discussion of selected articles that the author considers to provide a comprehensive description of cuprates across the temperature-doping phase diagram will be presented.

Crystal structure and classification

Cuprates are layered materials characterized by their copper-oxygen (CuO_2) planes, which are separated by spacer layers containing other atoms (Fig. 2.2). These spacer layers, often referred to as the charge reservoir layers, serve as a site for introducing dopant atoms. Typically, dopants are incorporated into the charge reservoir layer rather than directly into the CuO_2 planes. The excess electrons or holes from the dopants are primarily accommodated in the CuO_2 planes, allowing for both electron and hole doping. Doping in cuprates is commonly achieved through methods such as cation/anion substitution, modulation of the interstitial oxygen density, or the application of an electric field using electrostatic gating. The doping level is denoted as *p* for hole doping and *n* for electron doping, representing the number of added holes or electrons, respectively.

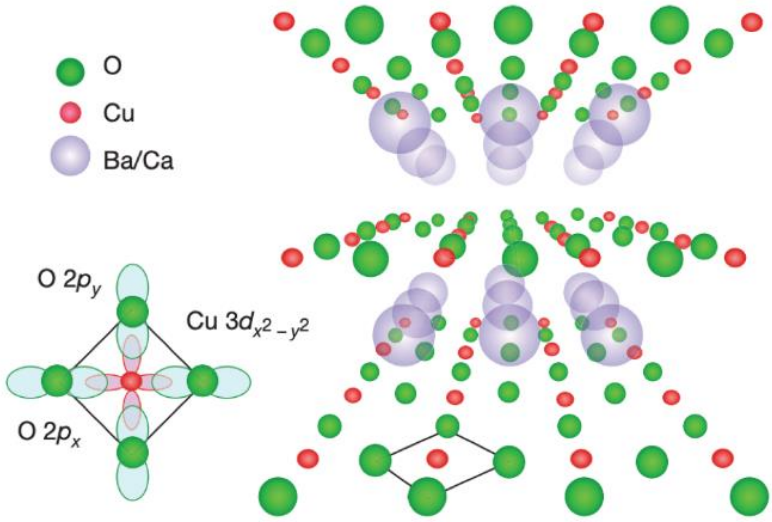

Figure 2.2: Schematic of the cuprates' CuO_2 sheet. Each of the copper atoms (red) within the CuO_2 layer is surrounded by four planar oxygen atoms (green). The bottom left figure illustrates the hybridization of Cu $3d_{x^2-y^2}$ and O $2p_{x,y}$ orbitals that is crucial to the unusual properties of the cuprate superconductors. Figure was reproduced from [21].

Cuprate superconductors exhibit a perovskite-like crystal structure with either tetragonal or orthorhombic symmetry. These compounds can be classified based on the number of CuO_2 layers present in a primitive cell, which can range from one to multiple layers. Another classification method is based on the heavy metal element incorporated in the structure, such as bismuth, mercury, or thallium. For convenience, cuprates are often represented using a four-digit abbreviation rather than their full chemical formula. The first symbol in the abbreviation indicates the heavy element present in the charge reservoir layer. This is followed by a hyphen and four digits that determine the cation ratio in the unit cell. The first digit represents the number of heavy metal cations in the charge reservoir layer, the second digit denotes the number of cations at the edge of the charge reservoir layer (typically Ba or Sr) per unit cell, the third digit represents the

number of cations separating the CuO_2 planes (usually Ca, Mg, or rare earth elements), and the last digit indicates the number of in-plane copper atoms in a unit cell. In this thesis, the focus is mainly on the Tl-1223 and Tl-2223 compounds, as illustrated in Fig. 2.3. It is worth noting that the abbreviation (Tl, Pb)-1223 or $Tl_{0.5}Pb_{0.5}$ 1223 signifies the composition where 50% of thallium is replaced by lead.

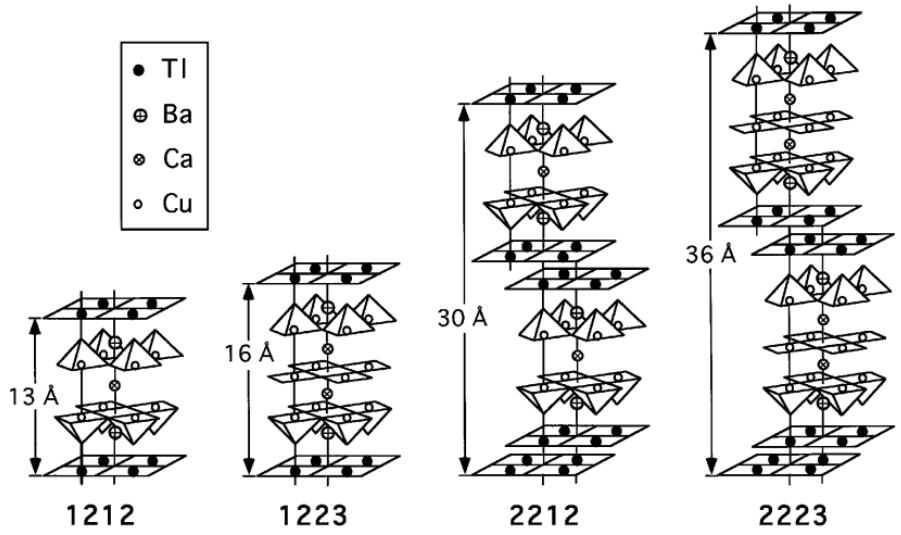

Figure 2.3: Cristal structure of the Tl-1212, Tl-1223, Tl-2212, and Tl-2223 cuprates. Figure adopted from ref. [22].

Electronic structure

The electronic structure of cuprates is determined by the hybridization of Cu $3d_{x2-y2}$ and O $2p_{x,y}$ orbitals, as depicted in Fig. 2.2. The presence of surrounding O^{2-} ions induces a Coulomb interaction that splits the five nominally degenerate Cu^{2+} 3*d* orbitals in energy. Among these orbitals, Cu $3d_{x2-y2}$ is the highest in energy. In the undoped parent compounds, the Cu^{2+} ions possess nine out of a maximum of ten 3*d* electrons, leading to a half-filled conduction band according to band theory. However, due to the strong onsite electron-electron interaction, these materials exhibit insulating behaviour. It incurs a significant energy cost (*U*) for two electrons to occupy the same Cu $3d_{x2-y2}$ orbital. Consequently, the undoped parent compounds are antiferromagnetic charge-transfer insulators. The strong onsite Coulomb interaction splits the Cu $3d_{x2-y2}$ band into a filled lower Hubbard band (LHB) and an empty upper Hubbard band (UHB), with a gap of energy *U*, as schematically shown in Fig. 2.4a. This state is known as a Mott-Hubbard insulator. Since the Hubbard *U* in cuprates is large, the O $2p_{x,y}$ band, known as the charge transfer band (CTB), is situated within this gap, and the chemical potential μ is pinned at the centre of the charge transfer gap Δ (Fig. 2.4 b). Consequently, electron hopping between Cu sites is suppressed, resulting in a charge-transfer insulating state. Numerous experiments, including X-ray

spectroscopy studies, have confirmed the charge-transfer character of cuprates, with a charge excitation gap $\Delta \approx 2 - 4$ eV, which is smaller than U [23, 24].

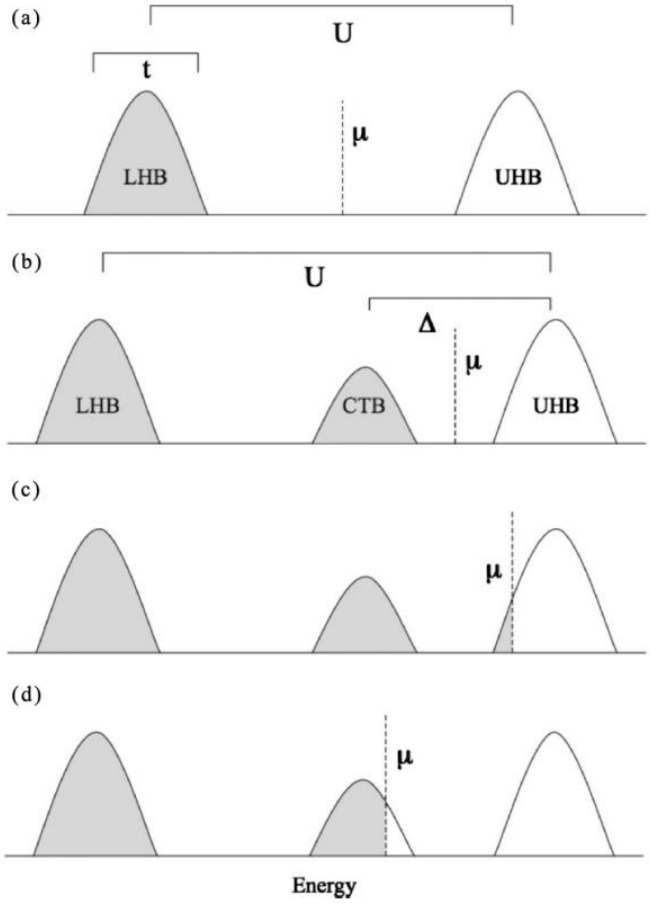

Figure 2.4: Schematic of Hubbard and charge-transfer insulator band structures. (a) Single-band Hubbard model with empty upper Hubbard band (UHB) and filled lower Hubbard band (LHB). μ denotes the chemical potential and lies in the middle of the Mott gap in the undoped compound. (b) Charge-transfer insulator. The charge-transfer band (CTB) lies between the UHB and the LHB. Δ is the charge-transfer gap between CTB and UHB. (c) Band structure of electron-doped cuprates. The chemical potential μ moves into the UHB upon doping with electrons. (d) Band structure of the hole-doped cuprates. The chemical potential μ moves into the CTB. Figure adapted from Ref. [25].

Upon doping the system with either electrons or holes, the chemical potential is shifted. Electrons doped into the CuO_2 planes primarily occupy the Cu sites, leading to the filling of the UHB (Fig. 2.4c). Conversely, doped holes predominantly reside in the O 2*p* orbitals, causing states to be removed from the CTB (Fig. 2.4d), resulting in the doping with electrons and holes, respectively.

In thallium-based cuprates, the Tl 6*s* orbital extends over a wide range of energies. It has an overlap with the Cu $3d_{x2-y2}$ antibonding orbital, thereby influencing the electronic properties of the conducting CuO_2 plane. In certain thallium cuprates (such as Tl-2201), the Tl 6*s* band even extends slightly below the Fermi level. This leads to the transfer of some electrons from the conducting

plane to the Tl 6*s* orbitals. Consequently, the CuO_2 plane gains additional charge carriers, specifically holes in this case [26].

Phase diagram

In the undoped state and at low carrier concentrations, cuprates exhibit **antiferromagnetic (AF)** Mott insulating behaviour, characterized by the presence of an antiferromagnetic order. The AF order arises from superexchange interactions, where the opposite spins of electrons residing on neighbouring sites are energetically favourable. The strength of the AF order is temperature-dependent, with a characteristic temperature called the Neel temperature (T_N) that varies with doping, as shown in Fig. 2.5a. The antiferromagnetic aspects of cuprates can be well described by the t-J model [27].

Upon further doping, the AF state is rapidly suppressed, and the strong correlations in the system give rise to various orders and ordering tendencies that persist even at high carrier concentrations. A schematic temperature-doping phase diagram for cuprates is presented in Fig. 2.5a, illustrating the emergence of different phases. One of the most complex regions in the cuprates' phase diagram is the **pseudogap (PG)** regime, located below a doping-dependent characteristic temperature T^* (Fig. 2.5a,b). The pseudogap was initially identified through NMR experiments and is characterized by a decrease in the density of states at the Fermi level [28, 29]. In particular, the pseudogap was extensively studied via angle-resolved photoemission spectroscopy (ARPES). These studies revealed that in the pseudogap regime the Fermi surface consists of disconnected fragments, so called Fermi arcs, depicted in Fig. 2.5b [21].

The pseudogap regime exhibits various orders and ordering tendencies, some of which are specific to certain compounds. These include translational symmetry-breaking charge density wave (CDW) order, stripes, spin density wave order (SDW), and indications of spatially modulated superconducting states such as pair density waves (PDW). Additionally, lattice symmetry-preserving magnetic orders with $\boldsymbol{q} = 0$, attributed to orbital loop currents, have been observed within the pseudogap regime [30]. Some of these orders may exist at a mesoscopic length scale, and superconducting fluctuations may also play a role in their formation.

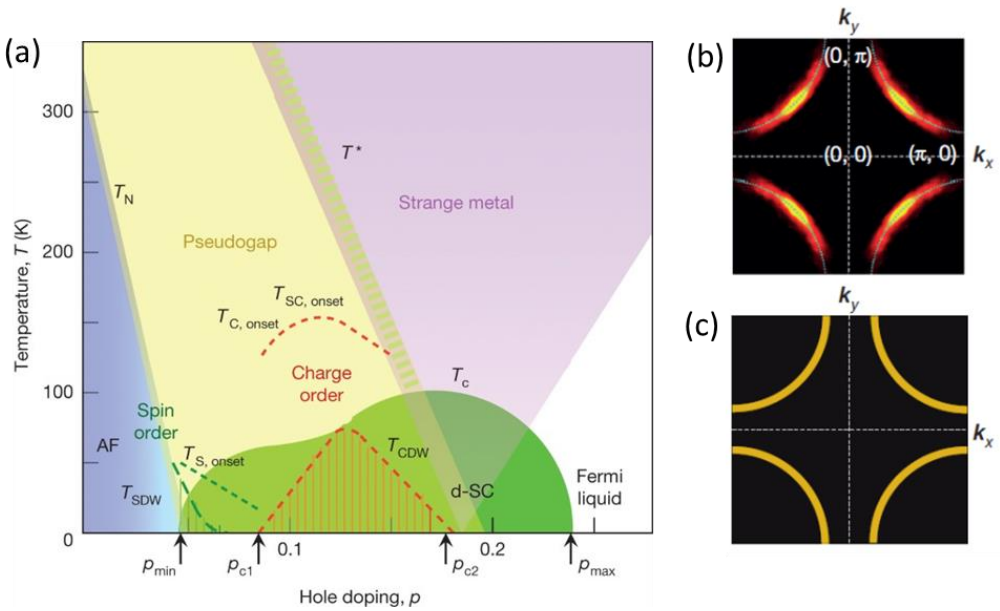

Figure 2.5: Phase diagram and evolution of the Fermi surface of hole-doped cuprates. (a) Schematic temperature-doping phase diagram (reproduced from ref. [21]) presenting the onset temperatures associated with the appearance of precursors or fluctuations of various orders: $T_{s,onset}$ (dashed, green line) for spin order, $T_{C,onset}$ and $T_{SC,onset}$ for charge order and superconductivity, respectively (both represented by red, dashed line). According to the presented phase diagram, fully developed spin density wave order appears below T_{SDW}, and the charge density wave order is considered long-range below T_{CDW}. T_N is the Neel temperature, T is the temperature below which the pseudogap is fully developed and T_c represents the transition to the SC state. Note, that the presence of the specific orders and exact onset temperatures are compound specific. (b) The measured Fermi surface in the pseudogap phase form of Fermi arcs. Gapless Fermi arcs exist only in the nodal directions. (c) The large, ungapped Fermi surface, as predicted by the band theory calculations, is revealed by scanning tunnelling spectroscopy and ARPES studies for overdoped compounds. (After Ref. [21]).*

The discovery of superconductivity in cuprates in 1986 propelled significant interest in these materials. The **superconducting (SC)** phase is observed in a moderate range of doping levels, emerging above a doping level of approximately $p \approx 0.5$. The optimal doping level, at which the critical temperature T_c reaches its maximum value, is around $p_{opt} \approx 0.16$ for both electron-doped and hole-doped cuprates. Increasing the doping level beyond p_{opt} leads to a decrease in T_c, and superconductivity eventually vanishes above a doping level of approximately $p \approx 0.30$. The shape of the superconducting phase in the phase diagram is similar across different cuprate compounds, forming a dome-shaped region as schematically shown in Fig. 2.5a.

The transition into the superconducting state is associated with the opening of an energy gap. The magnitude of this gap depends on temperature and reaches a few meV at absolute zero. Interestingly, the gap may change sign when measured along different directions, resulting in nodes (zero values) in certain directions. This gap with nodes is said to have *d* symmetry, in contrast to the node-less *s* symmetry, and is one of the distinct features of unconventional

superconductivity. Another characteristic of unconventional superconductivity is the absence of an isotope effect, which is typically observed in conventional superconductors due to electron-phonon coupling [31].

In the heavily overdoped regime cuprates exhibit a **Fermi liquid (FL)** behaviour, which has been well documented through a number of complementary experiments. The photoemission spectroscopy [32], angle dependent magnetoresistance [33] and quantum oscillation experiments [34] in overdoped $Tl_2Ba_2CuO_{6+\delta}$ (Tl-2201) revealed, a well-defined, approximately circular hole-like Fermi surface occupying about 60% of the Brillouin zone. These observations are consistent with the band structure calculations [35]. Within the overdoped Fermi liquid regime, the carrier density estimated from the Luttinger sum rule corresponds to $1 + p$ and agrees well with low temperature Hall coefficient measurements [36]. Concomitantly, resistivity exhibits quadratic temperature dependence, which is a signature of a Fermi-liquid behaviour, implying that the scattering rate is due to Umklapp electron-electron scattering. Furthermore, for applied *c*–axis magnetic fields (greater than the upper critical field) the Wiedemann-Franz law, relating the heat and charge transport, is obeyed [37].

The "normal state" regime above SC, between PG and FL is commonly referred to as **strange metal (SM)**. The name reflects the lack of ability to understand the properties of the cuprates in this regime. One of such properties is an unusually large magnitude of resistivity, suggesting that the mean-free path violates the Mott-Ioffe-Regel limit [38], however, as discussed in the next section this limit is never crossed. Another unusual behaviour is the linear temperature resistivity dependence which extends from very low to very high temperatures [39]. Since such a linear behaviour of resistivity is often associated with a linear temperature dependence of the scattering rate due to the presence of a quantum critical point [39], an extensive theoretical and experimental work was carried out in the search of the quantum criticality signatures [40]. However, systematic electronic transport (resistivity, magnetoresistance, Hall effect) measurements discussed in more detail in the following section revealed that the region of the strange metal is marked by the change of the effective carrier density, associated with the localization of charge carriers [41, 42] in agreement with the notion of the pseudogap formation and associated reduction in the density of states. Accordingly, it is exactly one hole per CuO_2 unit that becomes localized upon crossing from the FL regime at very high doping to the PG regime. The localization process explains numerous anomalies observed in cuprates and provides an understanding of the electronic transport across the phase diagram.

Electronic transport in cuprates

Since the discovery of the first cuprate superconductor, this class of materials was extensively explored via electronic transport measurements. Because resistivity corresponds to a weighted integration over the whole Fermi surface, it is highly sensitive to changes in electronic behaviour, and hence regularly used to detect phase transitions and determine phase diagrams. Yet for the same reason, the resistivity often exhibits complex dependences on stimuli such as temperature and magnetic field, which are then difficult to disentangle. Consequently, in the complex underdoped regime of cuprates, planar-resistivity (e.g. along the CuO_2 layers, Fig. 2.2) was first described in very vague terms (e.g., s-shaped, upturns, etc.) [43]. Nevertheless, over the last years, extracting the intrinsic properties and separating them from those compound specific, allowed the identification of rather simple and universal for cuprates properties.

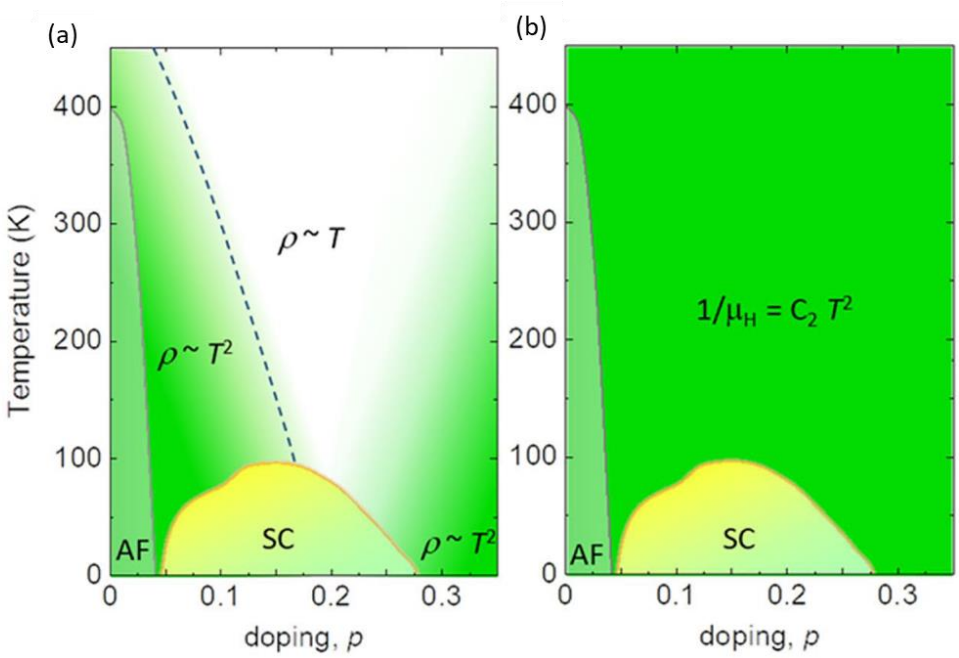

Figure 2.6: Phase diagrams summarising the electronic transport properties of hole doped cuprates from [44]. (a) Evolution of the compound independent sheet resistance, i.e. per number of CuO_2 layers in unit cell, evolves gradually across the phase diagram, from (Fermi liquid) quadratic to linear-like temperature dependence and back to (Fermi liquid) quadratic. The dashed line represents T, the temperature below which the PG is fully formed. (b) Phase diagram as deduced from Hall mobility measurements, which reveals a quadratic temperature dependence of the scattering rate, $1/\tau \propto T^2$. Remarkably, this behaviour is essentially compound and doping independent, and exhibiting the same universal slope for all cuprates ($1/\mu_H = C_2 T^2$, where $C_2 = 0.0175(20)\ K^{-2}$) [46, 41]. These results indicate that there is no change in the scattering rate upon crossing any characteristic temperatures marked in the schematic phase diagram shown in Fig. 2.4. The boundary of the long range antiferromagnetic order as well as the superconducting (SC) phase are also schematically shown.*

Figure 2.6a presents the doping-temperature phase diagram of cuprates, illustrating various regimes based on resistivity measurements. In the heavily overdoped regime, the resistivity

follows a quadratic temperature dependence ($\rho \propto T^2$), consistent with Fermi liquid metals. However, as the doping decreases and one enters the strange metal (SM) regime, the resistivity becomes linear in temperature ($\rho \propto T$). It then transitions back to a quadratic behaviour in the underdoped regime within the PG phase. One of the major challenges has been understanding the connection between these two regimes, which exhibit resistivity that is quadratic in temperature but are separated by the linear resistivity regime.

An important progress in understanding the electronic transport of cuprates has been made in recent years. Systematic electronic transport measurements allowed establishing a few fundamental properties of the cuprates. First, the carrier density observed in the underdoped cuprates is p, in contrast to $1 + p$ carriers in the overdoped FL regime. Consequently. a transition associated with the change of the carrier density around the optimal doping was first implied based on resistivity measurements [45]. Further understanding of the charge transport across the phase diagram came from a combined study of resistivity and Hall coefficient, which allowed to separate the contribution from the scattering rate τ and the impact of the carrier density on the electronic transport. The Hall mobility defined as the ratio of longitudinal and transverse resistivity ($1/\mu_H = \rho/R_H$) measures the (doping-independent) temperature dependence of the scattering rate. It was an important observation that this quantity remains unchanged across the normal state of cuprates, being essentially independent of regime or cuprate compound in which it is measured (Fig. 2.6b) [41, 47]. This striking experimental fact allowed further understanding of the normal state of cuprates. Although it was established rather early that the Hall mobility is quadratic in temperature at optimal doping ($1/\mu_H = C_2T^2$) [48], in contrast with the linear resistivity, but what reminded unnoticed for a long time was that the coefficient C_2 remains the same in electron and hole, underdoped, optimally doped, and overdoped cuprates; thus, it is universal as demonstrated in Fig. 2.6. [46, 47, 49] Notably, the quadratic temperature dependence was also observed in the case of the heavy-fermion system $YbRh_2Si_2$ in the proximity of field-tuned quantum criticality [50]. Initially, this behaviour was taken as an indication that the longitudinal and transverse scattering rates were different and was associated with spin–charge separation [51]. Yet in cuprates, exactly the same Hall mobility was observed from the underdoped to the overdoped limits of the SC dome, clearly indicating that transport itself is not exotic anywhere. In a Fermi liquid, the meaning of the transport coefficients is well defined [Hall coefficient: $R_H = 1/(n_{eff})$; Hall mobility: $1/\mu_H = m^*/(e\tau)$; resistivity: $\rho = R_H/\mu_H$]. With μ_H being fixed and universal, the difference between the underdoped

and overdoped regimes was then associated with variations in n_{eff}, which is the essential ingredient of pseudogap physics.

Evolution of the Fermi surface across the temperature-doping phase diagram

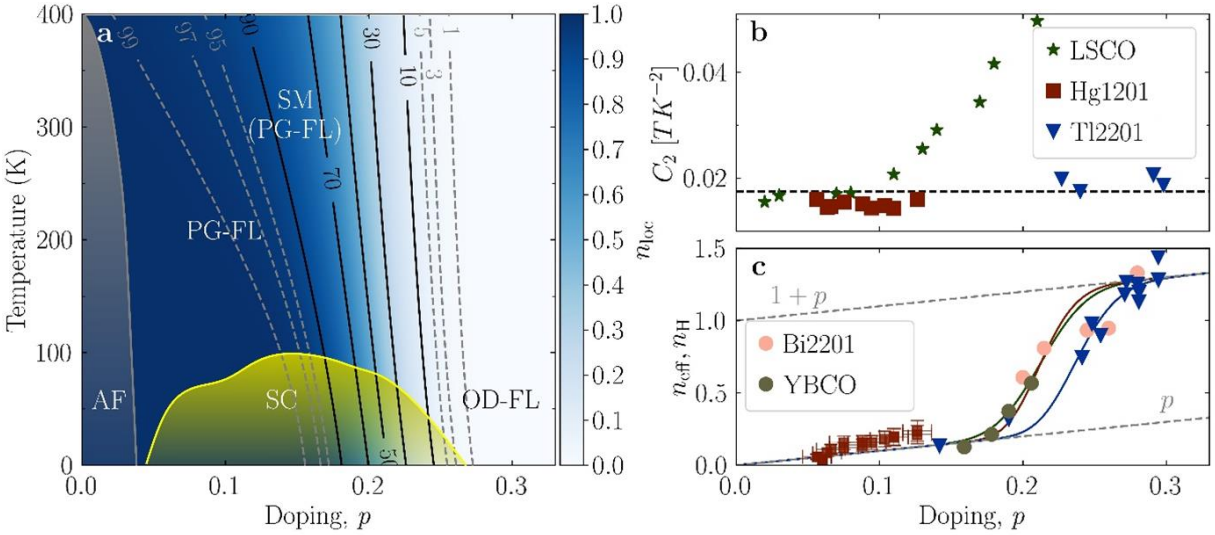

Figure 2.7: Phase diagram and carrier density in cuprates, from Ref.[49]. (a) Schematic phase diagram that captures the evolution of key universal features of cuprates. The approximate limit of the antiferromagnetic (AF) phase is shown in grey and the superconducting (SC) dome in yellow. The doping/temperature evolution of the density of localized charge, as extracted from the resistivity, is indicated by blue shading. Solid black and dashed grey lines are isodensity lines. In the OD-FL regime, all carriers contribute to electronic transport. Both, the pseudogap Fermi liquid (PG-FL, roughly corresponding to > 97% localized holes) and the strange metal (SM, marked by an intensive gradual delocalization) are also indicated, though there is no conceptual difference between them. b Measurements of the Hall mobility revealed that $C_2=(1/\mu_H)-C_0)/T^2$ is essentially universal in cuprates, with C_2 = 0.0175(20) TK^{-2} (indicated by the dashed line). However, C_2 in LSCO for p > 0.08 deviates strongly from the universal value. (c) Doping dependence (at T = 0 K) of the carrier density (n_{eff}) as determined from the resistivity (full lines), compared with values obtained from the Hall coefficient (solid points). Both quantities behave identically and reveal the p to 1 + p change in the carrier density.

The universality of μ_H in cuprates implied further that the effective mass and the scattering rate of the charge carriers themselves is unchanged [42]. Indeed, across the cuprate phase diagram, the underlying Fermi surface (the contour of the Fermi surface) contains always 1 + p states, as established experimentally by photoemission spectroscopy measurements [41, 42, 52]. In the highly overdoped regime, the underlying and actual Fermi surface coincide, as presented in Fig. 2.5c. With decreasing doping, a partial gap develops on the antinodal parts of the Fermi surface gradually affecting exactly one hole per CuO_2 unit [42, 41], leading to the formation of Fermi arcs which still contain p states (Fig. 2.5b) [42, 45, 53, 54]. Because those arc states exhibit the same character as the Fermi-liquid states observed in the overdoped regime, the normal state of cuprates is referred to as ”pseudogapped Fermi liquid” [42]. The whole complexity (sometimes referred to as ”non-Fermi-liquidity”) of cuprates stems from the coexistence of the second (localized)

electronic subsystem which delocalizes with increasing the temperature and doping, becoming part of the itinerant Fermi-liquid electronic subsystem by gradually repopulating the gapped part of the Fermi-surface [41, 42].

Coexistence of two electronic subsystems

Because the ratio m^*/τ is fixed by the universality of μ_H, the resistivity $\rho = R_H/\mu_H$ is a direct measure of carrier density n_{eff} [42,46]. This fact was recently used in a detailed analysis of resistivity in various compounds to find the effective carrier density n_{eff} as a function of temperature and doping [41]. As already noted in 2015 [42,46], the zero-temperature evolution of n_{eff} at $T = 0$ extracted from resistivity measurements showed a gradual change from p to $1 + p$ (Fig. 2.7). Somewhat later, high magnetic field (up to 88 T) measurements of Hall number in $YBa_2Cu_3O_y$ (Y123) yielded a rather sharp change of $n_H(T=0)$, from p to $1 + p$, at $p = 0.16$, which was attributed to a pseudogap critical point [55]. However, the discrepancy was resolved recently by considering the chain anisotropy, which lead to a smooth crossover for Y123 as well [56]. The evolution of the high-field Hall number $n_H(T=0)$ in two cuprate families, Tl2201 and $Bi_2Sr_2CuO_{6+\delta}$ (Bi-2201), which have simple single-band Fermi surfaces and do not suffer from the presence of the Lifshitz transition [57, 58], is similarly smooth as a function of p throughout the overdoped regime, so that $n_H(T=0)$ does not reach the value $1 + p$ until close to the far edge of the superconducting dome [56], agreeing remarkably well with the evolution of $n_{eff}(T=0)$ determined earlier from the resistivity (Fig. 2.7). Once the density of itinerant charges is determined, it is rather straightforward to determine the number of localized holes, because the total charge is always $1 + p$:

$$1 + p = n_{eff} + n_{loc}. \qquad (2.14)$$

The established doping dependence of n_{loc} is shown in Fig. 2.7c. This gradual nature of the hole localization process was furthermore associated with the well-known evolution of bond-angle disorder in cuprates [59, 60, 61]. In fact, such a disorder mandates that gaps, associated with the one localized hole per CuO_2 unit cell, are also disordered [42, 46], because the localization energy should strongly depend on the environment. This disorder results in a 50-meV-broad gap distribution and the associated percolation processes [41], which should not be surprising, because Mott localization is by its nature a first-order transition. Moreover, it does not break any symmetry (it is a $\boldsymbol{q} = 0$ transition) which leaves the Brillouin zone unfolded, so that the underlying Fermi surface does not change and the mobile carriers only experience a crossover in density, manifested by arc growth, instead of any transition induced by the localized subsystem. This dopant-induced arc growth scenario is corroborated by a one-body Fermi liquid DFT calculation [62].

The conclusions above were drawn solely from the universalities uncovered by transport measurements. However, it is noteworthy that several results obtained from advanced spectroscopic techniques, which are not discussed here, also align with these observations. Regarding the itinerant charges, though spectroscopic techniques are less sensitive than transport in the k_BT energy window around the Fermi surface, angular resolved photoemission reveals that the nodal Fermi velocity is compound- and doping-independent [63]. Doping-independence of the effective mass, as well as the doping dependence of the density of charge carriers inferred from optical conductivity, agrees with the n_{eff} extracted from transport [54].

Consequence for superconductivity

Based on a wealth of experimental data from electronic transport and optical spectroscopy measurements, it has been proposed that superconductivity arises from the interplay between the two electronic subsystems: the effective itinerant carriers n_{eff}, and the localised carriers n_{loc}. Direct observation from the optical conductivity in underdoped regime has provided the evidence that the itinerant carriers become superconducting [64]. This conclusion is supported by the fact that the superconducting state opens a gap in the coherent Fermi liquid part of the spectra [64]. On the overdoped side (as shown in Fig. 2.8), superconductivity vanishes concomitantly with the disappearance of the localized charge. This observation strongly suggests that the localized charge plays a crucial role in providing the glue for superconductivity [56]. Consequently, it has been proposed [56] that the superfluid density, ρ_S , is directly proportional to both the density of itinerant holes n_{eff} and density of localized holes n_{loc}:

$$\rho_S = n_{eff}\,(O_S\, n_{loc}). \qquad (2.15)$$

Here the densities of both electronic subsystems (n_{eff} and n_{loc}) can be directly identified from the normal-state charge transport properties, while O_S is a compound-dependent constant. Indeed, despite this simplicity, a remarkable agreement with experimental data is obtained, as shown in Fig. 2.8. As argued in Ref. [44], such a simple relationship between ρ_S and n_{loc} implies: (1) that the latter measures the effective SC coupling strength ("glue") and (2) a very local (and fast/ short-time) superconducting mechanism, in agreement with the notion that the size of the Cooper pair (coherence length) in cuprates is of the order of a unit cell. Consequently, superconductivity emerges from the normal state through a percolative process characterized by a (yet again) universal (emergent) energy scale of about 30–40 K [65, 66, 67]. Recently reported THz response measurements in the overdoped regime [68] are in full agreement with the picture proposed above. Again, the Fermi liquid charges condense in the SC state, with the superfluid density (Fig. 2.8)

that corresponds to Eq. 2.15. Therefore, in the overdoped regime the doping dependence of ρ_S is predominantly dictated by the changes in n_{loc} [56].

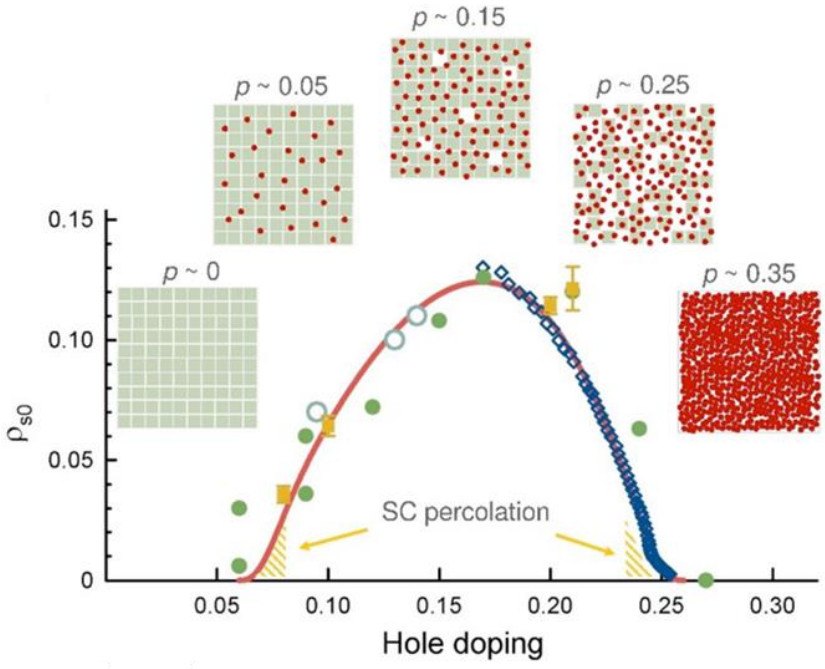

Figure 2.8. Superfluid density measured in LSCO (open and closed symbols) shows a dome-like doping dependence, which is captured well by Eq. (2.15) full line, corrected at very low superfluid densities (hashed areas) for percolation effects, as discussed in detail in Ref. [56]. The insets represent symbolically the ratio between n_{eff} (red dots) and n_{loc} (green squares). At low doping, ρ_S ($\rho s0$ in the figure) is limited by the density of mobile holes (n_{eff}) and by pair-breaking impurities, whereas at high doping, the limiting factor is the density of localized holes (n_{loc}). A percolation regime is expected on both ends of the superconducting (SC) dome due to spatial inhomogeneity of superconducting gaps. Figure from Ref. [56].

Thallium cuprates

Thallium-based cuprates are among the most extensively studied cuprate superconductors. Unlike other cuprates, Tl-based materials have a unique crystal structure that allows for the formation of highly anisotropic electronic bands without multiple competing electronic orders. This makes them ideal systems for studying the effects of dimensionality on superconductivity and other electronic phenomena. Furthermore, Tl-based cuprates exhibit strong one-dimensional behaviour due to the presence of chains of copper atoms along the crystallographic b-axis. This leads to the formation of one-dimensional electronic states and can result in enhanced superconductivity and other interesting phenomena, such as charge density waves. In addition, Tl-based cuprates also exhibit three-dimensional behaviour due to their layered crystal structure, which can affect their vortex properties and other transport properties.

There are various superconducting thallium compounds, differing in the number of thallium atoms (m = 1,2) and cuprate planes (n = 1,2,3,4) in the unit cell. Their abbreviated formula is Tl-m2(n-1)n.

For achieving high-T_c superconductivity, the oxygen stoichiometry plays a crucial role. While as-grown in the oxygen atmosphere Tl-2201 is not a superconductor, the same compound prepared in a reducing atmosphere (H_2, Ar) becomes a superconducting with a critical temperature of up to 85 K. Among thallium cuprates, optimally doped Tl-2223 exhibits the highest critical temperature (125 K-127 K) and surpasses its bismuth analogue Bi-2223 (110 K). However, (Hg,Tl)-1223 displays the highest critical temperature (138 K) among all cuprates.

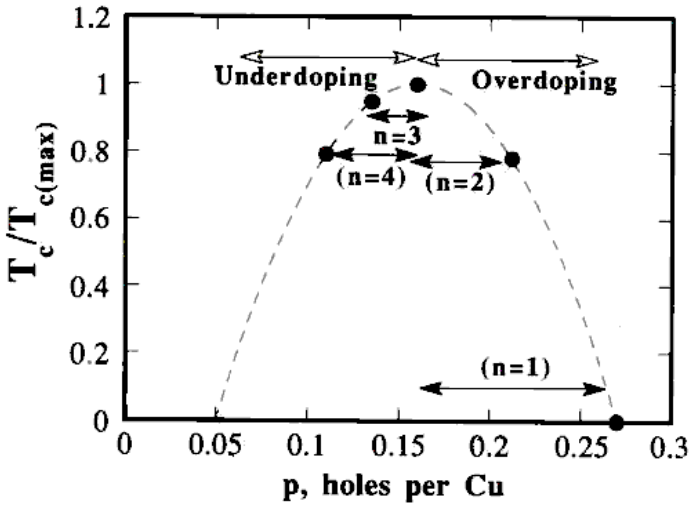

Figure 2.9: T_c dependence on hole doping for $Tl_2Ba_2Ca_{n-1}Cu_nO_y$ superconductors after Ref. [26].

Cuprates often have a non-uniform structure with defects and substitutions. Thallium cuprates, even without introducing any additional elements, undergo autosubstitution, where some thallium atoms are replaced by calcium. Unit cell size can also be modified by substituting barium with strontium. Lead (Pb^{4+}) can partially replace thallium, which stabilizes the oxygen stoichiometry of the entire compound. This happens because labile oxygen is located adjacent to the thallium site and is more strongly attracted to lead than thallium. Finally, substituting yttrium for calcium can modulate the critical temperature.

Fluctuations and dimensionality

The transition from superconducting to normal state is a second-order phase transition, which means that there is no latent heat involved during the phase change. This transition does not require any additional energy to be added to the system, and thermal fluctuations play a crucial role under

these conditions. Although in thallium cuprates, the superconducting state is believed to exist predominantly in two dimensions, thermal fluctuations can cause the superconducting state to fluctuate between different dimensions, and these fluctuations can be detected by observing changes in the superconducting properties of the material. Fluctuations can be observed in the broadening of the transition seen in DC resistance experiments. Another manifestation of fluctuations is an average AC susceptibility signal above the transition. The temperature range in which fluctuations cannot be neglected for bulk, clean, conventional superconductors is proportional to the critical temperature raised to the power of four. This can be expressed as $\Delta T/T_c \sim (T_c/\varepsilon F)^4$. While fluctuations are negligible for low-temperature superconductors, they become significant for high-temperature ones. Many cuprates fall into this category due to their high critical temperature.

Analysing these fluctuations, can provide insight into the dimensionality of the superconducting state in cuprates. Cuprate superconductors are typically classified as two-dimensional materials because the copper-oxide planes in which superconductivity occurs are only a few atoms thick and the electrons are confined to move within these planes. However, these compounds can also exhibit quasi-one-dimensional or three-dimensional behaviour depending on their specific crystal structure and composition. Studying the effects of dimensionality in cuprate superconductors, allows the determination of how changes in the dimensionality of a material affect its electronic and magnetic properties, and how these properties are related to superconductivity. For example, quasi-one-dimensional cuprate materials have been found to exhibit enhanced superconductivity and unusual charge and spin density wave behaviour, while three-dimensional cuprate materials have been found to have lower critical temperatures and different vortex properties compared to their two-dimensional counterparts. Studying dimensionality in cuprates is important because the obtained results can be used to develop theoretical models and to guide further experimental investigations of these materials to elucidate the underlying mechanisms of cuprate superconductivity.

Literature

1. H. Onnes, Further experiments with liquid helium. C. On the change of electric resistance of pure metals at very low temperatures etc. IV. The resistance of pure mercury at helium temperatures, KNAW, Proceedings, 13 II, 1910-1911, (1911); H. Onnes, The resistance of pure mercury at helium temperatures. Commun. Phys. Lab. Univ. Leiden (1911); H. Onnes, Leiden Communication, 124c (1911)
2. W. Keesom and M. Wolfke: Commun. Phys. Lab. Univ. Leiden 190b (1927); Versl. Kon. Akad. Amst. ***36***, 1204 (1927)
3. C. Gorter and H. Casimir, Physik. Z. **35**, 963 (1934); **15**, 539 (1934)
4. C. Gortel, Chapter I The two fluid model for superconductors and helium II, Progress in Low Temperature Physics **1**, 1-16 (1955) doi: 10.1016/S0079-6417(08)60076-1
5. W. Meissner and R. Ochsenfeld, Ein neuer effekt bei eintritt der supraleitfähigkeit, Naturwissenschaften **21** (44), 787-788 (1933)
6. F. London and H. London, The electromagnetic equations of the supraconductor, Proc. R. Soc. Lond. A **149** (866), 71-88 (1935) doi: 10.1098/rspa1935.0048
7. M. Tinkham, Introduction to superconductivity 2nd edition, McGraw-Hill, Inc. (1996) isbn: 0-07-064878-6
8. http://web.mit.edu/6.763/www/FT03/Lectures/Lecture4.pdf, access 15.05.2023
9. Y. Ivanchenko and A. Lisyansky, Physics of critical fluctuations, Springer Science & Business Media (1995) isbn: 9780387944142
10. A. Pippard, The coherence concept in superconductivity, Physica **19**, 765-774 (1953) doi: 10.1016/S0031-8914(53)80085-6
11. J. Bardeen, L. Cooper, and J. Schrieffer, Theory of superconductivity, Physical review **108** (5), 1175-1204 (1957) doi: 10.1103/PhysRev.108.1175
12. E. Maxwell, Isotope effect in the superconductivity of mercury, Physical Review 78 (4), 477 (1950) doi: 10.1103/PhysREv.78.477
13. J. W. Rohlf, , Modern Physics from alpha to Z_0, Wiley 1994 isbn: 978-0-471-57270-1
14. P. de Gennes, Superconductivity of metals and alloys, W. A. Benjamin, Inc., New York, Amsterdam (1966) isbn: 9780429965586

15. J. Hulm and B. Matthias, Overview of superconducting materials development (1981) In: S. Foner, B. Schwartz (eds) Superconductor Materials Science: Metallurgy, Fabrication, and Applications. NATO Advanced Study Institutes Series, **68**, Springer, Boston, MA. doi: 10.1007/978-1-4757-0037-4_1
16. D. Hinks, H. Claus, and J. Jorgensen, The complex nature of superconductivity in MgB_2 as revealed by the reduced total isotope effect, Nature **411**, 457–460 (2001) doi: 10.1038/35078037
17. R. Feynman, Feynmana wykłady z fizyki tom 3, wydanie trzecie (The Feynman lectures on physics vol. 3, 3rd edition), PWN S.A. (2001) isbn: 83-01-13489-5
18. S. Inderhees *et al.*, Specific heat of single crystals of $YBa_2Cu_3O_{7-\delta}$: Fluctuation effects in a bulk superconductor, Physical Review Letters **60** (1988) 1178 doi: 10.1103/PhysRevLett.60.1178
19. A. Kozłowski *et al.*, Specific heat of a high-temperature superconductor: $DyBa_2Cu_3O_7$, Physica C **184** (1-3), 113-118 (1991) doi: 10.1016/0921-4534(91)91507-Z
20. Solovjov *et al.*, Specific temperature dependence of pseudogap in $YBa_2Cu_3O_{7-\delta}$ nanolayers, Physical Review B **94** (22), 224505 (2016) doi: 10.1103/PhysRevB.94.224505
21. B. Keimer *et al.*, From quantum matter to high temperature superconductivity in copper oxides, Nature **518**, 179-186 (2015) doi: 10.1038/nature14165
22. M. Siegal *et al.* Synthesis and properties of Tl-Ba-Ca-Cu-O superconductors, Journal of Materials Research **12** (11), 2825-2854 (1997) doi: 10.1557/JMR.1997.0378
23. A. Fujimori *et al.*, Spectroscopic evidence for strongly correlated electronic states in La-Sr-Cu and Y-Ba-Cu oxides, Physical Review B **35** (16), 8814-8817 (1987) doi: 10.1103/physrevb.35.8814
24. A. Bianconi *et al.*, Localization of Cu 3d levels in the high T_c superconductor $YBa_2Cu_3O_{\sim 7}$ by Cu 2p X-ray photoelectron spectroscopy, Solid state Communications **63** (12), 1135-1139 (1987) doi: 10.1016/0038-1098(87)91063-5
25. S. Chakravarty *et al.,* An explanation for a universality of transition temperatures in families of copper oxide superconductors, Nature **428**, 53-55 (2004) doi: 10.1038/nature02348
26. R. Liu and P. Edwards, Effects of inherent (auto) doping and oxygen nonstoichiometry and their relationship to the band structure of Tl-based superconductors, In: A. Herman and J. Yakhmi (Eds.), Thallium based high temperature superconductors, 325-345, Marcel Dekker, Inc., New York*Basel*Hong Kong (1994) isbn: 0-8247-9114-2

27. J. Spałek *et al.*, Superconductivity in high-T_c and related strongly correlated systems from variational perspective: Beyond mean field theory, Physics Reports **959**, 1-117 (2022) doi: 10.1016/j.physrep.2022.02.003
28. W. Warren *et al.*, Cu spin dynamics and superconducting precursor effects in planes above T_c in $YBa_2Cu_3O_{6.7}$, Physical Review Letters **62** (10), 1193-1196 (1989) doi: 10.1103/physrevlett.62.1193
29. A. Puckov *et al.*, The pseudogap state in high-T_c superconductors: an infrared study, Journal of Physics: Condensed matter **8**, 10049-10082 (1996) doi: 10.1088/0953-8984/8/48/023
30. Y. Li *et al.*, Unusual magnetic order in the pseudogap region of the superconductor $HgBa_2CuO_{4+\delta}$, Nature **455** (7211), 372-375 (2008) doi: 10.1038/nature07251
31. J. Franck, Experimental studies of the isotope effect in high temperature superconductors, In: D. Ginsberg (Ed.), Physical properties of high temperature superconductors IV, 189-293, Word Scientific (1994), doi: 10.1142/9789814440981_0004
32. M. Platé *et al.*, Fermi surface and quasiparticle excitations of overdoped $Tl_2Ba_2CuO_{6+\delta}$, Physical Review Letters **95**, 077001 1-4 (2005) doi: 10.1103/physrevlett.95.077001
33. N. Hussey *et al.*, A coherent three dimensional Fermi surface in a high-transition temperature superconductor, Nature **425**, 814-817 (2003) doi: 10.1038/nature01981
34. B. Vignolle *et al.*, Quantum oscillations in an overdoped high-T_c superconductor, Nature **455**, 952-955 (2008) doi: 10.1038/nature07323
35. C. Osvaldo Rodriguez, Structural properties and electronic structure of $HgBa_2CuO_4$: Detailed description of the Fermi surface, Physical Review B **49** (2), 1200-1204 (1994) doi: 10.1103/physrevb.49.1200
36. A. Mackenzie *et al*., Normal-state magnetotransport in superconducting $Tl_2Ba_2CuO_{6+\delta}$ to millikelvin temperatures, Physical Review B **53** (9), 5848-5855 (1996) doi: 10.1103/physrevb.53.5848
37. C. Proust *et al*., Heat transport in a strongly overdoped cuprate: Fermi liquid and a pured-wave BCS superconductor, Physical Review Letters **89** (14), 147003 1-4 (2002) doi: 10.1103/physrevlett.89.147003
38. S. Uchida, High temperature superconductivity: The road to higher critical temperature. Tokyo, New York: Springer Japan Vol. 213, (2015) isbn: 978-4-431-55300-7
39. R. Cooper *et al.*, Anomalous criticality in the electrical resistivity of $La_{2-x}Sr_xCuO_4$, Science **323**, 603-607 (2009) doi: 10.1126/science.1165015

40. C. Putzke, Fermi surface and quantum critical phenomena of high temperature superconductors, Cham, Switzerland, Springer, (2016) isbn: 3319486454
41. D. Pelc *et al*., Unusual behaviour of cuprates explained by heterogeneous charge localization, Science Advances **5**, eaau4538 1-10 (2019) doi:10.1126/sciadv.aau4538
42. N. Barišić *et al.*, Evidence for a universal Fermi-liquid scattering rate throughout the phase diagram of the copper-oxide superconductors, New Journal of Physics **21**, 113007 1-36 (2019) doi: 10.1088/1367-2630/ab4d0f
43. N. Hussey, Phenomenology of the normal state in-plane transport properties of high-T_c cuprates, Journal of Physics: Condensed Matter **20** (12), 123201 1-31 (2008) doi: 10.1088/0953-8984/20/12/123201
44. N. Barišić and D. Sunko, High-T_c cuprates: a story of two electronic subsystems, Journal of Superconductivity and Novel Magnetism **35**, 1781-1799 (2022) doi: 10.1007/s10948-022-06183-y
45. N. Barišić *et al.*, Universal sheet resistance and revised phase diagram of the cuprate high-temperature superconductors, Proceeding of the National Academy of Sciences **110** (30), 12235-12240 (2013) doi: 10.1073/pnas.1301989110
46. N. Barišić *et al.*, Evidence for a universal Fermi-liquid scattering rate throughout the phase diagram of the copper-oxide superconductor, New Journal of Physics **21** (11), 113007 1-36 (2019) doi: 10.1088/1367-2630/ab4d0f
47. Li Y. *et al.*, Hidden Fermi-liquid charge transport in the antiferromagnetic phase of the electron doped cuprate superconductors, Physics Review Letters **117**, 197001 1-6 (2016) doi: 10.1103/PhysRevLett.117.197001
48. T. Chien, Z. Wang, and N. Ong, Effect of Zn impurities on the normal-state hall angle in single-crystal $YBa_2Cu_{3-x}Zn_xO_{7-\delta}$. Physics Review Letters **67** (15), 2088-2091 (1991) doi: 10.1103/PhysRevLett.67.2088
49. B. Knobloch-Klebel *et al.*, Transport properties and doping evolution of the Fermi surface in cuprates, arXiv:2303.05254v1 (2023) https://arxiv.org/pdf/2303.05254.pdf
50. S. Paschen *et al.*, Hall-effect evolution across a heavy-fermion quantum critical point, Nature **432** (7019), 881-885 (2004) doi: 10.1038/nature03129
51. P. Anderson, Hall effect in two dimensional Luttinger liquid, Physical Review Letters **67** (15), 2092-2094 (1991) doi: 10.1103/PhysRevLett.67.2092
52. I. Drozdov *et al.*, Phase diagram of $Bi_2Sr_2CaCu_2O_{8+\delta}$ revisited, Nature Communications **9** (1), 5210 (2018) doi: 10.1038/s41467-018-07686-w

53. Y. Ando *et al.*, Evolution of the Hall coefficient and the peculiar electronic structure of the cuprate superconductors, Physical Review Letters **92** (19), 197001 (2004) doi: 10.1103/PhysRevLett.92.197001
54. W. Padilla *et al.*, Constant effective mass across the phase diagram of high-T_c cuprates, Physical Review B **72**, 060511 (2005) doi: 10.1103/PhysRevB.72.060511
55. S. Badoux, *et al*. Change of carrier density at the pseudogap critical point of a cuprate superconductor. Nature **531**, 210 (2016) https://doi.org/10.1038/nature16983
56. C. Putzke *et al.*, Reduced Hall carrier density in the overdoped strange metal regime of cuprate superconductors, Nature Physics **17**, 826-831 (2021) doi: 10.1038/s41567-021-01197-0
57. P. Rourke *et al.*, A detailed de Haas-van Alpen effect study of the overdoped cuprate $Tl_2Ba_2CuO_{6+\delta}$, Journal of Physics **12** (10), 105009 (2010) doi: 10.1088/1367-2630/12/10/105009
58. Y. Ding *et al.*, Disappearance of superconductivity and a concominant Lifshitz transition in heavily overdoped $Bi_2Sr_2CuO_6$ superconductor revealed by angle-resolved photoemission spectroscopy, Chinese Physics Letters **36**, 017402 (2019) doi: 10.1088/0256-307X/36/1/017402
59. A. Bianconi *et al.*, $L_{2,3}$ xanes of the high T_c superconductor $YBa_2Cu_3O_{\approx 7}$ with variable oxygen, Solid State Communications **63** (11), 1009-1013 (1987) doi: 10.1016/0038-1098(87)90650-8
60. T. Egami and S. Billinge, Lattice effects in high temperature superconductors, Progress in Materials Science **38**, 359-424 (1994) doi: 10.1016/0079-6425(94)90005-1
61. F. Rullier-Albenque *et al.*, Disorder, metal-insulator crossover and phase diagram in high-T_c cuprates, EPL (Europhysics Letters) **81** (3), 37008 (2008) doi: 10.1209/0295-5075/81/37008
62. P. Lazić and D. Sunko, Fermi arcs and pseudogap emerging from dimensional crossover at the Fermi surface in $La_{2-x}Sr_xCuO_4$, EPL (Europhysics Letters) **112** (3), 37011 (2015) doi: 10.1209/0295-5075/112/37011
63. X. Zhou *et al.*, Universal nodal Fermi velocity, Nature **423**, 398-399 (2003) doi: 10.1038/423398a
64. C. Homes *et al.*, A universal scaling relation in high-temperature superconductors , Nature **430** (6999), 539-541 (2004) doi: 10.1038/nature02673

65. D. Pelc *et al*., Emergence of superconductivity in the cuprates via an universal percolation process, Nature Communications **9** (1), 4327 (2018) doi: 10.1038/s41467-018-06707-y
66. G. Yu *et al.*, Universal precursor of superconductivity in the cuprates, Physical Review B **99** (21), 214502 (2019) doi: 10.1103/PhysRevB.99.214502
67. P. Popčević *et al.*, Percolative nature of the direct-current paraconductivity in cuprate superconductors, npj Quantum Materials **3** (1), 42 (2018) doi: 10.1038/s41535-018-0115-2
68. F. Mahmood *et al.*, Locating the missing superconducting electrons in the overdoped cuprates $La_{2-x}Sr_xCuO_4$, Physical Review Letters **122**, 027003 (2019) doi: 10.1103/PhysRevLett.122.027003

3. Experimental methods

This thesis encompasses the application of multiple experimental methods for the preparation and analysis of samples. The optimization of precursor synthesis and final Tl-2223 samples primarily relied on X-ray powder diffraction and AC magnetic susceptibility techniques, complemented by occasional employment of SEM. Subsequently, the samples obtained under optimized experimental conditions underwent measurement using X-ray powder diffraction, AC magnetic susceptibility, resistivity, and, in select cases, SEM. The determination of superconducting properties, including critical temperature, critical current, and critical exponents, was carried out through AC magnetic susceptibility and magnetization, resistivity, and specific heat measurements. The subsequent section briefly introduces the techniques utilized by the author

3.1 X-Ray powder diffraction technique

The principle of X-ray powder diffraction revolves around the ability to observe the atomic arrangement within a sample by utilizing X-ray radiation. This method is based on the fact that the wavelength of X-rays is similar to the distances between atoms in the sample, allowing the collection of regularly spaced atoms to act as an atomic diffraction grating. In the case of a crystalline structure, X-ray powder diffraction enables the determination of important parameters such as the space group and the crystallographic structure, including lattice parameters and the positions of atoms. This information provides insights into the organization of atoms within the crystal lattice. Furthermore, X-ray powder diffraction can also provide an estimation of the grain size in polycrystalline samples. By analysing the diffraction pattern, it is possible to assess the size of individual crystallites present in the sample. Lastly, when the macroscopic density of the sample is known, a comparison can be made with the calculated density of a unit cell. This analysis allows for the estimation of the porosity of the sample, providing information about the presence of void spaces within the material.

The X-ray diffraction (XRD) apparatus comprises several essential components, namely the X-ray source, collimator, sample holder, and detector (refer to Fig. 3.1). In the experimental setup, the X-ray beam emitted by the source interacts with the sample (as depicted in Fig. 3.2). Constructive interference occurs when the Bragg condition is satisfied, establishing a connection between the reflection angle (θ), the distance between atomic planes within the crystal (d), and the wavelength of the X-rays (λ):

$$2d\sin(\theta) = n\lambda\,,$$

Here, '*n*' represents a natural number. The detector captures the "reflected" beam, and the resulting diffractogram typically takes the form of a graph plotting the intensity of the reflected X-rays against the 2θ angle.

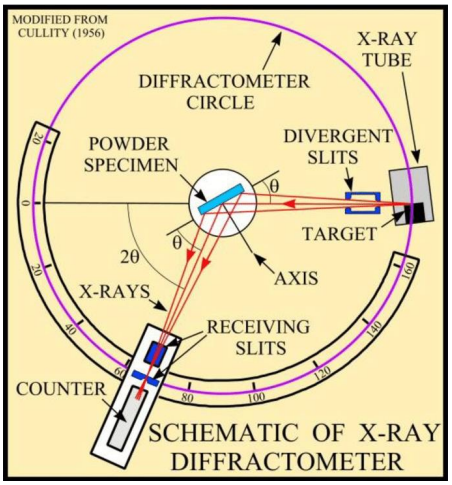

Figure 3.1: Schematic of X-ray powder diffractometerr (from Ref. [1]).

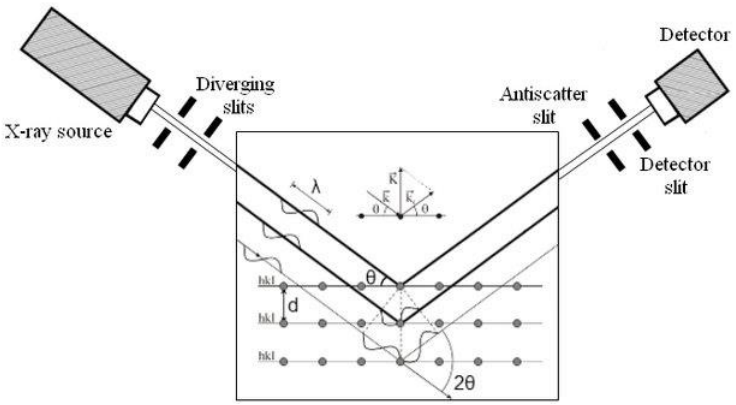

Figure 3.2: Principle of X-ray diffraction (XRD) method [2]. The X-ray beam generated by an X-ray tube undergoes diffraction upon interacting with atomic layers. The scattered intensity is amplified through diffraction and interference processes when the Bragg's condition is met. Refer to the text for further explanations and details.

The positions of reflections observed in the diffractogram are indicative of the lattice symmetry and lattice parameters of the material. As a result, valuable information regarding the phases present in the measured sample, including the percentage composition of each phase and their respective lattice parameters, can be extracted. The intensity of the peaks in the diffractogram is directly proportional to the quantity of the crystalline phase present in the sample. By analysing the area under each peak, it is possible to estimate the relative abundance or concentration of different crystalline phases. All XRD experiments were performed within the Solid State Physics Department of AGH University, utilizing an Empyrean Panalytical diffractometer equipped with CuK_{α} radiation. The measurements were carried out at room temperature, ensuring consistent conditions throughout the analysis.

3.2 Scanning electron microscopy (SEM)

The scanning electron microscope (SEM) allows for the visualization of the sample's surface by detecting electrons emitted when a high-energy electron beam impinges upon it. As the electron beam interacts with the sample surface, it induces the emission of secondary and backscattered

electrons, which provide valuable insights into the sample's surface topography and chemistry (refer to Fig. 3.3). These emitted electrons carry information that can be used to analyse the characteristics of the sample's surface at a high resolution.

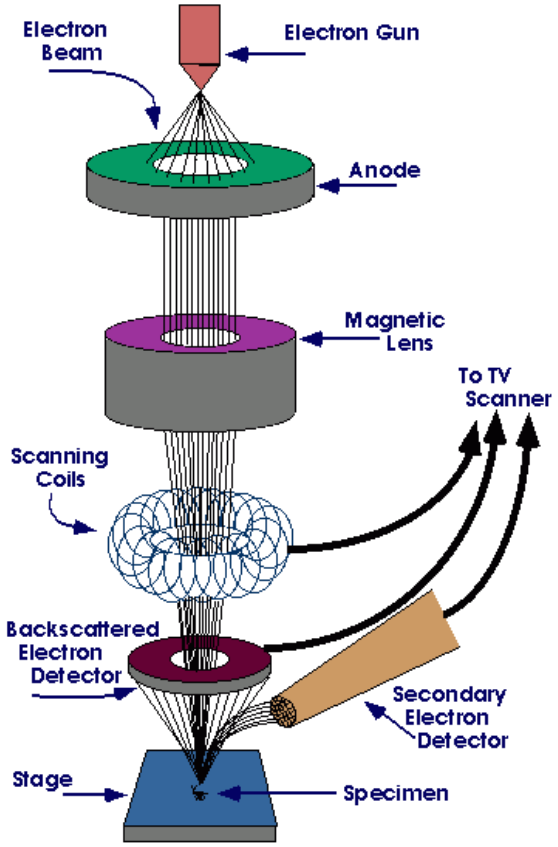

Figure 3.3: Functional scheme of the scanning electron microscope (SEM). Electron beam (formed using the anode and magnetic lens) hits the sample surface interacting with the atoms that make up the sample and producing signals that contain information about the sample's surface topography, composition and other properties such as electrical conductivity. Scanning coils enable the beam scan the sample surface. (after Ref. [2]).

The sample's response to an incoming electron beam involves two types of electrons: backscattered electrons (BSE) and secondary electrons (SE). BSE, resulting from elastic scattering, possess higher energy than SE and provide information from deeper regions within the sample. The intensity of BSE increases with the atomic number of the sample's constituents, resulting in visible chemical contrast, especially between lighter elements rather than neighbouring heavier elements. Furthermore, the intensity of BSEs also increases with the tilt angle of the flat sample.

BSEs from the lighter elements of the sample originate from deeper regions compared to BSEs from heavier elements. The depth at which BSEs are observed (known as escape depth) depends on the sample material, tilt angle, and beam energy. For instance, higher beam energy causes a shift in the distribution of BSE origins towards deeper regions. As a result, BSE images provide not only chemical contrast but also offer insights into the sample's topography.

The presented in this work BSE images may appear blurred due to the type of BSE detector used. Sharper images can be obtained from secondary electrons (SE), which have energies up to 15 eV. SEs are excited through inelastic scattering of electrons from the beam or BSEs. To be detected, SEs need to travel to the sample surface without losing excessive energy and overcome the work function. Typically, SEs originate from the region where the beam strikes the surface up to 1 nm below the surface (SE1), resulting in high-resolution images. Some detected SE electrons are produced when a BSE leaves the sample (SE2), providing similar information to that obtained in BSE images, such as sample chemistry. Additionally, there are SEs excited when parts of the microscope are struck by BSEs (SE3) or originating from the beam aperture (SE4).

Quantitative analysis of SE images is more challenging than in the case of BSEs. The escape depth and SE coefficient can significantly vary if the sample is covered by oxide layers, exposed to humidity, etc. Although the SE coefficient generally increases with the atomic number of the material, there are substantial uncertainties regarding this trend. The intensity of SE1 depends on the tilt angle, making SE images initially useful for assessing sample topography.

In this work, most images of granular superconductor samples and their precursors are secondary electron images that display the samples' morphology. The SEM technique is particularly used to examine the granular morphology and grain size of the samples. In some cases, the images may also contain information about the chemical composition of the sample, as they are result of backscattered electrons.

All the experiments conducted to study the samples prepared within the scope of this thesis were performed at the Solid State Physics Department of AGH University using a JEOL 5900LV scanning electron microscope.

3.3 Magnetic measurements

When a sample is exposed to a magnetic field H, it undergoes magnetization M. The magnetic response of the sample to the applied magnetic field [4], known as magnetic susceptibility, is denoted as χ and is given by the ratio of M to H ($\chi = M/H$). In the case of a constant magnetic field, the susceptibility is defined as the ratio of magnetization to the applied field and is referred to as DC susceptibility: $\chi_{dc} = \frac{M}{H}$. When the magnetic response to a small alternating magnetic field is measured, it is known as AC susceptibility, $\chi_{ac} = \frac{\partial M}{\partial H}$. AC susceptibility measurements provide information about the dynamic magnetic properties of the sample, such as its response to varying magnetic fields and frequencies. This characterization technique is valuable for studying

phenomena like magnetic phase transitions and the behaviour of magnetic materials under alternating magnetic fields.

Superconductors exhibit ideal diamagnetic behaviour, as discussed earlier. In other words, when the measurements are conducted below the critical temperature (T_c), the magnetic field is expelled from the sample, resulting in a substantial and negative magnetization response to the applied field. This unique characteristic allows magnetic measurements to be employed for assessing the superconducting state, particularly the transition temperature.

In this study, both AC magnetic susceptibility and magnetization in constant fields are measured and utilized for comprehensive sample characterization. These measurements serve various purposes, including the estimation of the critical current and the determination of critical exponents. By examining the magnetic properties of the superconductor, valuable insights can be gained regarding its behaviour, performance, and key parameters associated with its superconducting state.

3.3.1 AC magnetic susceptibility

The AC magnetic susceptibility is measured using a susceptometer, which comprises a primary coil and two secondary coils (refer to Figs 3.4). An alternating current is applied to the primary coil, generating an alternating magnetic field. The secondary coils are wound in opposite directions and serve to detect the electromotive force (EMF).

When the sample is placed in one of the secondary coils, the system loses its symmetry, resulting in the generation of a nonzero EMF. This change in the EMF is indicative of the magnetic response of the sample to the alternating magnetic field. By measuring this induced EMF, the AC magnetic susceptibility of the sample can be determined. This technique allows for the investigation of the sample's magnetic properties and provides valuable information about its superconducting behaviour and transition temperature.

The EMF generated in the secondary coil is directly proportional to the volume of the sample (V), the applied magnetic field (H), the magnetic field frequency (f), and the AC susceptibility. However, the EMF signal may be small and difficult to measure accurately. To address this issue, a Lock-in amplifier is commonly employed. The Lock-in amplifier is a specialized device capable of precisely measuring minute sinusoidal signals at a specific frequency, which is synchronized with the frequency of the coil driving signal. Additionally, it can account for any phase shift between the measured signal and the driving signal, helping to extract the desired signal from background noise and interference. By utilizing a Lock-in amplifier, the small EMF signal

resulting from the sample's magnetic response can be accurately detected and measured, allowing for precise determination of the AC magnetic susceptibility. This technique is instrumental in studying the magnetic properties and behaviour of materials, particularly in the context of superconductivity research.

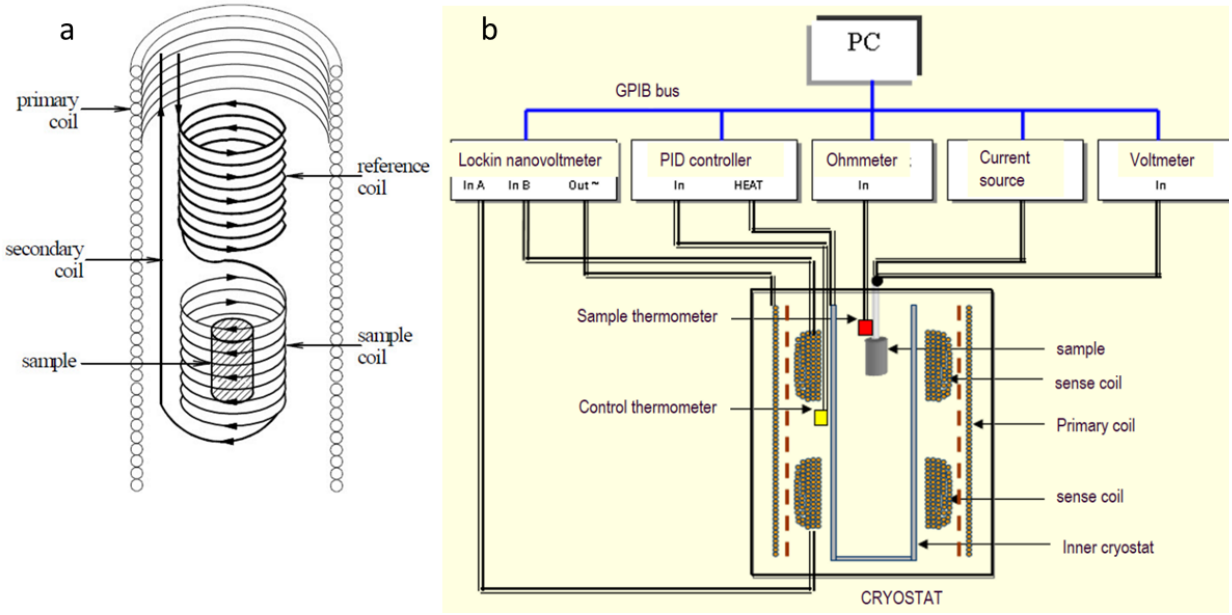

Figure 3.4: AC magnetic susceptibility measurement. (a) The scheme of set of coils used for the sceptibility measurements. (b) Scheme of the susceptometer used in the experiments. (after Ref. [5]).

The experimental setup employed by the author, located in the Solid State Physics Department at AGH University, utilized the Stanford SR830 Lock-in amplifier. The same cryostat and electronic equipment were used for both AC magnetic susceptibility (χ) and resistivity measurements, ensuring consistency and comparability between the two techniques.

The lock-in amplifier generated a sinusoidal output that supplied AC current to the primary coils or a current to the sample for resistance measurements. The resulting voltage was measured either in phase or out of phase with the driving current. This allowed for the registration of very small signals within a noisy environment, providing valuable data such as the in-phase component (X), the out-of-phase component (Y), and the signal amplitude; $(X^2 + Y^2)^{1/2}$.

To monitor the sample temperature, a chromel-gold-0.07% iron thermocouple from Lake Shore Cryotronics was positioned in close proximity to the sample (approximately 3 mm away). The second junction of the thermocouple was immersed in a mixture of water and ice. Additionally, an AsGaAl diode (TG120, Lake Shore Cryotronics) served as another thermometer and was placed outside the sample holder but inside the primary coil near the heater. Both thermometers were connected to an LS340 temperature controller (Lake Shore Cryotronics) for precise temperature

control. The temperature readout had an accuracy of 0.05 K, although the uncertainty of the sample temperature was approximately 1 K. All the instruments, including the lock-in amplifier, temperature PID controller, and the voltmeter measuring the excitation current, were connected to a computer via a GPIO (General Purpose Input/Output) board, enabling data acquisition and control for the experiments. This setup allowed for efficient and reliable measurements while ensuring proper synchronization and data management.

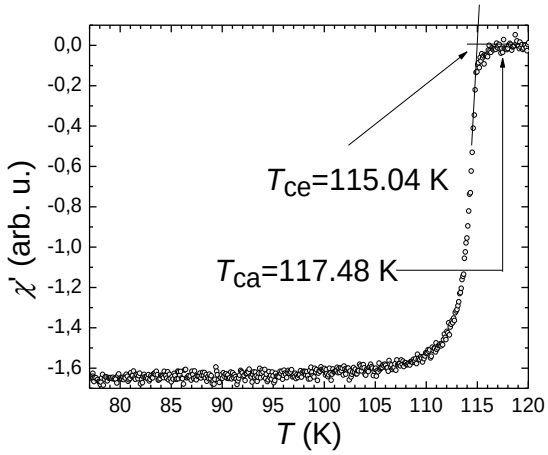

Figure 3.5: Determination of T_c (T_{ca} and T_{ce}) from AC susceptibility for sample #59N. Here, and in other figures below, experimental details and the results are often illustrated based on the samples prepared in this thesis. The references to the sample numbers, here #59N, are in Table 5.1.

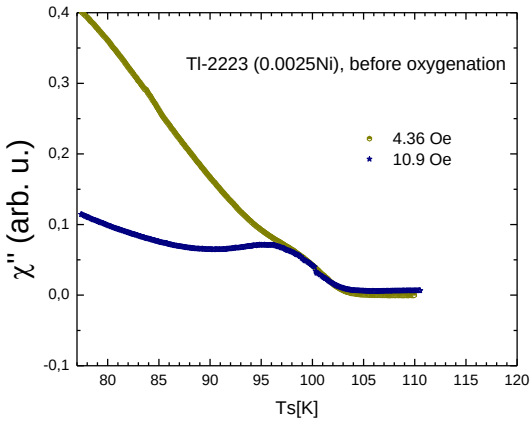

Figure 3.6: Absorption part of AC susceptibility measured for sample Ni63 (Table 5.1). While the intra-grain peak is clearly visible around 98 K, the inter-grain one is below 77.3 K and only the high-temperature side of the peak is visible in the measured range.

The AC susceptibility has a real and imaginary part ($\chi = \chi' + i\chi''$) since sample's response is usually delayed in respect to applied field. A real part of the AC susceptibility, dispersion, proportional to in-phase signal *X*, is used to distinguish between ferro-, dia- and paramagnetism of the sample. During an AC cycle some energy W_q is absorbed in the sample and this is connected to imaginary part of AC susceptibility, i.e. out of phase signal *Y*, according to the formula: $W_q = -2\pi\chi''\frac{B_a^2}{2\mu_0}$, where B_a is the amplitude of the applied magnetic field [4]. Usually, the absorption is largest during phase transition when the electronic or atomic system is reorganized, which is visualized by the χ'' peak at the critical temperature.

The dispersion part of the AC susceptibility was utilized in the present thesis to determine the critical temperature. The ceramic samples under investigation consisted of superconducting grains that are connected to one another, and both the superconducting properties of these grains and the inter-grain regions, as well as impurities, can be observed in the results obtained. Thus, two critical

temperatures can be identified from each AC susceptibility measurement, one for *intra-grain* and one for *inter-grain*. As shown in Fig. 3.5, the higher critical temperature, where the susceptibility significantly deviates from a constant value, corresponds to the *intra-grain* critical temperature (T_{ca}), while the lower critical temperature, estimated as the temperature where the two lines intersect, corresponds to the *inter-grain* critical temperature (T_{ce}).

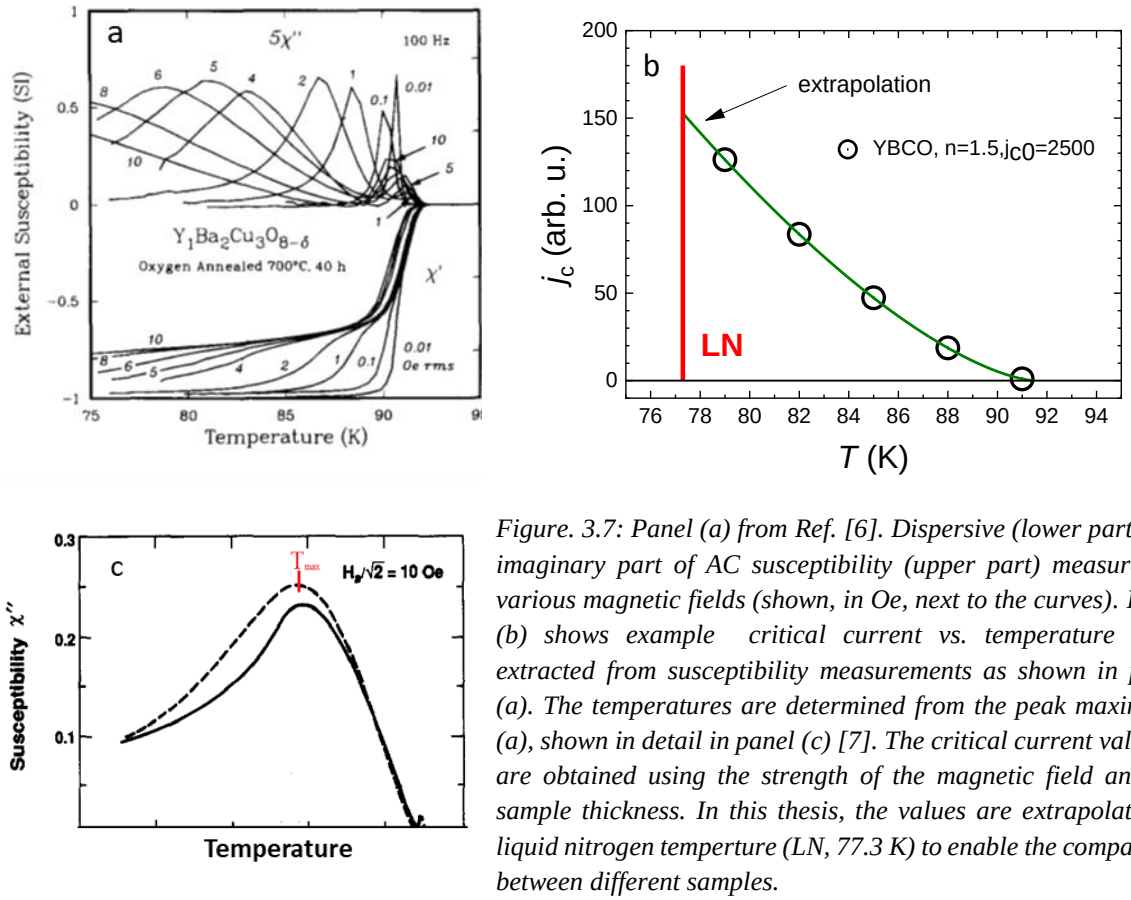

Figure. 3.7: Panel (a) from Ref. [6]. Dispersive (lower part) and imaginary part of AC susceptibility (upper part) measured in various magnetic fields (shown, in Oe, next to the curves). Panel (b) shows example critical current vs. temperature chart extracted from susceptibility measurements as shown in panel (a). The temperatures are determined from the peak maxima in (a), shown in detail in panel (c) [7]. The critical current values j_c are obtained using the strength of the magnetic field and the sample thickness. In this thesis, the values are extrapolated to liquid nitrogen temperture (LN, 77.3 K) to enable the comparison between different samples.

The absorption part (χ") was utilized to determine the critical current in this study. In the susceptibility of single-phase bulk high-temperature superconductor samples, there are typically two peaks observed in χ" versus temperature. These peaks arise from the intra-grain and inter-grain superconductivity effects. The peak at a lower temperature, which is not entirely covered in the accessible temperature range, originates from inter-granular spaces, while the peak at a higher temperature corresponds to properties within the grains themselves (see Fig. 3.6). The lower temperature peak can be attributed to energy losses caused by the penetration of magnetic field flux through grain boundaries or weak links between grains. On the other hand, the higher temperature peak arises from energy losses resulting from the screening of magnetic flux by surface currents on the superconductor [4]. The intra-grain peak is often not clearly discernible as

a separate structure and is typically overshadowed by the inter-grain peak. It is worth noting that while the low-temperature (inter-grain) peak shifts to lower temperatures with the application of higher AC magnetic fields [4], the maximum of the high-temperature (intra-grain) peak remains independent of the applied magnetic field (see Fig. 3.7a, which presents literature values of χ' and χ''). Naturally, in cases where the sample is composed of multiple phases, broadening of the peaks or the presence of multiple peaks can be observed. Sometimes, it is even possible to discern separate peaks corresponding to different phases.

The absorption part of AC susceptibility (χ'') may be also used in a contactless method for the determination of critical current. For this purpose several susceptibility runs in various H_{ac} magnetic fields are needed (as in Fig. 3.7a). From one run one obtains a single point (H_{ac}, T), where temperature T is identified with maximum of magnetic field absorption (Fig. 3.7c). Taking into account sample geometry (its thickness) and applying Bean's model [8, 9] one can calculate critical current from H_{ac} at given temperature. For flat samples j_c is equal to double H_{ac} amplitude divided by sample thickness as justified by GL model in the strong coupling limit (this is commented on in Appendix B) In the case of this thesis, j_c will be extrapolated to 77.3 K (Fig. 3.7b).

Finally, AC magnetic susceptibility vs. T relation may be used for critical exponent determination. For this purpose, the absolute value of susceptibility (of the complex value) should be presented in log χ vs. log τ parametrization, Fig. 3.8, and linear trends in log χ vs. log τ relation are linked to critical exponent. The exponent can be calculated from $|\chi|=|\chi'+i\chi''|$ in a given temperature range below the critical temperature.

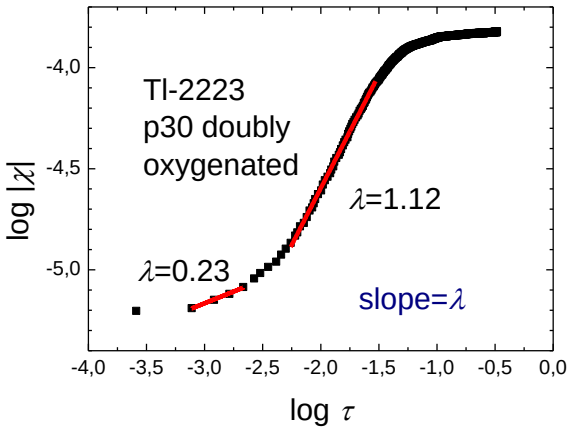

Figure 3.8: Log-log chart for AC susceptibility data fitted in order to extract the critical exponent λ for sample #30, doubly oxygenated (#30aa) listed in Table 5.1

In the case of a bulk sample, two critical temperatures exist: one associated with the intra-grain behaviour and the other with the inter-grain behaviour. Consequently, two sets of critical exponents are possible. The choice between these two sets will be discussed in Section 5.1.2.

3.3.2 DC magnetic susceptibility: Vibrating sample magnetometry

Magnetization and DC magnetic susceptibility measurements were performed using a vibrating sample magnetometer (VSM), as shown schematically in Fig. 3.9. In the instrument, such as the LakeShore VSM used in this study, the sample undergoes vertical vibrations in a uniform external magnetic field generated by an electromagnet (providing a field strength of approximately 0.92 T). The electromotive force (EMF) induced in the detection coils is directly proportional to the sample magnetization. This setup allows for the determination of various properties of granular superconductors, including primary magnetization curves, hysteresis behaviour, and the temperature dependence of magnetization.

The system is equipped with the flow cryostat (He or LN_2 flow is regulated by the needle valve), two thermometers Tg120 (one situated on the sample rod, close to the sample, the other, the control thermometer, is placed on the cryostat wall, close to the needle valve) and PID LS340 temperature controller. Correction coils, wound on the electromagnet poles are used to compensate the remanence field of electromagnet and the Earth field. The system is connected to the computer by GPIO board.

The superconducting samples investigated by the author consist of both superconducting grains and inter-grain regions. These two regions exhibit different properties, leading to distinct hysteresis signals from the grains (Fig. 3.10) and inter-grain regions (Fig. 3.11) within the same sample. This differentiation between intra-grain and inter-grain properties is also evident in the primary magnetization curve. In the primary magnetization curve, two well-defined minima can be observed (as shown in the inset of Fig. 3.10), with the lower-field minimum originating from the inter-grain regions and the higher-field minimum from the grains. Hysteresis loops and the primary magnetization curve provide valuable information about the superconducting properties, including penetration fields and critical currents, for both the grains and inter-grain regions.

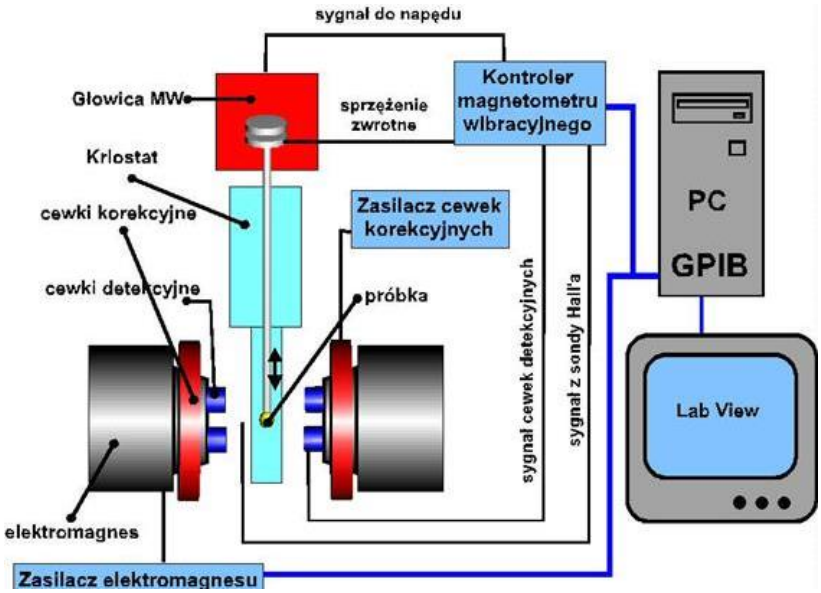

Figure 3.9: VSM : Schematics of the VSM apparatus from Ref. [10].

In the low magnetic field regime, the magnetic field can penetrate the inter-grain regions but does not penetrate the individual grains, resulting in a low field hysteresis signal (Fig. 3.11). The inter-grain penetration field, typically a few Oe in the measured samples, can be determined from the low-field minimum observed in the inset of Fig. 3.10, where the magnetization reaches a local saturation point.

At higher magnetic fields, both the grain and inter-grain regions allow penetration of the magnetic field. Therefore, the shape of the intra-grain hysteresis, which constitutes the main part of Fig. 3.10, reflects the properties of the individual grains. The intra-grain penetration field can be determined from the global minimum observed at higher field, typically on the order of hundreds of Oe, as shown in the inset of Fig. 3.10.

The critical current, j_c, is a parameter that can also be extracted from magnetization experiments. According to the Bean model (see Appendix B), it is proportional to the height of the hysteresis loop of a flat sample (with the magnetic field H applied along the sample surface) at a given magnetic field. The critical current can be calculated as:

$$j_c = 2\Delta M/d,$$

where ΔM is the height of the hysteresis loop, as marked in Fig. 3.10, and d represents the sample thickness (for intra-grain j_c) or grain size (for inter-grain j_c).

By measuring the intra-grain and inter-grain hysteresis loops from a single sample, as shown in Figs. 3.10 and 3.11, both critical currents can be determined.

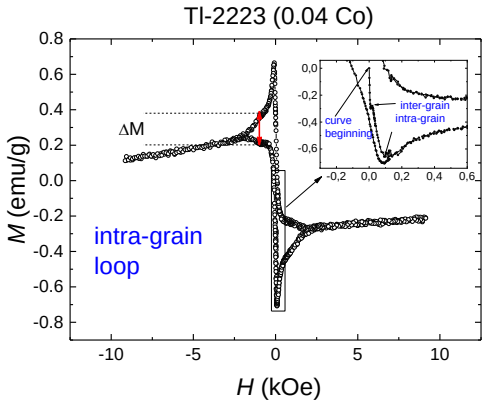

Figure 3.10: Typical hysteresis loop of synthetized superconductor (intra-grain loop). ΔM for H=1kOe is used for intra-grain critical current determination. In the inset the primary part of M(H) is presented with inter-grain and intra-grain minima (Co73N).

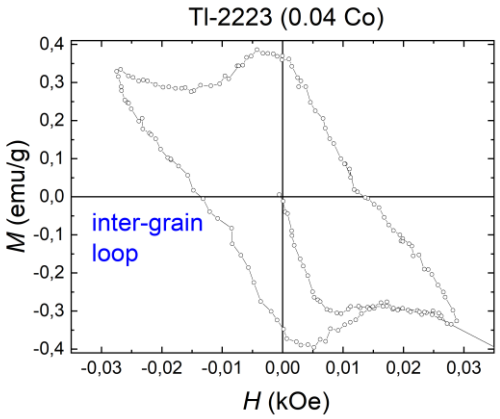

Figure 3.11: Inter-grain hysteresis loop of the superconductor from Fig. 3.10.

In this thesis, the intra-grain critical current was determined using a magnetic field of 1 kOe. The critical current, j_c, was obtained by averaging the results from the hysteresis loops measured at positive and negative magnetic fields. This method of determining the critical current of grains is preferred over using AC susceptibility, as the grain peak in AC susceptibility measurements is often smaller and can be overshadowed by the much larger inter-grain peak, making it difficult to accurately estimate the maximum of the grain peak.

Finally, from M vs T curves, critical temperature T_c can be determined as a sudden drop of M to negative, diamagnetic, values. The results for some of synthetized samples, are shown in Chapter 5.

Summarizing, the results from VSM measurements were used by the author to:

- determine the penetration field for grains and the inter-grain regions.
- determine the critical currents for grains and for selected sample also for the inter-grain regions.
- determine the critical temperature of the sample from $M(T)$ measurements.

3.3.3 Resistance and magnetoresistance measurements

Electrical resistance, R, is a result of carrier scattering in the sample due to various types of inhomogeneities. The resistivity, ρ, which is the sample resistance normalized by the sample geometry (cross-section, s, and length, l), is an intrinsic material property.

Carriers can be scattered by different mechanisms, including electron-phonon scattering (scattering on lattice vibrations), scattering on lattice defects (including unoriented magnetic moments), electron-electron scattering, and other less relevant mechanisms for the studied materials. A simple phenomenological model describes the resistivity as a sum of contributions from defects and phonons, while neglecting other contributions. Mathematically, it can be expressed as: $\rho = \rho_{def} + \rho_{ph}(T)$. The phonon part of resistivity is temperature dependent (and in many metals rises linearly with T) whereas the lattice imperfection part is constant. Resistivity from lattice defects is present at any temperature and is equal to the residual resistivity in the limit of absolute zero temperature. The electron-electron scattering contribution (i.e. also electron-electron coupling), although hardly visible in simple metals, may be of outmost importance in cuprates. This will be briefly discussed below.

Resistance can be accurately measured using the four-contact method, as shown in Fig. 3.12. This method involves making contacts as collinear as possible. Two contacts located on the edges of the sample are used to supply electric current to the sample, while two contacts in the middle of the sample are connected to a voltmeter. The measured voltage is directly proportional to the resistivity of the central part of the sample.

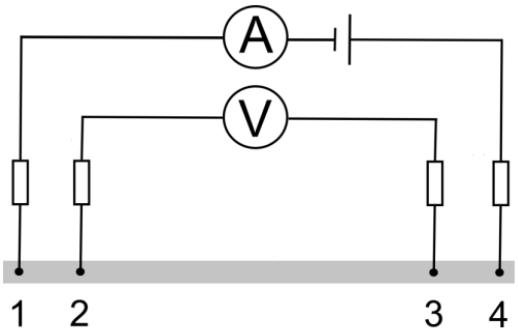

Figure 3.12: Schematics of the four contact resistivity measurements method. While the current with the known value is run through the contacts 1 and 4, the voltage is measured between contacts 2 and 3.

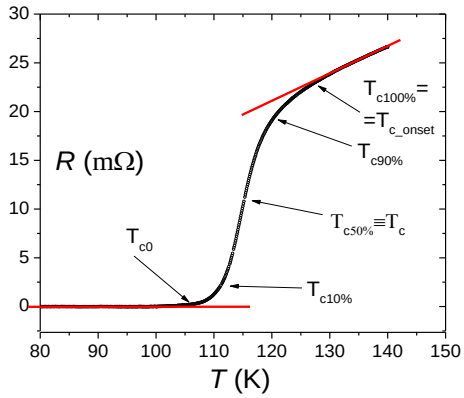

Figure 3.13: Resistance of Tl-2223 sample before oxygenation showing characteristic temperatures (#16).

The four-contact method is advantageous because it minimizes systematic uncertainties in resistance measurement. Since the voltage contacts are positioned in the middle of the sample, almost no current flows through them, reducing any potential errors caused by contact resistance.

Precise resistance determination is particularly important for low-resistance samples such as superconductors, represented here by a ceramic pellet. In superconductors, the critical current is a

crucial parameter that causes a voltage drop in an otherwise zero-resistance sample. Accurate measurement of resistance is necessary to determine this critical current accurately.

The results of resistance measurements provide the information about the critical temperature, the transition width, critical exponents, and the superconductivity response to magnetic fields.

Typical regions of temperature dependence of resistance is presented in Fig. 3.13. The transition is limited by T_{c0} from the low-temperature side and $T_{c100\%}$ (or T_{c_onset}) from the high-temperature side. The percentage in temperature marking is the experimental resistance divided by normal state resistance at this temperature extrapolated from high temperatures (red line at $T > T_{c100\%}$). The transition width, ΔT_c, is defined as $T_{c90\%}$ minus $T_{c10\%}$. $T_{c50\%}$ marks the middle of the transition, is close to the temperature where $R(T)$ slope is highest and is further referred to as T_c.

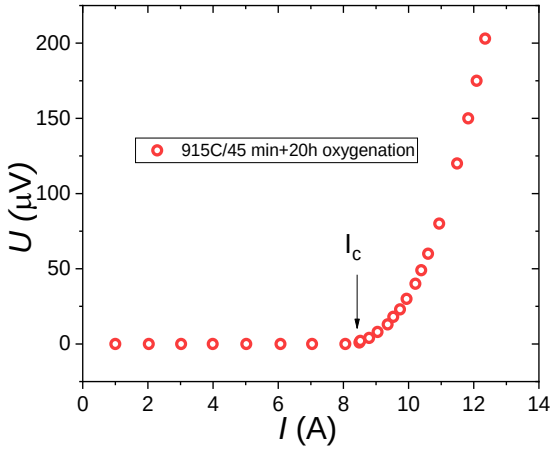

Figure 3.14: Transport method of finding the critical current I_c for oxygenated Tl-2.2 2 2 3 sample. (#30a)

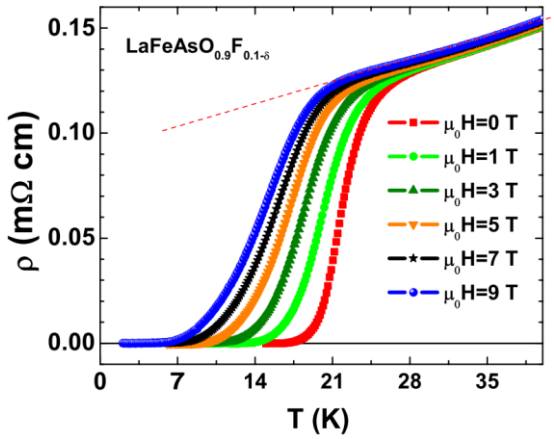

Figure 3.15: Magnetoresistance curves of a superconductor $LaFeAsO_{0.9}F_{0.1-\delta}$ from Ref. [11].

The temperature range from T_{c0} to above T_{c_onset}, where the resistance is very small, is referred to as the fluctuation-sensitive region. In this region, residual superconductivity exists above the transition temperature (T_c) due to the presence of constantly created and destroyed superconducting carriers. The resistance in this region provides valuable information about fluctuations of the order parameter.

The fluctuation-sensitive region extends over a temperature range of approximately 30 K, as indicated by the termination of this region at around 160 K where the resistance-temperature curve, $R(T)$, starts to exhibit a linear behaviour. This suggests that the effects of fluctuations gradually diminish, and the material behaves more like a normal conductor. The broader fluctuation region

above T_c highlights the importance of studying these fluctuations and their impact on the superconducting properties of the material.

The resistance versus temperature relation in this region can be used to calculate the critical exponent of the system. The first step is to find the linear trend of normal state (shown in red in Fig. 3.13). The resistance can now be changed into log $\Delta\sigma$ value, where $\Delta\sigma$ is defined as $1/R_{experimental}$-$1/R_{linear}$ and R_{linear} is an extrapolation of resistance above T_{c_onset} to the region below T_{c_onset}. Thus $\Delta\sigma$ is an additional conductance of sample in superconducting state compared with the normal state. The slope of the reduced τ ($\tau=(T-T_{c0})/T_{c0}$) dependency in log-log chart is the value of a critical exponent λ in the given temperature range. The value of exponent is mathematically bonded to the system's dimensionality.

The critical current I_c is the maximum current that can flow through a superconducting sample without the detection of a voltage difference between the contacts. To measure the critical current, a cuboid bar of the superconductor with a narrowing in the middle is used, and it is connected to a circuit using the four-contact method. In the measurement process, the current flowing through the sample is gradually increased until the critical current is reached. At this point, the voltage difference between the contacts exceeds zero, indicating the onset of resistive behaviour. This is illustrated in Figure 3.14, where the voltage is plotted as a function of the applied current. The critical current is an important parameter in characterizing the superconducting properties of a material and represents the maximum current carrying capacity in the superconducting state.

Finally, one can perform a set of resistance versus temperature runs in various DC fields. Such experiment allows to determine how the superconducting sample is resistant to DC magnetic field. When the field increases, the transition width becomes broader (Fig. 3.15), according to the formula $\Delta T=C+H^n$ [12, 13, 14]. For a few applied fields one can estimate values of C and n for a studied superconducting material. Also the critical temperature decreases with the increase of the external DC field.

3.3.4 Specific Heat

Specific heat, $C_v = dQ/dT$, was measured for a few samples using the PPMS. The basics of the used here relaxation technique is to supply certain amount of heat to the sample placed on a small calorimeter (see Fig. 3.16 a) and observe the rate with which this heat disperses to the surrounding (Fig. 3.16b). The relaxation time depends on heat capacity of the sample and calorimeter and, knowing the calorimeter specific heat, sample specific heat can be extracted. The system enables measuring the specific heat in temperature range from 4 K to 300 K.

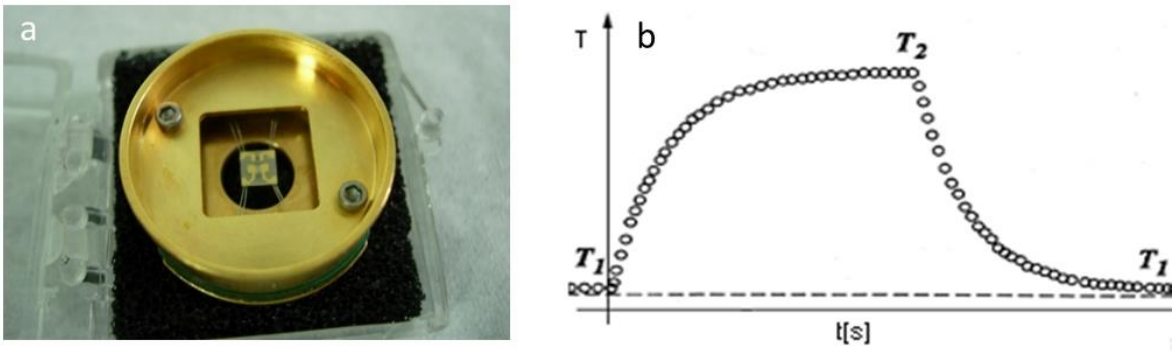

Figure 3.16: (a) The puck with the calorimeter used in the PPMS for heat capacity measurements, and (b) typical relaxation curves, on heating (T1 to T2) and on cooling (T2 to T1) from which heat capacity is obtained in PPMS system (b).

Although a peak in the specific heat is expected to occur at the superconducting critical temperature, the magnitude of the specific heat jump is relatively small compared to the total specific heat value. This is because the main contribution to the specific heat comes from lattice vibrations (lattice specific heat), while the specific heat jump at the critical temperature is mainly attributed to electronic processes. The electronic contribution to the specific heat jump is typically around 3% of the total specific heat.

The electronic specific heat above the critical temperature exhibits an exponential growth, which is directly related to the energy gap that Cooper pairs need to overcome to break into normal electrons. This exponential growth culminates at the critical temperature, resulting in a jump in the specific heat. The magnitude of this jump is determined by the strength of the coupling between the electrons and the lattice. In the C/T vs. T parametrization, the electronic part above the transition temperature should be constant and equal to γ, a value that is proportional to the electron concentration at the Fermi level.

Measuring the specific heat of thallium cuprates presents challenges. The samples are often multiphase, and the oxygen stoichiometry can vary across the sample. As a result, the specific heat jump in thallium cuprates is broadened and distorted, making it challenging to observe. Additionally, the parameters extracted from the peak can be uncertain and should be interpreted qualitatively. In this thesis, a specific heat peak was observed in only one sample and was used in Section 5.5 to determine critical exponents.

Literature:

1. A. Bordoloi, A detailed study on optical and physical properties of rice and its by-products, India Meteorological Department, Presentation (2018)
2. C. Charpentier, Investigation of deposition conditions and annealing treatments on sputtered ZnO:Al thin films: Material properties and application to microcrystalline silicon solar cells, Plasma Physics, Ecole Polytechnique, PhD Thesis (2012)
3. https://www.enfo.hu/en/node/3236, access 30.05.2023
4. N. Khan, CuTl-based high temperature superconductors, VDM Verlag Dr Müller, SaarBrücken (2010) isbn: 978-3-639-26844-7
5. W. Tabis, MSc thesis, Kraków, (2010)
6. K.-H. Müller, AC susceptibility of high temperature superconductors in a critical state model, Physica C **159** (6), 717-726 (1989) doi: 10.1016/0921-4534(89)90143-3
7. K.-H. Müller, Frequency dependence of AC susceptibility in high-temperature superconductors; Flux creep and critical state at grain boundaries, Physica C **168** (5-6), 585-590 (1990) doi: 10.1016/0921-4534(90)90081-O
8. C. Bean, Magnetization of hard superconductors, Physical Review Letters **8**, 250-253 (1962) doi: 10.1103/PhysRevLett.8.250
9. C. Bean, Magnetization of high-field Superconductors, Reviews of Modern Physics **36** , 31-39 (1964) doi: 10.1103/RevModPhys.36.31
10. https://home.agh.edu.pl/~tokarz/vsm/vsm.html, access 15.05.2023
11. X. Zhu *et al.*, Upper critical field, Hall effect and magnetoresistance in the iron-based layered superconductor $LaFeAsO_{0.9}F_{0.1-\delta}$, Superconductor Science and Technology **21**, 105001 (2008) doi: 10.1088/0953-2048/21/10/105001
12. M. Tinkham, Resistive transition of high-temperature superconductors, Physical Review Letters **61** (14), 1658-1661 (1988) doi: 10.1103/PhysRevLett.61.1658
13. W. M. Woch *et al.*, Effects of magnetic field on resistive transition of thin film thallium based superconductors, Acta Physica Polonica A **106** (5), 785-791 (2004) doi: 10.12693/APhysPolA.106.785
14. W. M. Woch *et al.*, Temperature and field dependence of critical currents, resistances and irreversibility fields of a $(Tl_{0.6}Pb_{0.24}Bi_{0.16})(Ba_{0.1}Sr_{0.9})_2Ca_2Cu_3O_y$ film on single-crystalline lanthanum aluminate, Physica C **434** (1), 17-24 (2006) doi: 10.1016/j.physc.2005.11.012

4. Synthesis of thallium cuprates

In this chapter, the synthesis and relevant experimental characterization aimed at achieving successful synthesis of samples is presented. Firstly, the preparation of precursors for the final synthesis, encompassing both pure Tl-2223 (Section 4.1) and doped Tl-2223 (Section 4.2) is described. Subsequently, their characterization is discussed in Section 4.3, utilising techniques such as X-ray diffraction (XRD) and scanning electron microscopy (SEM) to analyse their structural and morphological properties. Next, the synthesis of pure Tl-2223 superconductors and doped with Ni, Co, and Gd is presented in Section 4.4. The experimental techniques employed to optimize sample preparation, including synthesis and oxygenation, involved XRD, AC magnetic susceptibility, and, in some cases, SEM. The synthesis conditions were systematically optimized, leading to the successful production of samples referred to as "test" samples, labelled up to #53 in Table 5.1 (figures presenting the experimental results are numbered accordingly).

The characterization of Tl-2223 samples prepared by the author in the laboratory of the Institute of Physics in Slovak Academy of Sciences in Bratislava is also shortly discussed, although the synthesis was essentially identical to that used later by the author.

Optimal synthesis (and oxygenation) conditions were applied in preparation of both pure and doped Tl-2223 samples. Characterization of those samples, using XRD, AC magnetic susceptibility, SEM, resistivity to estimate the critical current, magnetization and, in some cases, specific heat, is presented in Chapter 5. One sample, #30 (i.e. from the "test" samples) is also presented here since its quality was high. Also, one Tl-1223 sample ($Tl_{0.8}Bi_{0.3}Sr_{1.8}Ba_{0.2}Ca_2Cu_3O_x$), synthesized earlier in the group was characterized by the author and the results are also presented there.

4.1 Synthesis of precursors for pure Tl-2223 superconductors

One of the methods for preparing thallium superconductor (1223 or 2223) [1] involves the synthesis of intermediate products, $BaCuO_2$ and Ca_2CuO_3 (so called precursors), followed by their mixing with thallium III oxide. This method, the author learned and mastered during his scientific visit to the group of Prof. Š. Chromik at the Slovak Academy of Sciences in Bratislava. In an alternative approach, the sample could be enclosed with a thallium source in a quartz tube. However, the reactions involved in combining compounds of Ba, Ca, and Cu are time-consuming and require high temperatures. With thallium oxide having the melting point of 717°C and a

boiling point of 875°C, this compound is volatile at the superconductor synthesis temperature. As a result, the final product would be thallium deficient. To address this issue, the idea was to first synthesize the precursors in the form of homogeneous, polycrystalline powders of $BaCuO_2$ and Ca_2CuO_3, and then combine them, incorporating also Thallium. The advantage of this procedure is the ability to produce a large quantity of complex oxides that would suffice for multiple samples synthesis. Moreover, the precursors and the final superconducting samples can be synthesized in separate furnaces; the final samples can be synthesised in specifically designed furnace which can handle toxic thallium oxide and without the need for an oxygen supply.

Considering the above, the synthesis process of a thallium superconductor consisted of several steps:

- Supplying the starting compounds: Tl_2O_3, $BaCO_3$, $CaCO_3$, and CuO.
- Synthesizing the precursors: Two heating sessions, lasting approximately 72 hours and 48 hours, respectively, were carried out.
- Mixing the precursors with Tl_2O_3 and forming them into pellets, which were then wrapped in silver foil.
- Heating the pellets in a tube furnace for around 30 minutes to activate the main synthesis.
- Allowing the sample to cool to room temperature, resulting in a ready Tl-based superconductor.
- Further improving the sample quality through additional thermal treatment, which lasted 20-40 hours.

Various oxides which can be used for the precursor synthesis are presented and discussed in Appendix D. Finally, the $BaCuO_2$ and Ca_2CuO_3 oxides were used and the procedure of the precursor synthesis consisted of the following steps:

- Reagent mixing: To synthesize a portion of the precursors, 4.1176 g of $BaCO_3$, 1.6598 g of CuO, 2.0884 g of $CaCO_3$, and 0.8299 g of CuO were used. The accuracy of the weight determination of the ingredients was 1 mg.
- First grinding: $BaCO_3$ was ground with 1.6598 g of CuO in an agate mortar for 1 h 20 min. During the grinding, isopropanol was added to the mortar in order to prevent from formation and releasing of small particles of the processed material. The same procedure was applied combine $CaCO_3$ with the second portion (0.8299 g) of CuO. After evaporation of isopropanol the mixtures were placed in the quartz crucibles.

- First part of the precursor synthesis: The crucibles were insert into a tube furnace. The precursors were formed in chemical reactions following the general equations:

$$BaCO_3 + CuO = BaCuO_2 + CO_2$$

and

$$2CaCO_3 + CuO = Ca_2CuO_3 + 2CO_2.$$

Note that the following is a general and condensed overview of a complex process. For a more detailed description, please refer to Appendix D.

The initial heating process involves subjecting the samples to 24 hours at 840°C followed by 48 hours at 940°C. The temperature profile of this heating procedure is illustrated in Figure 4.1.

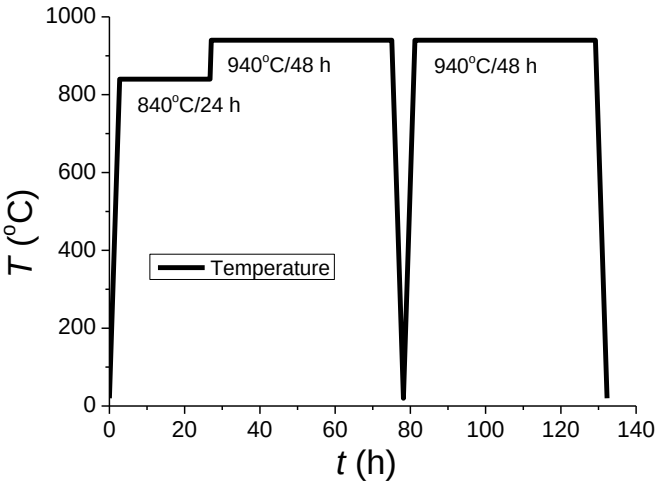

Figure 4.1: The temperature profile of the precursors synthesis. The process consists of one annealing at 840 ℃ for 24 h, and two subsequent heating processes at 940 ℃ 48 h each.

Following the initial heating, the precursors underwent grinding in mortars for 1 hour each. The second heating process involved a gradual temperature increase at a rate of 5°C per minute until reaching 940°C, holding this temperature for 48 hours, and subsequently cooling at a speed of 5 or 6°C per minute (refer to Fig. 4.1). It is important to note that due to the heat capacity of the furnace, the actual cooling rate is slower than the prescribed rate in the recipe. Prior to sealing the precursors in vials, they underwent an additional grinding step in mortars with the presence of isopropanol for an hour each.

4.2 Synthesis of precursors containing Gd, Ni, and Co

In order to examine the influence of magnetic dopants on the superconductivity of the prepared materials, certain modifications were made to the aforementioned procedure. Alongside investigating the impact of dopants on superconductivity, the objective was also to evaluate

whether the dopants themselves, or the manner in which they were introduced, influenced the formation of the thallium superconductor family.

To achieve Tl-2223 bulk superconductor doped with nickel, a nickel compound with a suitably low melting point, such as barium nickel oxide ($BaNiO_2$ or $BaNiO_3$), is required as a nickel-rich precursor. The synthesis of these compounds involved mixing and grinding $BaCO_3$ and NiO in equal molar proportions in a mortar. The resulting mixture was then formed into a pellet, placed in a quartz crucible, and subjected to vacuum conditions (10^{-5} bar). The pellet was heated at 970°C for half an hour to eliminate carbon dioxide from the barium carbonate, followed by heating at 1100°C for 2.5 hours to facilitate the synthesis of the precursor [2, 3]. The pressure versus temperature chart (Fig. 4.2) illustrates the reaction steps, with the first pressure peak corresponding to the initial decarbonation of the sample at 970°C. The second peak and subsequent pressure decrease are associated with further decarbonation and the primary synthesis. X-ray diffraction (XRD) analysis of the final powder revealed the presence of $BaCO_3$, indicating that not all of the carbonate reacted even at 1100°C. Upon cooling, once the temperature dropped below 537°C, the vacuum apparatus was opened, and the pellet was further cooled in ambient air. Subsequently, the precursor was ground, and X-ray diffraction was performed. The results of this analysis are presented in subchapter 4.3.

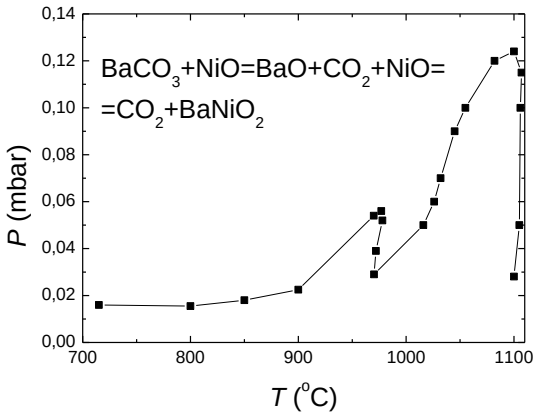

Figure 4.2: The pressure inside the vacuum apparatus versus temperature during synthesis of $BaNiO_2$.

For Co doping, $BaCoO_x$ was synthesized using equimolar amounts of $Ba(NO_3)_2$ and CoO. The two compounds were mixed in the presence of distilled water using an agate mortar and then allowed to dry. Subsequently, the resulting material was transferred into a quartz crucible and placed in a cold furnace. The heating process involved a gradual temperature increase at a rate of 5°C per minute until reaching 680°C, followed by maintaining a constant temperature of 680°C for 6 to 7 hours. The crucible was then removed from the hot furnace and allowed to cool down in ambient air at atmospheric pressure.

In contrast, the preparation and use of precursors containing gadolinium (Gd) were handled differently. The precursors served as a source of calcium (Ca), rather than barium. The appropriate amounts of CaO, CuO, and Gd_2O_3 were weighed and mixed. Subsequently, the material underwent the same thermal treatment as pure Ca_2CuO_3. Each superconductor containing gadolinium was synthesized using a separately prepared $Ca_{2-x}Gd_xCuO_{3+\delta}$ precursor.

4.3 Characterization of the precursors

The X-ray diffraction (XRD) technique was primarily employed to assess the quality of the precursors. XRD patterns were analysed using the Crystallography Open Database (COD) and Material Project as references, enabling a thorough examination of the crystal structures. In addition to XRD analysis, analytical chemistry methods were employed to characterize the barium-nickel oxide and barium-cobalt oxide precursors, providing further insight into their chemical composition and properties.

4.3.1 XRD characterisation of precursors

The analysis of the X-ray diffraction (XRD) pattern depicted in Fig. 4.3 revealed that the volume fraction of barium copper oxide obtained is approximately 99 wt%. Conversely, the synthesis efficiency of calcium copper oxide is lower, estimated to be between 80% and 85% based on the data presented in Fig. 4.4.

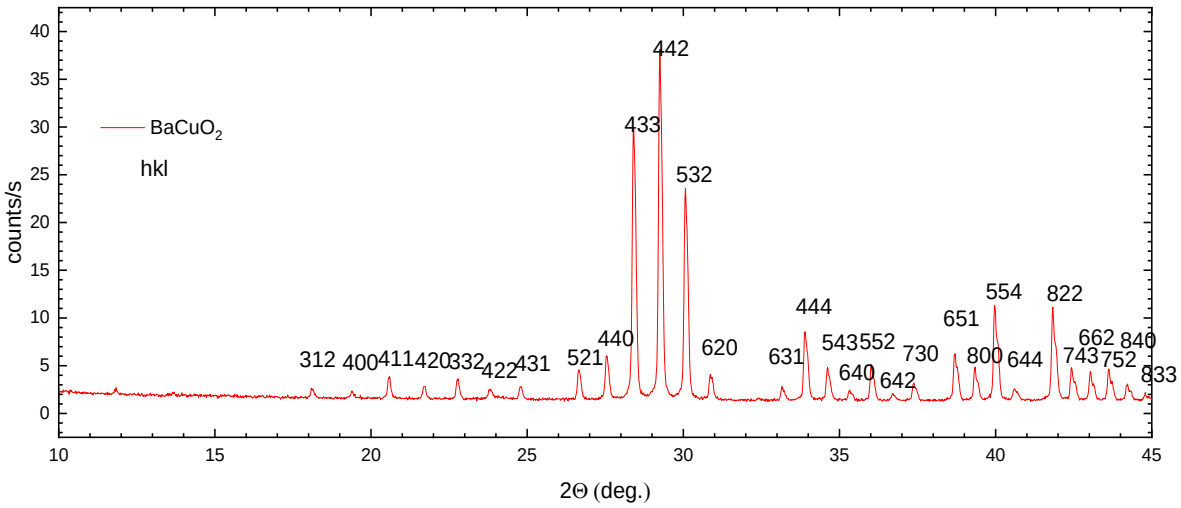

Figure 4.3: XRD pattern of $BaCuO_2$ precursor (synthesized 1.X.2018; this was later used for Tl-1223 and Tl-2223 synthesis). The Bragg reflexes are indicated.

The XRD spectra of the final precursors for the Ni-doped superconductors are presented in Fig. 4.5. The estimated mass composition of the material, determined through XRD profile analysis (also shown in Fig. 4.5), is approximately 55% $BaNiO_2$, 30% $BaNiO_3$, 8% $BaCO_3$, and 7% NiO. It is evident that the reaction was not entirely completed, and some of the nickel oxidized in the

presence of air after opening the vacuum apparatus. The total amount of nickel was subsequently determined more accurately using an analytical chemistry method involving dimethylglyoxime (DMG).

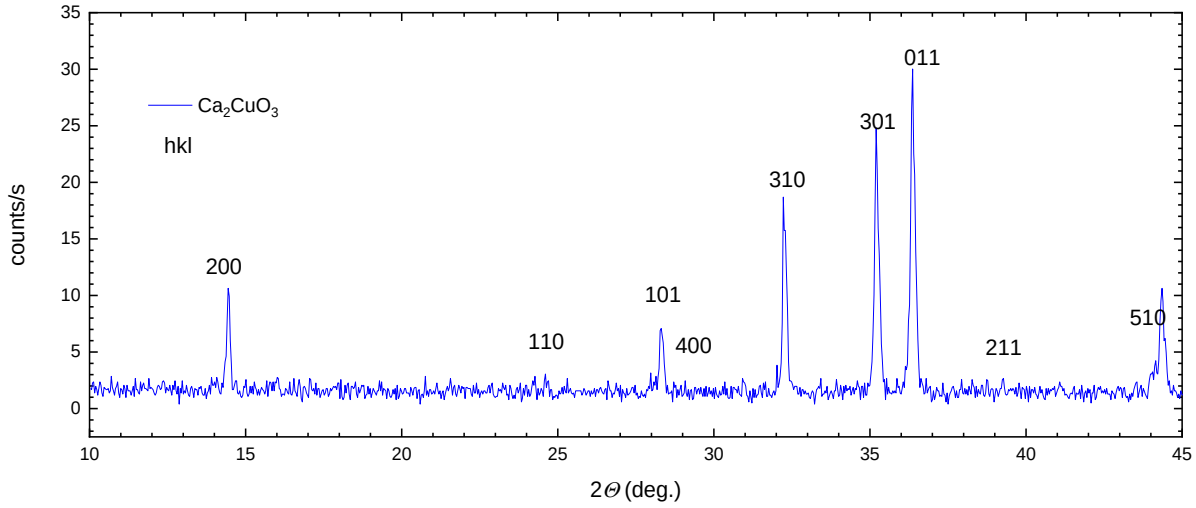

Figure 4.4: XRD pattern of Ca_2CuO_3 precursor (synthesized 25 V 2018; this was later used for Tl-1223 and Tl-2223 synthesis).

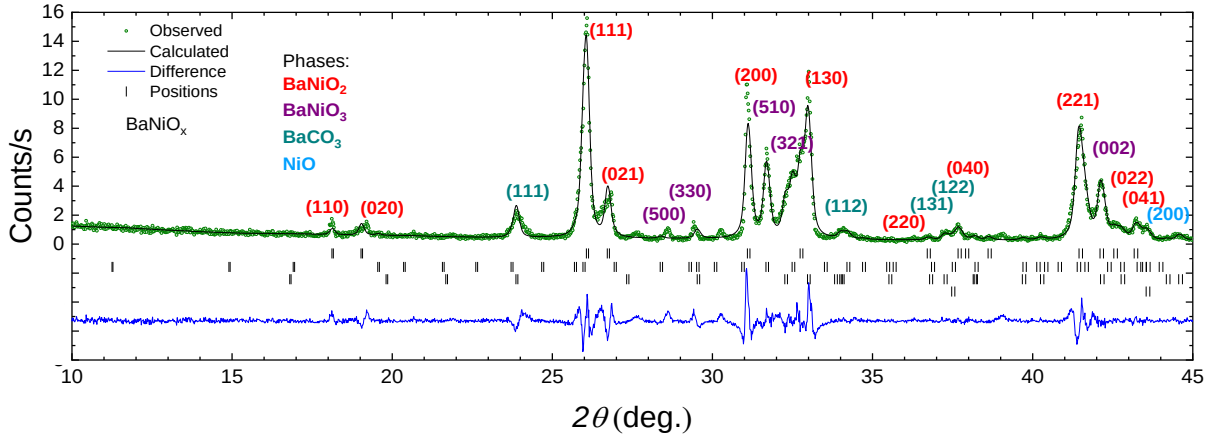

Figure 4.5: XRD pattern of barium-nickel-oxygen precursor. The phase analysis allowed to identify the fraction of other compositions. The Bragg indexes of each of the phases are marked in the color-code as indicated in the legend.

The effectiveness of $BaCoO_3$ preparation was c.a. 90% (Fig. 4.6). During the synthesis the furnace was deliberately opened [4, 5] because for the precursor preparation the contact with oxygen from air, necessary to change cobalt valence from +2 to +4, was needed.

After the last precursor synthesis the crucible became violet (which might be due to the presence of $CoCO_3$). The resulting material was black and had a bubbly structure, probably as a result of releasing the NO_x gases during the synthesis.

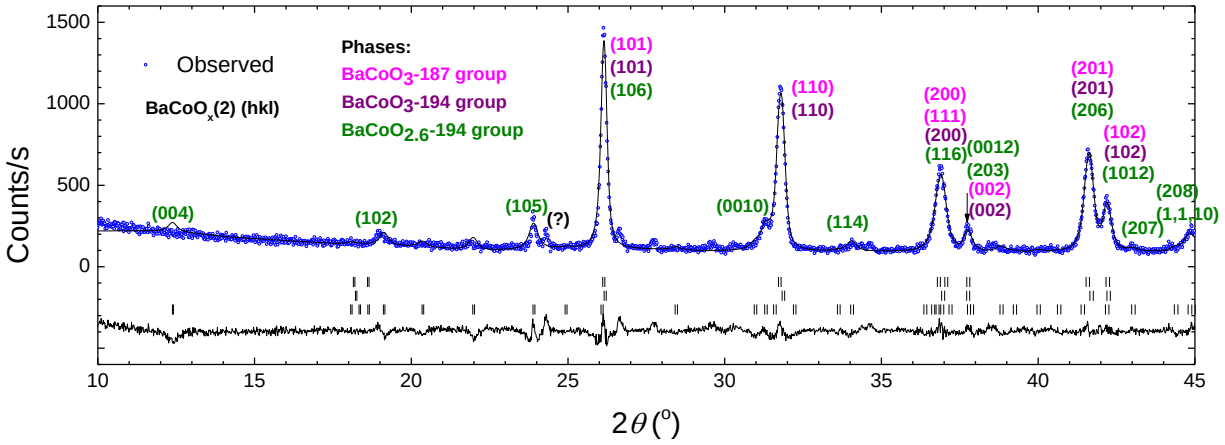

Figure 4.6: XRD pattern of barium-cobalt-oxygen precursor. The phase analysis allowed to identify three phases as indicated. The question mark indicates a reflection which does not correspond to the identified phases.

4.3.2 Analytical chemistry characterisation of precursors

It is crucial to accurately determine the content of nickel or cobalt in the precursor, and as such, more precise methods were employed for this purpose. The amount of nickel was determined by weighing the complex formed between nickel and dimethylglyoxime (DMG, $(CH_3)_2C_2(NOH)_2$), as depicted in Fig. 4.7 [6]. The barium-nickel-oxygen precursor was dissolved and reacted with DMG in an alkaline solution. The resulting precipitation yielded a distinctive strawberry red precipitate ($NiDMG_2$), which was subsequently dried and weighed. The nickel content was calculated based on the reaction shown in Fig. 4.7. The analysis revealed 30.3766 mg of nickel in 100 mg of the precursor, in comparison to 26.8 mg of nickel determined from the XRD analysis. Theoretically, $BaNiO_3$ contains 24.05 mg of nickel per 100 mg of material, while $BaNiO_2$ contains 25.74 mg of nickel per 100 mg of the compound. It should be noted that the precursor contain also some unreacted NiO (Fig. 4.5).

Cobalt, on the other hand, binds with ethylenediaminetetraacetic acid (EDTA) ($[CH_2N(CH_2CO_2H)_2]$) as shown in Fig. 4.8. Therefore, EDTA titration in the presence of eriochrome black indicator was employed to determine the cobalt content in the precursor [7]. The EDTA titration revealed that the cobalt precursor contained 20.4 wt% cobalt. To determine the barium content, a sediment of $Ba(CrO_4)_2$ was weighed after adding chromate to the solution containing the dissolved precursor. This analysis indicated that the cobalt precursor contained 60.0 wt% barium, whereas $BaCoO_3$ oxide should theoretically contain 56.2 wt% barium and 24.1 wt% cobalt.

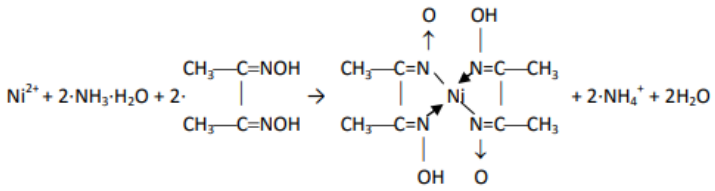

Figure 4.7: Reaction of DMG with nickel to determine nickel content, [8]

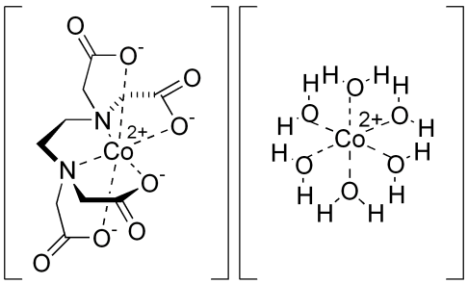

Figure 4.8: Cobalt ion before (right) and after (left) complexing with EDTA in aquatic solution. The charge on cobalt atom may differ. [9]

The error margin for the determination of cobalt and barium is 0.1 wt%. Despite the imperfect synthesis of the cobalt and nickel precursors, the author decided to proceed with their use in subsequent synthesis.

4.3.3 Scanning electron microscopy of cobalt precursor ($BaCoO_3$)

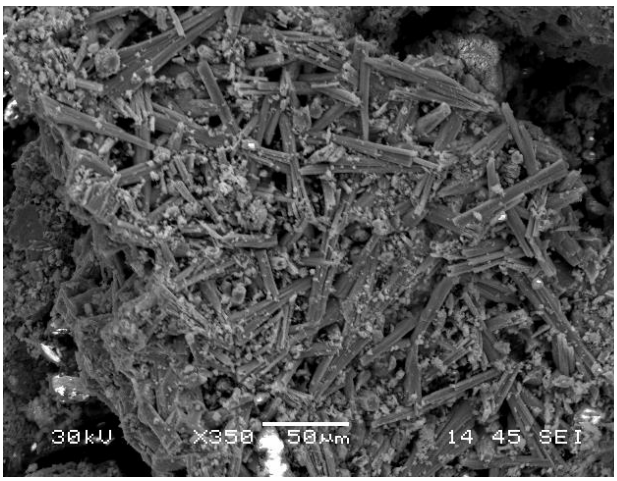

Figure 4.9: Bars of cobalt precursor, $BaCoO_3$ observed in secondary electron micrographs.

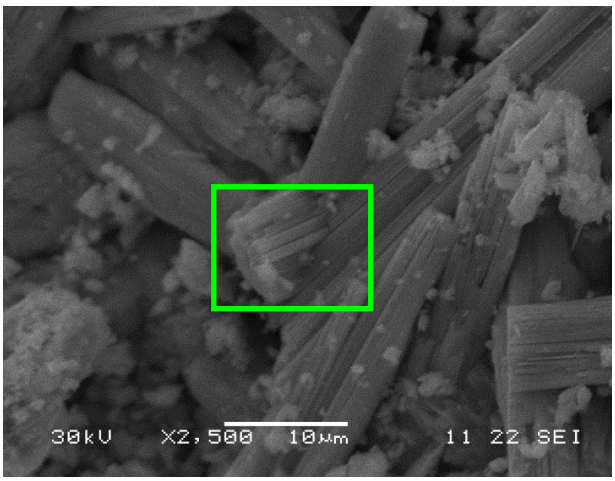

Figure 4.10: Bars of cobalt precursor, $BaCoO_3$ showing additional, needle-like substructure.

The morphology of the synthesized barium cobalt precursor is revealed in Fig. 4.9 and 4.10 through secondary electron micrographs. The structure exhibits a prominent presence of bar-like features, which likely correspond to polycrystalline regions of the precursor. Notably, certain bars (as shown in Fig. 4.10) exhibit longitudinal, needle-shaped structures within them.

4.4 Superconducting samples Tl-2223 synthesis and oxygenation

The three-layer thallium superconductors, Tl-2223, were synthesized from the precursors characterized above, according to the following reactions:

$Tl_2O_3 + 2BaCuO_2 + Ca_2CuO_3 (+ yO_2) = Tl_2Ba_2Ca_2Cu_3O_{10}$

and

$0.5Tl_2O_3 + 2BaCuO_2 + Ca_2CuO_3$ (+ yO_2) = $TlBa_2Ca_2Cu_3O_{8.5}$,

where the oxygen content of the products can vary depending on the synthesis conditions.

The relevant reactions for Co, Ni and Gd doped Tl-2223 were expected:

$Tl_2O_3 + (2-x)BaCuO_2 + Ca_2CuO_3 + xBaCoO_3$ (+ yO_2)= $Tl_2Ba_2Ca_2Cu_{3-x}Co_xO_{10}$

$Tl_2O_3 + (2-x)BaCuO_2 + Ca_2CuO_3 + xBaNiO_{2-3}$ (+ yO_2)= $Tl_2Ba_2Ca_2Cu_{3-x}Ni_xO_{10}$

$Tl_2O_3 + 2BaCuO_2 + Ca_{2-x}Gd_xCuO_3$ (+ yO_2)= $Tl_2Ba_2Ca_{2-x}Gd_xCu_3O_{10}$

For Co-doped Tl-2223, the samples with the following doping level were prepared: x_{Co}=0.000, 0.010, 0.020, 0.030, 0.040, and 0.050. Furthermore, five Ni doped samples were prepared and oxygenated: x_{Ni}=0.0012, 0.0025, 0.0035, 0.005, and 0.010 (No #61, #62, #63, #70, and #71).

Gd-doped sample series had gadolinium amount of: x_{Gd}=0.025, x_{Gd}=0.05, x_{Gd}=0.10, and the reference sample (x_{Gd}=0.00).

Note that the transition metal atoms occupy the nominal copper position within the CuO_2 planes whereas the rare earth element replaced calcium, situated between cuprate planes [10,11]

Following the synthesis, an additional thermal treatment, known as oxygenation, was implemented to regulate the carrier (hole-[12]) concentration (doping) and enhance the samples' quality [13]. Both the synthesis and oxygenation conditions were optimized by evaluating the quality of the obtained precursors and samples.

Initially, the author employed the synthesis procedure for Tl-2223 compounds developed in Bratislava. However, based on the characterization results of both the precursors and final cuprates, the synthesis parameters were gradually adjusted. The synthesis procedure encompassed the following key steps:

A. Weighing the appropriate amounts of $BaCuO_2$, Ca_2CuO_3, and Tl_2O_3 powders, followed by thorough grinding using an agate mortar and pestle.

B. Pressing the finely ground powder mixture into a pellet and securely wrapping it in silver foil. The presence of the silver foil serves the purpose of sample protection, preventing the escape of Tl, while allowing easy access to oxygen.

C. Placing the pellet in a furnace with a constant flow of oxygen at a temperature range of 860°C to 890°C. This step, known as thallination, constitutes the main stage of the synthesis process. The pellet remains in the furnace for approximately 30 minutes (occasionally up to 50 minutes) as

depicted schematically in Fig. 4.11. This controlled procedure ensures that the sample is not heated at uncontrolled temperatures, thereby preventing any potential loss of Tl [1, 14, 15]

D. Initial characterization of the samples is carried out. This includes AC susceptibility verification for all samples, with some undergoing additional XRD and SEM studies as specified in Table 5.1.

E. Oxygenation is a critical process for achieving superconductivity in high-temperature superconductors. The critical temperature of Tl-based superconductors strongly depends on the oxygen stoichiometry. This relationship is demonstrated in Fig. 2.9 (Section 2), which displays various phases of Tl-based superconductors with different oxygen content [16, 17, 18]. The oxygenation conditions play a crucial role in determining the superconducting properties of this series. Tl-2234 tends to be under-doped, while Tl-2212 and Tl-2201 are overdoped. Highly-oxygenated Tl-2201 is not even a superconductor [16 and reference therein: 17 and 18], while Tl-2223 can exhibit both underdoped and overdoped characteristics [19-"nearly optimum"].

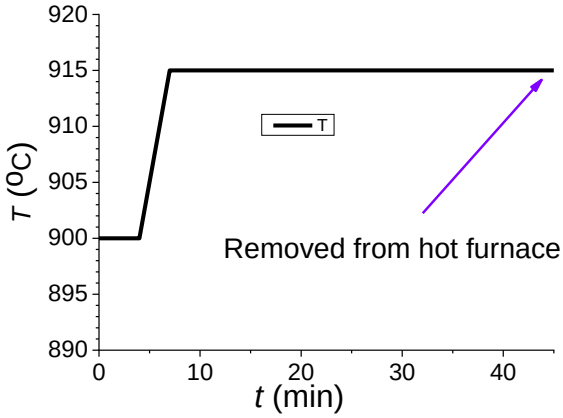

Figure 4.11: Scheme of sintering Tl-2223($Tl_2Ba_2Ca_2Cu_3O_{10+\delta}$) superconductor wrapped in silver foil.

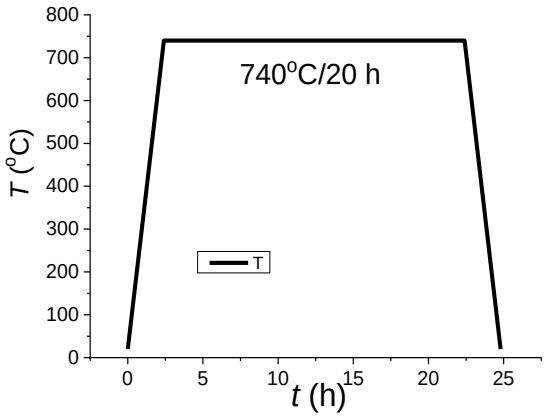

Figure 4.12: The temperature profile of the post-growth oxygenation process.

In the thallium cuprate series, the oxygen atoms can occupy different positions within the lattice: (a) between the electron reservoir and the CuO2 planes, (b) within the CuO2 planes, and (c) between thallium atoms. Reference [20] indicates that oxygen atoms in the third position are labile and can undergo removal or addition during sample reduction or oxygenation processes.

By repeating the oxygenation procedure (20 h, 740 °C), it is possible to increase the critical temperature and critical current of the Tl-2223 sample. However, it should be noted that after multiple oxygenations, there is a risk of over-saturation [21, 19], which can lead to a decrease in the critical temperature. This phenomenon is specifically observed in the Tl-2223 compound, as

shown in Fig. 2.9. The oxygenation process can be repeated until the optimal oxygen content is achieved.

F. Further detailed sample characterization was conducted to improve and optimize the synthesis procedure. This analysis primarily focused on samples marked from #48B to #53B. After implementing the optimized synthesis and post-synthesis oxygenation, additional samples marked as #54 and the following, as well as selected high-quality samples prepared during the optimization process (e.g., #30), were characterized. The characterization of these samples is described in Chapter 5.

In addition to the samples prepared as described above, five additional samples of Tl-2223 superconductor were synthesized by the author during a scientific visit to Bratislava. The preparation conditions for these samples were identical, involving the use of $BaCuO_2$, Ca_2CuO_3 precursors, and thallium (III) oxide. The ingredients were mixed in a mortar, and a pellet was formed using a press. The pellet was then placed in a silver vessel, followed by placement in a crucible. The crucible, containing the sample, was inserted into a vertical tube furnace and heated in the presence of an oxygen flow for a specific duration (either 30 or 45 minutes). Throughout the heating process, the furnace received a continuous supply of oxygen. After the specified heating time, the sample was carefully removed from the hot furnace.

Table 4.1 Heating conditions and the resistance critical temperature of samples from Bratislava.

Sintering temperature [°C]	Sintering time [min]	T_{c0} [K]	$T_{c\ onset}$ [K]
860 (pTl1)	30	85	121
860 (pTl2)	45	85	122
860 (pTl3)	45	93.9	124
860 (pTl4)	45	93.6	125
870 (pTl5)	30	94.9	130

To assess the critical temperatures of the synthesized samples, four electrical contacts were placed on the round pellet, and the resistance versus temperature dependence was measured. The estimated critical temperatures for each sample are listed in Table 4.1 below.

According to Table 4.1, the optimal conditions for sintering Tl-2223 were found to be 870°C for 30 minutes. Samples synthesized under slightly different conditions exhibited lower transition temperatures, with differences in T_c of up to 10 K. However, the general shape of the χ vs. T curve remained consistent across all samples (refer to Figs. 5.1 and 5.2 in Chapter 5).

In addition to the undoped Tl-2223 samples, attempts were made to dope the material with Co, Ni, and Gd. The cobalt-doped samples were analysed using AC susceptibility measurements before

and after oxygenation. XRD analysis was performed on six oxygenated samples, followed by magnetoresistance measurements. Scanning electron microscopy (both SE and BSE modes) was used to observe the microstructure of two samples (x_{Co}=0.030 and x_{Co}=0.050). Vibrating sample magnetometry, including primary curves and loops, was conducted on the oxygenated cobalt-doped series.

The nickel-doped samples underwent AC susceptibility measurements before and after oxygenation. XRD spectra were analysed for two of the samples (x_{Ni}=0.0025 and x_{Ni}=0.005) both before and after oxygenation. The detailed characterization results of these samples are presented in Chapter 5.

4.5 Synthesis conditions optimization (temperature, duration and oxidation)

The outcome of the synthesis process is influenced by several factors, including the reaction temperature, reaction time, and the oxygen gas flow rate during synthesis. It was observed that if the oxygen flow rate to the furnace is too high, the resulting sample has a lower critical temperature. Therefore, the flow rate was adjusted initially and maintained throughout the entire process.

The optimization procedure involved changing one parameter at a time, either the reaction time or the reaction temperature, while keeping the other parameters constant. A similar approach was presented in [1], where the final composition, determined by XRD analysis, was obtained by varying the starting composition and the synthesis time. In this study, the progress of the synthesis was monitored using AC susceptibility measurements and the critical temperature, T_c. Since each sample underwent oxygenation after synthesis, the optimal synthesis conditions were determined based on achieving the highest T_c after oxygenation, indicating the best superconducting phase. An alternative criterion for optimization is the critical current, which will be discussed in Chapter 5. The oxygenation process will be described separately in the following sections.

Constant synthesis time

The initial synthesis time was set to 30 minutes, in accordance with the literature data [1], and this was also the synthesis time used in the Bratislava synthesis. After synthesis, three out of the four measured samples exhibited superconductivity.

The critical temperature (Fig. 4.14) and the maximum of the absorption peak in the AC susceptibility measurements were quite similar for all the superconducting samples. The highest critical temperature was observed in the sample synthesized at 860^{o}C. On the other hand, the

sample synthesized at 890°C did not exhibit superconductivity even down to the boiling point of nitrogen, hence not shown.

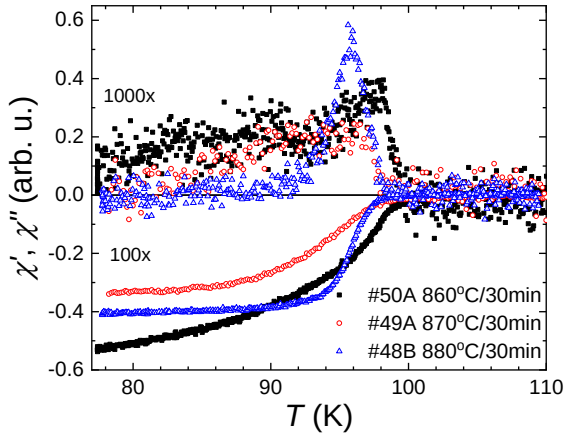

Figure 4.14: AC susceptibility of Tl-2223 synthesized at various temperatures (860°C-890°C) for 30 min. without oxygenation. (#50A,#49A,#48B). In this and the following plots of magnetic susceptibility, the absorption part χ'' is in the upper panel and dispersive part χ' of magnetic susceptibility in the lower panel. Furthermore, χ'' is magnified 1000 times and χ' 100 times.

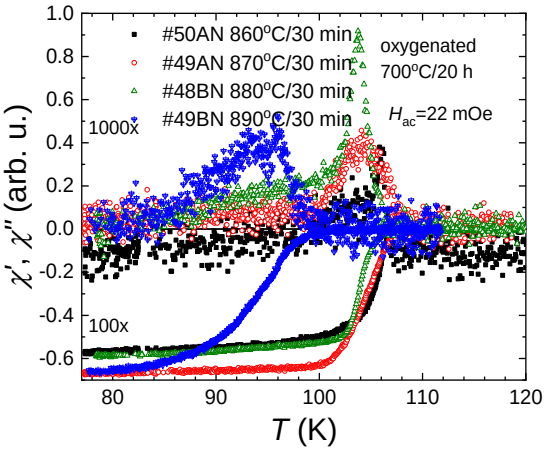

Figure 4.15: Same samples as in Fig. 4.14 but after oxygenation at 700°C for 20 h. (#50AN, #49AN, #48BN, #49BN)

After the oxygenation process, all the samples showed superconductivity. However, the sample (#49B) that did not exhibit superconductivity prior to oxygenation had the lowest T_c and the lowest position of the absorption peak in χ''. The sample synthesized at 860°C showed the best superconducting properties, although the differences between the three samples were small. Nevertheless, the optimal synthesis temperature of 880°C was chosen because the absorption peak for this sample (Fig. 4.15) was the narrowest. Additionally, at higher synthesis temperatures, such as 890°C, superconductivity degradation was observed, hence it was excluded from consideration.

Constant synthesis temperature

In order to further optimize the preparation conditions, synthesis durations ranging from 20 minutes to 50 minutes at 880°C were investigated. Prior to oxygenation, all samples exhibited a single peak in χ'', indicating a single-phase sample (Fig. 4.16). Based on the critical temperature and the maximum in χ'', the samples were ranked from best to worst as follows: 40 minutes, 30 minutes, 20 minutes, and 50 minutes of synthesis.

After oxygenation at 700°C (Fig. 4.17), the quality order of the samples changed to: 20 minutes, 50 minutes, 40 minutes, and 30 minutes. However, the situation became more complex as most

samples (with synthesis times of 50 minutes, 40 minutes, and 30 minutes) exhibited multiple peaks in χ". Due to these ambiguous results, it was challenging to precisely determine the optimal synthesis time. Therefore, a synthesis duration of 30 minutes was chosen as it appeared to be the closest to the optimal duration, based on the available information.

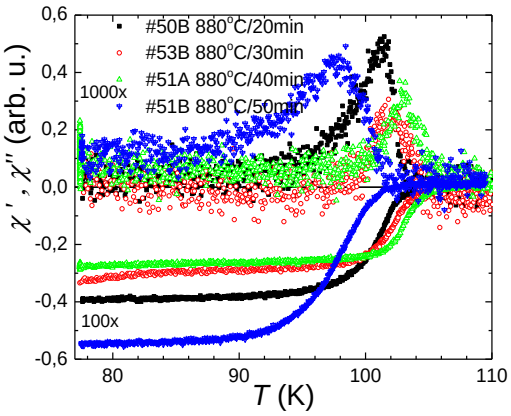

Figure 4.16: AC susceptibility of Tl-2223 synthesized at 880°C for various times (20 min-50 min). The Tl-2223 samples are marked as #50B, #53B, #51A, and #51B, respectively.

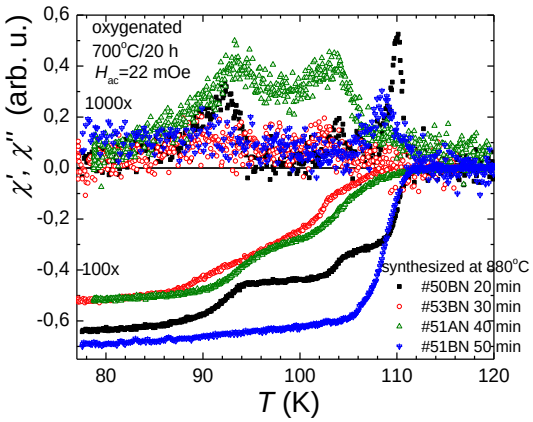

Figure 4.17: As Fig. 4.16 but for Tl-2223 oxygenated at 700°C for 20 h. (Samples #50BN, #53BN, #51AN, #51BN)

In summary, the optimal synthesis conditions for obtaining the best samples were determined to be at 880°C for a duration of 30 minutes, with a controlled oxygen gas flow of 0.2 bar that did not lead to any deterioration in the superconducting properties. These conditions were consistently applied to all the samples prepared and measured thereafter.

Table. 4.2 Optimization of the synthesis process (based on 8 samples): T_c, T_c deviation and the position of a peak in χ" for as-synthesised and later oxidized samples.

Sample (before oxygenation)	**Synth. Temp. [°C]**	**Synth. time [min]**	**T_c cross-section [K]**	**T_c deviation [K]**	***T* at Max χ" [K]**	**Sample (after oxygenation)**	**T_c cross-section [K]**	**T_c deviation [K]**	***T* at Max χ" [K]**
#50A	860	30	98.8	101.9	97.7	#50AN	106.6	108.1	106.1
#49A	870	30	98.0	100.0	95.2	#49AN	107.5	108.8	104.2
#48B	880	30	97.7	100.1	95.8	#48BN	105.4	108.1	103.8
#49B	890	30	--	--	--	#49BN	97.9	102.1	96.0
#50B	880	20	102.8	105.5	101.2	#50BN	110.9	113.4	110.0
#53B	880	30	104.1	105.8	101.9	#53BN	108.4	109.4	102.5
#51A	880	40	104.4	106.4	102.9	#51AN	108.8	112.3	103.3/93.5*
#51B	880	50	101.3	103.6	97.6	#51BN	111.1	112.6	108.4
#54A	880	30	102.4	105.4	99.8	#54AN700	109.1	111.6	108.0
						#54AN720	110.9	112.9	109.0
						#54AN740	113.1	114.5	112.0
						#54AN760	114.7	119.0	114.1

#54B	880	30	105.0	106.9	103.1	#54BN760	114.3	114.5	113.8
						#54BN780	113.1	113.8	103.6/111.3*
						#54BN800	115.8	117.2	113.3
						#54 BN820	--	--	--

* two values are provided in case a double-peak is observed in χ".

Oxygenation

After establishing the optimal synthesis conditions described earlier (e.g., synthesis temperature of 880°C and synthesis time of 30 min), the next step in the preparation optimization was to determine the optimal oxygenation temperature. The primary objective of the oxygenation process in cuprates is to control the carrier concentration and, consequently, the critical temperature [22]. For samples #48B to #53B, the oxygenation process was conducted in flowing oxygen (approximately 0.2 bar). An example of the heating protocol used, which involved warming up at a rate of 5°C/min, heating at 700°C for 20 h [13](750°C various times), and cooling at a rate of 5°C/min, is presented in Fig. 4.12.

The samples synthesized in this study typically contained both Tl-2223 and Tl-2212 compounds. The oxygenation of Tl-2223 was discussed in previous works [1, 23], which examined different temperature ranges. Specifically, the paper by Chu and Wu [23] analysed oxygenation temperatures of Tl-2223 up to 600°C. On the other hand, the oxygenation of Tl-2212 compound was investigated in [1, 24], focusing on temperatures above 600°C. These studies clearly demonstrate the significant influence of the additional thermal treatment, oxygenation, on the properties of the samples.

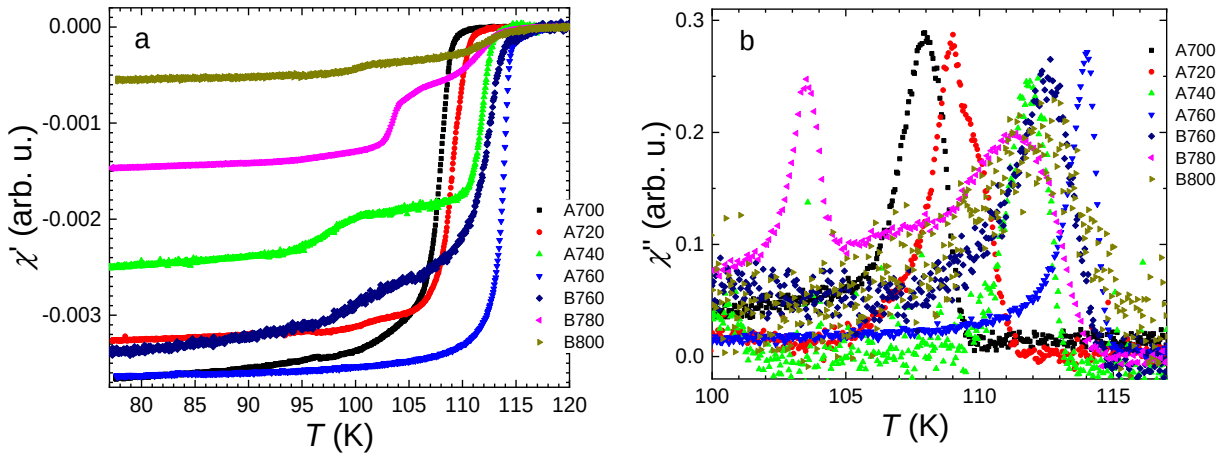

Figure 4.18: Dispersive (χ' in a) and absorption (χ'' in b) parts of AC susceptibility of Tl-2223 samples #54AN and #54BN oxygenated at various temperatures between 700°C and 800°C. The annealing temperatures are indicated in the figure.

To optimize the sample preparation process, the oxygenation time was set at 20 h, and the oxygenation temperature (T_{oxy}) was varied from 700°C to 820°C with an increment of 20°C. Two samples were synthesized in possibly similar conditions from the same mixed powder, #54A and #54B (that are, after oxygenation, renamed as #54AN700-#54AN760 and #54BN760-#54BN820, see Table 5.1 below. Both samples were divided into four pieces each. Each piece was then oxygenated at different temperature except temperature of 760°C at which two pieces were oxygenated to verify the reproducibility of the experiment.

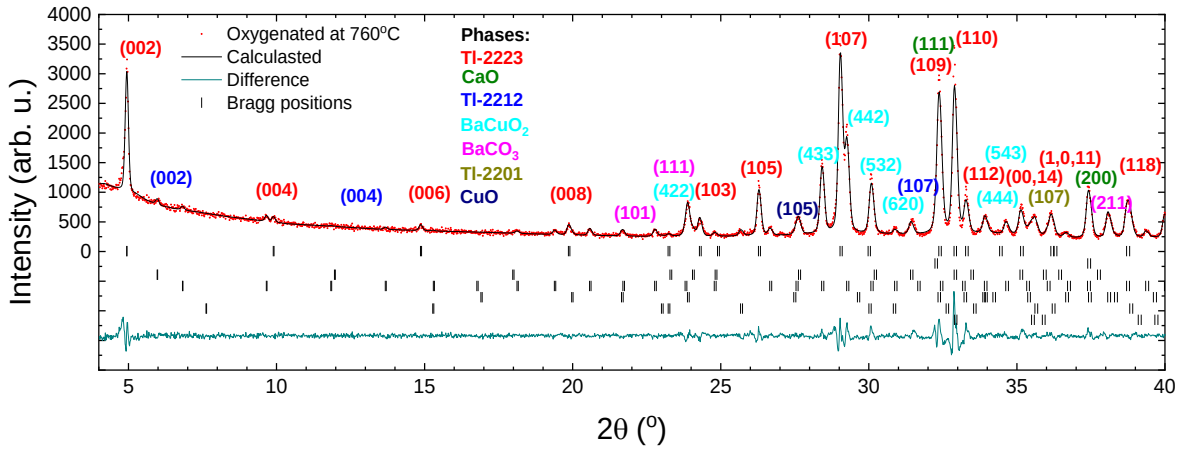

Figure 4.19: XRD pattern of Tl-2223 oxygenated for 20h at 760°C. Sample #54AN760.

The results, including AC susceptibility measurements and in a few cases XRD analysis, are presented in Figs. 4.18 and 4.19, respectively. It should be noted that the material oxygenated at the highest temperature of 820°C lost its superconductivity. Additionally, for higher oxygenation temperatures, signal of both parts of susceptibility becomes weaker.

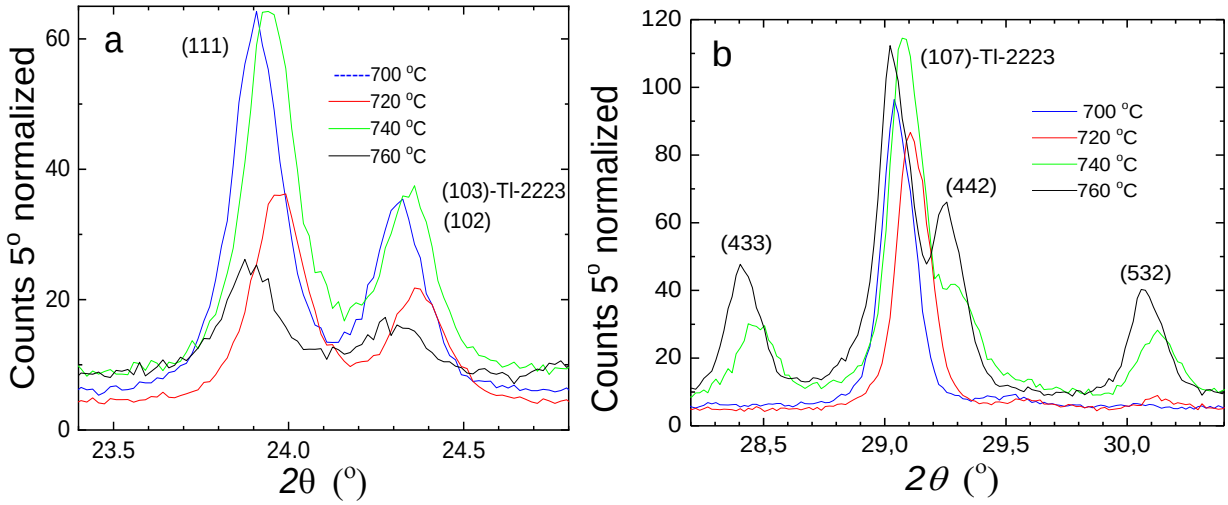

Figure 4.20: XRD patters of Tl-2223 samples annealed at temperatures indicated in the legends. The peaks of the phases present next to desired Tl-2223 phase for various oxygenation conditions: 700°C-760°C (panels a and b). Note the presence of unreacted $BaCO_3$ phase (a) . Picture (b) shows $BaCuO_2$ reflections.

In addition to the electronic properties observed through AC susceptibility, the oxygenation process also appears to affect the structural characteristics of the samples, particularly in terms of the number of pores and the presence of "impurities". SEM observations (Figs. 4.21a, b, c) indicate that the sample oxygenated at a higher temperature of 760°C exhibits primarily crystal-like structures and a higher number of pores (Fig. 4.21e) compared to the sample oxygenated at 700°C (Fig. 4.21d). Furthermore, the crystal-like structures tend to be larger after the oxygenation process.

Figures 4.22 a and 4.22 b illustrate the results of AC susceptibility measurements at various magnetic fields for two samples with the lowest and highest critical temperature, respectively, after oxygenation. It is important to note that the AC susceptibility measurements at different magnetic fields provide insights into several processes occurring within the samples.

Interestingly, the sample oxygenated at a higher temperature exhibits a sharper transition (χ') and a narrower absorption peak (χ''). This indicates a more pronounced and well-defined superconducting behaviour compared to the sample oxygenated at a lower temperature.

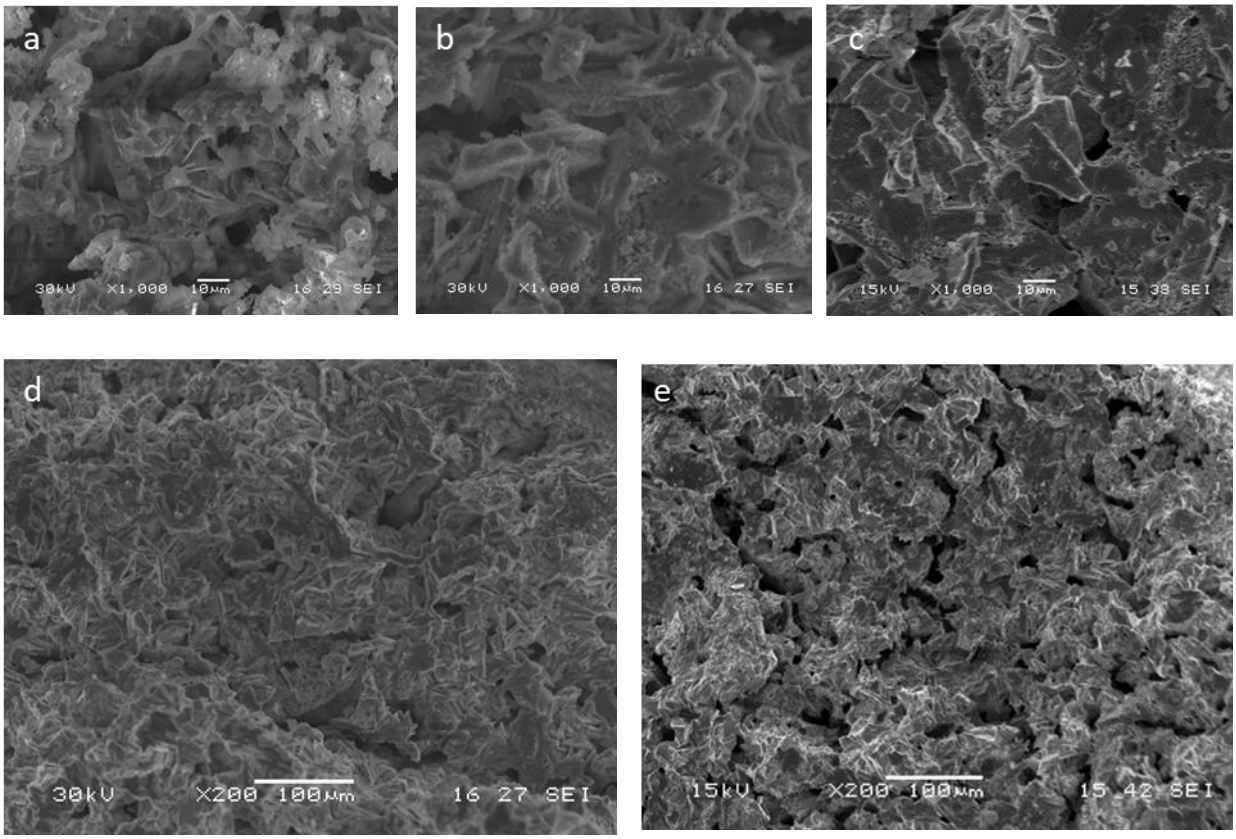

Figure 4.21: SEM images of Tl-2223 synthesized at 880ºC for 30 minutes before oxygenation (a), and after 20 h oxygenation (b, c, d, e): two oxygenation temperatures and two image magnifications.
(a) SEM image of not oxygenated Tl-2223 synthesized at 880 °C for 30 min, #54A. (b) SEM image of Tl-2223 synthesized at 880 °C for 30 min and oxygenated at 700 °C for 20 h, #54AN700. (c) SEM image of Tl-2223 synthesized at 880 °C for 30 min and oxygenated at 760 °C for 20 h, #54AN760. (d) SEM image of Tl-2223 synthesized at 880°C for 30 min and oxygenated at 700°C for 20 h, #54AN700. (e) SEM image of Tl-2223 synthesized at 880°C for 30 min and oxygenated at 760°C for 20 h, #54AN760.

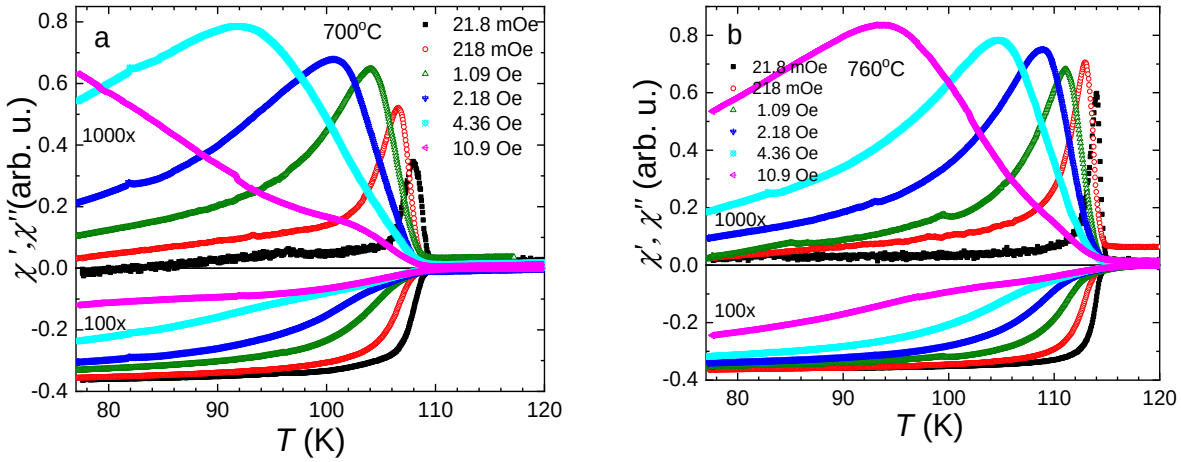

Figure 4.22: (a) AC susceptibility of Tl-2223 oxygenated in 700°C. The measurements for sample #54AN700 were performed at external magnetic fields as indicated. (b) AC susceptibility of Tl-2223 oxygenated in 760°C (series A). Sample #54AN760.

Figure 4.23 displays the critical temperatures of the oxygenated samples. The sample oxygenated at the lowest temperature, 700°C, demonstrates the lowest critical temperature, while the sample oxygenated at 760°C exhibits the highest intra-grain critical temperature. To ensure the reliability and reproducibility of the experiment, the oxygenation at 760°C was performed twice on different pieces. As a result, the oxygenation temperature of 760°C is considered optimal, as it consistently yields the highest critical temperature.

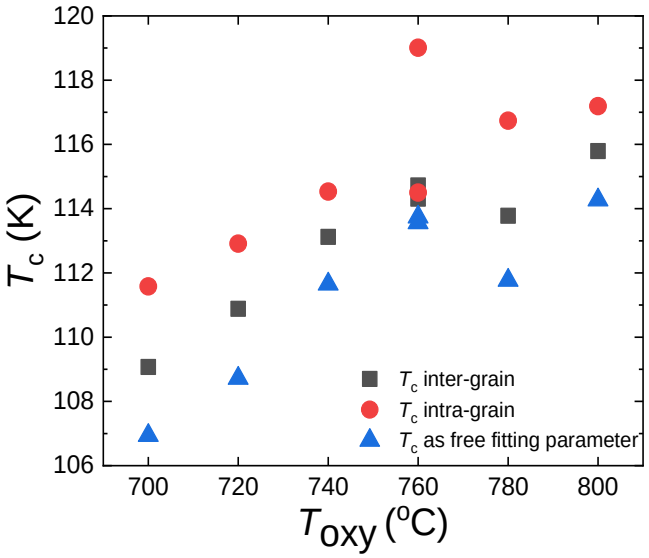

Figure 4.23: Critical temperatures versus oxygenation temperature of Tl-2223. The oxygenation process was carried out for the samples marked as #54AN700-#54BN760 and #54BN760-#54BN800.[25]

These results provide valuable complementary information to the literature findings on oxygenation of Tl-2212 [1, 24] and Tl-2223 [1, 23]. In the case of Tl-2212, the dependence of critical temperature on oxygenation temperature (T_{oxy}) was explored from room temperature (RT) to 800°C [1, 24]. The second reference investigated the oxygenation of the Tl-2223 compound at temperatures ranging from RT to 600°C [1, 23]. Although both papers indicated that the optimal oxygenation temperature was 400°C, the experiments described in those studies involved relatively low T_{oxy} and very short oxygenation times (30 minutes). In contrast, the present thesis implemented previously unexplored conditions (T_{oxy} and oxygenation time of 20 hours).

Furthermore, additional experiments were conducted to test different oxygenation times at $T_{oxy} = 760$°C in order to further optimize the preparation conditions. The results of these experiments are presented in Fig. 4.24.

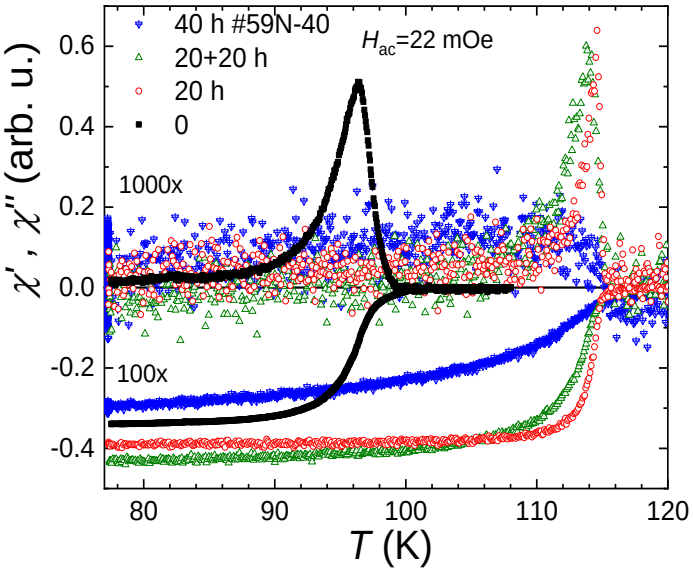

Figure 4.24: AC susceptibility of Tl-2223 oxygenated at T_{oxy}=760°C for various annealing times. Samples #59, #59N, #59NN, were annealed 0 h, 20 h or 2x20 h, respectively. Sample #59N-40h was annealed for 40 h in one cycle .

Here an as-grown sample (not oxygenated) was compared to the same sample after 3 oxygenation procedures: 20 h, 20 h + 20 h, and 40 h long. The inter-grain critical temperature of Tl-2223, drawn from 4.24, increases in sequence: before oxygenation (98.2 K), 20 h oxygenation (115.0 K), double 20 h oxygenation (115.4 K), and long 40 h oxygenation (116.0 K). For intra-grain critical temperatures the relevant temperatures are: 102.4 K, 117.5 K, 120.4 K, and 120.7 K, respectively.

In summary, the optimal conditions for the preparation of Tl-2223, although only partially successful, were as follows: synthesis at 880°C for 30 minutes under oxygen gas flow, followed by oxygenation at T_{oxy} = 760°C for 20 hours. The results presented below include data from the samples prepared in this section as well as new samples prepared under these conditions. Additionally, the measurements include samples synthesized by the author during his visit to Bratislava and one sample synthesized in collaboration with author's research group.

Despite the efforts made to achieve optimal samples of Tl-2223, the results presented above indicate that the success is only partial. Only a portion of the prepared samples contain the desired phase, while contaminations in the form of other superconducting phases and other compounds are present.

In the next section, the structure of the obtained samples will be presented in greater detail to provide a more comprehensive understanding of their characteristics.

4.6 Structure of the undoped samples

For selected samples, XRD analysis was conducted to investigate how the preparation conditions affect the abundance of the desired Tl-2223 phase. Some results have been presented earlier, while others can be found in Appendix E. The following summary is based on all the results obtained.

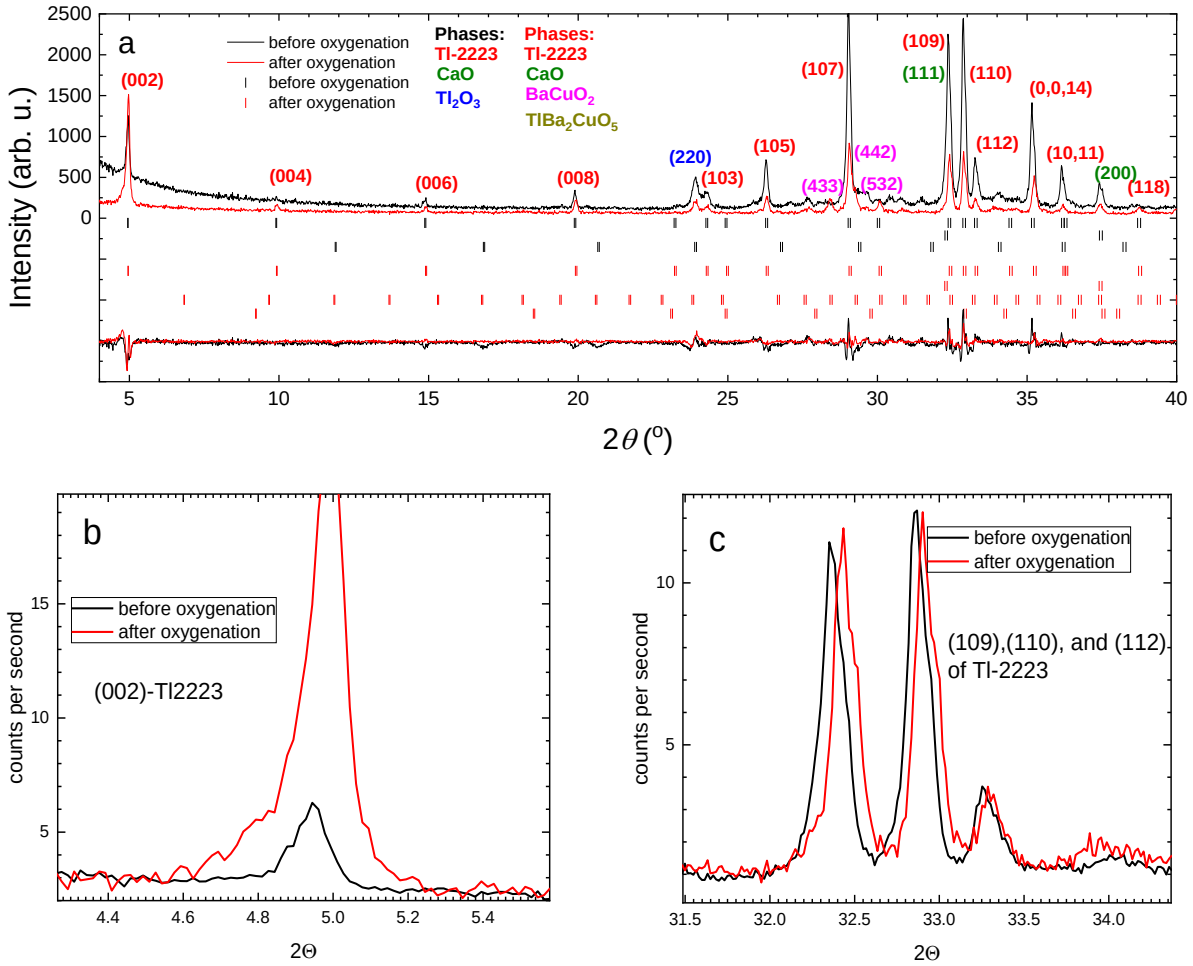

Figure 4.25: XRD spectra of stoichiometric Tl-2223 sample before (i.e. just after synthesis; black curve) and after oxygenation (red). (#59 and #59N). Panel (a) shows CuK$_\alpha$ diffractogram for θ from 4° to 40°. Panel (b) shows 002 reflection of the desired phase of Tl-2223 used for phase content identification. Panel (c) shows reflections' position shift due to size of unit cell, correlated with oxygen content in Tl-2223.

1. Coexistence of two superconducting phases:

The expected Tl-2223 superconducting phase often coexists with another superconductor, Tl-2212, which has a lower critical temperature. Both substances have a tetragonal primitive cell with a much longer c-axis compared to the other axes. Although their diffraction patterns are similar (Fig. E.3, sample #30a in Appendix E), low-angle reflections (002) can be utilized to determine the relative content of these two substances. These reflections are intense, and no impurity reflections are observed within the considered range. Generally, Tl-2212 is consistently present in all XRD diffractograms shown in Appendix E (except for samples #59 and #59N shown in Fig. 4.25), indicating that its content exceeds 5%. Oxygenation not only affects the superconducting properties of Tl-2223 but can also alter the amount of the desired phase. Fig. E.5 (in Appendix E) suggest that double oxygenation significantly increases the amount of Tl-2212. The crystallographic effect of oxygenation on Tl-2223 can be inferred from the changes in the size of

the primitive cell (Fig. 4.25 a and 4.25 c) during thermal treatment. As the peak position shifts to higher angles, the excess oxygen decreases the tetragonal c-axis.

2. CaO and CuO impurities:

CaO and CuO are simple oxides that can be produced during the synthesis process. Their primitive cells are small, resulting in Bragg patterns that start at higher angles. Below 40°, there are only two CaO reflections, (111) at 32.0° and (200) at 37.2°. Monoclinic CuO exhibits intense reflections of (11-1) and (111) at 34.8° and 35.7°, respectively. The reflections from these impurities may overlap with reflections from other substances, making their identification challenging. Only one of these two parasitic phases, CaO, was found in the nominally nonstoichiometric Tl-2.2 2 2 3 sample after oxygenation (E.3 in Appendix E). Additionally, the content of CaO appears to be similar in both singly and doubly oxygenated samples (Fig. E.5 in Appendix E).

3. Unreacted ingredients:

Unreacted Tl_2O_3 and $BaCuO_2$ are often observed in the obtained samples. Due to the volatile nature of thallium oxide, this compound is primarily present in specimens before oxygenation. $BaCuO_2$ can be either an unreacted substrate or a product of the decay of thallium superconductors during synthesis. Complex oxides such as $TlBa_2CuO_5$ may also form after synthesis. $BaCuO_2$ was found in many of the prepared samples, and its presence is visible in Fig. E.3 in Appendix E.

The synthesized sample can absorb CO_2 from the air, resulting in the presence of carbonates ($BaCO_3$ and Tl_2CO_3) or CO_2 intercalated in crystals, such as $BaCuO_2 \cdot 0.12CO_2$. Both oxides and carbonates are considered impurities, but their weight percentage can exceed 15%.

Oxygenation at different temperatures can alter the content of the parasitic phases $BaCuO_2$ and $BaCO_3$ (with a constant oxygenation time). The samples oxygenated at 700°C and 740°C exhibited the highest amount of carbonate relative to the main phase. The sample oxygenated at 720°C had a lower barium carbonate content, while the lowest carbonate content was detected in the sample oxygenated at 760°C (which is also the reason why this temperature, T_{oxy}=760°C, was chosen for further experiments). Barium carbonate was detected in all oxygenated samples, although the sequence of carbonate content with respect to oxygenation temperature may be coincidental (Fig. 4.20 a). The content of $BaCuO_2$ precursor appears to increase with the chosen oxygenation temperature (Fig. 4.20 b). This may be due to the decay of the main phase (Tl-2223) during oxygenation, which can occur more rapidly at higher temperatures. The samples oxygenated at lower temperatures of 720°C or 700°C showed no or only trace amounts of $BaCuO_2$. This suggests that barium copper oxide fully reacted during the primary synthesis, and the presence of $BaCuO_2$

observed at 760°C could be a result of its formation during the oxygenation at excessively high temperature (Fig. 4.20b). Repeated oxygenation does not appear to significantly affect the amount of $BaCuO_2$ (Fig. E.5 in Appendix E).

4. Other thallium superconductors:

In addition to the discussed Tl-2212, the presence of Tl-2201 is sometimes observed in XRD diffractograms as a result of Tl-2223 synthesis (Fig. E.2 in Appendix E). A comparison of singly (e.g., #25a, #30aa, Fig. E.5 in Appendix E) and doubly (e.g., #30aa, Fig. E.4 in Appendix E) oxygenated samples suggests that the amount of Tl-2212 is significantly higher when the total oxygenation time is longer. Singly oxygenated samples contain almost no Tl-2212 phase (with very weak peaks below 25°, Fig. E.2 and E.1 in Appendix E). Both samples also exhibit impurities such as $BaCuO_2$ (three reflections between 28° and 30°) and CaO (around 37.5°).

4.7 Structure of the doped samples

1. Cobalt doped samples

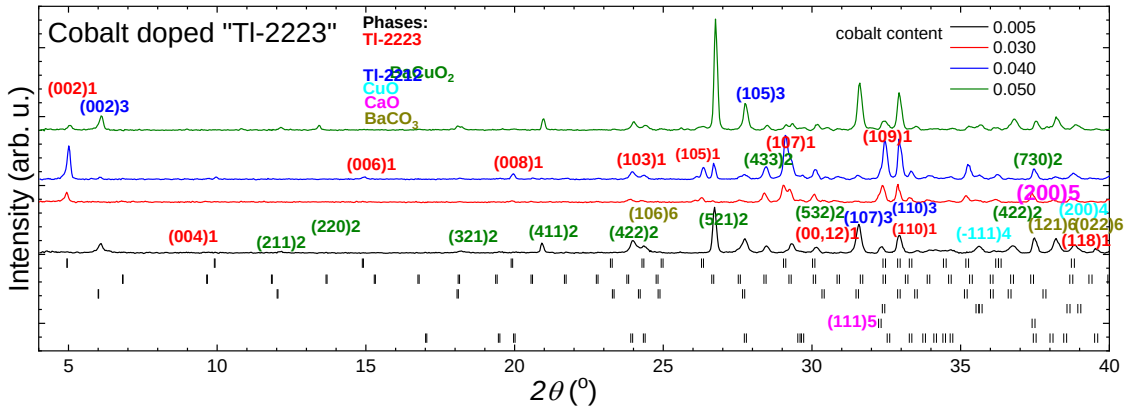

Figure 4.26: XRD spectra of cobalt doped Tl-2223 superconductors with doping from 0.005 to 0.050. (Co67N, Co74N, Co73N, Co75N)

Seven Co-doped samples, $Tl_2Ba_2Ca_2Cu_{3-x}Co_xO_y$, along with a reference sample without cobalt, were prepared (samples No. 66, 67, 68, 72, 73, 74, and 75). The XRD diffractograms for the oxygenated samples are shown in Fig. 4.26. For intermediate cobalt concentrations (x_{Co} = 0.030, x_{Co} = 0.040), Tl-2223 is the main superconducting phase, unlike the other (x_{Co}=0.005, x_{Co}=0.050) two samples. In the sample with the lowest cobalt content (x_{Co} = 0.005), both Tl-2223 and Tl-2212 superconductors are equally present, while in the sample with x_{Co} = 0.050 cobalt content, only Tl-2212 superconductor is present. This suggests that cobalt might favour the formation of Tl-2223 in a certain range of concentrations. Other cobalt compounds, apart from the superconducting phase, were not detected in the XRD analysis, due to the relatively low cobalt content. The

presence of other substrates such as $BaCuO_2$ and CuO is observed, with their weight percentages exceeding 10% (5% in the case of CaO). Although the content of the desired Tl-2223 phase is not high (ranging from 25% to 40%), it is sufficient for studying this phase using other experimental techniques, such as VSM, AC susceptibility, or contactless critical current measurements as presented in Chapter 5.

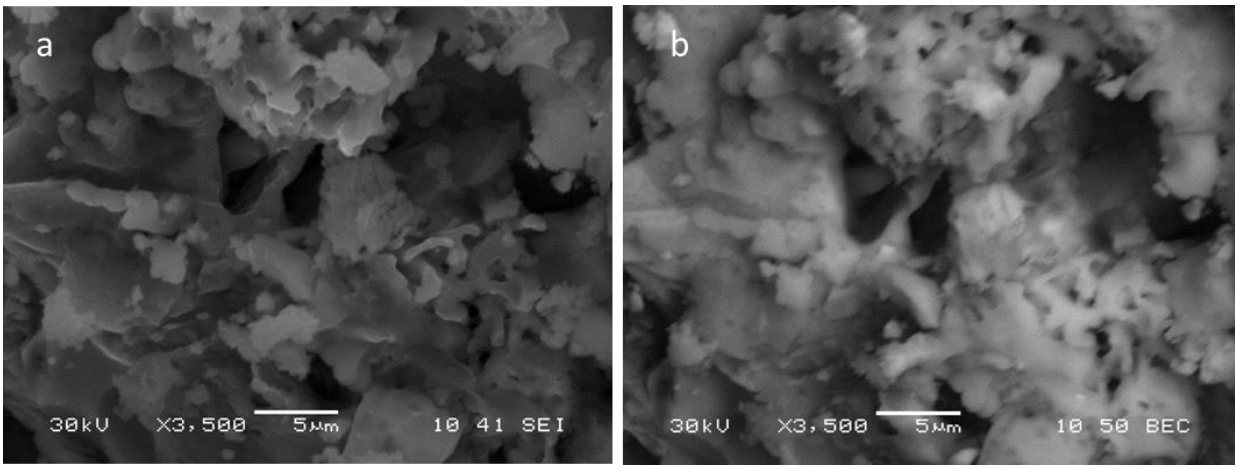

Figure 4.27: Impurities of oxygenated Tl-2223 doped with cobalt (Co75N) in the ratio of 0.05 atoms of cobalt for three copper sites. Panel (a) shows SE and panel (b) shows BEC image.

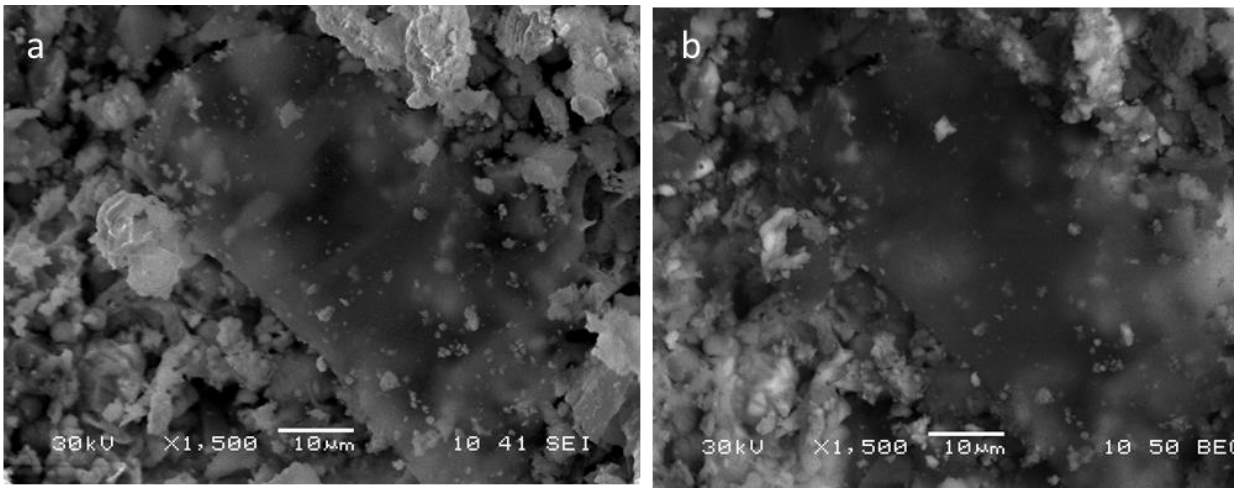

Figure 4.28: Melt of oxygenated Tl-2223 doped by 0.05 cobalt (Co75N) atoms for three copper sites. Panel (a) shows SE and panel (b) shows BEC image.

SEM observation brings additional data concerning the structure of obtained (synthesised and oxygenated) materials. The oxygenated sample with 0.050 atoms of cobalt per unit cell has high amount of impurities (Figs 4.27 a, b). Regions which have been melt are also present (Figs 4.28 a, b) and they contain averagely lighter elements than impurities (Fig. 4.28 b). Crystalline flat structures are also present (4.29 a, b) but they are surrounded by impurities (Fig. 4.29 a). The length of a found crystallite is 25 μm (Fig. 4.29 b).

The lower doped oxygenated sample with x_{Co}=0.030 exhibits structures that are not characteristic of ceramic superconductors (Figs 4.30a, b). Additionally, there are crystalline tables present (Figs 4.31a, b), but their surface does not appear lustrous. In this particular sample, the crystals seem to be covered by some kind of impurity, resulting in a rough surface (Figs 4.3 a, b) as compared to the smooth surface observed in Fig. 4.29b.

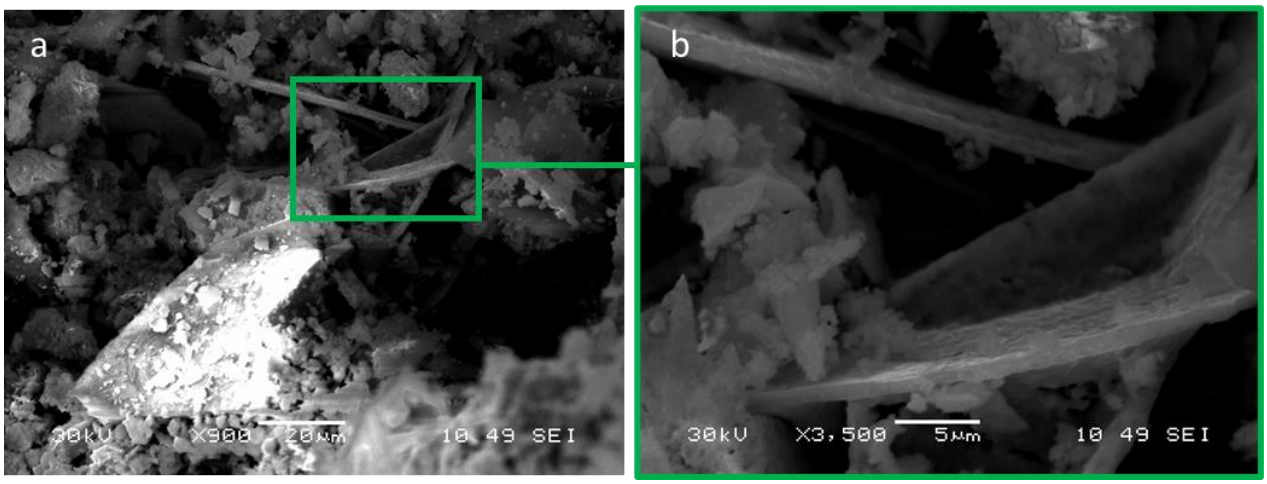

Figure 4.29: Panel (a) shows texture of oxygenated Tl-2223 with 0.05 cobalt doping (Co75N). Magnification of the region in the green square is presented in panel b.

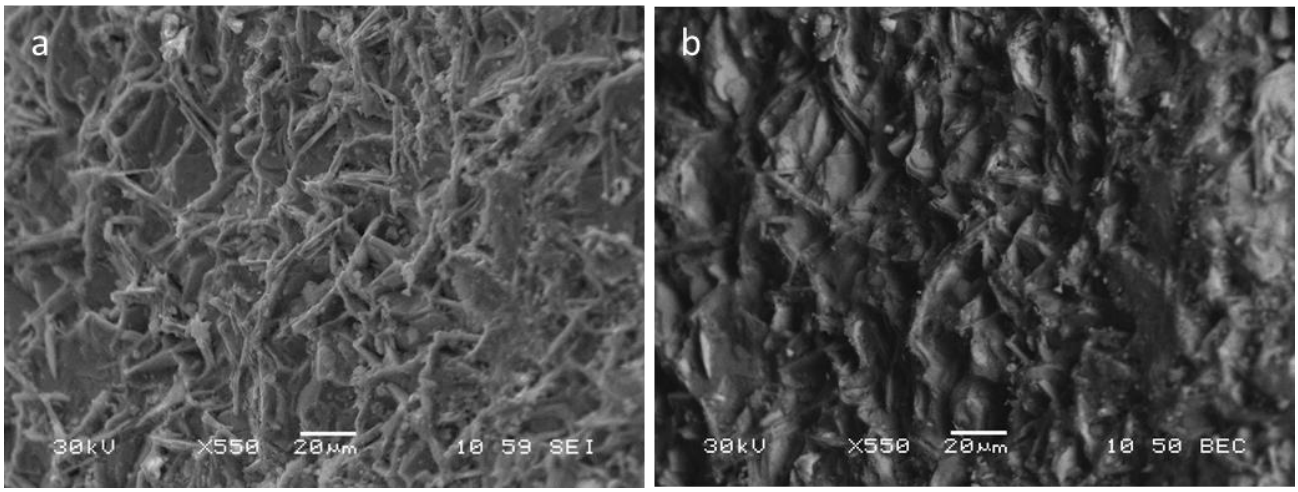

Figure 4.30: 0.03 cobalt doped oxygenated Tl-2223 bulk sample (Co74N). Panel (a) shows SE image and panel (b) shows BEC image. While tablet structures is visible in panel (a), no tablet structure is seen in (b).

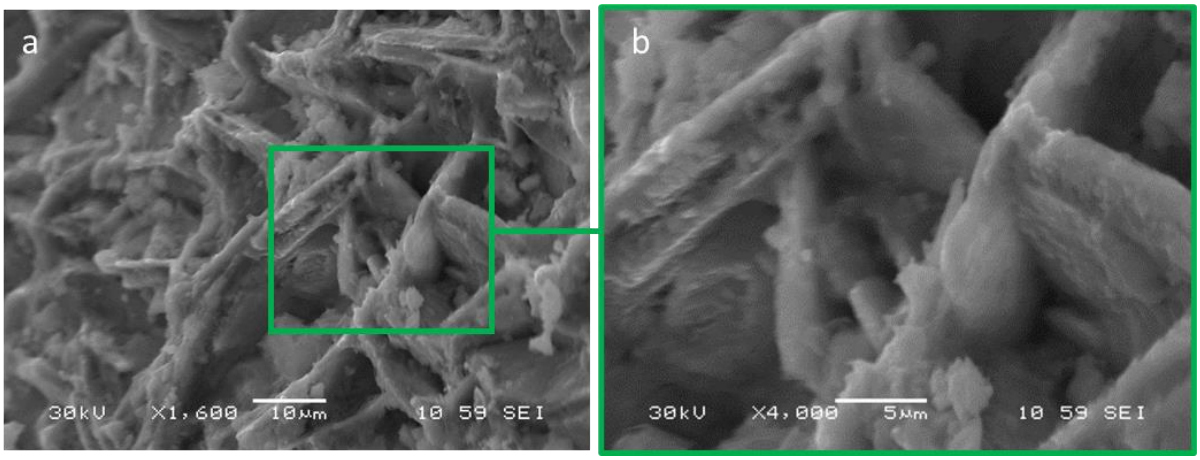

Figure 4.31: Panel (a) shows tablet structures covered with some of impurity observed for the 0.03 cobalt doped oxygenated Tl-2223 bulk sample (Co74N). Magnification of the region in the green square is presented in panel (b).

2. Nickel doped samples

As already outlined, five Ni doped samples, $Tl_2Ba_2Ca_2Cu_{3-x}Ni_xO_y$, were prepared ($x_{Ni}$= 0.0012, 0.0025, 0.0035, 0.0050, and 0.010 -No 61, 62, 63, 70, and 71, and oxygenated.

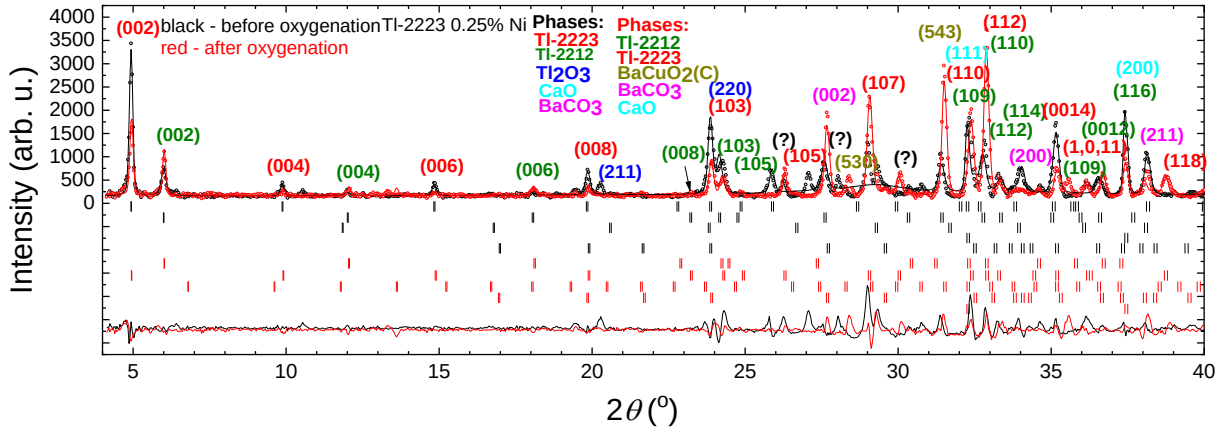

Figure 4.32: Nickel doped Tl-2223 superconductors. 0.0025 Ni atoms for three copper sites, assuming Tl-2223. Before (black) and after (red) the oxygenation. (Ni63 and Ni63N)

The synthesised material contains Tl-2223 in case nickel concentration is not too big (Fig. 4.32). For higher Ni concentration, mainly Tl-2212 superconductor, not Tl-2223, is formed (Figs. 4.33).

The effect of oxygenation is shown separately for x_{Ni}=0.0025 (Fig. 4.32) and for x_{Ni}=0.0050 (Fig. 4.33). For nickel concentration of 0.0025 the sample contains Tl-2223 both before and after oxygenation (Fig. 4.32) whereas for concentration of 0.005 of Ni formation of Tl-2223 is not detected. In latter case there is no Tl-2223 both before and after oxygenation.

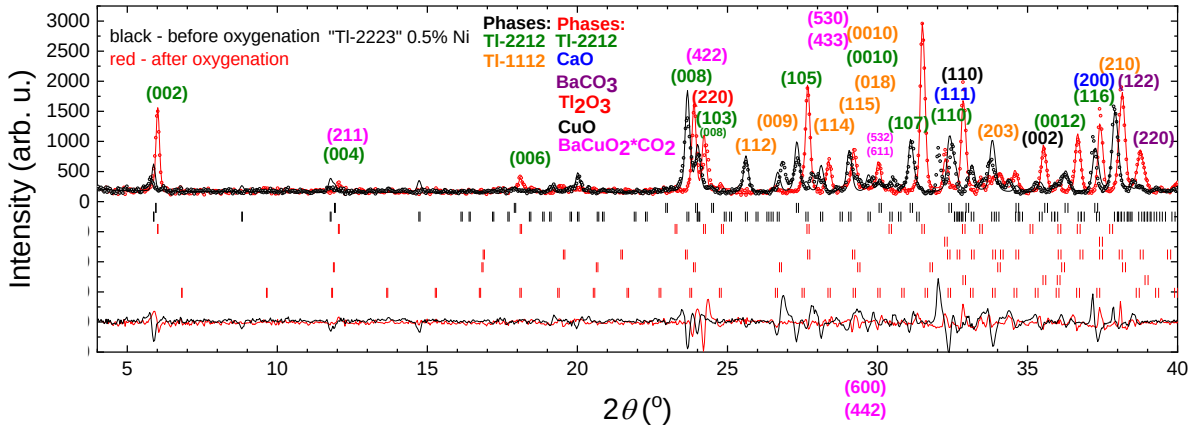

Figure 4.33: Nickel doped Tl-2223 superconductor with doping of 0.005 atoms of Ni for unit cell before and after oxygenation. (Ni62 and Ni62N)

As before, new hints concerning the structure of Ni doped samples are brought by SEM observation. Three types of surfaces of a fracture of Ni doped, oxygenated Tl-2223 samples can be singled out from Figs 4.34-4.36a, b. Each type is visible in SE signal as well as in BSE signal. Figs 4.34a, b show a granular structure which is not characteristic for HTS. There are no bars or crystalline tablets, that, however, can be seen in Figs 4.35a, b. Fig. 4.35b suggests that the chemistry of parts of presented region do not vary much compared to other probed regions. Thus this part of a sample (Fig. 4.35b) is chemically uniform. Spherical or kidney-shaped structures and pores are visible in Figs 4.36a, b under bigger magnification of 7000 times. These structures are also not characteristic for superconductors.

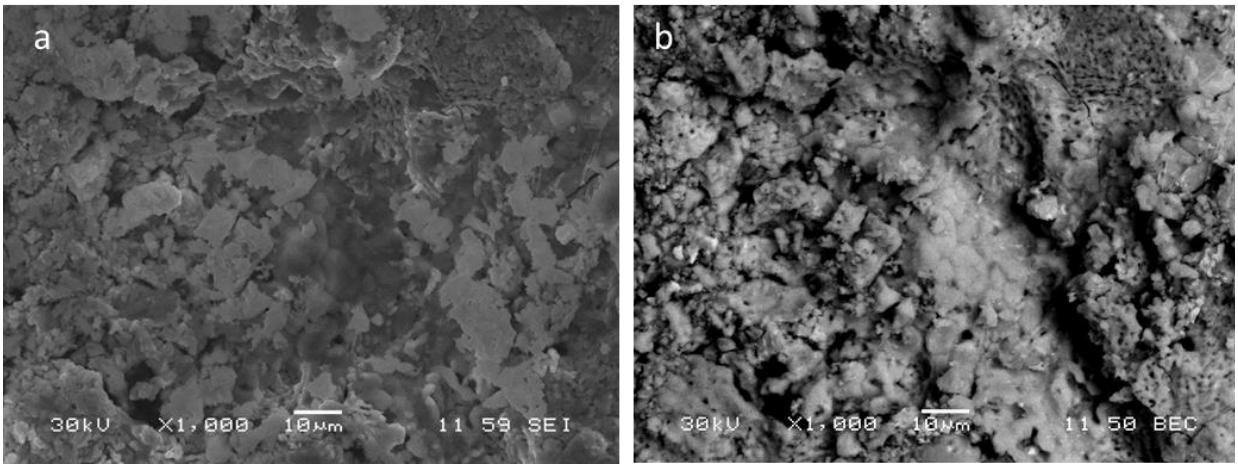

Figure 4.34: Oxygenated 0.01 Ni Tl-2223 (Ni61N) fracture. First example of the sample surface observed via SEM in the SE – panel (a) and BEC panel - (b) modes.

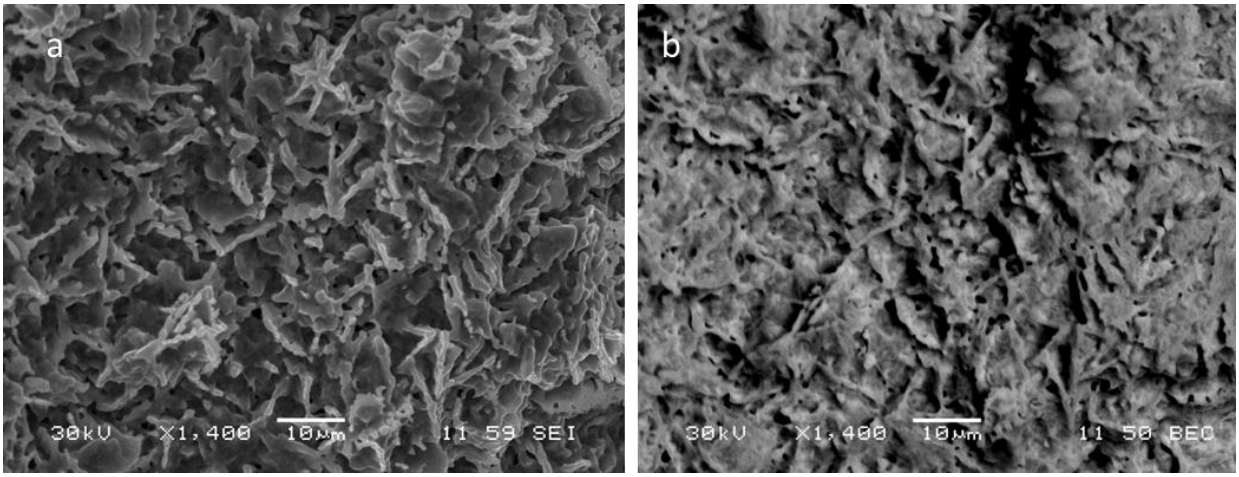

Figure 4.35: Oxygenated 0.01 Ni Tl-2223 (Ni61N) fracture. Second example of the sample surface observed via SEM in the SE – panel (a) and BEC - panel (b) modes.

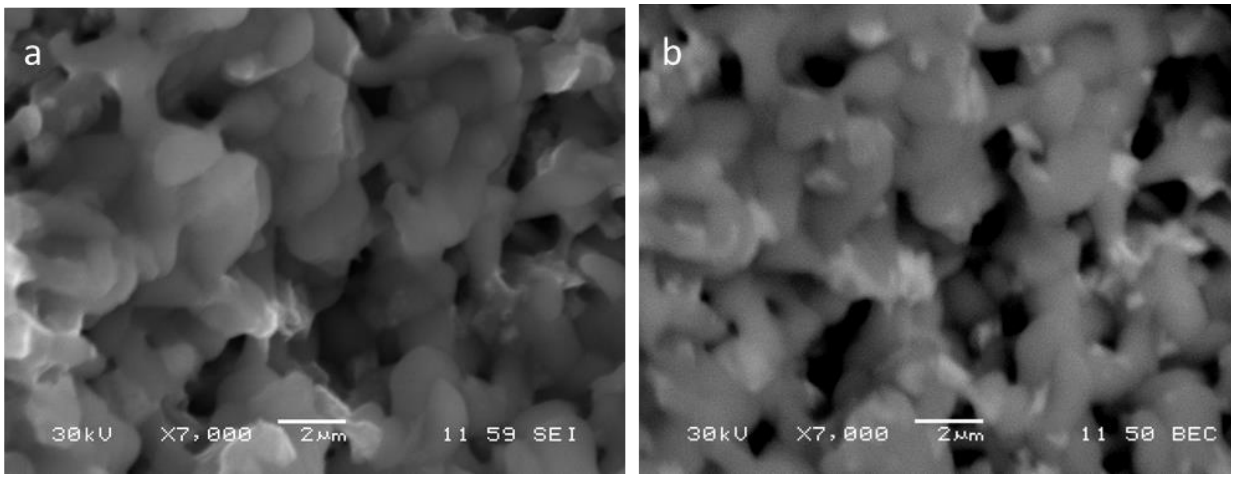

Figure 4.36: Oxygenated 0.01 Ni Tl-2223 (Ni61N) fracture. The third example of the sample surface showing rather round grains. The SEM images obtained in the SE – panel (a) and BEC - panel (b) modes. Note the difference in the magnification compared to the one used in Figs. 4.35 and 4.36.

3. Gadolinium doped samples.

Four Gd-doped samples with varying Gd concentrations (x_{Gd}=0.025, 0.05, 0.10, and 0.20) were synthesized, but XRD analysis was only performed on one sample (x=0.20, #32), as shown in Fig. 4.37. The XRD results indicate that no Tl-2223 phase was detected, and only other superconducting phases (Tl-2212 and Tl-1212) were formed. As is typical for unoxygenated samples, a certain amount of unreacted Tl_2O_3 was present. Interestingly, no other barium compounds besides the superconductor were detected, suggesting that one of the precursors may have decomposed into CaO and CuO.

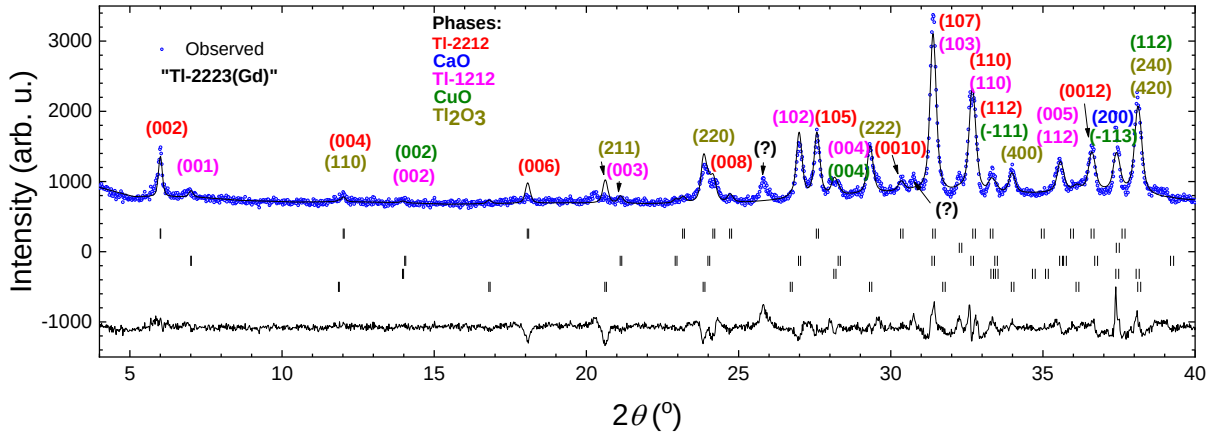

Figure 4.37: Gadolinium doped thallium superconductor with doping of 0.2 Gd atoms for unit cell, before oxygenation. (#32)

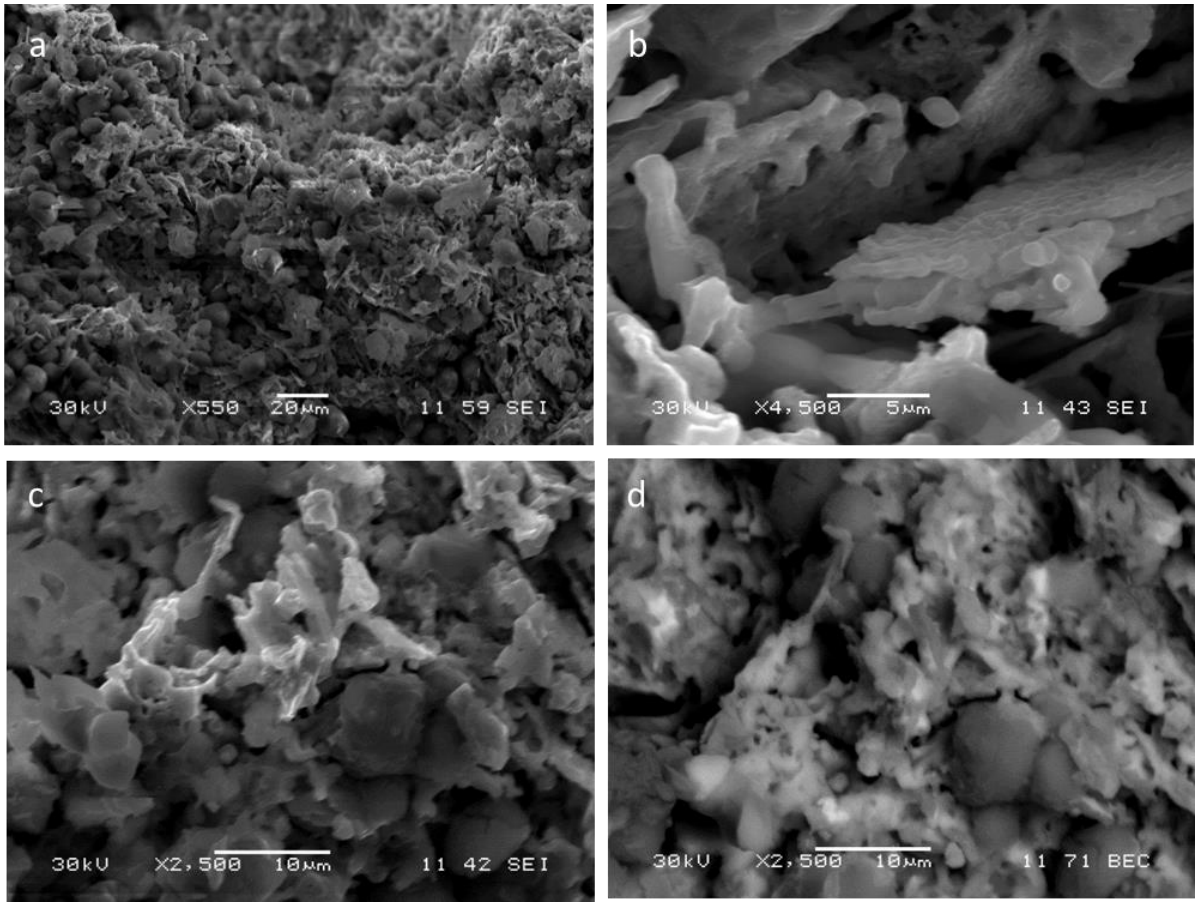

Figure 4.38: A fracture of oxygenated Gd doped Tl-2223 sample (Gd55N). 4.37Panels (c), and (d) are pictures of the same sample region in 2500x magnification but in different electron signal. Panel (a) shows SE image in 550x magnification. Panel (b) shows SE signal in 4500x magnification. Flat structures made of spheres are visible in panel (b).

Although the as-prepared sample with x_{Gd}=0.2 does not contain the desired phase, it was found to exhibit superconductivity with a critical temperature exceeding 100 K after oxygenation.

Furthermore, similar observations were made for other Gd-doped samples, where superconductivity was only achieved after oxygenation, resulting in critical temperatures also exceeding 100 K.

The microstructure of the oxygenated Gd-doped sample with x_{Gd}=0.1 was studied, revealing a variety of forms and structures. Figure 4.3 a and 4.38c show the presence of both "standard" impurities as well as spherical-shaped forms. Additionally, detailed examination revealed planes within these spherical forms (Fig. 4.38b). The impurities appeared bright in the BEC picture, indicating the presence of heavy metals (Fig. 4.38d).

In summary, the techniques employed in this chapter, such as XRD and SEM, provide qualitative and to some extent quantitative information about the atomic and microstructure of the synthesized materials. It is evident that while the desired superconducting Tl-2223 phase is present, it often coexists with other superconductors (Tl-2212, Tl-1212), unreacted substances, and various simple or complex oxides. The presence of nickel, cobalt, and gadolinium dopants appears to promote the formation of the Tl-2212 superconductor, with the effect being most pronounced in the case of gadolinium substitution.

Although the experimental procedure did not yield complete success, the author believes that a significant and important step has been taken. The samples should be further characterized in greater detail, which will be carried out in the subsequent Chapter 5.

Literature:

1. E. Ruckenstein, N.-L. Wu, Synthesis of Tl-based high-T_c superconductive oxides In: A. Hermann, Y. Yakhmi (eds), Thallium-based high-temperature superconductors, Marcel Dekker, Inc., New York*Basel*Hong Kong (1994) isbn: 0-8247-9114-2
2. H. Krischner, K. Torkar, and B. Kolbesen, Beiträge zum system BaO-NiO, Journal of Solid State Chemistry **3**, 349-357 (1971) doi: 10.1016/0022-4596(71)90070-3
3. R. Gottschall and R. Schöllhorn, Barium nickel oxide with $BaCuO_2$ type structure, Solid State Ionics **59** (1-2), 93-98 (1993) doi: 10.1016/0167-2738(93)90234-T
4. B. Gushee, L. Katz, and R. Ward, The preparation of barium cobalt oxide and other phases with similar structures, Journal of the American Chemical Society **79** (21), 5601-5603 (1957) doi: 10.1021/ja01578a004
5. S. Strauss, I. Fankuchen, and R. Ward, Barium cobalt oxide of the perowskite type, Journal of the American Chemical Society **73** (11), 5084-5086 (1951) doi: 10.1021/ja01155a019
6. G. Jeffery *et al.*, Textbook of qualitative chemical analysis, the fifth edition, Longman Scientific & Technical, Essex (1989) isbn: 0-582-44693-7
7. A. Cameron and N. Gibson, Edta titrations with extractive end-points: determination of cobalt, Analytica Chimica Acta **25** (1), 24-27 (1961) doi: 10.1016/S0003-2670(01)81512-9
8. http://zd2.chem.uni.wroc.pl/files/instrukcje/09_Ni.pdf, access 27.05.2023
9. https://en.wikipedia.org/wiki/Dicobalt_edetate, access 27.05.2023
10. C. Rao, A. K. Ganguli, and R. Vijayaraghavan, Superconducting (1:1:2:2)-type layered cuprates of the formula $TlCA_{1-x}L_xSr_2Cu_2O_y$ (L=Y or rare-earth element), Physical Review B **40**, 2565 (1989) doi: 10.1103/PhysRevB.40.2565
11. S. Isber *et al.*, Superconducting properties of Tl-2223 phase substituted by iron, Journal of Physics: Conference Series **43**, 450 (2006) doi: 10.1088/1742-6596/43/1/112
12. T. Kaneko *et al.*, A method for doping Tl-based cuprate superconductors with holes, Physica C **197**, 385-388 (1992) doi: 10.1016/0921-4534(92)90021-4
13. T. Kaneko *et al.*, Zero-resistance temperature of Tl-based „2223" superconductor increased to 127 K, Physica C **178** (4-6), 377-382 (1991) doi: 10.1016/0921-4534(91)90086-E
14. N.-L. Wu and E. Ruckenstein, A new method for the preparation of the superconducting $Tl_2CaBa_2Cu_2O_8$ compound, Materials Letters **7** (5-6), 169-171 (1988) doi: 10.1016/0167-577X(88)90003-1

15. E. Ruckenstein and C. Cheung, Reaction pathways in the formation of the Tl-Ca-Ba-Cu superconducting phases, Journal of Materials Research **4** (5), 1116-1122 (1989) doi: 10.1557/JMR.1989.1116
16. K. Yvon and M. François, Crystal structures of high-T_c oxides, Zeitschrift für Physik B Condensed Matter **76**, 413-444 (1989) doi: 10.1007/BF01307892
17. C. Torardi *et al.*, Crystal structure of $Tl_2Ba_2Ca_2Cu_3O_{10}$, a 125 K superconductor, Science **240** (4852), 631-634 (1988) doi: 10.1126/science.240.4852.631
18. A. Hewat *et al.*, Preparation and neutron diffraction of superconducting "tetragonal" and non-superconducting orthorhombic $Tl_2Ba_2Cu_2O_6$, Physica C **156**, 369-374 (1988) doi: 10.1016/0921-4534(88)90760-5
19. T. Kaneko *et al.*, Synthesis of Tl-based "2234" superconductors, Journal of Applied Physics **71**, 2347-2350 (1992) doi: 10.1063/1.351087
20. N. Khan, Cu,Tl-based high temperature superconductors, VDM Verlag Dr Müller, SaarBrücken (2010) isbn: 978-3-639-26844-7
21. Y. Shimakawa *et al.*, Variation in T_c and carrier concentration in Tl-based superconductors, Physical Review B **40**, 11400(R)-11402 (1989) doi: 10.1103/PhysRevB.40.11400
22. M. Presland *et al.*, General trends in oxygen stoichiometry effects on T_c in Bi and Tl superconductors, Physica C **176** (1-3), 95-105 (1991) doi: 10.1016/0921-4534(91)90700-9
23. H. Chu and N. Wu, Bull. Coll. Eng. Nat. Taiwan University **53**, 87 (1991)
24. N. Wu and H. Chu, Oxygenation and superconductivity of $Tl_2CaBa_2Cu_2O_{8-x}$, Physica C **167** (3-4), 267-270 (1990) doi: 10.1016/0921-4534(90)90340-K
25. M. Giebułtowski *et al.*, Dependence of oxygenation temperature on critical temperature and current for $Tl_2Ba_2Ca_2Cu_3O_x$, Acta Physica Polonica A **137** (5), 803-806 (2020) 10.12693/APhysPolA.137.803

5. Experimental results

The discussion of the main experiments of this thesis follows the presentation of the samples that were grown using the optimized procedure discussed in Chapter 4. Additionally, some of the samples that were previously described, and exhibited sufficiently high quality are further studied. The samples that are characterised and discussed in this chapter are listed in Table 5.1. The characterization procedure includes measurements of magnetic susceptibility, resistivity, DC magnetization, and in one case, specific heat.

The measurements of magnetic susceptibility provide information on the critical temperature (T_c) and critical current density (j_c) of the samples. Furthermore, the resistivity measurements yield values for T_c, critical exponents, and transition width. Finally, the DC magnetization measurements provide insights into the critical current density, trapped magnetic flux, and full penetration field.

Table 5.1 Complete list of the samples grown and characterized within the framework of the thesis.

Sample ***	Composition Tl/Ba/Ca/Cu	Sint *T* and time *	Oxygen *T* and time**	Wrapped during synthesis	XRD	SEM	R(T)
#13	Tl-2223	900ºC/45 min	-	single Ag			V
#15	Tl-2223	910ºC/45 min	-	single Ag			V
#16	Tl-2223	920ºC/45 min	-	single Ag			V
#25	Tl-2223	915ºC/45 min	-	used, single Ag			
#25a	Tl-2223	915ºC/45 min	740ºC/20 h	used, single Ag	V		
#30	Tl-2.2 2 2 3	915ºC/45 min		Single Ag layer on "legs"			
#30a	Tl-2.2 2 2 3	915ºC/45 min	740ºC/20 h		V		
#30aa	Tl-2.2 2 2 3	915ºC/45 min	2 x 740ºC/20 h		V		V
Gd32	$Tl_2Ba_2Gd_{0.2}Ca_{1.8}Cu_3O_{10+\delta}$	915ºC/45 min	-	Ag	V		
Gd33	$Tl_{2.2}Ba_2Gd_{0.2}Ca_{1.8}Cu_3O_{10+\delta}$	905ºC/45 min	-	Ag	V		
#48B	Tl-2223		-	double Ag			
#49A	Tl-2223	870ºC/30 min	-	double Ag			
#49B	Tl-2223	890ºC/30 min	-	double Ag			
#50A	Tl-2223	860ºC/30 min	-	double Ag			
#50B	Tl-2223	880ºC/20 min	-	double Ag			
#51A	Tl-2223	880ºC/40 min	-	double Ag			
#51B	Tl-2223	880ºC/50 min	-	double Ag			
#52A	Tl-2223	875ºC/30 min	-	double Ag, strong O_2 flow			
#52B	Tl-2223	875ºC/30 min	-	double Ag, strong O_2 flow			
#53A	Tl-2223	875ºC/30 min	-	double Ag			
#53B	Tl-2223		-	double Ag			
#48BN	Tl-2223		700ºC/ 21 h 13 min	double Ag			
#49AN	Tl-2223	870ºC/30 min	700ºC/ 21 h 13 min	double Ag			
#49BN	Tl-2223	890ºC/30 min	700ºC/ 21 h 13 min	double Ag			
#50AN	Tl-2223	860ºC/30 min	700ºC/ 21 h 13 min	double Ag			
#50BN	Tl-2223	880ºC/20 min	700ºC/20 h	double Ag			
#51AN	Tl-2223	880ºC/40 min	700ºC/20 h	double Ag			
#51BN	Tl-2223	880ºC/50 min	700ºC/20 h	double Ag			
#52AN	Tl-2223	875ºC/30 min	700ºC/20 h	double Ag,			

				strong O_2 flow			
#52BN	Tl-2223	875ºC/30 min	700ºC/20 h	double Ag, strong O_2 flow			
#53AN	Tl-2223	875ºC/30 min	700ºC/20 h	double Ag			
#53BN	Tl-2223		700ºC/20 h	double Ag			
#54A	Tl-2223		-	double Ag	V	V	
#54B	Tl-2223		-	double Ag			
#54AN700	Tl-2223		700ºC/20 h	double Ag	V	V	
#54AN720	Tl-2223		720ºC/20 h	double Ag	V		
#54AN740	Tl-2223		740ºC/20 h	double Ag	V		
#54AN760	Tl-2223		760ºC/20 h	double Ag	V	V	
#54BN760	Tl-2223		760ºC/20 h	double Ag			
#54BN780	Tl-2223		780ºC/20 h	double Ag			
#54BN800	Tl-2223		800ºC/20 h	double Ag			
#54BN820	Tl-2223		820ºC/20 h	double Ag			
Gd55	$Tl_2Ba_2Gd_{0.1}Ca_{1.9}Cu_3O_{10+\delta}$		-	double Ag			
Gd57	$Tl_2Ba_2Gd_{0.05}Ca_{1.95}Cu_3O_{10+\delta}$		-	double Ag			
#59	Tl-2223		-	double Ag	V	V	
Gd60	$Tl_2Ba_2Gd_{0.025}Ca_{1.975}Cu_3O_{10+\delta}$		-	double Ag			
Gd55N	$Tl_2Ba_2Gd_{0.1}Ca_{1.9}Cu_3O_{10+\delta}$			double Ag		V	
Gd57N	$Tl_2Ba_2Gd_{0.05}Ca_{1.95}Cu_3O_{10+\delta}$			double Ag			
#59N	Tl-2223			double Ag	V		V
Gd60N	$Tl_2Ba_2Gd_{0.025}Ca_{1.975}Cu_3O_{10+\delta}$			double Ag			
#59NN	Tl-2223		2x760ºC/ 20 h	double Ag			
#59N-40	Tl-2223		760ºC/ 40 h	double Ag			
Ni61	$Tl_2Ba_2Ca_2Ni_{0.01}Cu_{2.99}O_{10+\delta}$		-	double Ag			
Ni62	$Tl_2Ba_2Ca_2Ni_{0.005}Cu_{2.995}O_{10+\delta}$		-	double Ag	V		
Ni63	$Tl_2Ba_2Ca_2Ni_{0.0025}Cu_{2.9975}O_{10+\delta}$		-	double Ag	V		
#65	Tl-2223		-	double Ag			
Co66	$Tl_2Ba_2Ca_2Co_{0.0025}Cu_{2.9975}O_{10+\delta}$		-	double Ag			
Co67	$Tl_2Ba_2Ca_2Co_{0.005}Cu_{2.995}O_{10+\delta}$		-	double Ag			
Co68	$Tl_2Ba_2Ca_2Co_{0.01}Cu_{2.99}O_{10+\delta}$		-	double Ag			
Ni70	$Tl_2Ba_2Ca_2Ni_{0.0035}Cu_{2.9965}O_{10+\delta}$		-	double Ag			
Ni71	$Tl_2Ba_2Ca_2Ni_{0.0012}Cu_{2.9988}O_{10+\delta}$		-	double Ag			
Co72	$Tl_2Ba_2Ca_2Co_{0.02}Cu_{2.98}O_{10+\delta}$		-	double Ag			
Co73	$Tl_2Ba_2Ca_2Co_{0.04}Cu_{2.96}O_{10+\delta}$		-	double Ag			
Co74	$Tl_2Ba_2Ca_2Co_{0.03}Cu_{2.97}O_{10+\delta}$		-	double Ag			
Co75	$Tl_2Ba_2Ca_2Co_{0.05}Cu_{2.95}O_{10+\delta}$		-	double Ag			
Ni61N	$Tl_2Ba_2Ca_2Ni_{0.01}Cu_{2.99}O_{10+\delta}$			double Ag		V	
Ni62N	$Tl_2Ba_2Ca_2Ni_{0.005}Cu_{2.995}O_{10+\delta}$			double Ag	V		
Ni63N	$Tl_2Ba_2Ca_2Ni_{0.0025}Cu_{2.9975}O_{10+\delta}$			double Ag	V		
Ni65N	Tl-2223			double Ag			
Co65N	Tl-2223			double Ag			
Co66N	$Tl_2Ba_2Ca_2Co_{0.0025}Cu_{2.9975}O_{10+\delta}$			double Ag			
Co67N	$Tl_2Ba_2Ca_2Co_{0.005}Cu_{2.995}O_{10+\delta}$			double Ag	V		V
Co68N	$Tl_2Ba_2Ca_2Co_{0.01}Cu_{2.99}O_{10+\delta}$			double Ag	V		
Ni70N	$Tl_2Ba_2Ca_2Ni_{0.0035}Cu_{2.9965}O_{10+\delta}$			double Ag			
Ni71N	$Tl_2Ba_2Ca_2Ni_{0.0012}Cu_{2.9988}O_{10+\delta}$			double Ag			
Co72N	$Tl_2Ba_2Ca_2Co_{0.02}Cu_{2.98}O_{10+\delta}$			double Ag	V		
Co73N	$Tl_2Ba_2Ca_2Co_{0.04}Cu_{2.96}O_{10+\delta}$			double Ag	V		V
Co74N	$Tl_2Ba_2Ca_2Co_{0.03}Cu_{2.97}O_{10+\delta}$			double Ag	V	V	V
Co75N	$Tl_2Ba_2Ca_2Co_{0.05}Cu_{2.95}O_{10+\delta}$			double Ag	V	V	V
Tl0.8	$Tl_{0.8}Bi_{0.3}Sr_{1.8}Ba_{0.2}Ca_2Cu_3O_{8.5+\delta}$	(925ºC/15min+ 910ºC/10 h) x 2	730ºC/10 h	Ag			V

*when different from optimal ones: 880ºC and 30 min.

** when different from optimal ones: 760ºC, 20 hours.

*** capital letters A or B, like in #52A, #52B, mean that both samples were prepared from the same powder mixture however pressed and synthesized separately.

Table 5.2 Characteristics of the samples synthetised in Bratislava. The table contains the heating conditions and the critical temperatures obtained from resistivity measurements.

Sintering temperature [°C]	Sintering time [min]	T_{c0} [K]	$T_{c\ onset}$ [K]
860 (pTl1)	30	85	121
860 (pTl2)	45	85	122
860 (pTl3)	45	93.9	124
860 (pTl4)	45	93.6	125
870 (pTl5)	30	94.9	130

5.1 AC susceptibility results before and after single oxygenation

AC magnetic susceptibility measurements were performed to extract important parameters such as the critical temperature (T_c), the AC magnetic field dependence of T_c, and the critical current. T_c was determined by analysing both the real component (χ') and the imaginary component (χ'') of the AC magnetic susceptibility. The critical current was calculated using Bean's formula, which relates the critical current density to the magnetic field and sample dimensions (see Appendix B for more details).

The measurements were carried out using a specific method and apparatus described in Chapter 3. The frequency of the AC magnetic field was set at 189 Hz, and the magnetic field strength ranged from 8 mOe to 10.2 Oe. When using a 1 Ω resistor for magnetizing current measurements, a phase shift of 33.15° was observed. These parameters were carefully chosen to ensure accurate and reliable measurements of the AC magnetic susceptibility.

5.1.1 The shape of superconducting transition

Figures 5.1 and 5.2 display the AC susceptibility results for the same Tl-2223 sample at different low magnetic fields, both before (#25) and after (#25a) the oxygenation process. The comparison between selected results before and after oxygenation is shown in Fig. 5.3. Furthermore, Fig. 5.4 illustrates the effects of repeated oxygenation (without oxygenation, after the 1st oxygenation, and after the 2nd oxygenation) for another sample, Tl-2.2 2 2 3 (#30, #30a, #30aa, respectively).

Upon oxygenation, the superconducting transition regions (observed in the dispersive part of the susceptibility) became narrower and shifted towards higher temperatures. The critical temperature (T_c) increased from 114.2 K before oxygenation to 118.8 K after oxygenation. These observations indicate the positive influence of the oxygenation process on the superconducting properties of the sample.

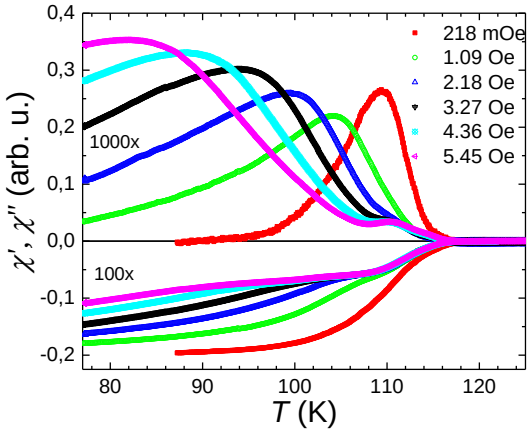

Figure 5.1: The absorption (top) and dispersive (bottom) part of AC susceptibility measured for Tl-2223 before oxygenation [1] (#25)

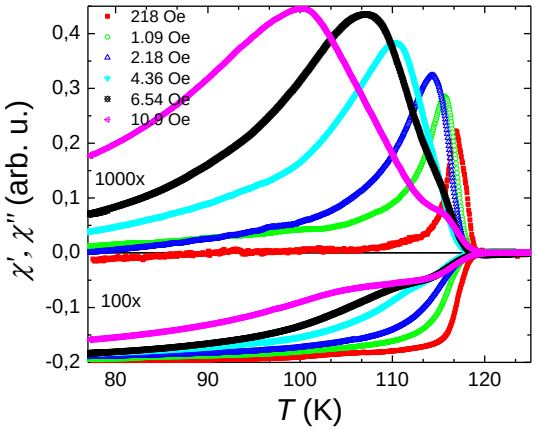

Figure 5.2: Measurements performed for the same Tl-2223 sample as in Fig. 5.1, after oxygenation [1](#25a)

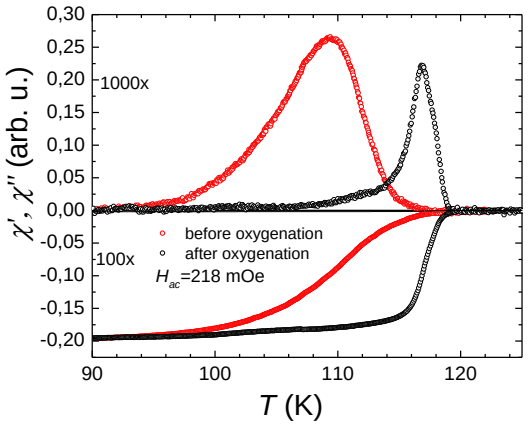

Figure 5.3: A Tl-2223 sample AC susceptibility before and after oxygenation. (#25, #25a) [1]

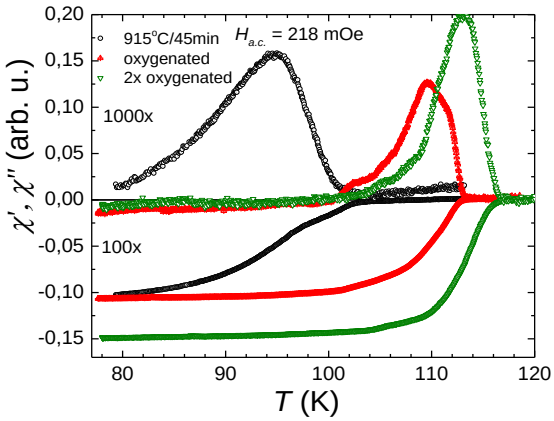

Figure 5.4: AC susceptibility of Tl-2.2 2 2 3 sample before, after single oxygenation, and after double oxygenation. (#30, #30a, #30aa) [2]

In addition, the absorption part of the susceptibility (χ") also undergoes changes after oxygenation. It becomes narrower, smaller in area, and shifts to higher temperatures. The transition temperature (T_c) determined from χ" increases from 109.3 K to 116.9 K after oxygenation.

When comparing measurements in various AC magnetic fields (Figs 5.1 and 5.2), the intra-grain critical temperature remains constant, while the inter-grain maximum of magnetic absorption shifts to lower temperatures and becomes broader as the AC magnetic field strength increases. At higher magnetic fields, a smaller intra-grain peak becomes visible at temperatures higher than the

main inter-grain peak. Once again, the transition observed in the oxygenated sample is sharper than in the unoxygenated sample.

The effect of the second 20 h oxygenation (Fig. 5.4) is similar to the first oxygenation, although less pronounced. The transition region is reduced and shifts towards higher temperatures compared to the sample after the first oxygenation. The absorption peak resulting from the second oxygenation is also shifted towards higher temperatures and has a narrower shape compared to the sample after the first oxygenation. However, the third oxygenation (not shown) destroys the sample's superconductivity, with the transition temperature not identified down to 77 K.

5.1.2 Critical exponent extracted from AC susceptibility

As explained in Chapter 2, the temperature dependence of certain physical quantities near the critical point follows a power law. Therefore, plotting the logarithm of a given quantity against the logarithm of the reduced temperature should result in a linear relationship within a certain temperature range. The slope of the linear fit provides the value of the critical exponent. Critical exponents contain information about the dimensionality of the superconducting system, and as demonstrated below, the dimensionality for the studied compounds appears to be temperature-dependent.

The system dimensionality (d) is equal to 4-2λ for Gaussian fluctuations, which applies to temperatures that are not very close to the critical temperature. In the immediate vicinity of the critical temperature, the dimensionality is given by d=3.5-1.5λ [3, 4, 5].

Critical exponents can be determined by analysing the log-log plot of a physical quantity (e.g., specific heat, magnetic susceptibility) against the reduced temperature. However, obtaining the reduced temperature requires prior knowledge of T_c, which can be determined from AC susceptibility in two ways: the higher value, intra-grain T_c (Fig. 5.5a - T_{ca}), or the lower value, inter-grain Tc (Fig. 5.5b - T_{ce}).

If the inter-grain critical temperature T_{ce} is considered, the exponents for all critical fields and temperature ranges can be recalculated to obtain the physical (non-negative) system dimension. This dimension appears to be around 3 close to T_{ce}, 2 in the intermediate temperature range, and 4 for temperatures away from T_{ce}. The dimensionality does not seem to depend on the applied AC magnetic field.

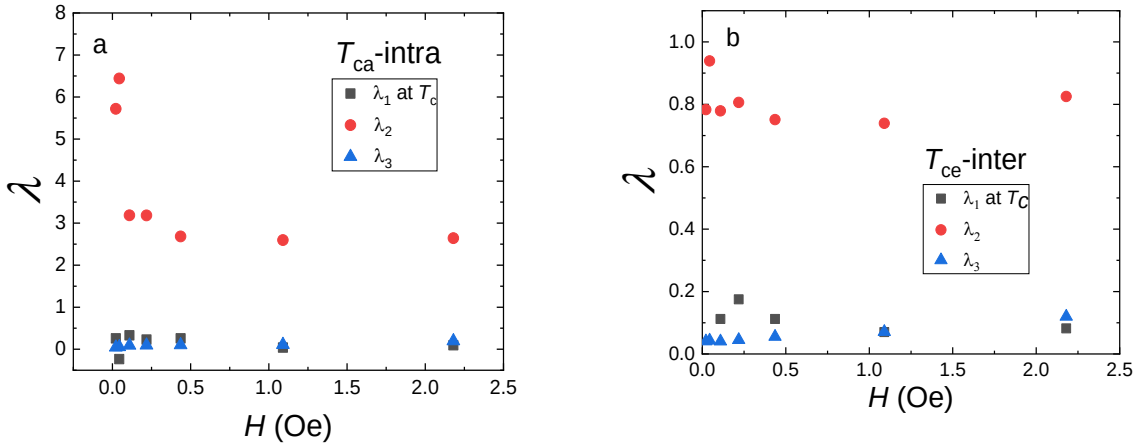

Figure 5.5: Critical exponents extracted from AC Susceptibility of oxygenated Tl-2223 bulk sample #59N. The intra-grain T_{ca} was used in panel (a), and inter-grain T_{ce} in panel (b).

In addition to determining T_c and the λ exponent, the critical current density (j_c) can also be obtained from the series of AC susceptibility measurements using the contactless Bean's method [Appendix B, 6, 7]. This method involves analysing the AC susceptibility data and applying the principles outlined in Section 3.3.1, along with the details provided in Appendix C, to calculate the critical current density.

5.1.3 AC susceptibility of doped Tl-2223

The optimal range of cobalt content (x_{Co}) in the cobalt-doped Tl-2223 ($Tl_2Ba_2Ca_2Cu_{3-x}Co_xO_{10}$) samples appears to be between x_{Co}=0.010 and x_{Co}=0.040. The samples with x=0.030 and x=0.040 exhibit a very sharp transition and a single narrow absorption peak in the AC susceptibility data (Fig. 5.6). The samples with x_{Co}=0.010 and x_{Co}=0.020 also show high inter-grain critical temperature, but a multi-peak pattern is observed in the absorption part of the AC susceptibility.

In the case of Gd-doped samples ($Tl_2Ba_2Ca_{2-x}Gd_xCu_3O_{10}$), the quality of the sample decreases with increasing gadolinium content (x) (Fig. 5.7). The Gd-free sample exhibits the best susceptibility signal. The sample with x_{Gd}=0.025 has slightly lower inter-grain critical temperature and a shifted position of the absorption peak. The most significant difference in inter-grain critical temperature and the position of the absorption peak (of approximately 10 K) is observed between the x=0.050 and x_{Gd}=0.025 samples. The sample with x_{Gd}=0.10 appears to be of the lowest quality, with an inter-grain critical temperature of 100 K and a maximum absorption peak at 96 K in low AC fields.

The presence of nickel (Ni) in the $Tl_2Ba_2Ca_2Cu_{3-x}Ni_xO_{10}$ samples has a detrimental effect on superconductivity of the Tl-2223 material. Fig. 5.8a shows that when the Ni content exceeds x=0.0035, the superconductivity below 95 K is residual, and no significant absorption peak is

visible in the AC susceptibility data. Varying the AC fields does not significantly alter this picture. For a low amount of Ni (x_{Ni}=0.0025), before oxygenation, the AC susceptibility signal appears similar to that of the undoped sample (Fig. 5.8b), as observed in previous data (e.g., Fig. 5.1).

The critical temperatures of the nickel-doped samples before oxygenation are lower than those of the samples doped with cobalt at the same concentration (Fig. 5.9). The results in this case strongly depend on the applied AC magnetic field.

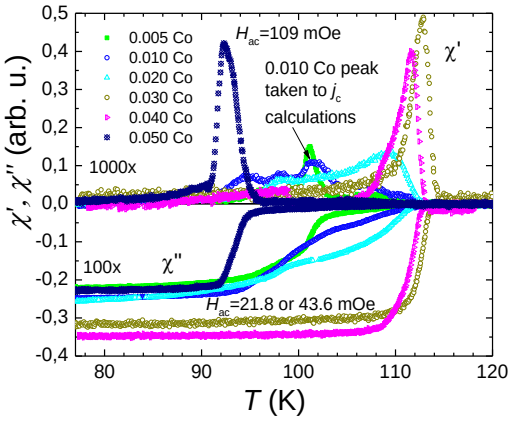

Figure 5.6: AC susceptibility of cobalt doped oxygenated Tl-2223. (Co67N, Co68N, Co72N, Co74N, Co73N, and Co75N) [8]

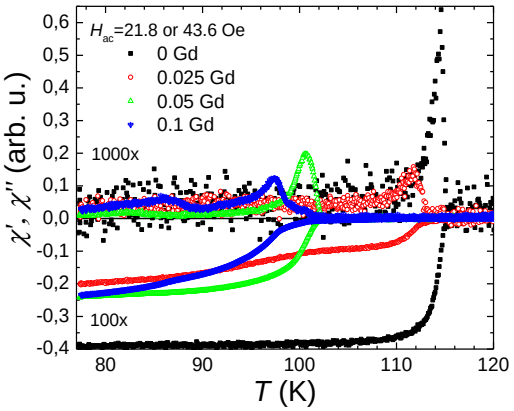

Figure 5.7: AC susceptibility of gadolinium doped Tl-2223, oxygenated at 760°C for 20h. (#59N, #60N, #57N, #55N)

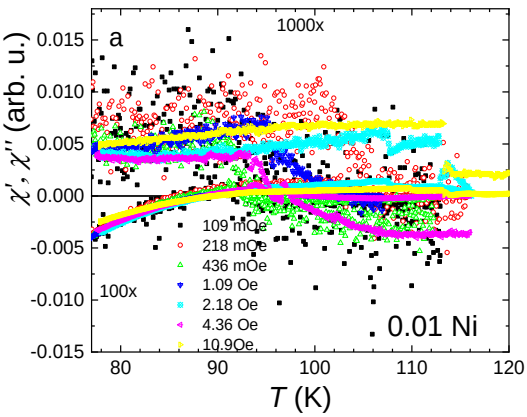

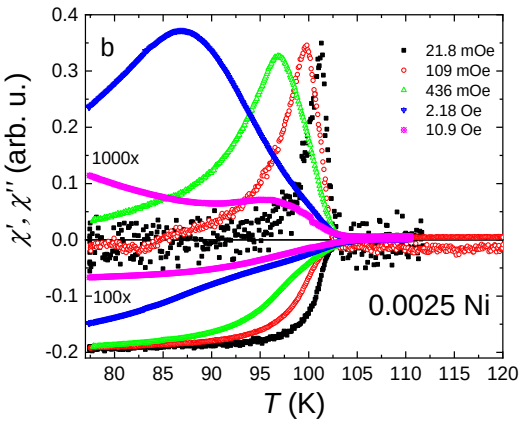

Figure 5.8: AC susceptibility of nonoxygenated nickel doped Tl-2223 samples. In panel (a), the results of 0.01 Ni (Ni61) sample are shown, and 0.0025 Ni (Ni63) in panel (b).

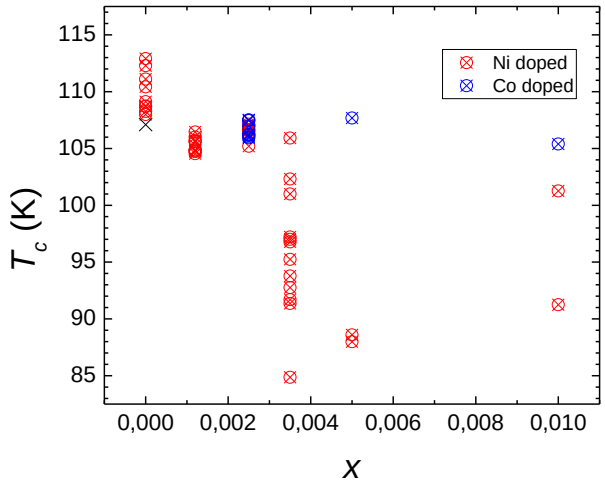

Figure 5.9: Critical temperatures versus Ni or Co concentration of Tl-2223 synthesized at 880°C for 30 minutes, before oxygenation. Black cross is the data point from [9]. (#65, #54, Ni61, Ni62, Ni63, Ni70, Ni71, Co66, Co67, Co68)

5.2 Resistance and magnetoresistance measurement

The results of resistance (R) and magnetoresistance (MR) measurements provide important parameters such as T_c, critical exponents, and critical currents. Fig. 5.10 presents the results of $R(T)$ measurements of Tl-2223 samples that were obtained under a slightly different procedure in Bratislava.

T_c is extracted from a drop in resistance which corresponds to a transition from normal state to superconducting state. As discussed later, the critical exponents can also be extracted from the resistance data. Additionally, the critical current can be determined from the magnetoresistance measurements.

The conductivity of a superconductor near T_c is a combination of contributions from normal electrons and superconducting carriers. As discussed in Chapter 3, the second contribution, represented by $\Delta\sigma$, is proportional to the carrier concentration and the square of the magnitude of the Ginzburg-Landau (GL) order parameter, $|\phi|^2$. This component provides valuable information about the superconducting state, particularly the critical exponent of the system, which is related to the dimensionality of the system.

To determine the critical exponent, the lower-temperature side of the transition, T_{c0}, is analysed. This region of the conductivity curve, as shown in Fig 3.13, allows for the extraction of the critical exponent and provides insights into the dimensionality of the superconducting system.

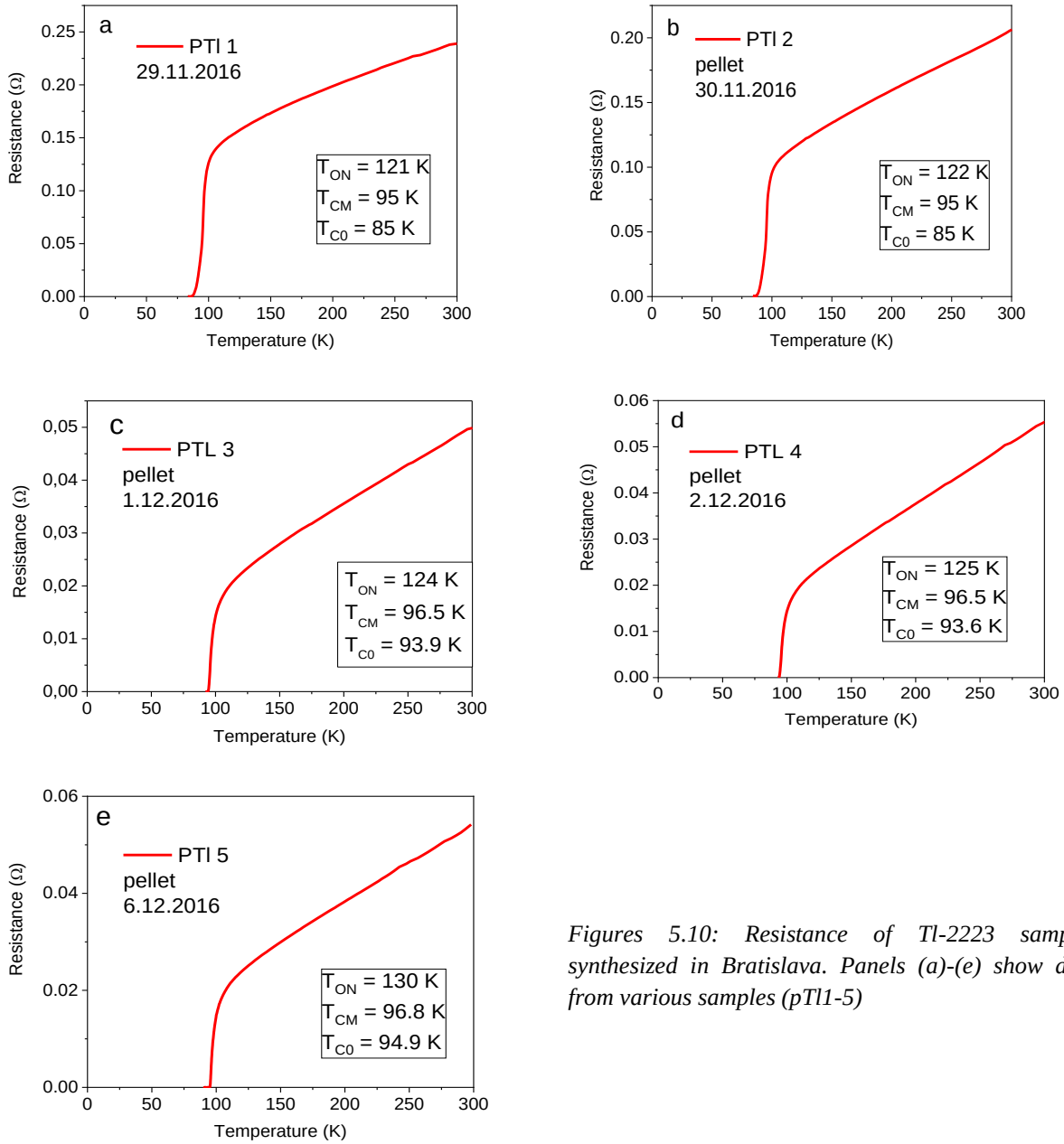

Figures 5.10: Resistance of Tl-2223 samples synthesized in Bratislava. Panels (a)-(e) show data from various samples (pTl1-5)

5.2.1 Width of the superconducting transition

The resistance versus temperature curves are affected by the presence of a DC magnetic field, as shown in Figs 5.11, 5.12, and 5.14. The application of a stronger DC magnetic field results in a broader transition region in the resistance curve. While the $T_{c\text{-onset}}$[3] remains unchanged for different values of applied fields up to 2 kOe, the T_{c0} (lower-temperature side of the transition) decreases with increasing magnetic field. Furthermore, the rate of T_{c0} decrease is faster for lower fields.

[3] Characteristic temperatures in R vs. T are defined in Fig. 3.13. In particular, the transition is limited by T_{c0} from the low temperature side and $T_{c100\%}$ (or T_{c_onset}) from the high temperature side. The transition width, ΔT_c, is defined as $T_{c90\%}$ minus $T_{c10\%}$ while $T_{c50\%}$ marks the middle of the transition and is referred to as T_c.

It is important to note that the resistance of the samples is also influenced by factors such as the thermal treatment history, the presence of substituted elements, and the initial composition (specifically, the thallium stoichiometry). However, despite these variations, the general behaviour of the resistance remains consistent. In Fig. 5.11, three distinct regions are observed, as discussed in section 3.3.3 and presented in Fig. 3.13.

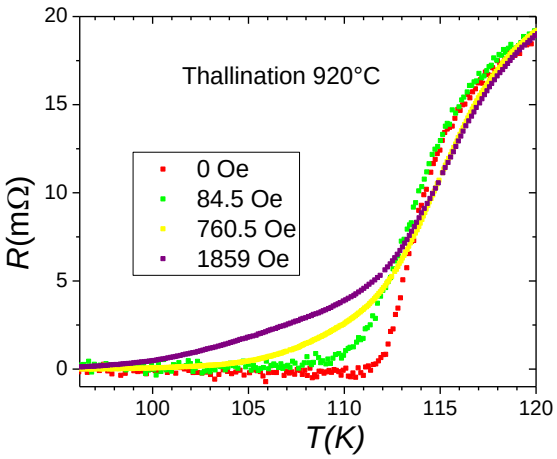

Figure 5.11: Magnetoresistance of Tl-2223 sample (#16) without oxygenation, after thallination at 920°C.

Figure 5.11 displays the magnetoresistance of an unoxygenated Tl-2223 sample. The relatively high critical T_{c0} temperature of 112 K for a sample without additional thermal treatment can be attributed to two factors. Firstly, the high synthesis temperature just below the material's melting point may have contributed to the enhanced critical temperature. Secondly, the sample was wrapped in a single layer of silver foil, which could have increased its exposure to the oxygen gas supplied to the furnace. In contrast, most samples were synthesized in double silver foil, which might have limited their oxygen exposure to some extent.

Sample #59N was oxygenated at 760ºC for 20 h that resulted in the critical temperature T_{c0} of 116 K (Figs 5.12 and 5.13). The inset of Fig. 5.12 shows a linear dependence of resistance in T range 130 K to 280 K. Application of magnetic field, in four steps (84.5 Oe, 422 Oe ,1267 Oe, 2113 Oe) causes a nonlinear decrease of T_c. Ultimately, H= 2113 Oe decreases T_c to T_{c0}=105 K.

In the case of the double-oxygenated Tl-2.2 2 2 3 sample (Fig. 5.14), the T_{c0} critical temperature reaches 117 K in zero field. However, when a magnetic field of 2 kOe is applied, the T_{c0} decreases to 113.5 K. Interestingly, this sample appears to be less sensitive to the presence of a DC magnetic field compared to the unoxygenated Tl-2223 sample (Fig. 5.11) and the singly oxygenated Tl-2223 samples (Fig. 5.10 and 5.12).

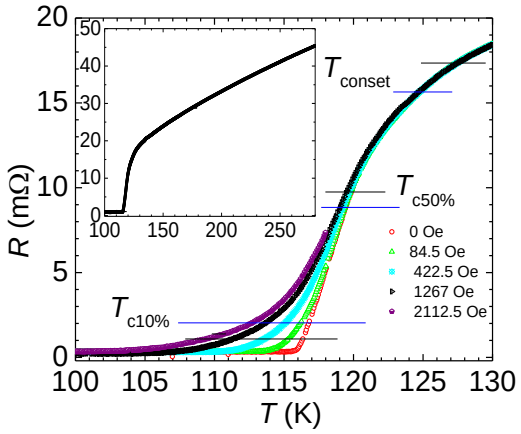

Figure 5.12: Magnetoresistance of oxygenated Tl-2223. (#59N). In a the whole R(T) for B=0 is presented in the inset and the vicinity of transition is shown for various magnetic fields. Horizontal lines cross-section with experimental trends indicates T_{c10}%, T_{c50}%, and $T_{c\text{-}onset}$. Two types of choosing the lines. Black and blue series.

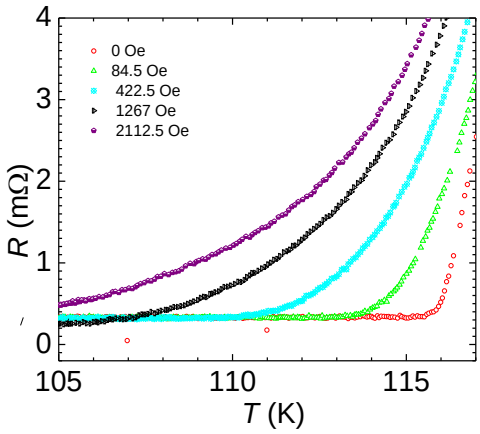

Figure 5.13: The picture shows R values close to zero for the same sample and DC magnetic fields as in 5.12.

Indeed, comparing the magnetic field influence on T_c in the singly and doubly oxygenated samples shown in Fig. 5.12 with the results from Fig. 5.11 or Fig. 5.14 is challenging due to the differences in sample preparation. These differences include variations in initial thallium stoichiometry, the number of silver wrappings, and the duration of the oxygenation process. These varying parameters can contribute to different sensitivities of the samples to the applied magnetic field. Therefore, it is important to consider these factors when interpreting the observed effects of the magnetic field on T_c in the different samples.

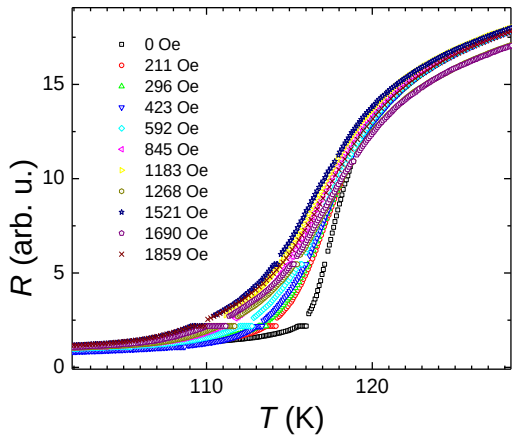

Figure 5.14: Magnetoresistance of double-oxygenated Tl-2.2 2 2 3 sample. (#30aa)

The magnetic field dependence of the transition width ΔT_c is also seen in yet another sample (Fig. 5.15a). Similar to the previous results (Figs 5.12 and 5.13) ΔT_c exhibits a faster growth for lower

fields compared to stronger fields. However, no saturation of ΔT_c versus H is observed up to 2 kOe, as depicted in Fig. 5.1b.

An attempt was made to describe the ΔT_c versus H dependency using a power law equation [10]. It is worth noting that high-temperature superconductors typically exhibit a wider transition even in low fields, requiring the addition of a constant term to the power law expression [10,11,12]. Consequently, the resulting formula for ΔT is given as:

$$\Delta T = C + H^n \tag{5.1}$$

where n represents the exponent, which is theoretically predicted to be 2/3 [10]. However, in practice, it is usually fitted to experimental results (e.g., see Fig. 5.15b) to capture the specific behaviour observed in the samples.

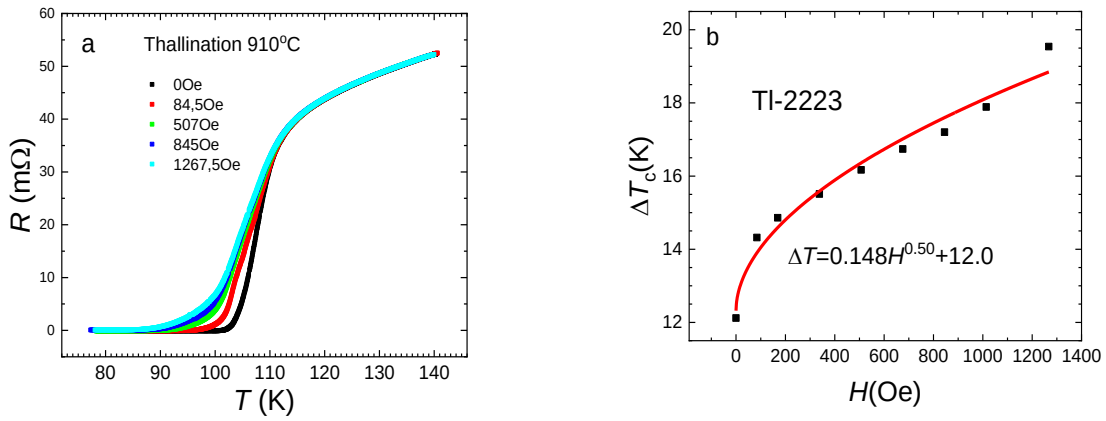

Figure 5.15: Magnetoresistance (panel a) and the resulting width of the transition (panel b) of nonoxygenated Tl-2223 sample (#15).

5.2.2 Resistivity and magnetoresistivity of doped Tl-2223

The magnetoresistance results of four cobalt-doped thallium cuprates are presented in Figs 5.16a-d. Based on the XRD pattern shown in Fig. 4.19c, these samples were found to be mixtures of two thallium superconductors: Tl-2212 and Tl-2223. It is observed that the critical temperature T_{c0} of moderately doped samples (x_{Co}=0.030 and x_{Co}=0.040) is higher, measuring 112.5 K and 113.7 K respectively, compared to the low and high doped samples (x_{Co}=0.005 and x_{Co}=0.050) which have T_{c0} values of 103.3 K and 95.4 K respectively. The transition width in zero field or in a 2 kOe field is also similar between the moderately doped samples, approximately 8 K and 13 K respectively. Additionally, the transition width is more narrow in the moderately doped samples compared to the other samples. On the other hand, the x_{Co}=0.005 and x_{Co}=0.050 samples exhibit significantly

different transition widths in zero field, measuring 9.1 K and 13.1 K respectively, indicating that they are not similar to each other in the same way as the moderately doped samples.

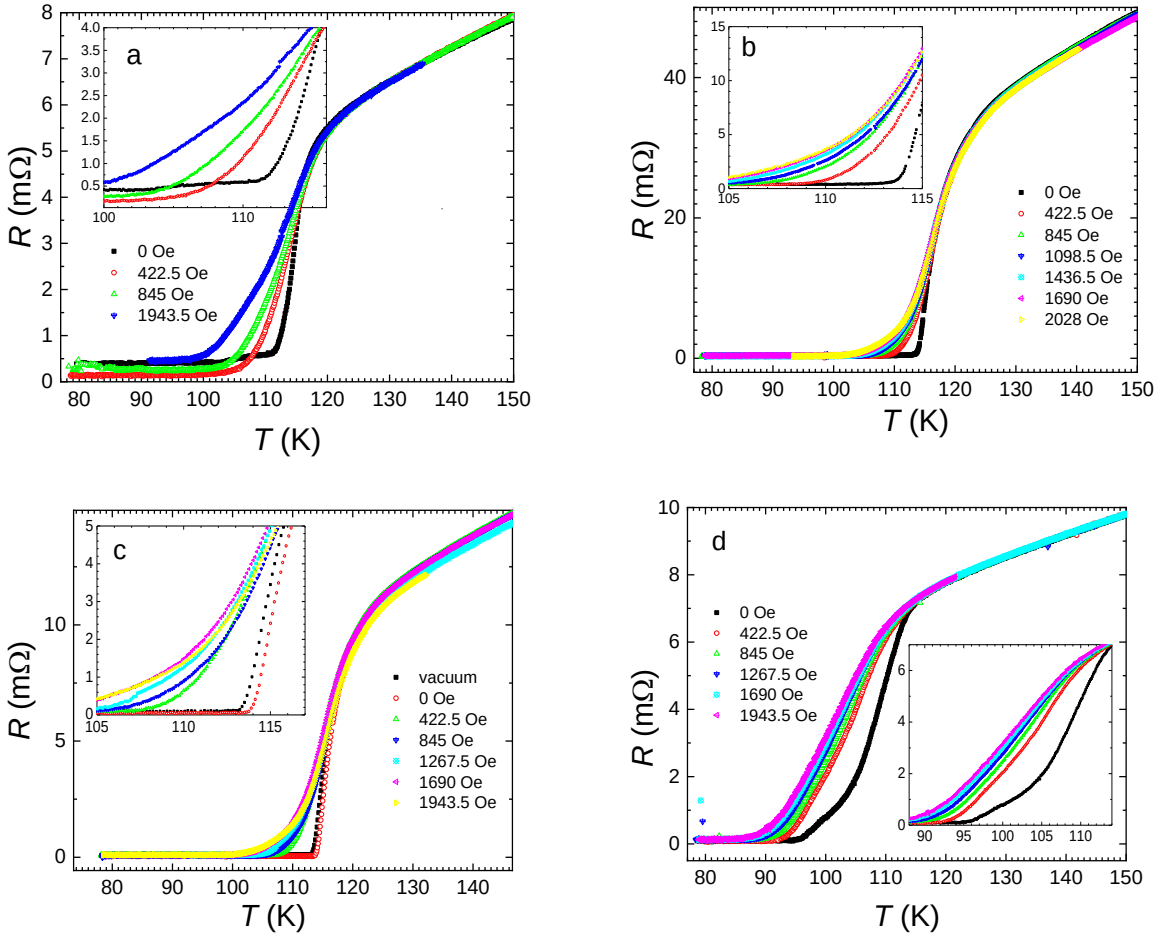

Figure 5.16: Magnetoresistance of bulk Tl-2223 doped with cobalt after oxygenation. (Panels: (a): x=0.005, i.e. Co67N; (b): x=0.030, Co74N; (c): x=0.040, Co73N; (d): x=0.050, Co75N)

Figure 5.17 demonstrates that the ΔT_c vs. H dependence in doped superconductors can be described by the formula (5.1), which includes a power law with an additional constant term. This finding indicates that the transition width of these samples exhibits a magnetic field dependence that follows a similar behaviour to what has been observed in other superconducting systems.

The extracted information from the magnetoresistance results of the Co-doped samples is summarized in Table 5.3. This table provides a concise overview of the superconducting transition temperature T_{c0} and the width of the transition ΔT (defined as $T_{c90\%}$ - $T_{c10\%}$) for each of the studied doping levels.

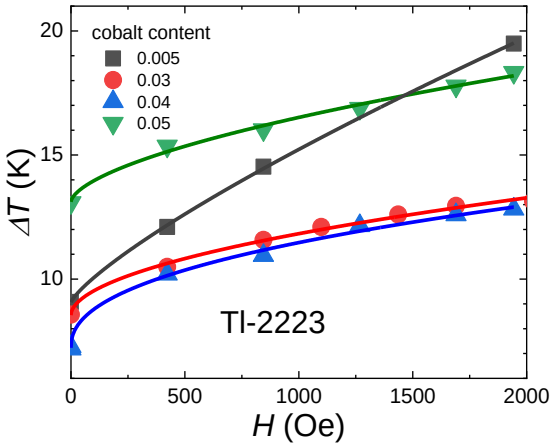

Figure 5.17: Magnetic field dependence of resistive transition width of bulk Tl-2223 samples doped with cobalt, after oxygenation. (x=0.005, Co67N; x=0.030, Co74N; x=0.040, Co73N; x=0.050, Co75N) [8]

Table 5.3 Resistive properties of cobalt doped bulk Tl-2223.

Cobalt content x	T_{c0} [K], H=0	ΔT ($T_{c90\%}$ -$T_{c10\%}$) [K]
0.005 (Co67N)	103.3	9.1 / 19.5 (1943.5 Oe)
0.030 (Co74N)	112.5	8.6 / 13.1 (2028 Oe)
0.040 (Co73N)	113.7	7.2 / 12.8 (1943.5 Oe)
0.050 (Co75N)	95.4	13.1/18.3 (1943.5 Oe)

**For example 9.1/19.5 means that transition width is 9.1 K without DC magnetic field and 19.5 K in magnetic field which strength is in brackets.*

Among doped superconductor samples only those with cobalt have T_c and transition width measured by $R(T)$. This is because after earlier measurements (AC susceptibility, SEM) cobalt doped samples seemed to exhibit best superconducting properties.

5.2.3 Choice of linear range of resistance

The resistance versus temperature relationship exhibits a zero resistance state below the superconducting transition temperature, while for temperatures well above the transition, the resistance shows a linear dependence, as discussed in Section 2.2. This characteristic is crucial for determining the critical exponent. The linear behaviour of $R(T)$ is typically observed in moderately doped CuO_2 planes, near the optimal doping level. However, selecting the appropriate linear region of $R(T)$ and understanding its impact on the critical exponents can be a challenging task, which will be further discussed below.

One approach is to select a wide temperature range to include a larger number of data points for a more accurate linear fit. On the other hand, a smaller temperature range allows for consideration of only those points with minimal deviations from linearity. A typical procedure for determining the linear part of $R(T)$ is illustrated in Fig. 5.18a, while the corresponding $log\ \Delta\sigma$ (additional conductivity) versus $log\ \varepsilon$ ($\varepsilon = (T - T_c) / T_c$) plot is shown in Fig. 5.18b. In this plot, three linear regions are indicated, each resulting in a different value of the critical exponent, depending on the

assumed temperature range of linearity. The calculated critical exponents λ are presented in Fig. 5.18c. It can be observed that the critical exponents do not vary significantly when the lower temperature limit (T_{lower}) of the linear range is above 165 K. Therefore, the temperature range of T_{lower} =165 K to T_{upper} = 300 K is considered optimal for Tl-1223 samples. This temperature range is also acceptable for Tl-2223 samples with a critical temperature similar to that of the Tl-1223 compound. Similar data for an oxygenated bulk sample of Tl-2223 are presented in Table 5.4, where T_{upper} is set to 280 K.

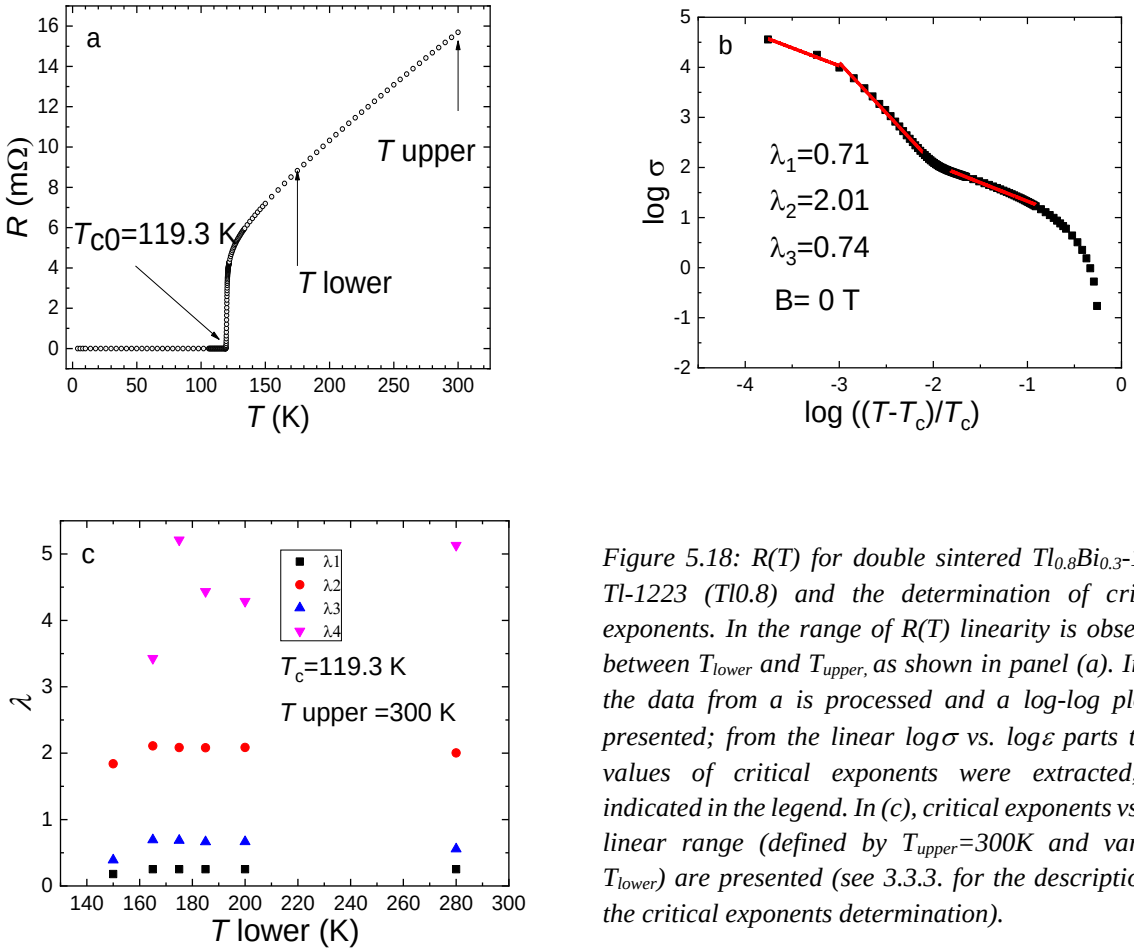

Figure 5.18: R(T) for double sintered $Tl_{0.8}Bi_{0.3}$-1223 Tl-1223 (Tl0.8) and the determination of critical exponents. In the range of R(T) linearity is observed between T_{lower} and T_{upper}, as shown in panel (a). In (b) the data from a is processed and a log-log plot is presented; from the linear logσ vs. logε parts three values of critical exponents were extracted, as indicated in the legend. In (c), critical exponents vs. the linear range (defined by T_{upper}=300K and various T_{lower}) are presented (see 3.3.3. for the description of the critical exponents determination).

The experiments conducted by the author consistently indicate that the linear region of resistance versus temperature above the superconducting transition is not influenced by the applied DC magnetic field. Therefore, it is reasonable to choose the linear range, and consequently the slope, of $R(T)$ measured in zero magnetic field. This slope, obtained in zero magnetic field, can then be utilized to calculate the critical exponents (λ) in non-zero magnetic fields. The methodology for this calculation will be presented in the following sections.

Table 5.4 Critical exponents calculated for oxygenated, bulk Tl-2223 sample in zero magnetic field. The exponents are calculated assuming various ranges of linearity of R(T) dependency.

Resistance linearity range		**Calculated critical exponent**	
Min temperature T_{lower} [K]	**Max temperature T_{upper} [K]**	**Near T_{c0}**	**Further above T_{c0}**
260	280	0.289	1.04
230	280	0.290	1.10
200	280	0.292	1.17
185	280	0.292	1.21
175	280	0.293	1.24
165	280	0.293	1.28
150	280	0.293	1.22
Published values*: (#59N)		0.259	1.13

**Published [13] values vary from testing values in the table because various sets of points might be chosen into regression in log-log charts.*

5.2.4 Critical exponent extracted from resistivity

The critical exponents and their magnetic field dependence were calculated based on the linear part of the log $\Delta\sigma$ vs. *log* ε plots. The magnetic field dependence of the conductivity (σ) and the critical exponents are presented in Fig. 5.19a and 5.19b, respectively. In the presence of a magnetic field, only two out of the three determined exponents are physically meaningful, as they yield positive system dimensionality. Notably, the most significant changes are observed at low magnetic field intensities (between 0 and 0.2 T). The values of all exponents exhibit minima at an applied magnetic field of 0.4 T, while the field dependence of the exponents becomes marginal for higher DC magnetic fields.

For the Tl-2223 superconductor, as shown in Fig. 5.20, two of the exponents are physically meaningful, while one exhibits a relatively high value. The exponent closer to T_{c0} is small, suggesting a dimensionality around 3. On the other hand, the exponent further from T_{c0} increases with magnetic field from 1.0 to 1.5, indicating a decrease in dimensionality from 2 to 1. In other words, close to T_c, the superconducting system behaves as 3D, but further away from T_c, the dimensionality of the system is reduced.

The curve slope indicates that both close and far from T_c the system, Tl0.8, is 2.5 dimensional whereas in the intermediate range the superconductor is granular (zero dimensional), Fig. 5.18b).

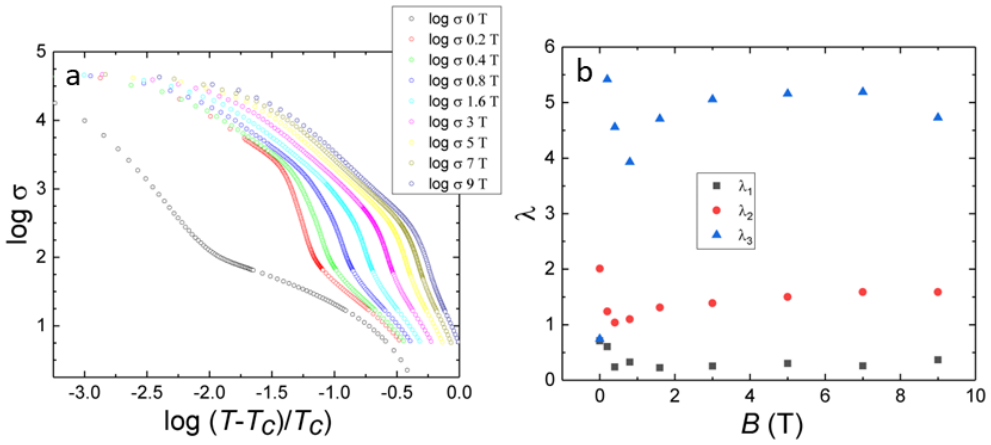

Figure 5.19: (a) Log $\Delta\sigma$ vs. log ε plots for in various DC magnetic fields of thallium cuprate sample double sintered $Tl_{0.8}Bi_{0.3}$-1223 (Tl0.8) are in panel (a). Panel (b) shows critical exponent values derived from the data.

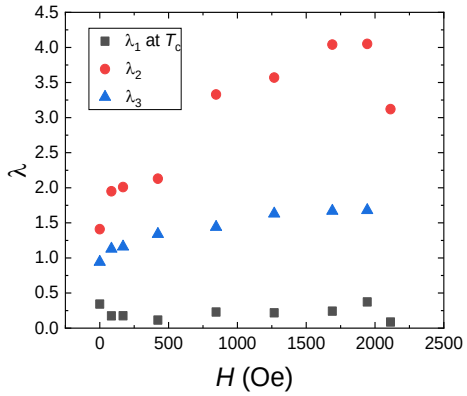

Figure 5.20: The critical exponents of oxygenated Tl-2223 bulk sample (p59N) estimated from three regions of resistivity, plotted as a function of external magnetic field. See text for details.

Figures 5.21a and 5.21b provide a comparison of the critical exponents for the same Tl-2223 bulk sample, calculated from the temperature dependence of resistivity (Fig. 5.21a) and susceptibility (Fig. 5.21b).

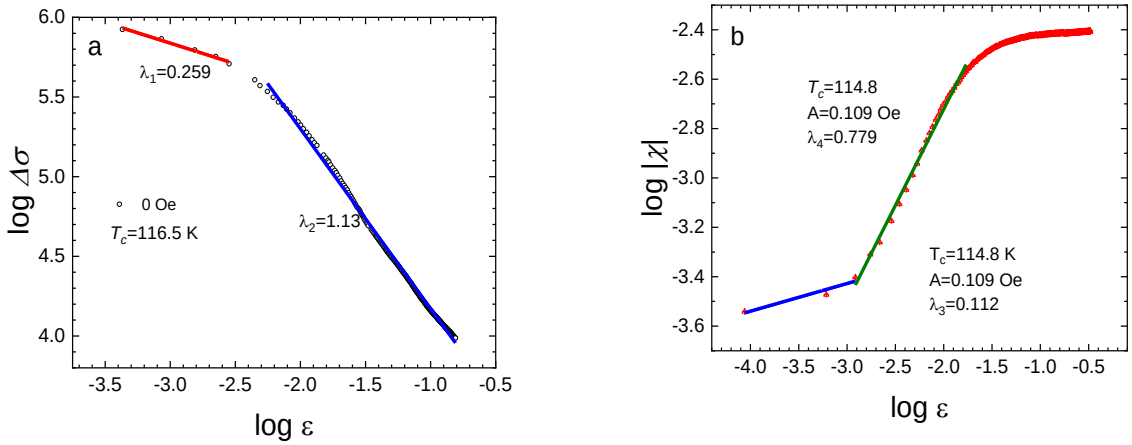

Figure 5.21: Log-Log plots (log $\Delta\sigma$ vs. log ε) for oxygenated Tl-2223 (#59N) sample of data obtained from conductivity (a), susceptibility (b) data. Linear regions from which the critical exponents are calculated are indicated [13].

The analysis reveals that the system exhibits 3D behaviour close to T_c, both below and above it. However, further from T_c, the system transitions to a 2D behaviour. This finding is consistent with the theoretical considerations of Prober regarding the dimensionality of layered superconductors [14].

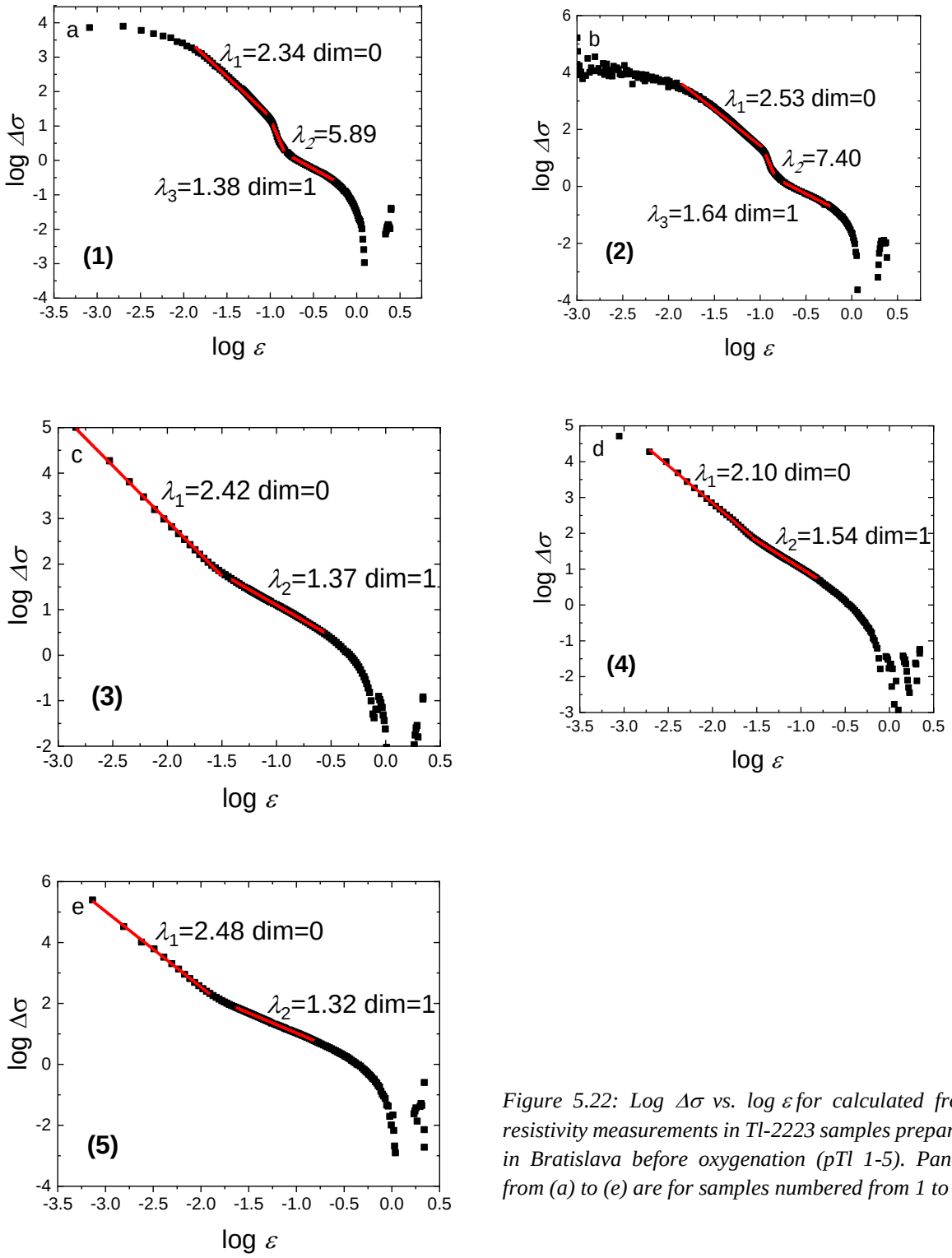

Figure 5.22: Log Δσ vs. log ε for calculated from resistivity measurements in Tl-2223 samples prepared in Bratislava before oxygenation (pTl 1-5). Panels from (a) to (e) are for samples numbered from 1 to 5.

The dimensionality of the Tl-2223 bulk superconductor prepared in a different manner in Bratislava (as shown in Fig. 5.22 and Table 5.5) and without oxygenation appears to be different. The analysis indicates that the system exhibits a granular (zero-dimensional) behaviour close to T_c, while transitioning to a one-dimensional behaviour further from T_c. This qualitative trend is observed in all five prepared samples. Notably, the log-log relationship for Tl-2223 before oxygenation tends to be convex (Fig. 5.22), whereas after oxygenation, it becomes concave (Fig. 5.21 a - pure Tl-2223 and Fig. 5.23 - cobalt-doped Tl-2223). It is worth mentioning that the samples studied before oxygenation were synthesized in Bratislava, while the results for the sample after oxygenation were obtained for samples synthesized in Krakow.

Table 5.5 Critical exponents extracted from R vs T measurements for samples prepared in Bratislava before their oxygenation. System dimensionality is indicated in brackets.

Samples	Critical exponent (system dimension)		
	Near critical temperature	Intermediate temperatures	Away from critical temperature
No 1 (pTl1)	2.34 (-0.0)	5.89	1.38 (1.2)
No 2 (pTl2)	2.53 (-0.3)	7.40	1.64 (0.7)
No 3 (pTl3)	2.42 (-0.1)		1.37 (1.3)
No 4 (pTl4)	2.10 (+0.4)		1.54 (0.9)
No 5 (pTl5)	2.48 (-0.2)		1.32 (1.4)

5.2.5 Critical exponents of doped Tl-2223

The temperature dependence of resistance in oxygenated Co-doped Tl-2223 samples is shown in Fig. 5.16, while the conductivity for the same samples, in the *log* σ vs. *log* ε parametrization, is shown in Fig. 5.23a-e. The calculated critical exponents, as listed in Table 5.6, suggest that in all samples except for x_{Co}=0.005, the dimension of the order parameter is 3D close to T_c. This is the only consistent feature observed across the different samples. However, further from T_c, the calculation fails as it yields unphysical values of the critical exponent, indicating a negative system dimension. In some temperature ranges far from T_c, the calculated system dimension is either one or two.

In the case of x_{Co}=0.005 (Fig. 5.16 a), $R(T)$ does not drop to zero below T_c, and the estimation of T_c itself can be done in two ways. Consequently, the critical exponent and the system dimensionality become vague and less meaningful in this particular case. It is worth noting that oxygenation affects the resistivity behaviour: the log σ vs. log ε relation of undoped Tl-2223 before

oxygenation tends to be convex (Fig. 5.22a-e), whereas it changes to concave after oxygenation, both for undoped (Fig. 5.21a) and Co-doped samples (Fig. 5.23a-e).

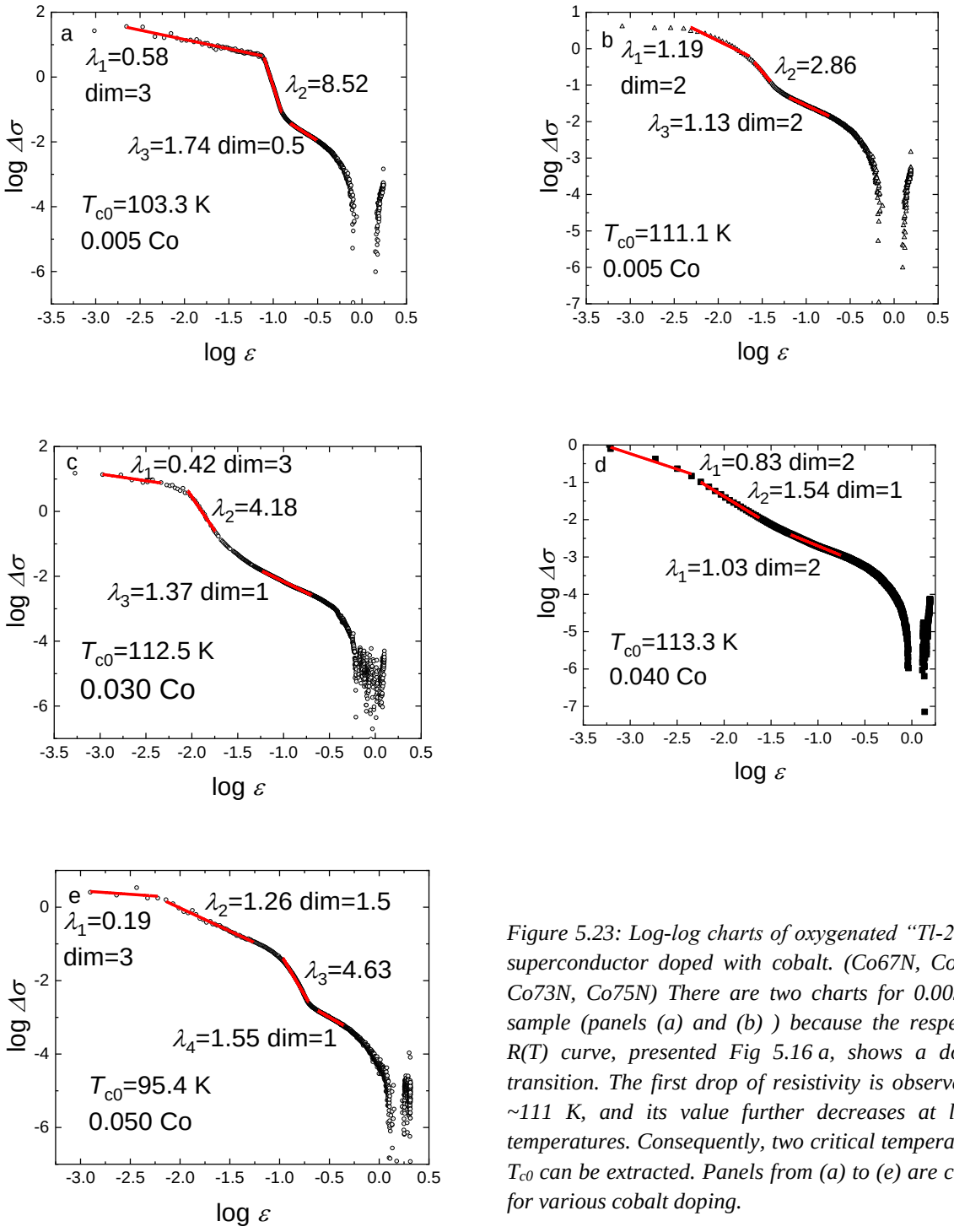

Figure 5.23: Log-log charts of oxygenated "Tl-2223" superconductor doped with cobalt. (Co67N, Co74N, Co73N, Co75N) There are two charts for 0.005 Co sample (panels (a) and (b)) because the respective R(T) curve, presented Fig 5.16 a, shows a double transition. The first drop of resistivity is observed at ~111 K, and its value further decreases at lower temperatures. Consequently, two critical temperatures T_{c0} can be extracted. Panels from (a) to (e) are charts for various cobalt doping.

Table 5.6 Critical exponents extracted from log-log charts of cobalt doped "Tl-2223" after oxygenation.

	Resistive critical exponents (system dimension)			
Cobalt content x (T_{c0})	**Close to T_{c0}; λ_1**	**λ_2**	**λ_3**	**Away from T_{c0}; λ_4**
0.005(103.3 K) (Co67N)	0.58 (2.6)	8.52	1.74 (0.5)	
0.005 (111.1 K) (Co67N)	1.19 (1.8)	2.86	1.13 (1.8)	
0.030 (112.5 K) (Co74N)	0.42 (2.9)	4.18	1.37 (1.3)	
0.040 (113.3 K) (Co73N)	0.83 (2.3)	1.54 (0.9)	1.03 (1.9)	
0.050 (95.4 K) (Co75N)	0.19 (3.2)	1.26 (1.5)	4.63	1.55 (0.9)

5.3 Critical current determination

This chapter focuses on presenting the critical current (j_c) in Tl-2223 samples that were grown under optimal conditions as discussed in Chapter 4. The optimization process was found to be complex, requiring multiple iterations of sample growth and measurements of various properties, including j_c, to achieve the desired sample properties. Given the importance of j_c as a test parameter for sample optimization, the author decided to include all the results of $j_c(T)$, including those obtained during intermediate steps of the preparation process. This is done to demonstrate that using j_c as an optimization parameter does not always lead to a unique direction or outcome.

The samples studied in this thesis are bulk superconductors with a granular structure, as evidenced by the SEM pictures presented in Figs 4.20a-e. It is important to note that only 20-40 wt% of the material is actually a superconductor, as determined from the XRD data. The granular structure of the samples allows them to be modelled as a matrix of Josephson junctions. This modelling approach is relevant due to the presence of multiple grains and the interplay between them in the superconducting phase.

The critical current density, j_c, plays a crucial role in the context of superconductor applications. However, it is not an intrinsic material property [15], as it strongly depends on the sample's preparation and subsequent processing. There are two methods commonly used to determine j_c: direct and contactless methods. In the direct method, a current is applied to the sample, and the critical current density is identified as the lowest current density at which a voltage drop, and thus the appearance of resistance, is observed in the sample.

In this thesis, the focus is on the contactless method for determining the critical current density using AC magnetic susceptibility. Among the various models available for j_c determination, the simplest one, known as the Bean model (described in Appendix B), was chosen. The Bean model

assumes that the lower critical field is zero and that the sample is uniformly filled with a constant eddy current density throughout its volume.

The Bean model, used in this thesis allows for the determination of j_c at a specific temperature. However, in order to compare results across different samples, an extrapolation of j_c to a specified temperature is necessary. In this thesis, the temperature chosen for extrapolation is 77.3 K.

The extrapolation is performed using a nonlinear fitting function based on the Ginzburg-Landau (GL) strong coupling limit, represented by the equation $j_c = j_{c0}(1-T/T_c)^n$ [16, 17], This fitting function involves three parameters: j_{c0}, n, and T_c. j_{c0} represents the critical current at absolute zero temperature, n is the exponent characterizing the temperature dependence of j_c, and T_c is the critical temperature of the superconductor.

To extrapolate the critical current to 77.3 K, the T_c needs to be determined first. It can be obtained from AC susceptibility data, either as the inter-grain temperature (lower value) or the intra-grain temperature (higher value), as discussed in section 3.3.1. It is worth noting that the choice of critical temperature for the extrapolation does not significantly affect the extracted value of j_c.

The j_c varies significantly depending on the synthesis and oxygenation processes undergone by the sample, even if the nominal elemental composition of the samples is the same. Additional thermal treatment in the presence of flowing oxygen can enhance or degrade the j_c of Tl-2223. The volatility of thallium (III) oxide and oxygen balance in the sample are important factors during the synthesis and oxygenation processes. Therefore, the critical current can serve as an indicator of the sample's preparation conditions. However, the influence of precursor quality was not considered in this thesis.

5.3.1 Description of performed experiments

Within the framework of this thesis, four experiments were conducted to investigate the j_c of undoped samples.

The **first experiment** aimed to compare the j_c in samples with different synthesis duration while keeping the synthesis temperature (880°C) and oxygen flow constant. The synthesis durations investigated were 20 minutes, 30 minutes, 40 minutes, and 50 minutes. After synthesis, the j_c was measured, and subsequently, all the samples underwent oxygenation under the same conditions (20 hours at 700°C).

The **second experiment** focused on comparing j_c in four samples of nominal Tl-2223 synthesized for 30 minutes under the same oxygen flow. The synthesis temperatures used were 860°C, 870°C,

880°C, and 900°C. After synthesis, the samples underwent oxygenation for 20 hours at 700°C, and the j_c measurements were repeated.

In the **third experiment**, the j_c was measured for Tl-2223 samples with varying degrees of oxygenation. The first version of the experiment involved synthesizing a nonstoichiometric Tl-2.2 2 2 3 sample, and j_c was determined for the as-prepared sample, after the first 20 hours of oxygenation, after two cycles of oxygenation, and after three cycles of oxygenation (20 hours each). However, the sample lost its superconducting properties after the third cycle of oxygenation, leading to the termination of the experiment. In the second version of the experiment, j_c measurements were conducted on a stoichiometric Tl-2223 sample (in terms of initial ingredients). The critical current was measured immediately after synthesis, after 20 hours of oxygenation, after 40 hours of oxygenation, and after two cycles of 20 hours of oxygenation. These two versions of the third experiment aimed to compare the behaviour of stoichiometric and nonstoichiometric Tl-2223 samples in terms of their critical currents.

In the **fourth experiment**, two Tl-2223 samples were synthesized using the same powder under optimal conditions (880°C, 30 min, oxygen flow). Each pellet was divided into four parts. Each part underwent a 20-hour oxygenation process, but the oxygenation temperature varied among the sample parts, ranging from 700°C to 820°C with an increment of 20°C. Two parts were oxygenated at the same temperature of 760°C to assess the reproducibility of the experiment.

Furthermore, the properties of bulk Tl-2223 samples doped with Co, Ni, and Gd were investigated with respect to the dopant concentration. After oxygenation, the critical current extrapolation to 77.3 K was performed for the Co-doped samples. Additionally, the critical current of Co and Ni-doped samples before oxygenation was also measured and analysed.

5.3.2 Results of j_c vs T studies

The results of the first experiment, conducted with a constant synthesis temperature of 880°C, are shown in Figs 5.24 and 5.27. On the other hand, the results of the second experiment, conducted with a constant synthesis time of 30 minutes, are presented in Figs 5.25 and 5.28. In these figures, panels (a) display the estimation of critical current using T_c extracted from the absorption part of the magnetic susceptibility (χ" vs. T), while panels (b) utilize T_c as a fitting parameter. It is worth noting that either the inter-grain T_c or the intra-grain T_c can be employed as an experimental parameter for j_c determination, and the determination of these two temperatures is demonstrated in Fig. 5.26. These critical temperatures will be used for the subsequent analysis of other results.

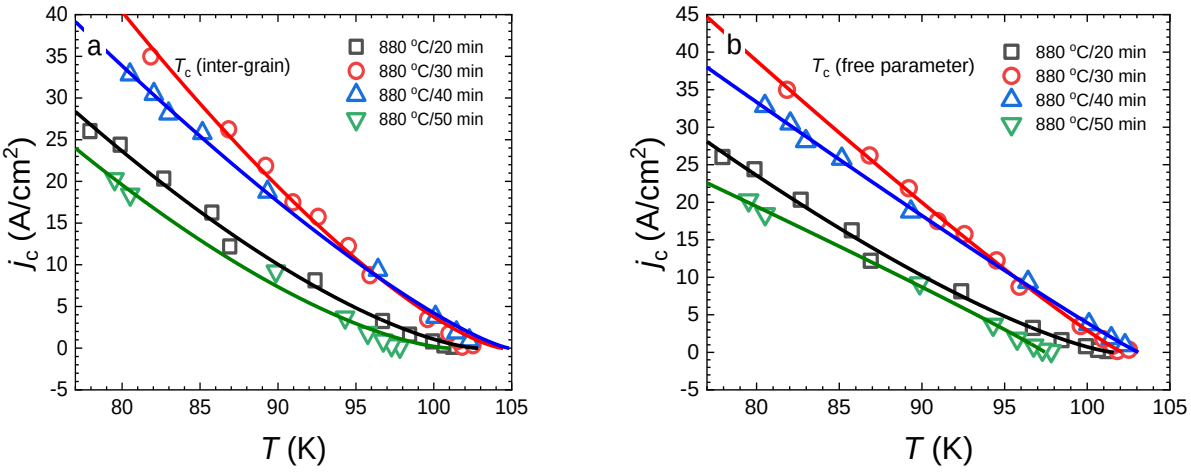

Figure 5.24: Critical currents of Tl-2223 synthesized at 880°C for various times (20 min-50 min). Panel (a) shows results of fitting with T_c fixed as T_c inter-grain. In panel (b) fits were obtained from changeable parameter of T_c. The lines are fit according to GL model. (#50B, #53B, #51A, #51B).

The presented results suggest that the critical current density, j_c, does not monotonically increase with the synthesis time, t_s, and the optimal synthesis time was found to be 30 minutes.

However, after oxygenation at 700°C for 20 hours the situation is more complicated, e.g. the absorption part of AC susceptibility is often split into at least two peaks what results in multiple values of critical current for the same samples. For the purpose of j_c (77.3 K) determination, high temperature peaks, subscribed as "*H*" (for "higher *T*") in figures below, are considered, since these values are more relevant to the intrinsic properties of samples (Figs 5.27 and 5.28).

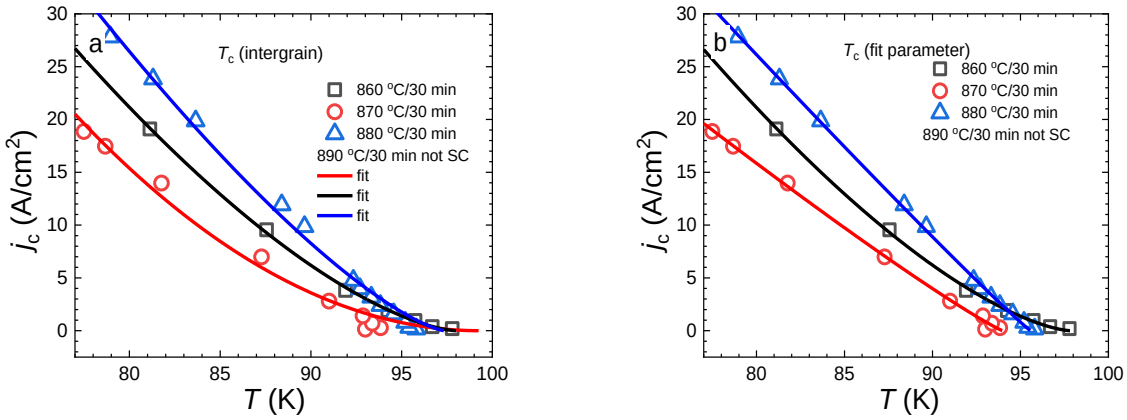

Figure 5.25: a, b: Critical currents of Tl-2223 synthesized at various temperatures (860°C-890°C) for 30 min. (#50A, #49A, #48B). Lines are the result of fitting according to GL model, but with different choice of fitting parameters: inter-grain T_c was fixed and j_{c0}, and the exponent n were fitted (a); T_c , j_{c0} and n were fitted (b).

As discussed in Chapter 4, oxygenation has significant effects on sample properties. In the case of the samples synthesized for 50 minutes, it can be observed that after oxygenation, they exhibit the highest critical current (as shown in Fig. 5.27). This indicates that the oxygenation process has a positive impact on the superconducting properties of the samples, improving their critical current performance. It is noteworthy that even though these samples were initially of lower quality before oxygenation, the optimization through oxygenation has resulted in enhanced superconducting characteristics, including higher critical currents.

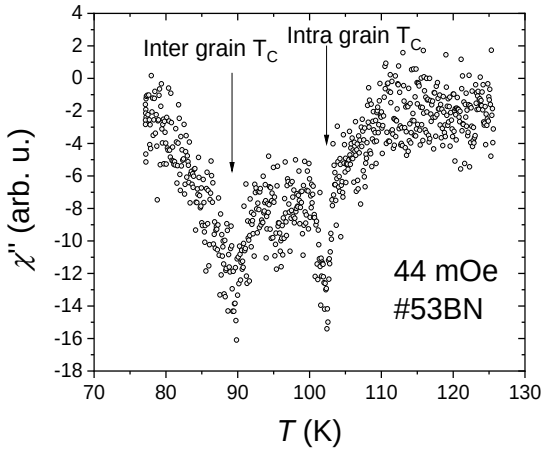

Figure 5.26: Typical curve of the absorption part of the AC susceptibility (χ'') near the superconducting critical temperature in cuprates. Multiple peaks can be identified. The j_c determined using the two T_c values (intra-grain and inter-grain) result in two values of extrapolated critical current.

In the case of the samples with a constant synthesis time of 30 minutes, a comparison of different synthesis temperatures reveals interesting findings. Initially, for these samples, the optimal synthesis temperature for achieving the highest critical current was 880°C, as shown in Fig. 5.25. However, it should be noted that the sample synthesized at 890°C exhibited signs of melting and did not exhibit superconductivity down to 77.3 K.

Interestingly, as shown in Fig. 5.28, after the oxygenation process, the situation is reversed. The sample synthesized at 890°C, which initially did not show superconductivity, demonstrated the highest critical current after oxygenation. On the other hand, the sample synthesized at 880°C, which initially had the highest critical current, experienced a decrease in critical current after oxygenation.

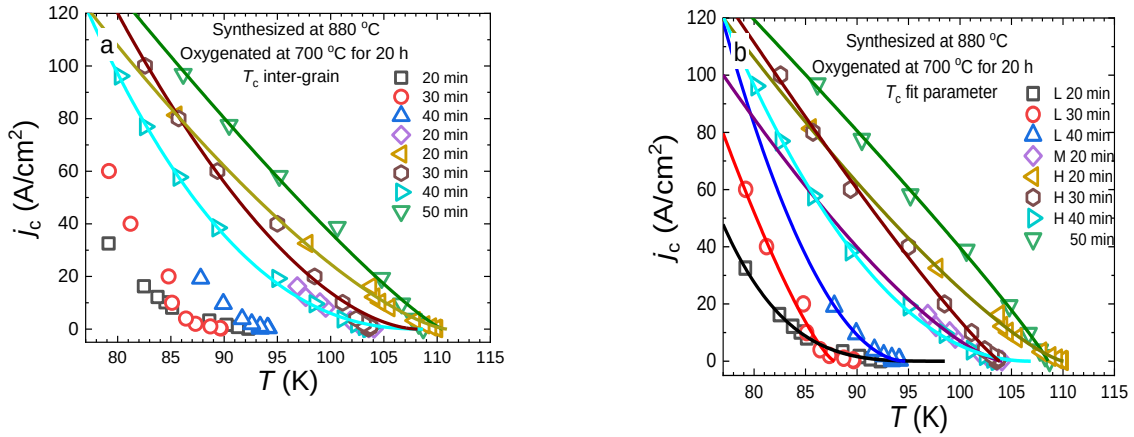

Figure 5.27: The critical current density as a function of temperature for Tl-2223 samples as in Fig. 5.24, but after oxygenation at 700 °C for 20 h. (#50BN, #53BN, #51AN, #51BN) The lines are fit according to GL model. Some χ'' charts are multipeak. j_c data from high temperature peak is subscribed H. M means j_c from medium peak and L means data from low temperature peak. The highest critical currents are obtained from high temperature peaks. Fits in panel (a) were performed for constant critical temperature – the inter-grain one. Fitting in panel (b) was performed with the use of 3 changeable parameters where T_c was one of them.

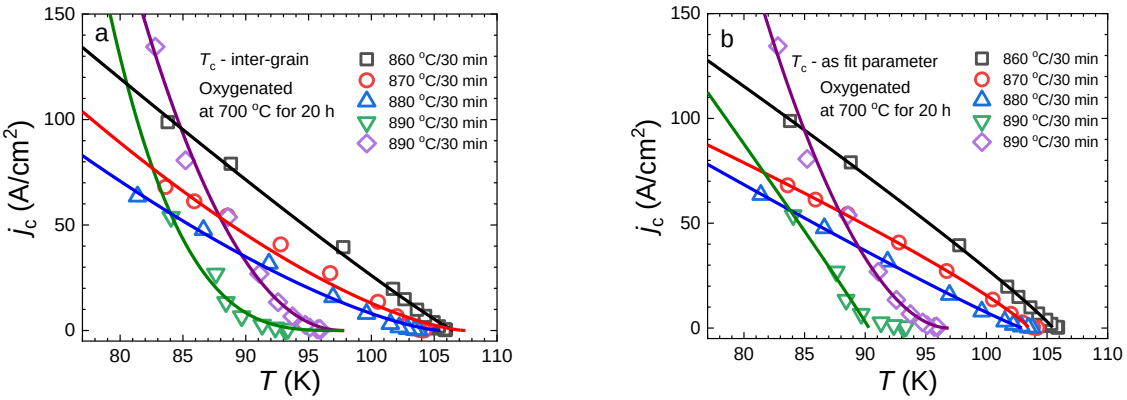

Figure 5.28: As Fig. 5.25 but for Tl-2223 oxygenated at 700 °C for 20 h. (p50AN, p49AN, p48BN, 49BN) The lines are fit according to GL model. Sample synthesized at 890°C has two absorption peaks in AC susceptibility, so there are two sets of data to determine critical current. Fitting in panel (a) was obtained from constant critical temperature – the inter-grain one. Fitting in panel (b) was obtained with use of 3 changeable parameters and T_c was one of them.

These results highlight the complex interplay between synthesis temperature, oxygenation, and the resulting critical current in Tl-2223 samples. It suggests that the optimal conditions for achieving high critical currents may differ before and after the oxygenation process.

In the third experiment, which involved varying the oxygenation time and using a nonstoichiometric sample, the initial sample with an excess of thallium exhibited a low critical current, similar to the stoichiometric samples (Fig. 5.29). However, after the first 20 hours of

oxygenation, there was a dramatic increase in the critical current, reaching 400 A/cm2. Subsequently, after the second 20 hours of oxygenation, the critical current further increased to 1310 A/cm2 (Fig. 5.29).

It is important to note that the third oxygenation resulted in a loss of superconductivity and the corresponding diamagnetic response above 77.3 K. As a result, it was not possible to measure the critical current after the third oxygenation due to the absence of superconductivity.

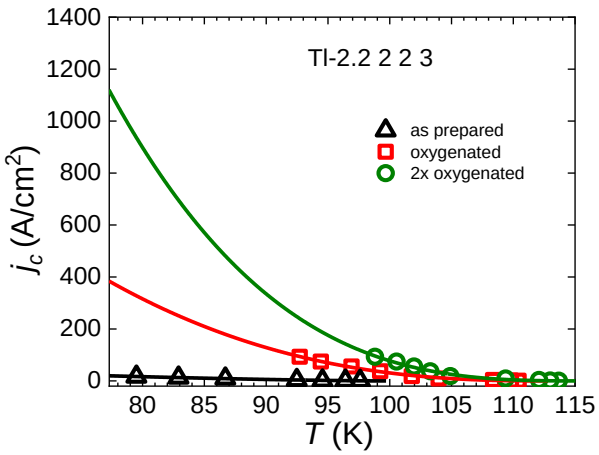

Figure 5.29: Critical currents of Tl-2.2 2 2 3 (#30) sample before oxygenation (black triangles), after single oxygenation (squares) and double oxygenation (circles) (#30a, #30aa, #30) The oxygenations at 740°C lasted 20 h each. The lines are fit according to GL model.[2]

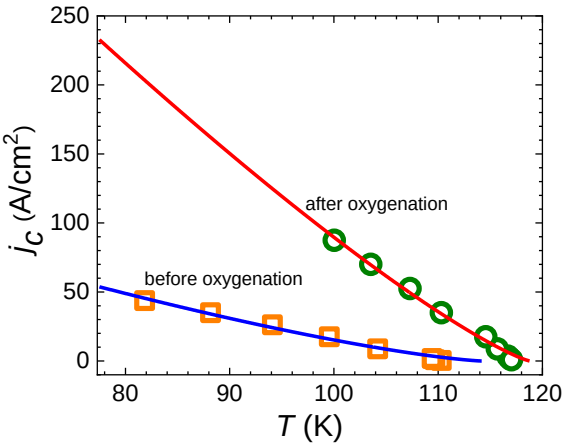

Figure 5.30: Critical current densities of Tl-2223 before and after oxygenation. (#25, #25a) The lines are fit according to GL model. [1]

After achieving satisfying results for the nonstoichiometric sample in terms of the critical current, the experiment was repeated for a stoichiometric sample of Tl-2223. In this case, a significant increase in j_c was observed after the first 20 hours of oxygenation, with the value rising from 50 A/cm^2 to 230 A/cm^2 (Fig. 5.30).

However, when the experiment was repeated for another stoichiometric sample labelled as #59, and the results of several treatments (before oxygenation, after 20 hours of oxygenation, after 40 hours of oxygenation, and after double 20 hours of oxygenation) were compared, different results were obtained. This is illustrated in Fig. 5.31, where it can be seen that the extrapolated j_c value to 77.3 K does not exceed 200 A/cm^2, regardless of whether one or two oxygenation cycles were performed. The original results of the AC susceptibility used for this analysis are presented in Fig. 4.24.

These findings suggest that for stoichiometric Tl-2223 samples, the optimal oxygenation time is shorter than 40 hours and does not necessarily require multiple oxygenation cycles to achieve the highest critical current.

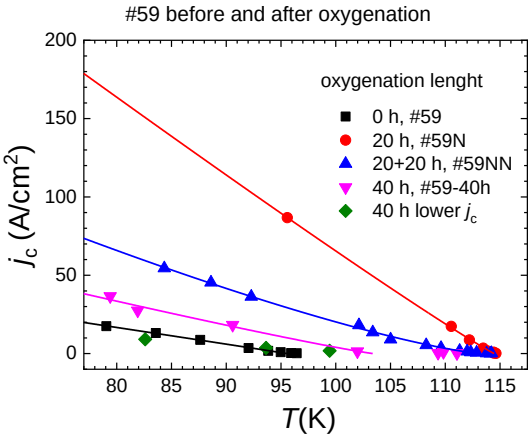

Figure 5.31: Temperature dependence of critical current for different oxygenation times for Tl-2223 sample (unoxygenated sample, #59; 20 h, #59N; 40 h, #59N-40h, and 20 h+20 h, #59NN).

In the fourth experiment, the dependency of j_c on the oxygenation temperature was investigated. The GL fitting curves of j_c for all oxygenated samples, except for the non-superconducting sample oxygenated at 820°C, are presented in Fig. 5.32 (for samples oxygenated at 700°C-760°C, referred to as series A) and in Fig. 5.33 (for samples oxygenated at 760°C-800°C, referred to as series B).

Series A and B correspond to two different pellets made from the same homogenous powder, synthesized under the same conditions but oxygenated at different temperatures. The graphs in Figs 5.32 and 5.33 illustrate the variation in j_c with different oxygenation temperatures for each series.

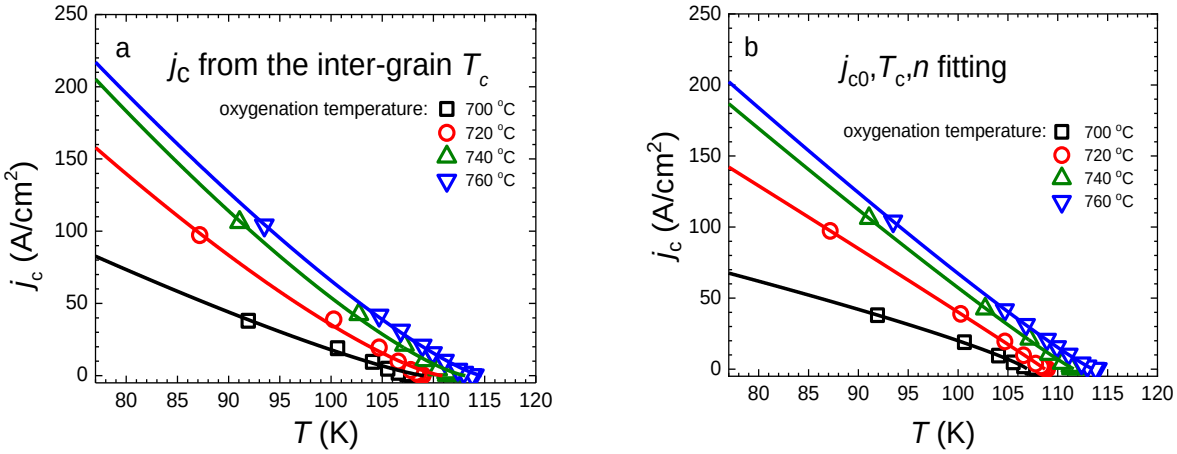

Figure 5.32: Critical current versus temperature dependency of Tl-2223 (series A, oxygenation 700°C-760°C). Fitting in panel (a) was obtained from constant critical temperature – the inter-grain one. Fitting in panel (b) was obtained with use of 3 changeable parameters and T_c was one of them. The lines are fit according to GL model. (p54AN700-760)

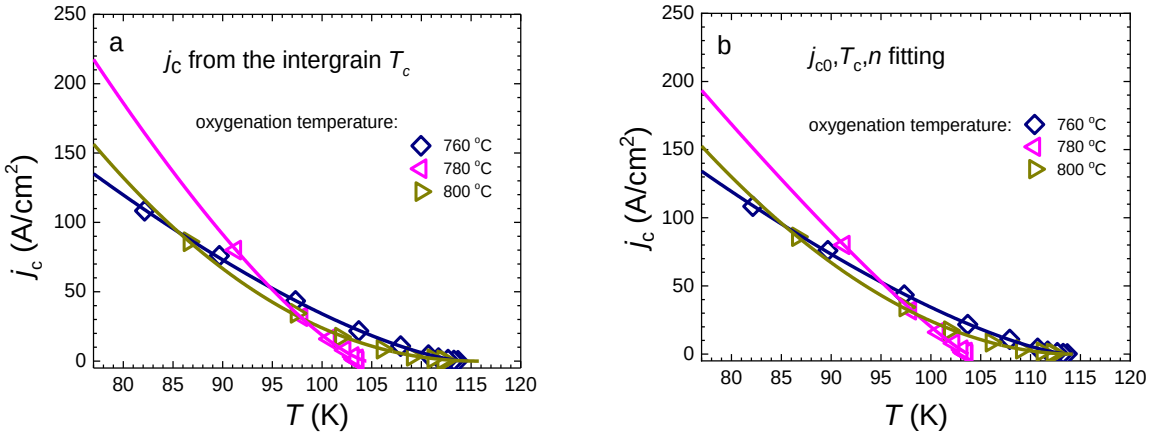

Figure 5.33: Critical current versus temperature dependency of Tl-2223 (series B, oxygenation 760°C-800°C). Fitting in panel (a) was obtained from constant critical temperature – the inter-grain one. Fitting in panel (b) was obtained with use of 3 changeable parameters and T_c was one of them. The lines are fit according to GL model. (#54BN760-800)

In Fig. 5.34, the values of critical current extrapolated to 77.3 K are summarized. It can be observed that the optimal oxygenation temperature, in terms of achieving the highest critical current, lies between 760°C and 780°C. The uncertainty in the optimal temperature can be estimated based on the difference between the results obtained from the two different approaches used to determine the critical current values. Specifically, the difference is approximately 15 A/cm^2 for an oxygenation temperature of 760°C and 25 A/cm^2 for an oxygenation temperature of 780°C.

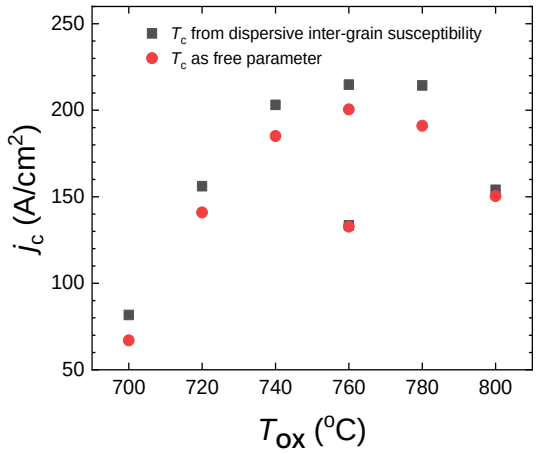

Figure 5.34: Critical currents depending on oxygenation temperature of Tl-2223. (#54AN700-760, #54BN760-800)[9]

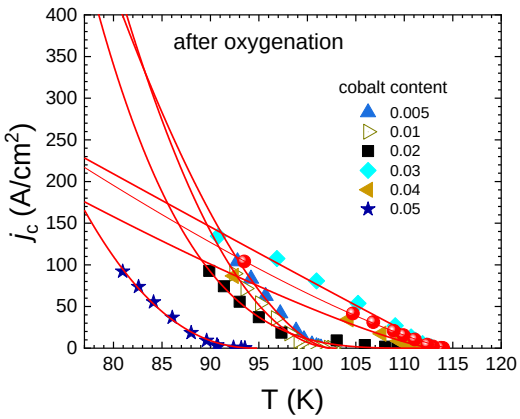

Figure 5.35: Critical current jc versus temperature with the fit based on GL approach for Co doped oxygenated Tl-2223. (Co67N, Co68N, Co72N, Co74N, Co73N, Co75N). The data for x=0 concerns p54AN760 (see Fig. 5.32 a) [8]

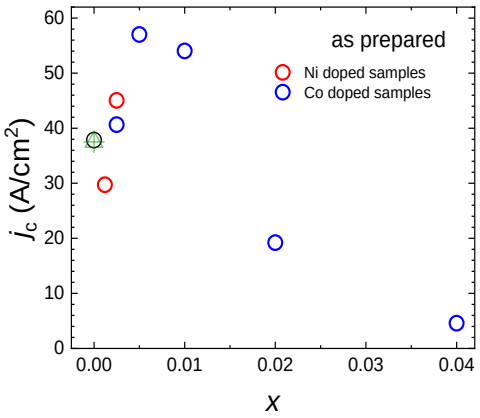

Figure 5.36: Critical current at 77.3 K versus Ni or Co concentration of Tl-2223 synthesized at 880°C for 30 minutes before oxygenation. Black circle is a reference sample x=0. Green triangle is the data from [9]. j_c of Ni doped Tl-2223 samples with x=0.0035, 0.0050 and 0.0100 is not displayed since no peak of susceptibility absorption part χ" down to 77.3 K was visible (only a part of the peak is visible for x= 0.0035 Ni). (#54, #65, Ni71, Ni63, Co66, Co67, Co68, Co72, Co73) Sample #65 – reference for Ni-doped and Co-doped series- had pour quality so its j_c was not depicted in the chart.

Furthermore, in Fig. 5.35, the temperature dependence of j_c for Co-doped Tl-2223 samples is presented. Generally, as discussed earlier the oxygenation increases the critical current. However, the value of j_c extrapolated 77.3 K decreases with increasing cobalt content. The exception is the reference sample without cobalt, where the j_c is lower compared to the general tendency. Furthermore, for samples with x_{Co}=0.030 and 0.040, the behavior of $j_c(T)$ is different, as the parameter n in the GL-based fitting is lower than for the other cobalt-doped samples.

Finally, in Fig. 5.36, the critical current extrapolated to 77.3 K for Ni and Co-doped samples before oxygenation is shown. For cobalt doping, there is an optimal cobalt content around x_{Co}=0.005 where the critical current is highest. On the other hand, the presence of nickel strongly suppresses superconductivity, as only the samples with the lowest nickel content exhibit measurable critical current. Samples with higher nickel content (x_{Ni}=0.0035, 0.0050, 0.0100) are not displayed because they do not show a peak maximum in the absorption part of AC susceptibility, making the determination of the critical current impossible.

5.4 Vibrating sample magnetometry

In Chapter 3.3.2, it was discussed that measurements of magnetization using Vibrating Sample Magnetometry (VSM) can be used to determine the critical temperature (T_c), full penetration field

at a given temperature (H_p), and critical current (j_c) of a superconductor such as Tl-2223. It is important to note that ceramic samples of Tl-2223 consist of superconducting grains and inter-grain regions, and these regions exhibit different properties.

The differences in properties between the grains and inter-grain regions are reflected in the hysteresis curves obtained from magnetization measurements. The hysteresis curve of the primary curve shows two distinct minima. The lower field minimum corresponds to the inter-grain regions, while the higher field minimum corresponds to the grains. This indicates that the penetration field and critical current in these regions are different from each other.

By analysing the hysteresis curves, information about the properties of both the grains and inter-grain regions can be obtained, providing insights into the behaviour of the superconductor at different magnetic field strengths.

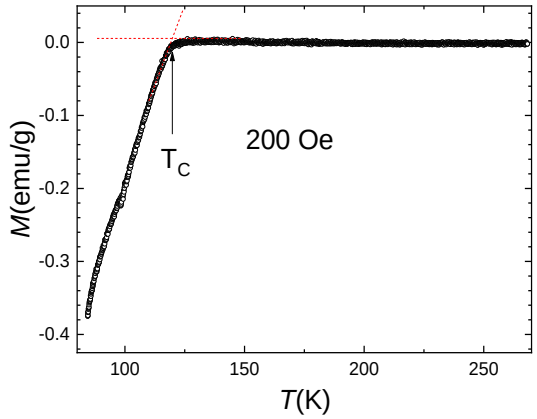

Figure 5.37: M(T) in H=200 Oe for not doped, oxygenated Tl-2223. T_c that can be drawn from this data is indicated. (#59N)

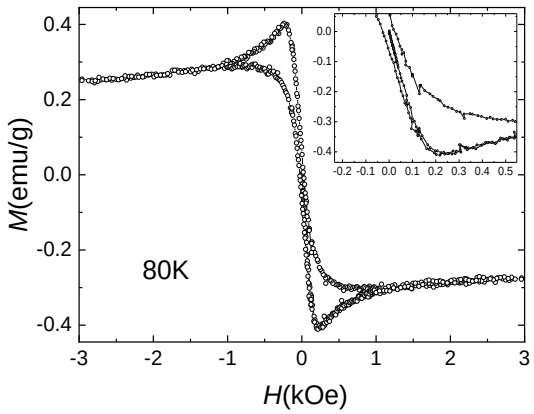

Figure 5.38: Hysteresis of the same sample as in Fig. 5.37 with the initial magnetization in the inset. (#59N)

The samples where H_p and j_c were estimated using VSM were primarily undoped $Tl_2Ba_2Ca_2Cu_3O_x$ and cobalt doped $Tl_2Ba_2Ca_2Cu_{3-x}Co_xO_{10}$. In preparation for the magnetization measurements, the Tl-2223 samples were cut and ground to obtain a cylindrical shape. The resulting samples had a height of approximately 2 mm and a diameter of 5 mm. It is important to note that these samples may contain impurities and other parasitic phases, as discussed in Chapter 4. However, these impurities typically produce very weak magnetic signals and are not considered in the current analysis of magnetization.

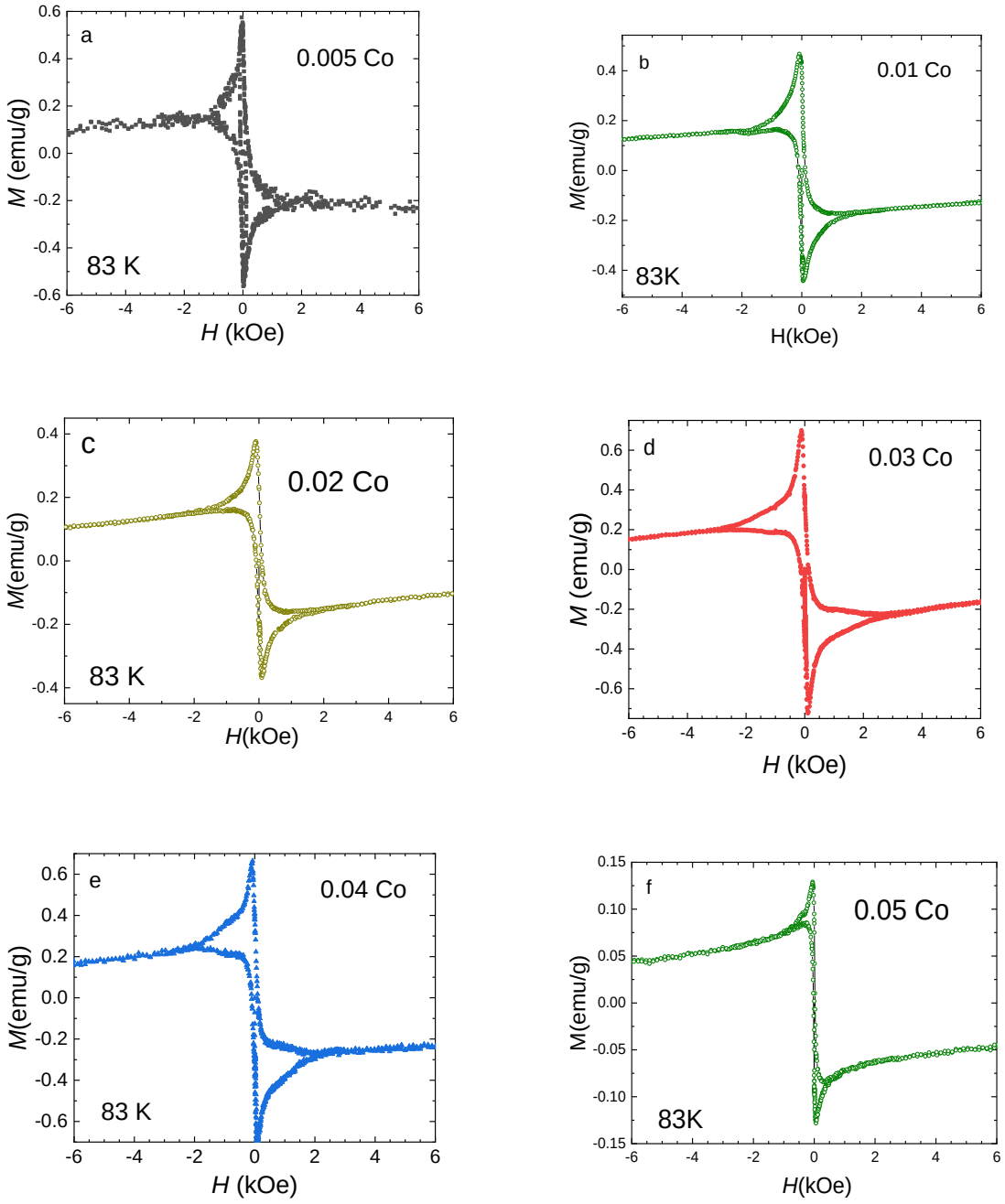

Figure 5.39: Hysteresis loops of bulk Tl-2223 doped with various cobalt doping and after oxygenation. Panels (a), (b), (c), (d), (e), and (f) are hystereses for various cobalt doping. (Co67N,Co68N, Co72N, Co74N, Co73N, Co75N)[8]

The $M(T)$ relationship is depicted in Fig. 5.37, showing the characteristic behaviour of magnetization with temperature. Below the critical temperature, as indicated in Fig. 5.37, the magnetization is negative (due to the Meissner effect) and increases linearly with rising temperature. Above the critical temperature, the magnetization approaches zero. Critical temperatures for both undoped and Co-doped samples were taken however from AC susceptibility

measurements, with T_c ranging from 112 K to 115 K, except for the sample with the highest Co doping (94.8 K) and the sample with the lowest cobalt doping (102.4 K). The specific values can be found in Table 5.7.

Figure 5.38 presents the intra-grain hysteresis loop for the undoped Tl-2223 sample, with the initial magnetization curve shown in the inset. Critical currents were determined from this relationship as well as from the inter-grain hysteresis (Figs 5.39 and 3.11).

Hysteresis loops of six Tl-2223 samples with varying cobalt content, as well as an undoped sample, were measured at temperatures ranging from 77 K to 83 K. These hysteresis loops are presented in Fig. 5.39. A comparison with the undoped sample is shown in Fig. 5.40, highlighting the impact of cobalt doping on the hysteresis behaviour. Additionally, the low-field hysteresis, which is used for determining the inter-grain critical current, is displayed in Fig. 5.41.

Finally, the primary curves for the Co-doped samples are presented in Figs 5.42a and 5.42b. These primary curves, as discussed in Chapter 3.3.2, provide information about the full penetration fields. The values of the full penetration fields for each sample are compiled in Table 5.7

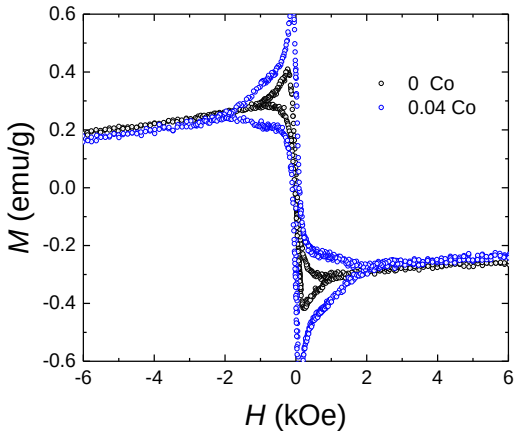

Figure 5.40: Comparison of cobalt doped and not doped Tl-2223 oxygenated bulk sample. (#59N and Co73N)

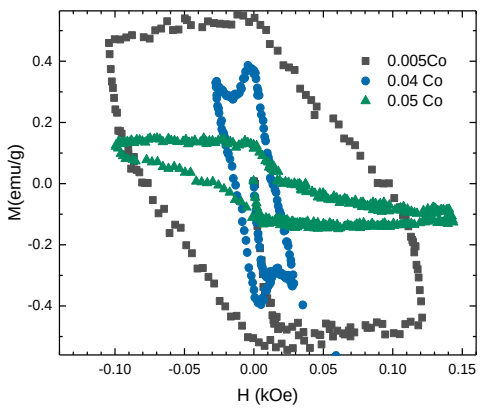

Figure 5.41: Low field VSM hysteresis of Tl-2223 samples doped with cobalt. (Co67N, Co73N, Co75N)

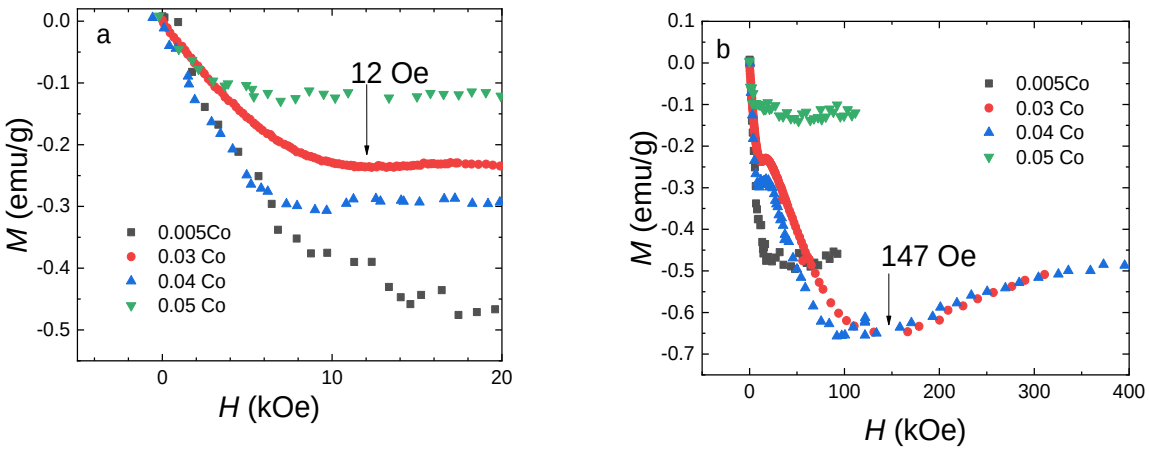

Figure 5.42: Primary magnetization curves of cobalt doped, oxygenated samples. Panel (a) shows inter-grain magnetism whereas panel (b) shows magnetism of interiors of grains. (Co67N, Co74N, Co73N, Co75N)

In particular, for the sample with x_{Co}= 0.030, the full penetration field of the inter-grain regions is approximately 12.0 Oe, whereas the full penetration field for the grains of this sample reaches 146.7 Oe (Fig. 5.42a and 4.42b, respectively; Table 5.7). It can be observed that, except for two samples (x_{Co}=0.020 and x_{Co}=0.000), the full penetration fields of the grains tend to decrease with increasing cobalt content. The addition of cobalt Favours the penetration of the magnetic field into the inter-grain regions of the sample and suppresses superconductivity.

From the higher field hysteresis curves, as shown in Fig. 5.40 for the Co-doped sample and Fig. 5.38 for the pristine sample, the intra-grain critical current was determined by measuring the change in magnetization (ΔM) in a magnetic field of 1 kOe (see Chapter 3.3.2). The critical current was obtained by averaging the results for both positive and negative magnetic fields. Among the samples, the highest critical current of 155 kA/cm^2 was observed in the grains of the 0.030 Co sample (Table 5.8). The critical currents of the grains in the other samples ranged from 15.4 kA/cm^2 to 155 kA/cm^2, without a clear monotonic trend with respect to cobalt concentration. It is worth noting that the sample with the highest doping level, x=0.050, did not exhibit superconductivity in a 1 kOe field.

Note that hysteresis loops used here for critical current determination were measured at relatively high temperature. Therefore, the error bar for the determined critical currents may be substantial. The hysteresis have triangular, rather than trapezoidal shape. Critical current determination has sense only for a given applied magnetic field.

Trapped magnetic flux is yet another parameter that can be extracted from the hysteresis loops. For example, for Co doped sample with x_{Co}=0.030, the trapped magnetic flux after removing the

external magnetic field (H=0) corresponds to the magnetization of 0.39 emu/g as measured by VSM (Fig. 5.39d). Generally, the trapped magnetic flux extracted from the intra-grain parameters for Co doped samples is in the range of 0.09-0.55 emu/g, and 0.12-0.55 emu/g for the inter-grain parameters. For the samples with the extreme doping levels, x_{Co}=0.050 and x_{Co}=0 the intra-grain flux is however much smaller, corresponding in both cases to approximately 0.085 emu/g. Furthermore, the inter-grain trapped magnetic flux for 0.005 Co and 0.040 Co is comparable 0.53 and 0.54 emu/g.

All the data drawn from $M(T)$ and hysteresis loops measurements are presented in Tables 5.7 and 5.8, respectively.

Table 5.7: Parameters extracted from VSM measurements of $Tl_2Ba_2Ca_2Cu_{3-x}Co_xO_{10}$.

Co doped Tl-2223			**Intra-grain parameters**				**Inter-grain parameters**			
X	T [K]	T_c [K]	M span [emu/g]	H span [Oe]	H_p [Oe] Full penetration field	Trapped magnetic flux emu/g (H=0)	M span [emu/g]	H span [Oe]	H_p [Oe] Full penetration field	Trapped magnetic flux emu/g (H=0)
0.000	80	114.8	0.8189	2442	229.3	0.086	--	--	--	--
0.005	83	102.4	1.1409	2709	479.7	0.5528	1.1021	249.1	21.7	0.5401
0.010	83	112.9	0.9061	3922	425.6	0.3810	--	--	15.0	--
0.020	83	112.2	0.7474	4040	119.9	0.2243	--	--	11.5	--
0.030	77	113.5	1.4227	6578	146.7	0.3874	--	--	12.0	--
0.040	83	112.8	1.3662	5080	101.0	0.4031	0.7835	55.9	9.6	0.5329
0.050	83	94.8	0.2553	1851	57.7	0.0849	0.2795	239.9	7.1	0.1213

- Span is the difference between maximal and minimal value of M(emu/g) or H(Oe)

Table 5.8:Intra-grain critical currents of $Tl_2Ba_2Ca_2Cu_{3-x}Co_xO_{10}$ read from hysteresis loops

X	**M span(1 kOe) [emu/g]**	**d [cm]**	**j_c [kA/cm^2]**
0.000	0.0110	0.10	15.4
0.005	0.0670	0.12	75.8
0.010	0.0370	0.23	21.6
0.020	0.0290	0.18	21.9
0.030	0.1370	0.12	155.0
0.040	0.1388	0.19	99.2
0.050	0.0	0.22	0

*Tl-2223 grain density was assumed to be 6.79 g/cm^3

5.5 Specific heat measurements

Superconducting phase transition is reflected in a peak in the heat capacity at the critical temperature. However, in high-T_c superconductors in general, and in Tl-based superconductors in particular, the specific heat jump is small compared to the total specific heat value. This is because the main contribution to the specific heat comes from the lattice, while the jump in specific heat is due to the electronic contribution.

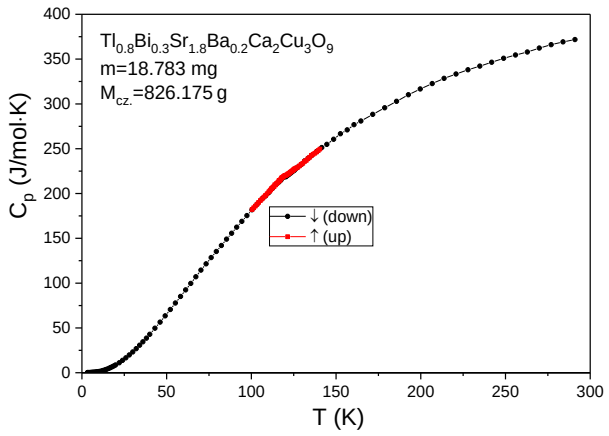

Figure 5.43: Specific heat of Tl-0.8Bi-0.3 223 bulk sample. (Tl0.8)

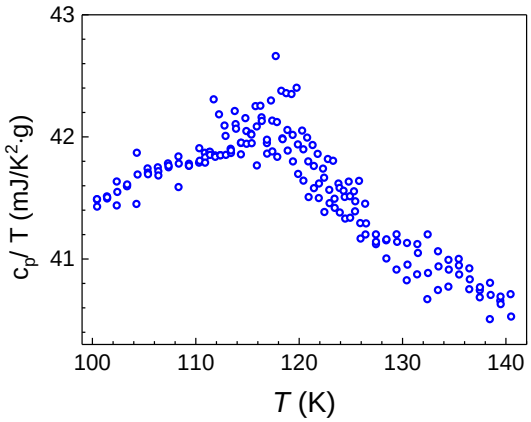

Figure 5.44: Specific heat jump of Tl-0.8Bi-0.3 223 bulk sample. (Tl0.8)

Specific heat measurements were performed using a Physical Property Measurement System (PPMS) in the temperature range from 4 K to 300 K. Three samples were investigated: as-grown and oxygenated Tl-2223 samples, as well as a Tl-0.8Bi-0.3 2 2 3 sample. While no clear peak was observed in the specific heat data for the Tl-2223 samples, a distinct anomaly at T_c was observed for the Tl-0.8Bi-0.3 2 2 3 sample. The results are presented in Fig. 5.43, and after subtracting the heat capacity baseline, they are also shown in Fig. 5.44 in the form of C_p/T vs. T. These results were then used to estimate the critical exponents in log-log plots below (Fig. 5.45a) and above (Fig. 5.45b) the critical temperature.

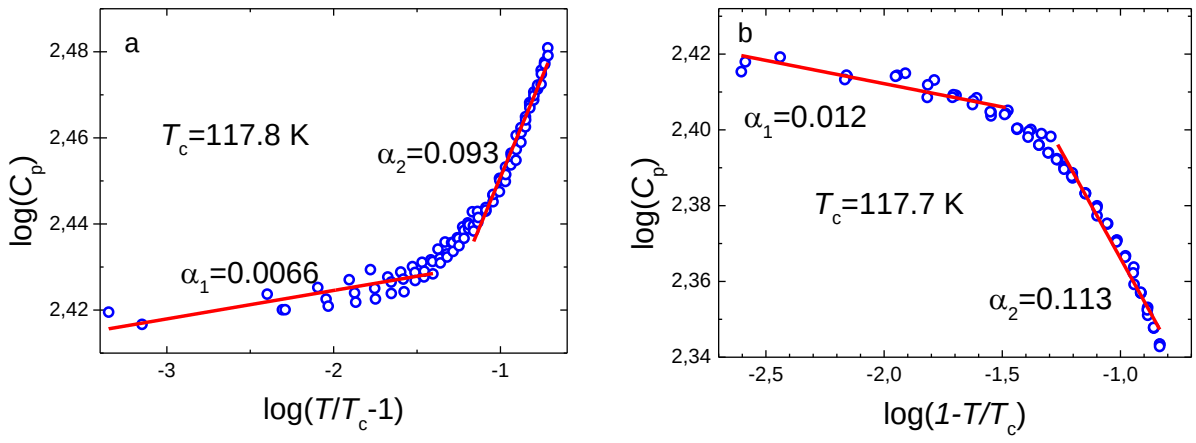

Figure 5.45: Log-log charts of specific heat of Tl-0.8Bi-0.3 223 bulk superconductor sample above (a) and below (b) T_c. (Tl0.8)

Literature:

1. M. Giebułtowski *et al*., Critical currents of $Tl_2Ba_2Ca_2Cu_3O_z$ bulk superconductors, Acta Physica Polonica A **135** (1), 24-27 (2019) doi: 10.12693/APhysPolA.135.24
2. M. Giebułtowski *et al.*, Critical currents and critical temperature of Tl-2223 bulk superconductors, Proceedings of SPIE – The International Society for Optical Engineering **11054**, 110540K (2019) doi: 10.1117/12.2525433
3. P. Hohenberg and B. Halperin, Theory of dynamic critical phenomena, Reviews of Modern Physics **49** (3), 435 (1977) doi: 10.1103/RevModPhys.49.435
4. C. Lobb, Critical fluctuations in high-T_c superconductors, Physical Review B **36** (7-1), 3930 (1987) doi: 10.1103/PhysRevB.36.3930
5. W. Woch *et al.*, Electrical conductivity and magnetic susceptibility of thallium 1223-based superconductor in the fluctuation range, Journal of Superconductivity and Novel Magnetism **32** (2), 159-165 (2019) doi: 10.1007/s10948-018-4697-5
6. C. Bean, Magnetization of hard superconductors, Physical Review Letters **8** (6), 250-253 (1962) doi: 10.1103/PhysRevLett.8.250
7. C. Bean, Magnetization of high-field superconductors, Reviews of Modern Physics **36** (1), 31-39 (1964) doi: 10.1103/RevModPhys.36.31
8. M. Giebułtowski *et al.*, Cobalt substitution effects on critical current, inter-grain full penetration field, and critical temperature study for Tl2Ba2Ca2Cu3-xCoxOy bulk superconductor, where x is from 0.005 to 0.050, Ceramics International **47** (13), 18998-19006 (2021) 10.1016/j.ceramint.2021.03.244
9. M. Giebułtowski *et al.*, Dependence of oxygenation temperature on critical temperature and current for $Tl_2Ba_2Ca_2Cu_3O_x$, Acta Physica Polonica A **137** (5), 803-806 (2020) 10.12693/APhysPolA.137.803
10. M. Tinkham, Resistive transition of high-temperature superconductors, Physical Review Letters **61** (14), 1658-1661 (1988) doi: 10.1103/PhysRevLett.61.1658
11. W. M. Woch *et al.*, Effects of magnetic field on resistive transition of thin film thallium based superconductors, Acta Physica Polonica A **106** (5), 785-791 (2004) doi: 10.12693/APhysPolA.106.785
12. W. M. Woch *et al.*, Temperature and field dependence of critical currents, resistances and irreversibility fields of a $(Tl_{0.6}Pb_{0.24}Bi_{0.16})(Ba_{0.1}Sr_{0.9})_2Ca_2Cu_3O_y$ film on single-crystalline lanthanum aluminate, Physica C **434** (1), 17-24 (2006) doi: 10.1016/j.physc.2005.11.012

13. M. Giebułtowski *et al.*, Resistance and Susceptibility of ceramic $Tl_2Ba_2Ca_2Cu_3O_x$ superconductor in the critical region, Acta Physica Polonica A **138** (5), 744-747 (2020) doi: 10.12683/APhysPolA.138.744
14. D. Prober, M. Beasley, and R. Schwall, Fluctuation-induced diamagnetism and dimensionality in superconducting layered compounds: TaS_2 $(pyridine)_{1/2}$ and $NbSe_2$, Physical Review B **15**, 5245-5261 (1977) doi: 10.1103/PhysRevB.15.5245
15. M. Murakami, Processing of Bulk YBaCuO, Superconductor Science and Technology **5**, 185-203 (1992)
16. W. M. Woch *et al.*, Properties, magnetic susceptibility, critical currents and irreversibility fields of $(Tl_{0.5}Pb_{0.5})Sr_2(Ca_{1-x}Gd_x)Cu_2O_z$ bulk superconductors, Superconductor Science and Technology **21** (8), 085002 1-7 (2008) doi: 10.1088/0953-2048/21/8/085002
17. [Bartolf] H. Bartolf, Fluctuation mechanisms in superconductors, Springer Fachmedien Wiesbaden, (2015) isbn: 9783658122461

6. Summary and conclusions

The focus of this PhD thesis is on the synthesis and characterization of $Tl_2Ba_2Ca_2Cu_3O_x$ (Tl-2223) cuprate bulk superconductors and their variants doped with ferromagnetic elements (Co, Ni, Gd). The main objective was to optimize the synthesis process and investigate the superconducting properties of the materials with and without doping.

The synthesis process for Tl-2223 bulk superconductors was developed, with optimal conditions involving heating the precursor materials ($BaCuO_2$, Ca_2CuO_3, and Tl_2O_3) in an oxygen atmosphere at temperatures ranging from 860°C to 890°C for a duration of 20 to 50 minutes. It was observed that wrapping the reagents in silver foil during synthesis is necessary to obtain a thallium superconductor. It is because the silver coating helped maintain oxygen saturation while minimizing thallium loss.

Post-synthesis oxygenation proved to be crucial for further enhancing the superconducting properties of the samples. Oxygenation was performed at temperatures in the range of 760°C to 780°C for a duration of 20 hours. This step had a significant influence on the critical temperature (T_c) and other superconducting characteristics, including the width of the superconducting transition (ΔT_c).

Chapter 5 of the thesis presents a comprehensive characterization of the achieved materials, employing various techniques to investigate their properties. The critical temperature, T_c, and the width of the transition, ΔT_c, were determined through AC susceptibility, resistivity, and magnetization measurements. The full penetration magnetic field (H_p) was utilized in magnetization experiments to gain insights into the granular structure of the superconducting samples. The critical current density (j_c), a crucial parameter for technological applications, was studied using AC susceptibility versus temperature, resistance, and magnetization measurements. The study also included measurements of magnetoresistance to examine the influence of magnetic fields on the superconducting properties. Furthermore, specific heat measurements were conducted to provide quantitative characterization of the transition to the superconducting phase.

Furthermore, the investigation expanded to include the effects of doping stoichiometric $Tl_2Ba_2Ca_2Cu_{3-x}M_xO_{10}$ superconductors with ferromagnetic dopants M, which were Co, Ni, and Gd. The presence of nickel in the quantity of $x_{Ni} > 0.0035$ was found to suppress superconductivity in the bulk samples, resulting in the absence of possibility of j_c determination at temperatures down

to 77 K. On the other hand, the addition of cobalt initially increased j_c for doping level of up to x_{Co}= 0.005, however, further increase of cobalt concentration significantly decreased j_c. The critical temperature was decreasing with cobalt concentration.

The oxygenated samples, $Tl_2Ba_2Ca_{2-x}M_xCu_3O_{10+\delta}$, exhibited a decrease in j_c with increasing cobalt content. Interestingly, the intra-grain $M(H)$ hysteresis for oxygenated samples did not appear to depend on the cobalt concentration for $x_{Co} < 0.050$. The critical temperature for x_{Co}=0.03 and x_{Co}=0.04 was considerably higher than for x_{Co}=0.005 and x_{Co}=0.050. In the case of gadolinium-doped samples, the critical temperature decreased with increasing gadolinium concentration. In terms of the highlights, the Tl-2.2 2 2 3 sample (#30aa) achieved the highest, excellent critical current density of 1310 A/cm^2, after the sample was oxygenated for 20 hours twice.

Finally, two critical exponents, α and λ, were determined from the experimental data. The α exponent, calculated from the specific heat versus temperature dependence, is expected to be zero in the 2D or 4D Ising model (for 3D α=0.11), resulting in a logarithmic function for the specific heat. This exponent is temperature-dependent, and two regimes can be identified both below and above T_c. On the other hand, the λ exponent characterizes quantities proportional to the square of the absolute value of the order parameter. It can be extracted from the temperature dependence of both resistance and magnetic susceptibility. Additionally, the value of λ provides insights into the dimensionality of the superconducting system. By analyzing resistance and susceptibility measurements, the author was able to determine whether the samples, prepared under specific conditions and measured within a certain temperature range, exhibited spatial, layered, whisker, or granular properties. These properties are indicative of the dimensionality of the system, which can range from 3D to 0D.

The investigated Tl-2223 samples exhibited granular behaviour (0D) near T_c prior to oxygenation. However, the dimensionality of the samples transitioned to a whisker-like behavior (1D) away from T_c. Interestingly, after oxygenation (including both pure and cobalt-doped samples), the Tl-2223 samples displayed a 3D nature in the vicinity of T_c, while exhibiting lower dimensionality further away from T_c. This observation highlights the complex interplay between oxygenation and dopant effects on the dimensional characteristics of the superconducting samples.

In conclusion, this research has yielded valuable insights into the synthesis and characterization of Tl-2223 superconductors and their doped variants. The optimized synthesis conditions, along with additional thermal treatment and the utilization of comprehensive characterization techniques, have significantly contributed to a deeper understanding of the superconducting

properties of these materials. The findings obtained from this study provide a foundation for future developments in the synthesis of single crystals of Tl-2223 and related compounds. Furthermore, further investigations and refinements in the synthesis and characterization procedures are recommended to fully unlock the potential of these materials for both scientific and technological applications. A noteworthy discovery from this research is the indication that superconductivity in cuprates may exhibit a three-dimensional nature, despite the clearly two-dimensional crystal structure of these compounds. This significant observation is expected to stimulate further theoretical investigations in the pursuit of formulating a comprehensive theory of unconventional superconductivity.

7. Appendix

A. Appendix - Furnace temperature calibration

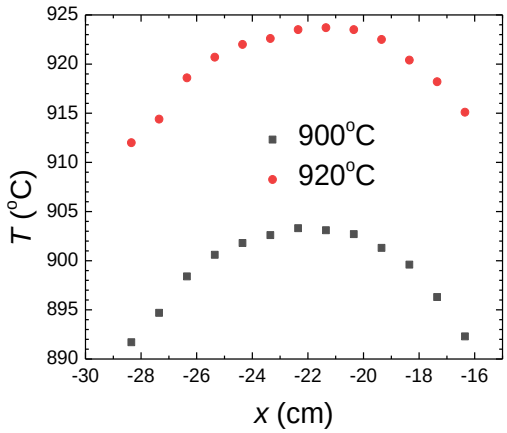

Figure A1: Furnace temperature T versus position of measurement x conducted with K-type thermocouple.

The length of the tube furnace used in the experiment is 49.15 cm, with the position being measured from one of the furnace ends. In Fig. A1, the points represent the temperatures indicated by the K-type thermocouple. The temperatures mentioned in the legend correspond to the set-temperatures displayed by the furnace controller. The observed asymmetry is attributed to the presence of room temperature oxygen gas, which was supplied from the left end of the furnace, corresponding to the higher negative numbers in Fig. A1. The measurement was carried out using a K-type thermocouple.

Appendix B. - Bean's method of magnetic field penetration

Bean [1] and London [2] introduced the critical state model to describe type II superconductors. The model proposes that when a magnetic field is applied to the superconductor, it induces eddy currents within the sample. These eddy currents are critical, denoted as j_c, and they flow in the sample to counteract the external magnetic field. In this model, the first critical field is assumed to be zero, meaning that the sample gradually allows the penetration of an arbitrarily small magnetic field.

Based on this, Bean illustrated how magnetic field penetrates into the sample. This model describes type II superconductor magnetization curves under assumption that critical current density does not depend on B. j_c controls the magnetic flux in the sample according to the formula: $dB/dx=\mu_0 j_c$ once magnetic field strength H is applied (see fig. B1 adapted from [3]). Superconducting critical current density creates M that, while H is increasing, opposes H, making B initially zero. With increasing H, B gradually penetrates the sample. Once $H=H_p=j_c d/2$ the whole sample is penetrated and from that time on M is constant (and equal to $M=- j_c d/4$). If now the H lowers, the slope of B(x) is reversed and once $H= j_c d$, M starts to be positive stabilizing at $M= + j_c d/4$ forming hysteresis loop as presented in Fig. B1d.

Observation of either H_p or the jump in M allows calculating the critical current j_c. Alternatively, j_c can be calculated from the imaginary part of AC susceptibility measured in various alternating magnetic fields H_{ac}. Penetration field H_p at certain temperature T is that H_{ac} for which χ" has a maximum at T. As above, $j_c=2H_{ac}/d$ if the sample thickness d is sufficiently small.

Although the Bean's model only approximately describes real experimental data, this is widely used to calculate j_c. Also in this thesis a critical current is drawn from field of full penetration, $j_c=2H_p/d$.

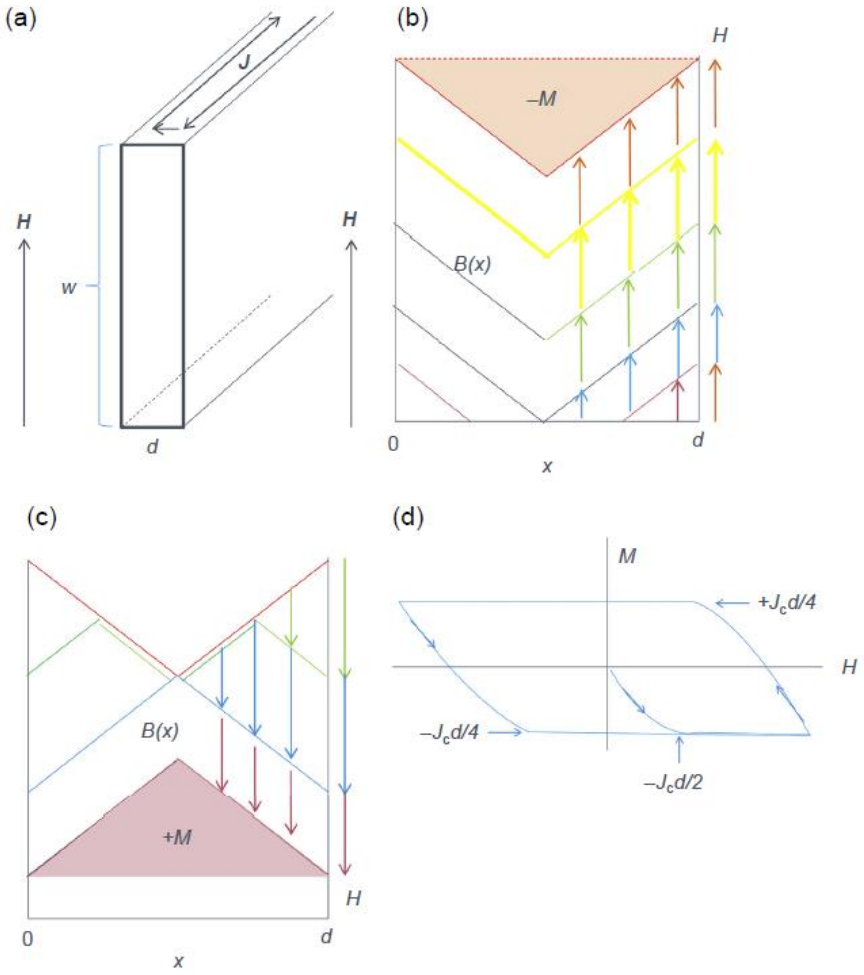

Figure B1:. In Bean's model magnetic field with strengths H is applied to the thin sample(a) and magnetic field B gradually enters the sample. Superconducting eddy currents prevent total penetration, but above $H=j_c d/2$ the whole sample is penetrated (b,d). With H lowering eddy currents are reversed lowering M and B untill M is comletely reversed (and equal to $M= + j_c d/4$, (c)). Thus, the hysteresis loop M vs. H is formed (d) (based on [3]).

C. Appendix – Ginzburg-Landau strong coupling limit

The critical current in this study was determined using a contactless method based on Bean's model of magnetic field penetration into the sample. The critical current versus temperature dependence was extrapolated to 77.3 K, which is the temperature of boiling nitrogen. The theoretical framework used to approximate the critical current is the Ginzburg-Landau (GL) theory, specifically the strong coupling approach.

In the GL theory, the kinetic energy of conduction electrons is compared to the energy gain resulting from the formation of the superconducting state. If the kinetic energy exceeds the energy of the superconducting state, the superconductivity is suppressed. This consideration gives rise to a thermal dependence of the critical current [4]:

J_c= const $H_c(T)/\lambda(T)$.

Similar formula can be obtained on grounds of London theory. Some approximation of penetration depth and critical magnetic fields: $\lambda \sim (1-t^4)^{-1/2}$, $H_c \sim 1-t^2$ results in celebrated GL strong coupling limit formula:

$J_c = J_{c0}(1-t)^n$, where n is exponent theoretically equal 1.5.

Obtained j_c can be interpreted as current of Cooper pairs breaking because of pinning. In experimentally obtained superconductors pinning force is not high enough to break the superconductivity carriers. Measured critical currents are at least order of magnitude smaller than predicted currents of pair breaking [5] but the power function for j_c is still valid.

The n exponent can be, however, slightly different than 3/2. It probably because not all factors were taken into account in theoretical description. Exponent n can depend on vortex behaviour in various temperatures as well as pinning force.

Appendix D – precursor formation

To synthesize high-quality thallium cuprate superconductors, a multi-step synthesis process is required. Initially, the precursors need to be synthesized, followed by the main reaction involving thallium. Subsequently, additional thermal treatment is often necessary to enhance the properties of the obtained superconductors.

The precursors serve as intermediate products in the synthesis of the superconductors. They consist of oxides of multiple metals and possess a polycrystalline structure. Various methods can be employed to synthesize these precursors from starting compounds. For Tl-1223 and Tl-2223, the starting compounds include oxides or salts of Ca, Sr, Ba, and Cu.

The inclusion of precursors in the superconductor synthesis process is essential due to the volatile nature of thallium oxide. This compound has a melting point of 717°C and boils at 875°C. Wrapping the material in silver foil can help slow down the evaporation of Tl_2O_3. However, the other starting compounds often require an extended period, typically a few days, in the solid-state reaction method. Without the presence of precursors, a significant amount of thallium oxide would evaporate before the other ingredients could react effectively. [6, 7].

$Ba_2Ca_2Cu_3O_x$ compound, which is commonly used in thallium superconductor synthesis, is not a single substance but rather a mixture of simpler yet still complex oxides. These oxides consist of the necessary metals for cuprate superconductor synthesis, namely barium, calcium, and copper. Additionally, strontium is considered due to its chemical similarity to barium and calcium, and it often replaces barium atoms in cuprate superconductors. The classification of these oxides can be based on the metals they contain, as well as the metal-metal molar ratio. However, it should be noted that compounds with the same metal-metal molar ratio can still exhibit variations in oxygen stoichiometry, which in turn affects lattice constants and, in some cases, crystal system. The chemistry of alkaline earth and copper oxides is quite diverse and has been extensively described in Ref. [8].

Barium (Ba), calcium (Ca), and strontium (Sr) have a valence of +II, which corresponds to the noble gas electron configuration of xenon (Xe), argon (Ar), and krypton (Kr), respectively. In complex oxides, oxygen is generally assumed to have a valence of -II, which corresponds to the electron configuration of neon. It is important to note that there are exceptions, such as compounds like BaO_2, which have different oxygen valences. With the uptake of oxygen in complex oxides, the valence of copper (Cu) can vary depending on how many of its 3*d* spin orbitals are filled with

electrons. This variation in Cu valence is an important factor in determining the properties of the complex oxide.

Table 1: Calcium copper oxides. Lattice symmetry according to Material Project

Composition	Crystal system	Stability	Characterised in
Ca_2CuO_3	Orthorhombic	Up to 1034°C	[9, 10]
$Ca_{1-x}CuO_2$, x=0.172	Tetragonal	Up to 755°C in air or 835°C in oxygen	10
$CaCu_2O_3$	Orthorhombic	985°C to 1018°C	[9,10]

In the case of calcium-copper oxides only 1:1, 1:2, and 2:1 stoichiometries were showed in [10]. "1:1" compound does not have an ideal 1:1 stoichiometry but in fact it is $Ca_{1-x}CuO_2$ with x=0.172. This compound is stable up to 755ºC. However, the 2:1 Compound is stable up to the high temperatures of 1034ºC. The last mentioned compound (1:2) is stable only in a narrow temperature range from 985ºC to 1018ºC.

In the case of strontium-copper oxides, there exist 2:1, 1:1, and 3:5 stoichiometries. 3:5 stoichiometry is in fact in the form $Sr_{14}Cu_{24}O_{41-x}$. 2:1 compound with calcium seems to be isostructural with 2:1 oxide with strontium and both share the same space group, Immm(71), belonging to the orthorhombic crystallographic system (Material Project). On the other hand, "1:1" strontium-copper and calcium-copper oxides have slightly different metal stoichiometry.

Table 2: List of barium copper oxides collected by [8] and [11].

Chemical formula	Crystal system	Characterized in:
$BaCuO_2$	Cubic	[12]
$BaCuO_{2.3}$	Tetragonal	[13]
$BaCuO_{2.5}$	?, Orthorhombic according to mp-772788 (Material Project)	[13]
$BaCuO_{2.63}$	-	Misidentified by [13] Turned out to be $Ba_2Cu_3O_{5+x}$ [14]
Ba_2CuO_3	Orthorhombic	[15]
$BaCu_2O_2$	Tetragonal	[16, 17]
$Ba_2Cu_3O_{5+x}$	Tetragonal	[18]
$Ba_3Cu_2O_{4+x}$		[19]
$BaCu_3O_4$	Orthorhombic	[20]
Ba_3CuO_4	Rhomboedric	[21]
$Ba_3Cu_5O_8$		[22]
$Ba_5Cu_3O_{6+x}$		[19]

There are nine barium-copper oxides described in the review article, Ref. [8]. Their cation ratios are 1:1, 2:1,1:2, 2:3, 3:2, 1:3, 3:1, 3:5, and 5:3. Phase diagrams presented in Ref. [11] show only 1:1, 2:1,1:2, and 2:3 stoichiometries and a single diagram does not show all of them.

Some barium-copper oxides, although the same metal-metal molar ratio, differ in oxygen content and crystallographic system. There are (Table 2) so: cubic $BaCuO_2$, tetragonal $BaCuO_{2.3}$, and orthorhombic $BaCuO_{2.5}$. Ref. [13] mentions the existence of $BaCuO_{2.63}$ but according to Ref. [14] it turned out to be another barium copper compound.

The most common $BaCuO_{2\text{-}2.12}$ reacts with additional oxygen with difficulty. For example at 350^{o}C in an oxygen atmosphere, only 2.1 oxygen stoichiometry is formed. Further heating of the $BaCuO_{2.1}$ compound at 600^{o}C causes oxygen loss to 2.0 stoichiometry. Reaction analogous to $BaNiO_2+1/2O_2=BaNiO_3$ is not observed [13].

Oxygen stoichiometry (alternatively Cu valence) can be determined in several methods. The most popular is iodometric titration. The simplified reaction in a flask is $O+H_2O+KI=KOH+I_2$. Iodine ions also lowers the Cu valence to +I [23]. Presence of molecular iodine is indicated by complex with starch. Also thermogravimetric analysis (TGA) can be useful to determine oxygen stoichiometry. When heated, sample loose oxygen and its mass lowers. Oxygen content has also influence on IR[Khan2010] and XRD [24, 25] sample spectra. Oxygen content has influence on size of crystalline cell.

Precursor synthesis can take place in various atmospheres. The easiest and most common gas choice is air. If someone uses oxygen as a gas surrounding the precursor it tends to be more oxidized. In the case of using inert gas as argon the synthesis product would be less oxidized than in the two mentioned cases [27].

More oxygen can be incorporated into the precursor crystalline structure of the product by using oxygen-rich substrates. According to [8] $BaCuO_{2.29\text{-}2.36}$ or $BaCuO_{2.5}$ is obtained from BaO_2 not from $BaCO_3$ or BaO.

Complex oxides differ in stability. They can decompose while interacting with humidity or CO_2 in the air. It is desired to have a stable precursor for further superconductor synthesis. Barium compounds such as $BaCuO_2$ and $Ba_2Cu_3O_5$ are generally stable. On the other hand, Ba_2CuO_3 is unstable in air. Ca_2CuO_3 and CaO have also good stability.

The general reaction of obtaining Tl-2223 (alternatively, after small modification, Tl-1223) reads:

$$Tl_2O_3+2BaCu_xO_{1+x}+2CaCu_{1.5-x}O_{2.5-x}\ (+O_2)=Tl_2Ba_2Ca_2Cu_3O_{10}. \quad (D.1)$$

Its realizations are for example:

$Tl_2O_3+2BaCuO_2+Ca_2CuO_3$ (+O2) $=Tl_2Ba_2Ca_2Cu_3O_{10}$ for x=1 (D.2) and

$Tl_2O_3+2CaCuO_2+Ba_2CuO_3$ (+O2)$=Tl_2Ba_2Ca_2Cu_3O_{10}$ for x=0.5 (D.3).

The general reaction contains also cases with simple oxides reacting: BaO for x=0 and CaO for x=1.5. The general reaction for x=0 needs $Ca_2Cu_3O_5$ but there is no experimental evidence of existing of this compound. For x=0.5 there is unstable barium-complex oxide (Ba_2CuO_3) and experimentally accessible $CaCuO_2$ has not exact 1:1 stoichiometry. For x=1 all reacting oxides exist and are stable. The x=1 (D.2) reaction is realized in this thesis to obtain superconducting thallium cuprates. Also, reaction with x=1.5 is potentially possible because the ingredients are stable.

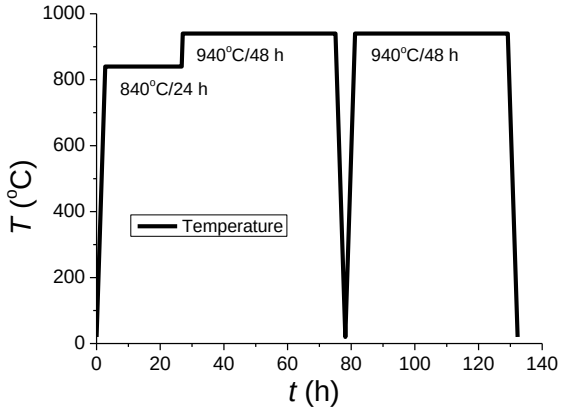

Figure D1: The temperature profile of the synthesis of the precursors

In this thesis, the author obtained precursors of $BaCuO_2$ and Ca_2CuO_3 in solid-state reaction method. Precursor-obtaining reactions follow the equations:

$BaCO_3+CuO = BaCuO_2+CO_2$ (D.4) and

$2CaCO_3+CuO=Ca_2CuO_3+2CO_2$ (D.5).

These reactions can be split into two processes: decarboxylation and bounding. This split has a reflection in the heating temperature profile (Fig. D.1). In the first stage 24 h at 840°C probably most of the decarboxylation takes place. When CO_2 has been removed from precursors the temperature is raised to 940°C and the bonding process – synthesis of complex oxides is believed to take place in what lasts 48 h. Then the powders are ground and heated once more at 940°C for 48 h to finish the reaction. The precursor heating and grinding schema is presented below (Fig. D.2). The grindings took place before, between, and after heating processes.

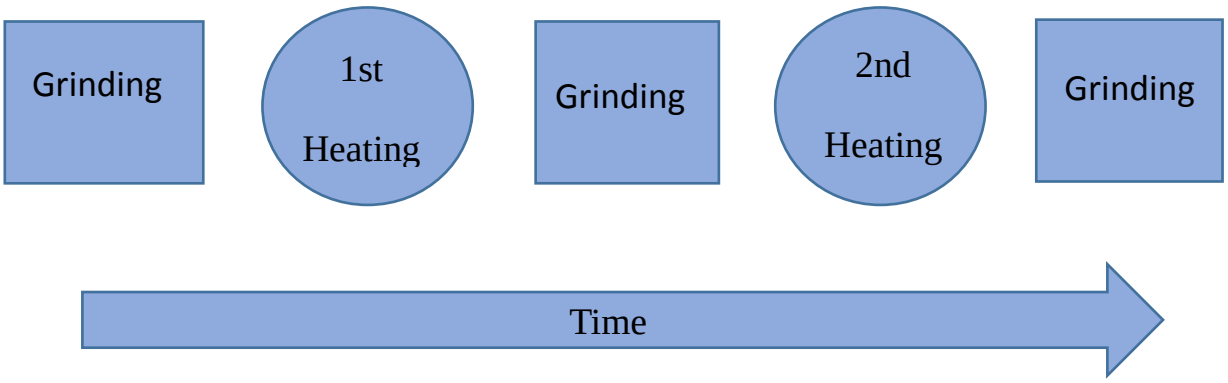

Fig. D2: Heating and grinding schema of precursor synthesis.

To synthesize a portion of precursors author used 4.1176 g of BaCO3, 1.6598 g of CuO, 2.0884 g of $CaCO_3$, and 0.8299 g of CuO. The accuracy of the weight of the ingredients is 1 mg. A larger amount of $BaCuO_2$ was limited by the size of the crucibles.

Here other methods of obtaining cuprate precursors are going to be mentioned. The precursors can be synthesized from carbonates [e.g. 26]. Another method is obtaining precursors from nitrates and simple oxides [27]. The ingredients can be also dissolved in the presence of a complexing agent [28]. After drying gel is formed and later it is calcined which results in obtaining the proper precursor.

The initial solvent in the sol-gel method does not have to be fully aquatic. Adding glycerine or ethanol to the solvent can improve the quality of the resulting superconductor. The transition width of the superconductor is smaller when the precursor was prepared in the presence of glycerine. This effect is explained by that various metal ions are bound to the same glycerine (or another complexing agent) molecule. The mixture is more homogenous in this case.

Preparing thallium cuprates via precursors can be done by many methods. The chemistry of alkaline earth and copper have been oxides detailly searched for after the discovery of oxide superconductors ([29]) which can be seen in e.g. review [8] and references therein. Some of these oxides were studied earlier [13, 30].

Appendix E

Appendix E collects XRD patterns of Tl-2223 material omitted in the main body of the thesis.

The initial presentation of the Tl-2223 sample will include the diffraction patterns of the oxygenated sample. Figure E.1 (9.3) displays the spectra of the stoichiometric Tl-2223 sample that has undergone oxygenation at 760°C for 20 hours. A similar result obtained from oxygenation at 740°C is presented in Figure E.2 (9.6). Additionally, Figures E.3 (9.1) and E.4 (9.7) showcase the diffraction patterns of the singly and doubly oxygenated samples with thallium excess, referred to as "Tl-2.2 2 2 2 3", respectively.

In Figure E.5 (9.8), a comparison is presented between the singly oxygenated Tl-2223 sample (#25a) and the doubly oxygenated Tl-2.2 2 2 3 sample (#30aa). These samples were selected as representative examples of the best-synthesized ones.

In the main text of the thesis, XRD patterns of Co-doped samples with various Co concentrations were presented. In Appendix E, Figure E.6 (9.10) displays the diffractogram of a nickel-doped Tl-2223 material with a doping level of x=0.0025 before and after oxygenation. This is provided as a comparison to the nickel-doped Tl-2223 material with a doping level of x=0.0050 before and after oxygenation, shown in Figure E.7 (9.11). Additionally, the XRD pattern of the gadolinium-doped sample (x=0.2) is presented in Figure E.8 (9.12).

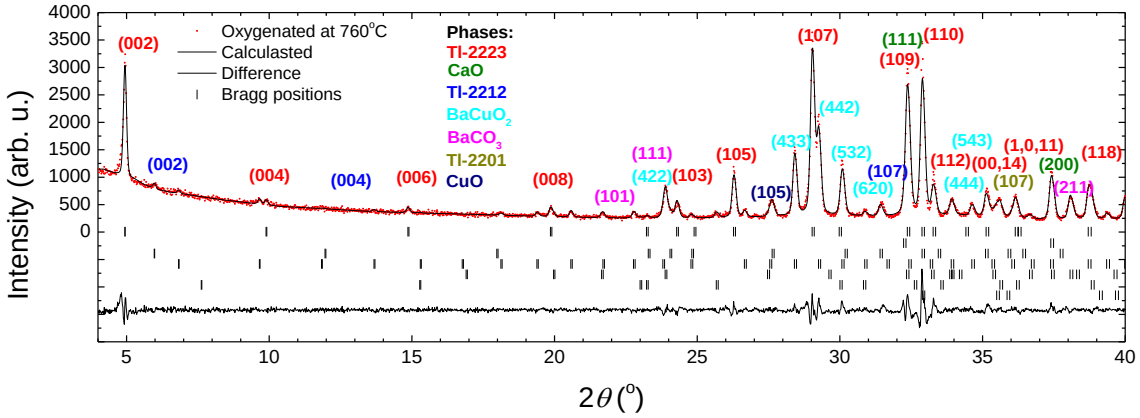

Figure E1: 9.3 XRD spectrum of Tl-2223 oxygenated at 760 °C for 20h. #54AN760

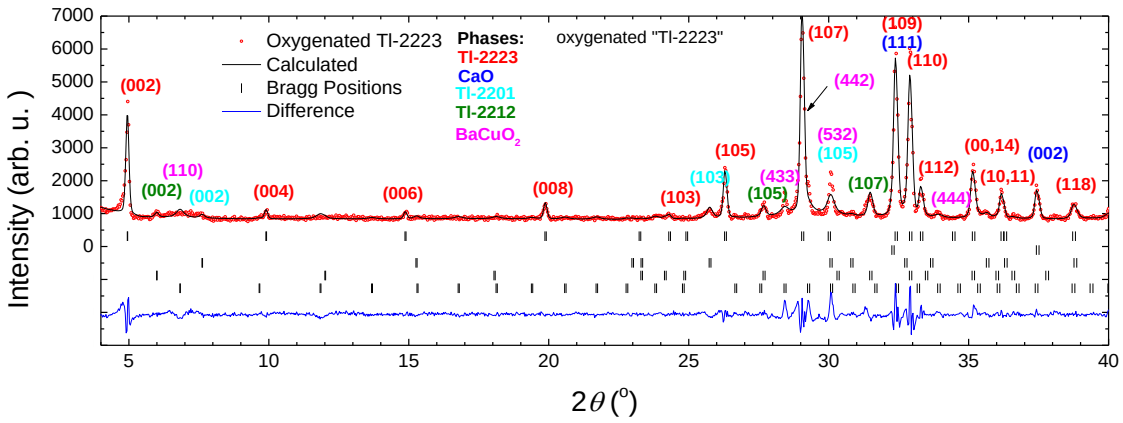

Figure E2: 9.6: 20 h oxygenated Tl-2223. #25a

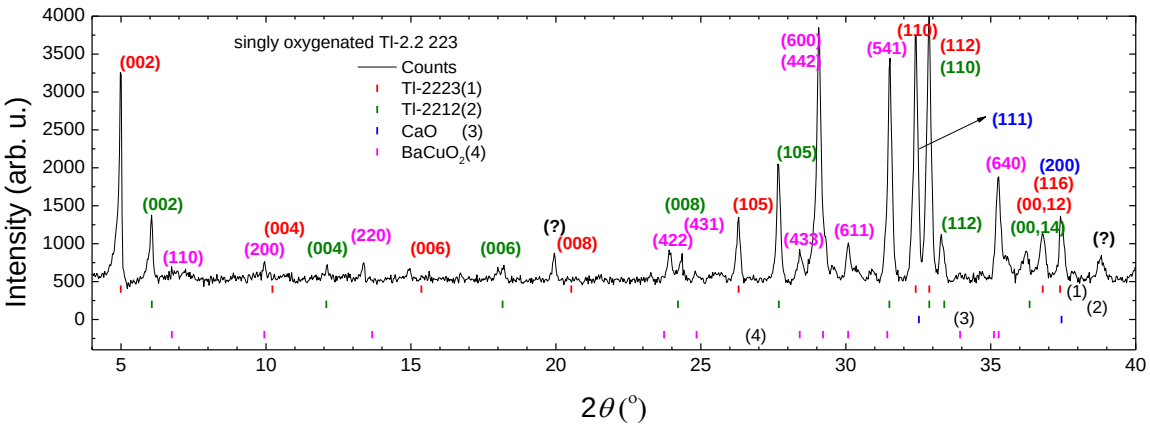

Figure E3: 9.1: XRD spectrum of Tl-2.2 2 2 3 oxygenated for 20h. #30a

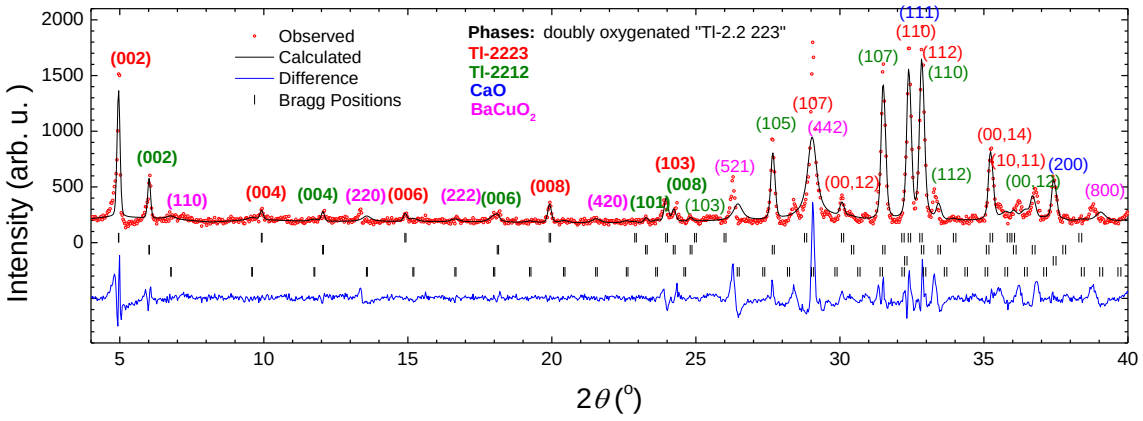

Figure E4: 9.7: Tl-2.2 223 doubly oxygenated Tl-2.2 2 2 3. #30aa

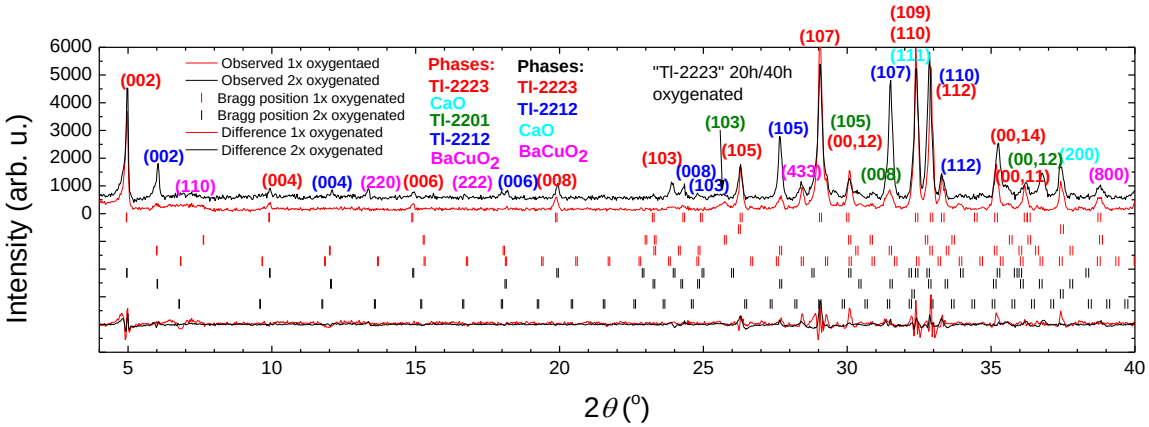

Figure E5: 9.8: Tl-2223 singly oxygenated and Tl-2.2 2 2 3 doubly oxygenated #25a and #30aa

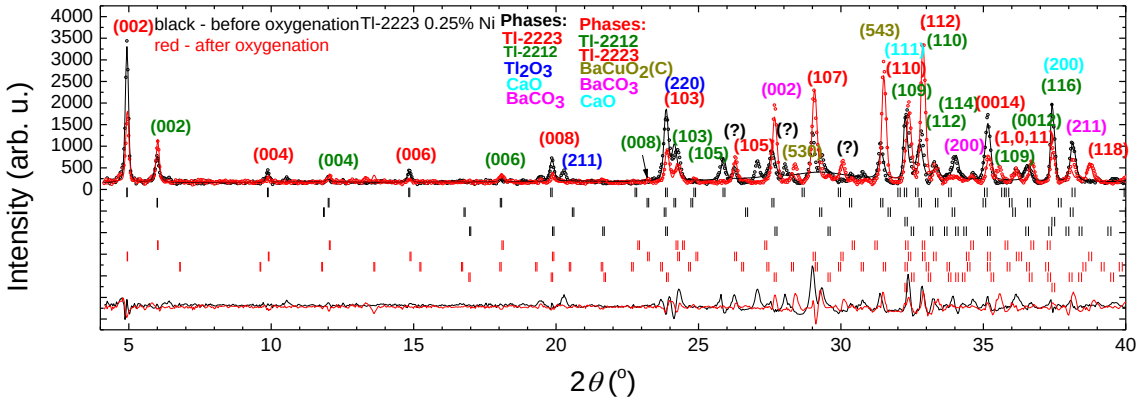

Figure E6: 9.10: Nickel doped Tl-2223 superconductors. 0.0025 of Ni atoms for three copper sites. Before (black) and after (red) the oxygenation.

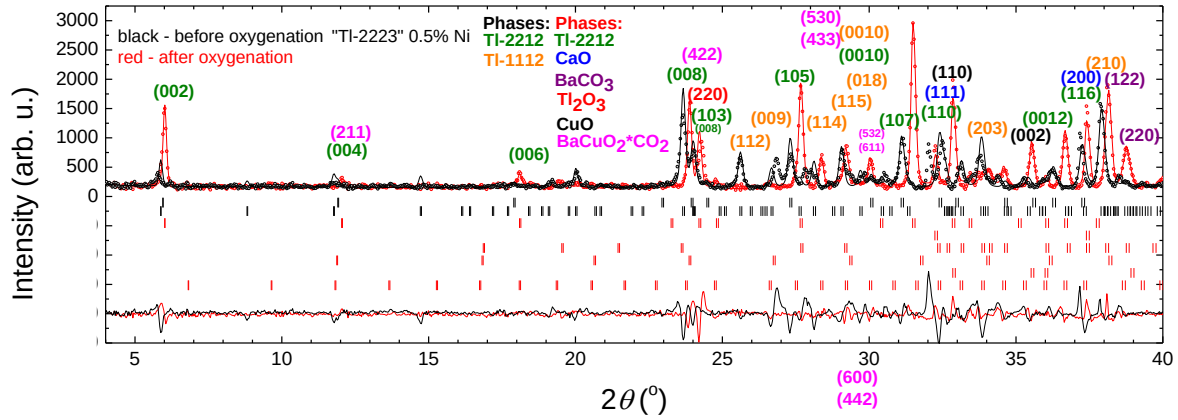

Figure E7: 9.11: Nickel doped Tl-2223 superconductor with doping of 0.0050 Ni atoms for three copper sites before and after oxygenation.

.

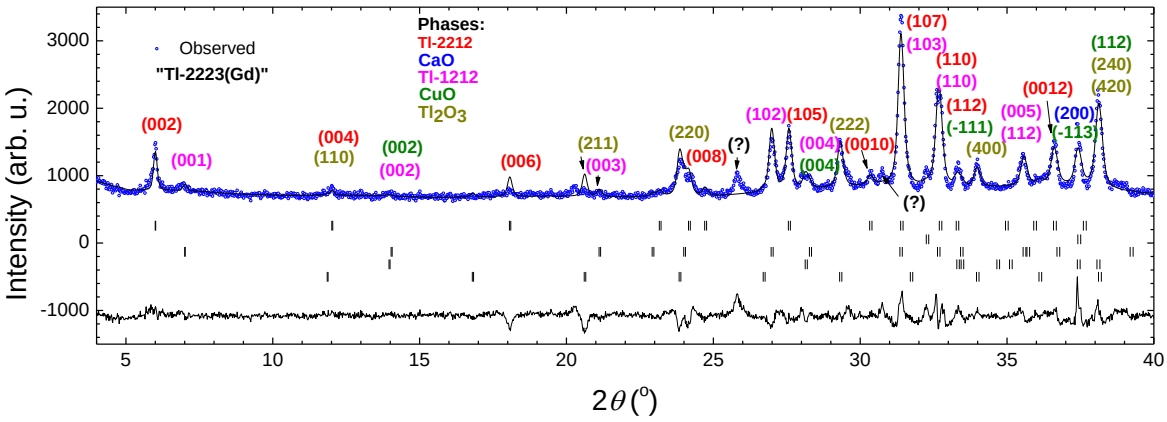

Figure E8: 9.12: Gadolinium doped thallium superconductor with doping of 20% before oxygenation. #32

Literature:

1. C. Bean, Magnetization of hard superconductors, Physical Review Letters **8** (6), 250-253 (1962) doi: 10.1103/PhysRevLett.8.250
2. H. London, Alternating current losses in superconductors of the second kind, Physics Letters **6**, 162-165 (1963) doi: 10.1016/0031-9163(63)90527-4
3. C. Rey and A. Malozemoff, Superconductors in the Power Grid, Materials and Applications, Woodhead Publishing Series in Energy, , (2015) isbn: 978-1782420293
4. G. Burns, High-temperature superconductivity – an introduction, Academic Press, (1991) isbn: 978-0121460907
5. R. Zalecki, Wnikanie pola magnetycznego i prądy krytyczne wysokotemperaturowych nadprzewodników talowych i bizmutowych, AGH-UST Kraków, PhD Thesis (2012)
6. E. Ruckenstein and C. Cheung, Reaction pathways in formation of the Tl-Ca-Ba-Cu superconducting phases, Journal of Materials Research **4** (5), 1116-1122 (1989) doi: 10.1557/JMR.1989.1116
7. S. Narrain and E. Ruckenstein, Effect of temperature on the formation of Thallium based superconductors, Superconductor Science and Technology **2** (4), 236-248 (1989) doi:10.1088/0953-2048/2/4/007
8. W. Wong-Ng and L. Cook, A review of crystallography and crystal chemistry of compounds in the BaO-CuO_x system, Powder Diffraction **9** (4), 280-289 (1994) doi: 10.1017/S088571560001900X
9. R. Roth *et al.* , Phase equilibria of the system SrO-CaO-CuO, Journal of the American Ceramic Society **72** (8), 1545-1549 (1989) doi: 10.1111/j.1151-2916.1989.tb07704.x
10. R. Roth *et al.*, Phase equilibria in the systems CaO-CuO and CaO-Bi_2O_3, Journal of the American Ceramic Society **74** (9), 2148-2151 (1991) doi: 10.1111/j.1151-2916.1991.tb08274.x
11. J. Whitler and R. Roth (eds.), Phase diagrams for high T_c Superconductors, The American Ceramic Society, Westerville (1991)
12. R. Kipka and H. Müller-Buschbaum, Uber oxocuprate, XX. Ein erdalkalioxocuprat (II) mit geschlossenen naugruppen: $BaCuO_2$, Zeitschrift für Naturforschung Teil B **32**, 121-123 (1977) doi: 10.1515/znb-1977-0201
13. M. Arjomand and D. Machin, Oxide chemistry. Part II. Ternary oxides containing copper in oxidation states -I, -II, -III, and -IV, Journal of the Chemical Society, Dalton Transaction **11**, 1061-1066 (1975) doi:10.1039/DT9750001061

14. A. Maiorova *et al.*, Thermochemical characteristics of nonstoichiometric $Ba_2Cu_3O_5$, II. Thermal transformation, Physica C **218**, 137-140 (1993) doi: 10.1016/0921-4534(93)90276-V
15. W. Wong-Ng *et al.*, Standard X-ray diffraction powder patterns of fifteen ceramic phases, Powder Diffraction **3** (1), 113-121 (1988) doi: 10.1017/S0885715600013130
16. D. Dube *et al*., Occurrence of $BaCu_2O_2$ in plasma-sprayed YBaCuO coatings, Materials Letters **9** (10), 353-356 (1990) doi: 10.1016/0167-577X(90)90065-T
17. Chr. Teske and H. Müller-Buschbaum, Alkaline earth metal oxocuprates. VI. On $BaCu_2O_2$, Zeitschrift für Naturforschung Teil B **27**, 296-301 (1970) doi: 10.1515/znb-1972-0314
18. I. Halash *et al*., Thermoanalytical and X-ray diffraction investigations of $Ba_2Cu_3O_{5+d}$ for preparation of Y-Ba-Cu-O superconductors, Journal of Crystal Growth **91**, 444-449 (1988) doi: 10.1016/0022-0248(88)90267-9
19. L. Klinkova, I. Soikina, and I. Romanenko, Phase transformation in the Y-Ba-Cu-O system, Zhurnal Neorganicheskoi Khimi **35**, 253-257 (1990)
20. A. Bertinotti *et al*., Structure of new type of satellite phase in $YBa_2Cu_3O_{7-d}$, Physica C **160** (3-4), 227-234 doi: 10.1016/0921-4534(89)90054-3
21. P. Abbattista *et al.*, Some equilibrium relationships in the barium rich part of BaO-CuO-O system, Materials Research Bulletin **23** (10), 1509-1520 (1988) doi: 10.1016/0025-5408(88)90277-2
22. D. De Leeuw *et al.*, Compounds and phase compatibilities in the system Y_2O_3-BaO-CuO at 950^{o}C, Physica C **152** (1), 39-49 (1988) doi: 10.1016/0921-4534(88)90071-8
23. N. Khan, CuTl-based high temperature superconductors, VDM Verlag Dr Müller, SaarBrücken (2010) isbn: 978-3-639-26844-7
24. B. Howe, Crystal structure and superconductivity of $YBa_2Cu_3O_{7-x}$, Minnesota State University, Master Thesis, (2014)
25. S. Miyoshi *et al.*, In situ XRD study on oxygen-excess $LaMnO_3$, Solid State Ionics **175** (1-4), 383-386 (2004) doi: 10.1016/j.ssi.2004.01.082
26. N.-L. Wu and E. Ruckenstein, A new method for the preparation of the superconducting $Tl_2CaBa_2Cu_2O_8$ compound, Materials Letters **7** (5-6), 169-171 (1988) doi: 10.1016/0167-577X(88)90003-1
27. S. Loureiro *et al*., The importance of the precursor in high-pressure synthesis of Hg-based superconductors, Physica C **272** (1-2), 94-100 (1996) doi: 10.1016/S0921-4534(96)00566-7

28. T. Brylewski *et al.*, Soft-chemistry synthesis of $Ba_2Ca_2Cu_3O_x$ precursor and characterization of high-T_c $Hg_{0.8}Pb_{0.2}Ba_2Ca_2Cu_3O_{8+\delta}$ superconductor, Journal of Advanced Ceramics **5**, 185-196 (2016) doi: 10.1007/s40145-016-0189-x
29. J. Bednorz and K. Müller, Possible high Tc superconductivity in Ba-La-Cu-O system, Zeitschrift für Physik B Condensed Matter **64**, 189-193 (1986) doi: 10.1007/BF01303701
30. H. Migeon *et al.*, Etude de la non-stechiometrie et des proprieties de $BaCuO_{2+x}$ (avec $0<x<0.12$), Revue de Chimie Minérale **14** (5), 498-502 (1977)